COMPUTATIONAL MODELING OF GLASS CURTAIN WALL SYSTEMS TO SUPPORT FRAGILITY CURVE DEVELOPMENT

Edward Gil

Thesis submitted to the Faculty of

Virginia Polytechnic Institute and State University

in partial fulfillment of the requirements for the degree of

Master of Science
in
Civil Engineering

Matthew R. Eatherton, Co-Chair

Georg Reichard, Co-Chair

Madeleine M. Flint

August 15, 2019

Blacksburg, Virginia

Keywords: Glass Curtain Walls, Fragility Curves, Multi-Hazards, Earthquake, Hurricane, Performance Based Engineering

COMPUTATIONAL MODELING OF GLASS CURTAIN WALL SYSTEMS TO SUPPORT FRAGILITY CURVE DEVELOPMENT

Edward Gil

ABSTRACT

With the increased push towards performance-based engineering (PBE) design, there is a need to understand and design more resilient building envelopes when subjected to natural hazards. Since architectural glass curtain walls (CW) have become a popular façade type, it is important to understand how these CW systems behave under extreme loading, including the relationship between damage states and loading conditions. This study subjects 3D computational models of glass CW systems to in- and out-of-plane loading simulations, which can represent the effects of earthquake or hurricane events. The analytical results obtained were used to support fragility curve development which could aid in multi-hazard PBE design of CWs.

A 3D finite element (FE) model of a single panel CW unit was generated including explicit modeling of the CW components and component interactions such as aluminum-to-rubber constraints, rubber-to-glass and glass-to-frame contact interactions, and semi-rigid transom-mullion connections. In lieu of modeling the screws, an equivalent clamping load was applied with magnitude based on small-scale experimental test results corresponding to the required screw torque. This FE modeling approach was validated against both an in-plane racking displacement test and out-of-plane wind pressure test from the literature to show the model could capture in-plane and out-of-plane behavior effectively.

Different configurations of a one story, multi-panel CW model were generated and subjected to in- and out-of-plane simulations to understand CW behavior at a scale that is hard to test experimentally. The structural damage states the FE model could analyze included: 1) initial glass-to-frame contact; 2) glass/frame breach; 3) initial glass cracking; 4) steel anchor yielding; and 5) aluminum mullion yielding. These were linked to other non-structural damage states related to the CW's moisture, air, and thermal performance. Analytical results were converted into demand parameters corresponding to damage states using an established derivation method within the FEMA P-58 seismic fragility guidelines. Fragility curves were then generated and compared to the single panel fragility curves derived experimentally within the FEMA P-58 study. The fragility curves within the seismic guidelines were determined to be more conservative since they are based on single panel CWs. These fragility curves do not consider: the effects of multiple glass panels with varying aspect ratios; the possible component interactions/responses that may affect the extent of damages; and the continuity of the CW framing members across multiple panels.

Finally, a fragility dispersion study was completed to observe the effects of implementing the Derivation method or the Actual Demand Data method prescribed by FEMA P-58, which differ on how they account for different levels of uncertainty and dispersion in the fragility curves based on analytical results. It was concluded that an alternative fragility parameter derivation method should be implemented for fragility curves based on analytical models, since this may affect how conservative the analytically based fragility curves become at a certain probability of failure level.

COMPUTATIONAL MODELING OF GLASS CURTAIN WALL SYSTEMS TO SUPPORT FRAGILITY CURVE DEVELOPMENT

Edward Gil

GENERAL AUDIENCE ABSTRACT

Performance-based engineering (PBE) can allow engineers and building owners to design a building envelope for specific performance objectives and strength/serviceability levels, in addition to the minimum design loads expected. These envelope systems benefit from PBE as it improves their resiliency and performance during natural multi-hazard events (i.e. earthquakes and hurricanes). A useful PBE tool engineers may utilize to estimate the damages an envelope system may sustain during an event is the fragility curve. Fragility curves allow engineers to estimate the probability of reaching a damage state (i.e. glass cracking, or glass fallout) given a specified magnitude of an engineering demand parameter (i.e. an interstory drift ratio during an earthquake). These fragility curves are typically derived from the results of extensive experimental testing of the envelope system. However, computational simulations can also be utilized as they are a viable option in current fragility curve development frameworks.

As it's popularity amongst owners and architects was evident, the architectural glass curtain wall (CW) was the specific building envelope system studied herein. Glass CWs would benefit from implementing PBE as they are very susceptible to damages during earthquakes and hurricanes. Therefore, the goal of this computational research study was to develop fragility curves based on the analytical results obtained from the computational simulation of glass CW systems, which could aid in multi-hazard PBE design of CWs. As

opposed to utilizing limited, small experimental data sets, these simulations can help to improve the accuracy and decrease the uncertainties in the data required for fragility curve development.

To complete the numerical simulations, 3D finite element (FE) models of a glass CW system were generated and validated against experimental tests. 11 multi-panel CW system configurations were then modeled to analyze their effect on the glass CW's performance during in-plane and out-of-plane loading simulations. These parametric configurations included changes to the: equivalent clamping load, glass thickness, and glass-to-frame clearance.

Fragility curves were then generated and compared to the single panel CW fragility curves derived experimentally within the FEMA P-58 Seismic Fragility Curve Development study. The fragility curves within FEMA P-58 were determined to be more conservative since they are based on single panel CWs. These fragility curves do not consider: the effects of multiple glass panels with varying aspect ratios; the possible component interactions/responses that may affect the extent of damages; and the continuity of the CW framing members across multiple panels.

Finally, a fragility dispersion study was completed to observe the effects of implementing different levels of uncertainty and dispersion in the fragility curves based on analytical results.

ACKNOWLEDGEMENTS

This work was supported by the National Science Foundation (NSF) under Grant No. CMMI-1455466. Any opinions, findings, and conclusions or recommendations expressed in this material are those of the authors and do not necessarily reflect the views of the National Science Foundation. In-kind funding was provided by Kawneer in the form of material donations to support the small scale testing. The authors acknowledge Advanced Research Computing at Virginia Tech for providing computational resources and technical support that have contributed to the results reported within this research study. URL: http://www.arc.vt.edu.

I would like to thank Dr. Matthew Eatherton and Dr. Georg Reichard for their continuous guidance and support throughout my research. A special thanks to Dr. Eatherton for being a great mentor and assisting me in my future engineering endeavors. Thank you to Dr. Madeleine Flint for being a part of my committee and providing me feedback. I would like to extend my gratitude towards Dr. Ioannis Koutromanos and Dr. Eric Jacques for their assistance to my questions related to FE analysis in ABAQUS and glass analysis, respectively. I appreciate the technical support and expertise provided by Kawneer's representatives regarding their curtain wall system. A special thanks goes out to Kawneer technical representative and Hokie alumni, Matthew Miller, for the continuous correspondence which proved integral in my research.

To my mom and dad, thank you for your support, guidance and prayers throughout my graduate studies, it has truly been a blessing. Thank you both for teaching me the importance of always putting my faith in God first in my life and in everything I do. Thank

you to Gabriel and the rest of those at CRBC for keeping me in your prayers as well. To all my friends here at Virginia Tech and back home, thank you all for the support you have given me. A special thanks to Cody, Mehrshid, Raul, Bishal, Amir, Joey, Wendy, and Kumar for helping me make my time here at Virginia Tech so memorable.

TABLE OF CONTENTS

LIST OF FIGURES

LIST OF TABLES

Chapter 1

Introduction

1.1. Background

In today's built environment, the use of architecturally attractive and modern building envelopes for many low-, mid- and high-rise buildings has become more desirable for building owners. Therefore, due to its lightweight, aesthetic appeal and ease of construction, the architectural glass curtain wall (CW) system as shown in Figure 1-1 has been used more prevalently as a popular façade choice by architects. In light of glass curtain wall damages observed during recent natural hazard events, particularly earthquakes and hurricanes, engineers have begun moving towards developing and implementing performance-based engineering (PBE) design methods and tools to improve the resiliency of building envelopes during these natural hazards.

a) Loyola University Chicago Marcella Niehoff School of Nursing, Maywood, Illinois (Kawneer 2019a)

b) Great America Building, Cedar Rapids, IA (Architectural Engineering Institute 2013)

Figure 1-1: Examples of glass curtain wall systems

1.2.Motivation

A useful tool implemented for PBE design of structural and non-structural components of buildings is a fragility curve. Fragility curves allow engineers to estimate the probability of reaching a damage state (e.g. glass cracking, or glass fallout) given a specified magnitude of an engineering demand parameter (e.g. specified magnitude of interstory drift ratio). As a result, research over the years has been completed for the development and implementation of these fragility curves to assist in PBE design and analysis specifically for glass curtain wall systems.

For instance, in support of the FEMA P-58 PBE methodology for earthquakes, implementation of a fragility curve development framework has been established based on relevant structural damage states observed during experimental testing of glass CWs. However, this has led to a rather limited seismic fragility database for a selected number

of glass CW configurations. Additionally, the main damage states observed for these fragility curves were related to structural limit states (i.e. serviceability and ultimate limit states) at the CW component level such as gasket/seal degradation, glass cracking, and glass fallout. Unfortunately, a similar PBE methodology for fragility curve development based on glass CW's subjected to hurricane related hazard aspects has not yet been established. The generation and implementation of fragility curve development methods for hurricane events is necessary for engineers to be able to practice multi-hazard PBE design during the preliminary design phase for these CW systems.

Another issue is that the results required for earthquake related CW fragility development are primarily gathered from experimental tests on different CW configurations. Additionally, the seismic fragility framework requires numerous experimental tests be run for a CW configuration to account for various levels of uncertainty and variability in a set of results. However, engineers can be limited to obtaining small data sets due to the costs of implementing these experiments. Using small data sets ultimately can lead to inaccuracies and larger uncertainties in the generated fragility curves which leads to inaccuracies in PBE of CW systems.

As an alternative to executing experimental tests, engineers can perform numerical analyses to predict the in-plane or out-of-plane glass curtain wall behaviors due to an earthquake or hurricane event, respectively. Even though there is no specified numerical analysis procedure in the current glass CW seismic fragility framework, it does account for using drift capacity results derived from the analytical modeling of CWs. Similarly, within the structural building codes (i.e. IBC and ASCE 7) for structural and non-structural components, it is stated that engineering analysis (i.e. numerical analysis) can be completed

in lieu of experimental results to obtain specified capacity limits. Numerical analysis using finite element (FE) modeling of CWs has proven to be a cheaper alternative to experimental tests. Previous analytical FE attempts have separately captured in-plane and out-of-plane responses observed in earthquakes and hurricanes, respectively. The previous simplified FE modeling procedures and assumptions implemented in approximating the CW system's response with such models has worked to an extent to help approximate structural damage states (i.e. glass cracking). However, it would be advantageous for engineers to only generate one FE model to run both in-plane and out-of-plane simulations. Also, key complex component interactions have not been explicitly modeled in previous approximate FE models. Modeling of such component interactions can lead to key structural damage states being analyzed, and subsequently non-structural damage states. In this study, non-structural damage states are related to limit states that have been reached due to a breach in one of the CW envelope barriers as a result of structural damages during a hazard event. These barriers in a CW envelope must protect the building interior from moisture, air, vapor, and thermal impacts. Therefore, it is beneficial to have an FE model that can better represent key structural interactions to capture additional key structural damage states, which in turn capture non-structural damage states as well.

In summary, it is necessary to: 1) capture additional key CW damage states which have been observed during experimental tests or natural hazard events (i.e. earthquakes and hurricanes) through the explicit modeling of CW components and component interactions within the CW system; 2) develop enhanced FE models that can capture both out-of-plane and in-plane behaviors necessary for multi-hazard analysis; and 3) implement the enhanced FE models and simulations as a validated numerical analysis method for approximating

damage states in glass CWs analytically. These analytically derived damage state results obtained can then be utilized for the development of seismic-related and hurricane-related fragility curves needed in multi-hazard performance based engineering of glass CWs.

1.3. Research Objective

The first objective of this computational research study is to develop 3D non-linear finite element models of architectural glass curtain walls that can be subjected to generalized in-plane racking displacements and out-of-plane uniform pressures. Both of which are related to earthquake and hurricane intensity measures, respectively. Once validated against experimental results, these non-linear FE models will be able to approximate important structural behaviors (i.e. stress propagation on CW components). Likewise, interactions of a glass curtain wall system during either generalized loading simulation can be modeled due to explicit modeling (i.e. generating extrusions of cross-sections) of CW components and the interactions between the different components. These interactions will include: 1) aluminum-to-rubber constraints 2) rubber-to-glass interactions/constraints 3) glass-to-frame interactions and 4) semi-rigid transom-mullion framing connections. In doing so, occurrences of key structural damage states related to either natural hazard events can be approximated such as: 1) glass-to-frame contact 2) glass cracking and 3) glass/frame breach. As a result, approximation of when non-structural damage states (i.e. water intrusion and air infiltration related damages) may occur in such hazard events will be possible as well. Likewise, explicit modeling of CW components would allow for examining different variations in CW configurations. This was not easily

replicated/justified in previous simplified FE models since these incorporated simplified assumptions to capture each component behaviors during simulations.

The second objective will be to enlarge the validated glass curtain wall system model to represent a larger CW section containing multiple glass panel sizes. A set of different configurations of this designed CW section will be modeled to represent CWs which could be designed, constructed, and observed in the field. To replicate a CW system attached to an actual structural system, steel anchor connections were also generated to observe additional damage states such as 1) yielding of the steel anchors and 2) yielding of the aluminum mullion members. With these different configurations of the larger scale glass CW models, in-plane displacement and out-of-plane uniform pressure loading will be applied in separate analysis simulations to approximate when and how each damage states related to each hazard event can occur. These results will then be converted into the required fragility parameters necessary for the development of fragility curves for seismic events and hurricane events, the primary focus of this study.

The purpose for these objectives is twofold: 1) Reinforce the effectiveness of implementing 3D finite element model as an established and valid numerical analysis method for completing the analysis of glass curtain walls subjected to in-plane and out-of-plane simulations, an alternative to carrying out experimental tests; 2) Establishes an analytical approach which can be used in engineering practice today to develop fragility curves required to complete multi-hazard performance based engineering of glass CW's during the preliminary design phase of a project. Development of these fragility curves can help engineers design for more resilient building envelopes for different hazards as a result. This is accomplished due to the approximation of certain earthquake- and hurricane-related

damage states that may occur during each simulated scenario, which are required in creating fragility curves for glass curtain walls for these types of hazard events.

1.4. Scope

To create sets of refined non-linear 3D finite element models of glass curtain walls that can be subjected to in-plane and out-of-plane loadings for fragility curve development, several tasks were executed to make this computational study viable. The following tasks were carried out:

1) Conduct a literature review that encompasses the background of architectural glass curtain walls; current design/performance criteria; applicable damage states observed for earthquake and hurricanes events; an overview of previous FE modeling attempts of glass curtain walls; and CW related fragility curves.
2) Identify a glass curtain wall system to base the initial FE model after, to represent a common configuration used in practice.
3) Find earthquake-related and hurricane-related experimental test studies of glass CW subjected to in-plane displacements and out-of-plane wind pressures, respectively. Results from studies will be used for the validation of the FE model.
4) Complete a small scale experimental test study to determine the equivalent clamping force produced at a screw located along the CW pressure plate

which is tightened up to a required screw torque. The force obtained will be implemented in the FE model.

5) Generate a non-linear 3D finite element model of one glass curtain wall unit, containing a 6’ x 5’ glass panel, which can approximate both in-plane and out-of-plane structural behavior within the same model. Validate the model with sets of experimental studies and allow for necessary calibration of model to better capture complex interactions observed within CW unit.
6) Based on what the FE model can accurately capture, identify a set of in-plane and out-of-plane related structural damage states that can also equate to non-structural damage states (i.e. air infiltration and water intrusion damage states).
7) Create a larger FE model that contains a one-story glass CW section containing multiple glass panel sizes using techniques previously implemented in the validated single unit CW. This larger CW section will be based on and representative of what is designed, constructed, and observed in the field.
8) Conduct a parametric study on the large scale CW section to observe how different configurations effect the structural behavior of the CW subjected to either generalized in-plane or out-of-plane simulations. Record when earthquake- and hurricane-related damage states occur during these FE simulations.

9) Account for different levels of uncertainty and dispersion resulting from using this FE modeling approach and see how these affect the development of a set of fragility curves from the larger CW section.
10) Develop a set of fragility curves for the identified damage states resulting from the larger CW models subjected to in-plane and out-of-plane simulations. These are related to seismic story drift and hurricane wind pressures, respectively.

1.5. Thesis Overview

This thesis will include seven chapters. The first chapter consists of a brief background overview on the current glass curtain wall topic, research motivation, objectives and the scope of the project. The scope highlights what will be carried out in this study to develop fragility curves for glass curtain walls subjected to earthquake- and hurricane-related finite element simulations.

The second chapter presents a literature review on the background of architectural glass curtain walls and related design/criteria measures, earthquake- and hurricane-related damage states observed either in reconnaissance reports or experimental tests, previous FE modeling attempts, and fragility development. This chapter will also give an overview on the two experimental testing studies which will be used to validate the FE model generated herein for in-plane and out-of-plane loading.

The third chapter will go over the experimental testing of a glass CW frame specimen to determine the equivalent clamping force provided by the required screw torque, which is applied to keep the glass in place within the glazing unit.

The fourth chapter will go into the development of a glass CW 3D finite element model and the consequent calibration of the model. It will also include the validation section in which the refined, calibrated model analysis will be compared to in-plane and out-of-plane experimental test results presented in Chapter 2.

The fifth chapter will go over the generation of the larger scale, one-story tall glass curtain wall model and the accompanying set of varying CW configurations; the identification of the relevant damage states focused on during each hazard simulation; and the results obtained during each of the in-plane and out-of-plane simulations.

Chapter 6 will go over the development of a set of fragility curves using the damage state results found in Chapter 5. And it will highlight the effects of accounting for dispersions (a fragility parameter) on a few fragility curves created.

Finally, the seventh chapter will present a summary of the findings in this analytical research study and include a discussion of future considerations and developments.

Chapter 2

Literature Review

2.1 Architectural Glass Curtain Walls in Practice/Design

As one of the most predominantly constructed façade system in the built environment today, glass curtain wall systems have been the most popular choice for architects and building owners out of all the types of glazed façade systems. The aesthetic appeal, lighter components and ease of construction is what drives its popularity in low- and mid-rise building. It is also commonly implemented in high-rise structures as well. Curtain walls have been around since the early 1900's, becoming popular as aluminum extrusion production increased due to the availability of aluminum materials for use after World War II (Vigener and Brown 2016a). Since then curtain walls have come in various configurations and combined different materials within the aluminum frame openings such as: light natural thin stone, metal cladding, brick veneer, pre-cast concrete, glass fiber-reinforced concrete (GFRC), fiber-reinforced plastics (FRP), terra cotta, and architectural glazing (glass) (Architectural Engineering Institute 2013; Vigener and Brown 2016b). For the architectural glass curtain wall, the focus of this study, the structural glass panels fitted within the aluminum framing systems are what acts as the protective shield for the building enclosure against the outdoor environment and from most normal weather and climate conditions. As such, the glass curtain wall must be designed and constructed to create a

manageable and comfortable interior environment for the people residing or working in the building.

2.1.1 Typical Performance Requirements/Criteria of Architectural Glass Curtain Walls

As already stated, the primary focus of the architectural glass curtain wall (CW) is to act as a protective skin for the building enclosure as the building's main defense against a wide range of weather elements that can occur in the structure's vicinity. The four primary elements that designers and engineers must design for are air, heat, moisture and vapor (Ander 2016; Barluenga et al. 2016; Vigener and Brown 2016b). Occupants are usually protected against these elements by an enclosure system that utilizes different layers in a general wall system. For the glass curtain wall system, the structural glass panel is the main layer of protection against these four elements. Further protection is provided with other CW components along material interfaces, such as the sealants or rubber gaskets as seen in Figure 2-1, as it is installed into the CW framing system. In addition to protecting against these primary elements, the components in a glass curtain wall system must be able to survive natural hazards during its lifespan such as hurricanes, earthquakes, or tsunamis while still keeping its aesthetic appeal such as the natural lighting and lightweight illusion they provide.

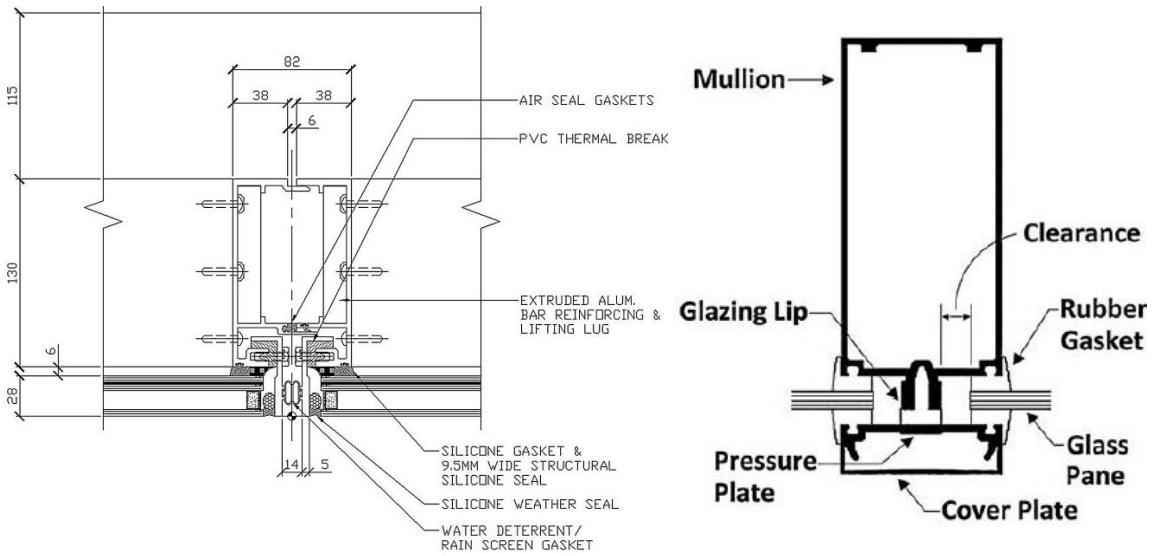

a) Plan view of a structural silicone glazing (SSG) curtain wall system; wet-glazed

b) Plan view of a dry-glazed stick built glass curtain wall system

Figure 2-1: Plan view of two general types of glass curtain wall system configurations and components (Architectural Engineering Institute 2013)

Currently, these curtain wall systems are considered as a non-structural component in most standard building codes, such as in ASCE 7-16, for seismic and wind designs (American Society of Civil Engineers 2017). The codes are meant to help such non-structural systems perform well enough to not cause safety concerns and loss of life. However, the CW's performance after the hazard event is not the primary focus of these designs. This causes a higher loss of functionality which leads to higher repair/replacement costs after such events. That is why a big thrust towards implementing performance-based engineering (PBE) designs for glass curtain wall systems has initiated due to the increased benefit of designing enclosures to remain functional and resilient after natural hazard events. While not fully developed or incorporated into practice, current PBE frameworks assisting in the design of glass curtain walls have primarily been developed for

earthquakes, as has been completed by FEMA and the ATC using experimental tests (Memari et al. 2011a). The same cannot be said for glass CWs designed for hurricane events as similar PBE frameworks have not yet been developed. While these performance-based engineering design protocols are still being developed, as will be discussed later on in this study herein, there are still many standardized test protocols that engineers and contractors can use to test the design and construction quality of glass CW's to make sure they meet design loads in addition to providing protection against the primary weather elements mentioned earlier.

2.1.1.1 Typical Wind Testing Protocols for Glazing Systems

As will be presented in the following sections based on researched literature, it is evident that there are more test protocols for curtain wall performance against wind/windstorm events than there are for seismic events. Although not fully comprehensive, below is a representative list of the most common test protocols that engineers and architects can choose from to test the glass curtain walls performance due to out-of-plane loadings and weather elements, both for lab and field testing. The list of out-of-plane test protocols include:

ASTM E283 (Lab)	Test Method for Determining Rate of Air Leakage Through Exterior Windows, Curtain Walls, and Doors Under Specified Pressure Differences Across the Specimen
ASTM E330/330M (Lab)	Test Method for Structural Performance of Exterior Windows, Doors, Skylights and Curtain Walls by Uniform Static Air Pressure Difference

ASTM E331 (Lab)	Test Method for Water Penetration of Exterior Windows, Skylights, Doors, and Curtain Walls by Uniform Static Air Pressure Difference
ASTM E783 (Field)	Test Method for Field Measurement of Air Leakage Through Installed Exterior Windows and Doors
ASTM E997 (Lab)	Test Method for Evaluating Glass Breakage Probability Under the Influence of Uniform Static Loads by Proof Load Testing
ASTM E998 (Lab)	Test Method for Structural Performance of Glass in Windows, Curtain Walls, and Doors Under the Influence of Uniform Static Loads by Nondestructive Method
ASTM E1233/E1233M (Lab)	Test Method for Structural Performance of Exterior Windows, Doors, Skylights and Curtain Walls by Cyclic Air Pressure Differential
ASTM E1886 (Lab)	Test Method for Performance of Exterior Windows, Curtain Walls, Doors, and Impact Protective Systems Impacted by Missile(s) and Exposed to Cyclic Pressure Differentials
ASTM E1996 (Lab)	Specification for Performance of Exterior Windows, Curtain Walls, Doors, and Impact Protective Systems Impacted by Windborne Debris in Hurricanes

For all the ASTM test procedures completed in the lab, as indicated above, the standard testing apparatus used is an air pressurized test chamber which can hold either a glass curtain wall specimen vertically as shown in Figure 2-2 (E06 Committee 2004, 2013, 2014a; b, 2016a, 2017), or just the structural glass panel specimen. For the latter configuration, the glass panel is held within a special frame that similarly represent the simply supported boundary conditions within actual CW aluminum frames as shown in Figure 2-3 (E06 Committee 2012, 2015). Using controlled air pressure differentials within the chamber, uniform wind pressures can be applied statically (E06 Committee 2004, 2012, 2014a, 2015, 2016a) or cyclically (E06 Committee 2013, 2014b, 2017) onto the various test specimens. Besides air pressures, additional conditions can also be added such as debris impacts (E06 Committee 2013, 2017) and water pressures (E06 Committee 2016a) to

capture more realistic conditions during hurricanes or typical windstorms. At the end of these procedures, the engineer can have a better understanding of how their glass CW performs, specifically the aluminum framing system, seals and structural glass unit, when tested for their structural resistance, resistance against airflow infiltration and/or water infiltration, and debris/missile impact resistance (E06 Committee 2004, 2012, 2013, 2014a; b, 2015, 2017).

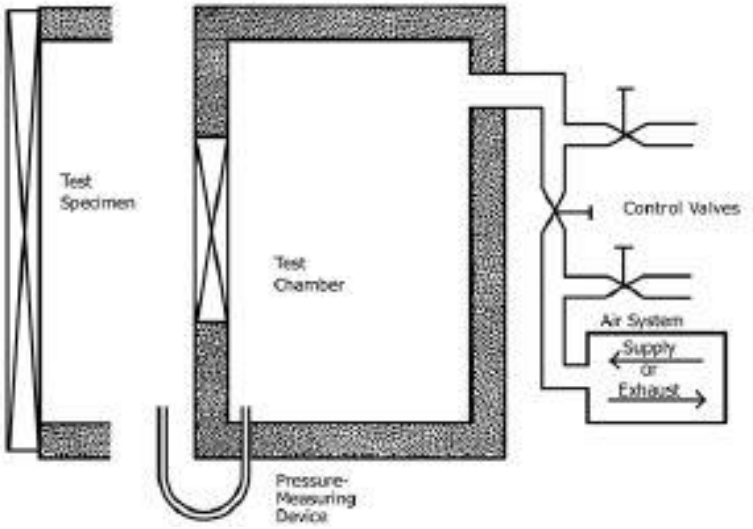

Figure 2-2: General test apparatus layout for standardized tests of curtain wall specimens (E06 Committee 2014a)

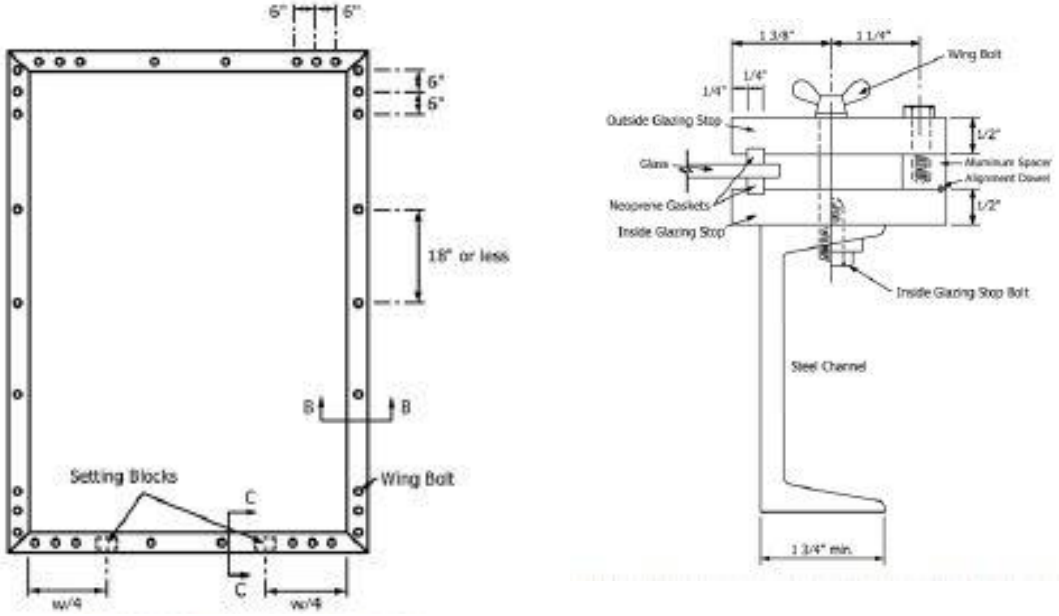

Figure 2-3: Plan and section view of a general test frame for supporting a glass panel during standardized tests (E06 Committee 2015)

Since the design of glass curtain walls is a fairly open ended process, engineers have to look to multiple design guides that can aid in their design procedures for these CW systems against out-of-plane loading. One such guide that the IBC refers to is the AAMA TIR-A11 document that helps in setting maximum deflection limitations for framing systems that contain brittle materials such as the glass CW (International Code Council, Inc. 2015). The AAMA TIR-A11 maximum deflection criteria is as follows: for aluminum framing members up to 13'-6" the max deflection is set at L/175, for members above 13'-6" it is L/240 + ¼" (American Architectural Manufacturers Association 2015).

2.1.1.2 Typical Seismic Testing Protocols for Glazing Systems

In the literature there are few seismic design provisions that engineers can follow to help with the design of these glass curtain walls. In the ASCE 7-16, engineers can look in the seismic design chapters for the architectural components section to find general design criteria that must be satisfied for glass in glazed curtain walls ((American Society of Civil Engineers 2017). During seismic events there is relative in-plane displacement of the glass panel within the CW framing system as increasing story drift occurs due to the dynamics of a seismic event. Thus, engineers are required by ASCE 7-16 equation 13.5-2., as shown below in Equation 2-1, to make sure that the relative seismic displacement of a glass curtain wall component under consideration, D_{pl}, does not exceed the relative displacement when glass fallout is observed, $\Delta_{fallout}$.

$$\Delta_{fallout} \geq 1.25\ D_{pl} \tag{2-1}$$

However, an exception within ASCE 7-16 states that if the engineer provides enough clearance between the glass panel edges and the frame, then the glass curtain wall does not need to satisfy ASCE equation 13.5-2, but rather it must satisfy ASCE equation 13.5-3 which is shown in Equation 2-2:

$$D_{clear} \geq 1.25\ D_{pl} \tag{2-2}$$

where the D_{clear} is the relative seismic displacement along the curtain wall component where an initial glass-to-frame contact has occurred. D_{clear} can then be calculated for rectangular glass panels using Equation 2-3 below:

$$D_{clear} \geq 2c_1\left(1 + \frac{h_p}{b_p}\frac{c_2}{c_1}\right) \quad (2\text{-}3)$$

where c_1 and c_2 are the vertical and horizontal glass-to-frame clearances, respectively, and h_p and b_p are the glass panel height and width, respectively (American Society of Civil Engineers 2017). A schematic drawing of this glass clearance concept and how the above equation can be derived with rectangular panel geometry is shown in Figure 2-4.

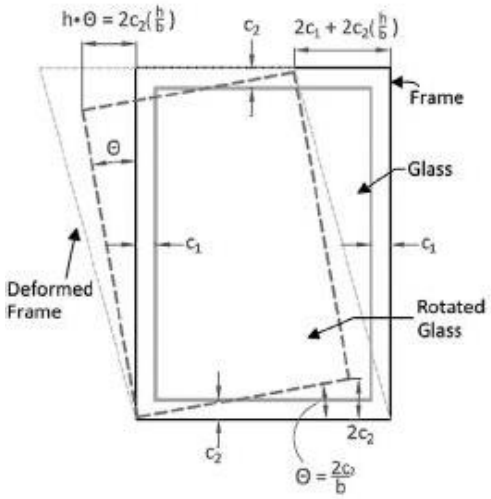

Figure 2-4: Geometric parameters illustrated for the derivation of equation determining drift at initial glass-to-frame contact (Architectural Engineering Institute 2013)

Another way that glass curtain wall designers can validate their design for its seismic performance is by testing the systems with in-plane testing protocols set by the American Architectural Manufacturers Association (AAMA). These protocols are displacement racking test procedures which are performed in the lab on a single glass curtain wall panel or a section of the glass curtain wall system. The main protocols are:

AAMA 501.4	Recommended Static Test Method for Evaluating Curtain Wall and Storefront Systems Subjected to Seismic and Wind Induced Interstory Drifts
AAMA 501.6	Recommended Dynamic Test Method for Determining The Seismic Drift Causing Glass Fallout from a Wall System

Both tests must be carried out on a test apparatus (example shown in Figure 2-5) that can hold the specimen between two sliding steel members and attached onto them in a manner closely matching how these framing systems are anchored to building floors in the field. If employing AAMA 501.4, the glass curtain wall specimen has a static monotonic displacement applied horizontally up to a design displacement so that serviceability limit states can be evaluated for such as air infiltration, water penetration and structural integrity (AAMA 2009a). When enlisting AAMA 501.6, the horizontal racking is applied dynamically in a cyclic crescendo protocol that ramps up the displacement amplitude in an incremental concatenated sine wave, which includes ramp up and constant cycles as shown in the Figure 2-6 (AAMA 2009b). This dynamic procedure assists in evaluating the drift that causes ultimate limit states that occur during an excessive amount of story drift to the curtain wall specimen, specifically the glass fallout, $\Delta_{fallout}$ (AAMA 2009b). AAMA 501.6 states that the glass fallout occurs when a glass fragment of at least 1.0 in^2 (645 mm^2) is observed to have fallen out of the glazing system during the cyclic racking protocol. Subsequently, engineers can use this glass fallout drift in ASCE 7-16 equation 13.5-2 to see if it satisfies the relative seismic drift limit.

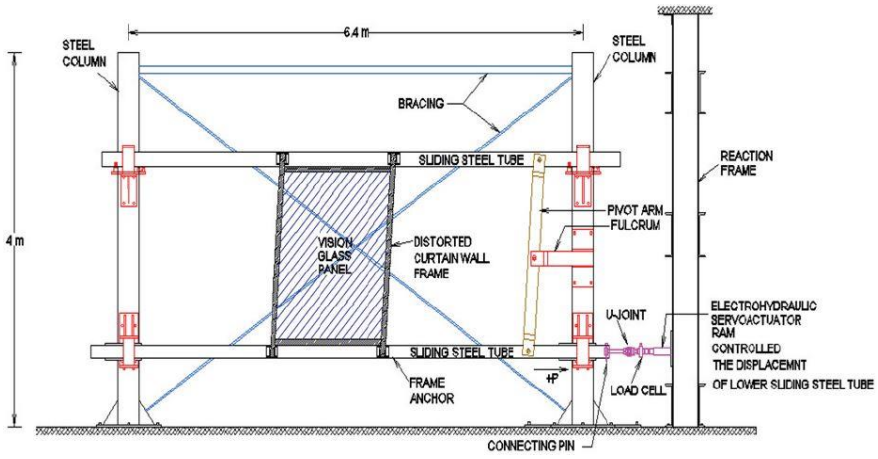

Figure 2-5: Typical racking test apparatus for various curtain wall mock-up configurations (Memari et al. 2011a)

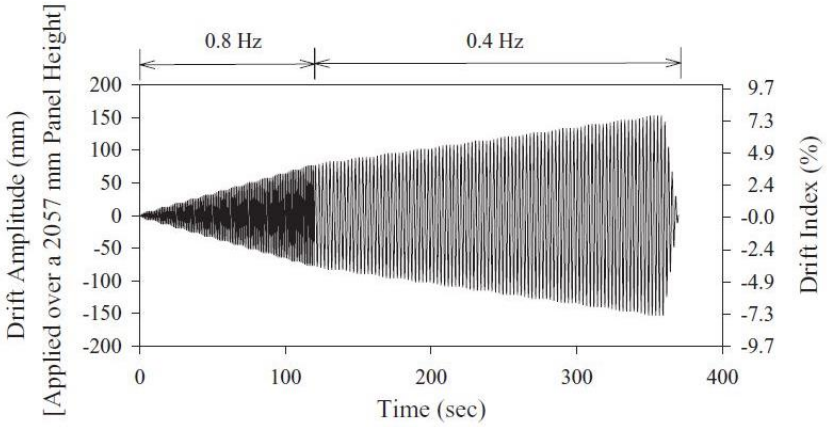

Figure 2-6: Standard drift time-history for dynamic racking crescendo test implemented in AAMA 501.6 for glass curtain wall mock-ups (Architectural Engineering Institute 2013)

2.2 Architectural Glass Curtain Wall Configurations Effecting Performance

Curtain walls in general are considered non-load bearing because they do not support or carry any of the vertical dead loads from the building structure, other than their own self-weight. However, they must also resist live loads produced by out-of-plane wind

pressures which are applied per transverse area. The common load path continued from this applied pressure onto the glass is then distributed through the mullions in the CW framing system, and then into each of the supporting steel anchor connections which are attached to the structural system.

Curtain walls are also different from infill façade types because they are actually supported and hung off the face of a building structure, specifically by connecting the vertical mullions to the structure's floors (concrete floor slabs, steel girders, composite beams, etc.) with the use of anchorage devices as shown in Figure 2-7. For glass curtain walls, once the horizontal transom members are attached to the vertical mullions, the structural glass panel is installed into the framing members with the use of pressure plates and seals (either rubber gaskets or sealant). Due to these various materials and components, as well as the potential for different construction methods used in the field, it is important to summarize the different components of the glass curtain wall system that can potentially affect the performance during natural hazards such as earthquakes or hurricanes. Several of these will in turn also effect fragility curve development as will be discussed in greater detail later in this literature review.

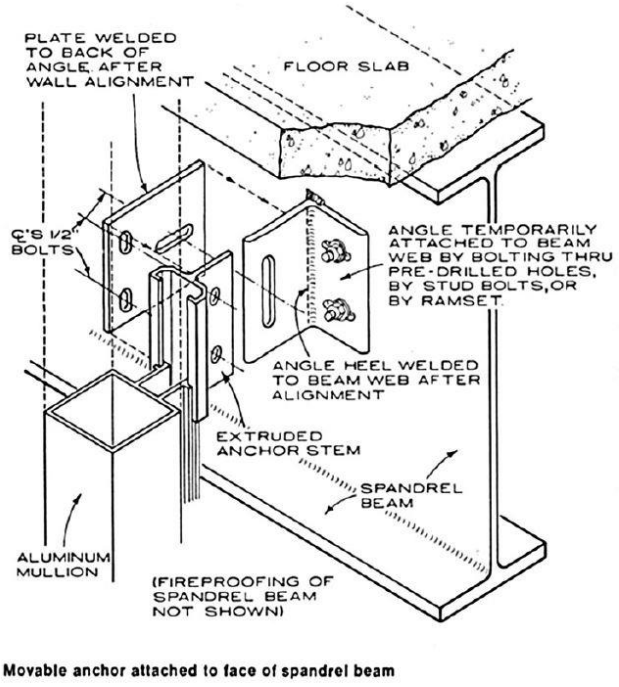

Figure 2-7: Typical representation of steel anchorages attaching a curtain wall frame to a structural member (Architectural Engineering Institute 2013)

2.2.1 Glass Unit Types

There are several different types of glass units that can be used to provide a barrier against the four weather elements previously described while maximizing the vision area provided to the user. This section will cover the three main types of glass unit configurations that have been used for practice and research. The 1997 GANA standards have categorized these commonly used glass types as monolithic, insulated glass units (IGU's) and laminated glass units (Architectural Engineering Institute 2013).

2.2.1.1 Monolithic Glass

Monolithic glass refers to a glass panel consisting of a single glass panel layer. This means that a monolithic glass panel must act as the sole barrier against the natural 4 elements with just this single glass layer. Monolithic glass can be used for many different areas of the curtain wall such as over the spandrel sections (anywhere floor slabs or beams/girders are visible) or for the entire façade of a high rise building. These monolithic layers can vary in thickness from the more common ranges of 3 mm (0.125 inch) through 12 mm (0.5 inch) to much large sizes if needed depending on the strength requirements dictated by wind loads or visual appearance (Architectural Engineering Institute 2013). Since it comprises of one layer only, the monolithic glass types usually have poor thermal performance as compared to other types of glass lite configurations (Vigener and Brown 2016a).

2.2.1.2 Insulated Glass Unit (IGU)

A more commonly used glazing type in the field with a much better thermal and energy performance is the insulated glass unit (IGU). This configuration usually consists of at least two glass panel layers that are separated by a continuous seal/spacer between all edges of the two panels to create an air pocket between them as shown in Figure 2-8 (Architectural Engineering Institute 2013; Vigener and Brown 2016a). Whether the IGU contains a least two glass panel layers or more (i.e. 3 glass panels each separated with a continuous seals), the entire multi-layer IGU configuration is still considered to be one glass unit. Furthermore, within the IGU each glass layer can either be monolithic glass or

a laminated glass unit (LGU). The use of LGUs layers within an IGU is more common in severe hurricane zones and areas where blast/ballistic hazards are expected due to their properties and configurations (Architectural Engineering Institute 2013; Haldimann 2006; Vigener and Brown 2016a). This LGU will be explained further in the next section.

Within the IGU glass layers, the continuous spacer is usually held in place by a primary seal which is non-curing, for example a butyl composition, and a secondary seal which is cured, for example silicone (Architectural Engineering Institute 2013; Vigener and Brown 2016a). The spacer itself has a desiccant to keep the sealed off air pocket dehydrated which is necessary to keep heat gain/loss in check during its life time and create an optimal thermal barrier which performs much better than the monolithic glass panes (Vigener and Brown 2016a). To optimize the thermal performance for an IGU, the designer can vary the amount of reflectance the glazing provides, usually by varying the glazing tints or applying a special low-emissivity coating, but also can change the width of the air space and/or modify the continuous spacer type with various materials (Architectural Engineering Institute 2013; Vigener and Brown 2016a).

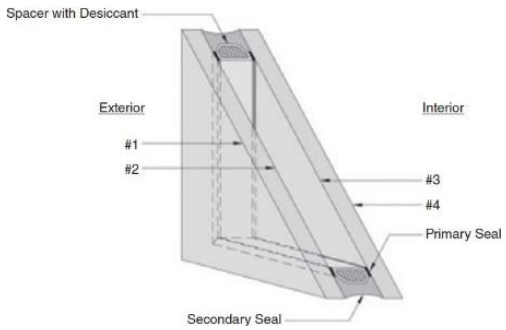

Figure 2-8: Isometric view of an insulated glass unit (IGU) (Architectural Engineering Institute 2013)

2.2.1.3 Laminated Glass Units (LGU)

The last major type of glass panes used in the glazing industry today is the laminated glass units (LGU), which also exhibit good thermal performance as well as having additional energy absorption features which are used in various applications in the field. Laminated glass units are comprised of at least two outer layers of glass panes with an interlayer membrane, usually polyvinyl butyral (PVB), which is bonded or laminated between the glass panes to create a multi-layered glass pane unit (Architectural Engineering Institute 2013; Behr et al. 1985; Vigener and Brown 2016a). With the ability to catch broken fragments from fall-out once the outer (or inner) glass panes crack/fail by adhering to the added PVB interlayer, the LGU helps increase the prevention of injuries to pedestrians/residents in the near vicinity of the glazing system. This post-breakage behavior of LGUs is very advantageous and shows why it is commonly used for areas that experience extreme natural hazards such as earthquakes and hurricanes (Architectural Engineering Institute 2013; Haldimann 2006; Vigener and Brown 2016a).

Additionally, LGU's exhibit good energy absorption characteristics, which also include enhanced performance in blast and impact resistance scenarios, as well good acoustical performance by decreasing sound transmittance through the glass unit. This makes the LGU panes capable of being used for many locations of a façade and different configurations to increase the panes strength such as for safety glazing, overhead glazing (in skylight applications), and missile impacts zones (whether by windborne debris impacts during a heavy wind event such as hurricane or explosions/blasts) (Architectural Engineering Institute 2013; Behr et al. 1985; Vigener and Brown 2016a).

2.2.2 Glass Strengths

Soda-lime-silicate float glass has been the most commonly used structural flat glass for many of today's building façades. A key factor behind its commercial popularity is its ability to be manufactured in vast quantities coupled with a low production cost, largely in part to the commercialized float glass process. The float glass process itself is the most commonly used glass manufacturing process due to its production of about 90% of all flat glass (Haldimann 2006). During this float glass process, soda lime-silicate glass requires only a relatively low melting temperature, approximately 1500 °C (Haldimann 2006; Shelby 2007). Once the raw materials have melted, the molten glass flows and forms into a thin sheet on top of a denser, shallow tin bath, which gradually cools down the glass ribbon to about 600 °C (Haldimann 2006). The still heated, thin ribbon is then passed onto controlled rollers, to create the desired glass thickness, and then finally rolled into an annealed lehr oven to allow the glass to slowly cool to reduce the residual stresses present within the glass (Haldimann 2006). The finished soda-lime-silicate glass is then cut and trimmed to desired sizes and ready to use for architectural glazing purposes.

At this point, additional heat strengthened processes can be performed to help increase the strength or better the performance of the float glass which could be advantageous in certain events where this increased performance is warranted when glazed in glass curtain walls. Therefore, the next sections will present different types of heat-strengthened process' in increasing level of performance and strength.

2.2.2.1 Annealed Glass

When float glass is produced through the float glass process without any additional treatments performed after the annealed lehr stage, it is considered annealed glass. Typically, annealed glass displays unfavorable characteristics in strength and failure modes even though it is the most common type of glass. Normally glass is strong in compression but weak against tension (Architectural Engineering Institute 2013). But in addition to having little to no residual stress along either surfaces (E06 Committee 2016b), annealed glass has no added resistance against cracking that occurs and initiates due to surface flaws. Therefore, once annealed glass fails, breakage can lead to large glass fragments, as shown in Figure 2-9, which can be very unsafe to people once the large fragments fallout. This shows how necessary the tempering process is to increase safety and performance of the annealed glass. Therefore, even though this finite element study will deal primarily with monolithic, annealed glass, it is important to understand how this glass performs in relation to glass that has had tempering of glass.

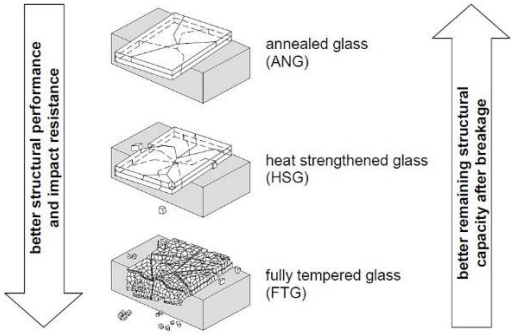

a) Post breakage behavior laminated glass units comprised of different glass strengths

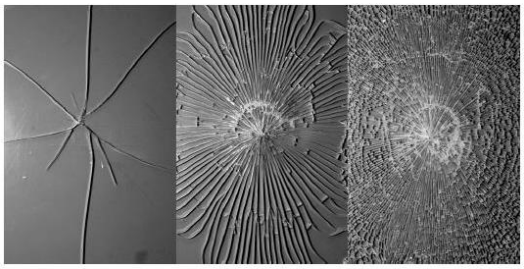

b) Typical fracture pattern for annealed, heat strengthened and fully tempered glass types (from left to right)

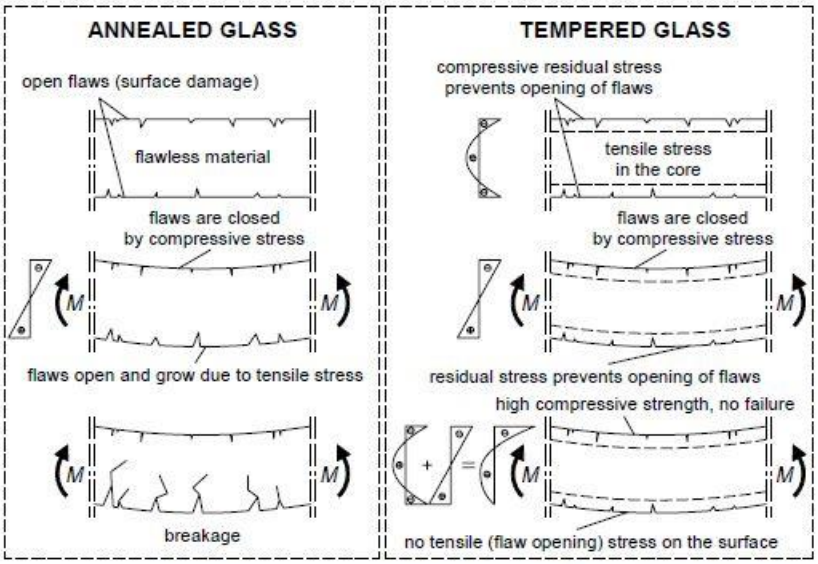

c) Principle cracking mechanics of annealed vs tempered glass

Figure 2-9: Cracking mechanics and fracture patterns for different strengths of glass (annealed, heat-strengthened, and fully tempered) (Haldimann 2006)

2.2.2.2 Heat-Tempered and Fully Tempered Glass

Tempering of glass is a valuable heat treatment process that helps annealed glass to gain higher strength, increase resistance to tensile forces and allows for more favorable breakage/failure states. During the heat treatment process, annealed glass is reheated

through a 620-675 °C furnace and then cooled at a controlled rate by uniformly blowing cooled air on the glass surfaces (Haldimann 2006; Shirazi 2005). Both heat-tempered and fully tempered glass go through the same tempering process with the exception that fully tempered glass is cooled at a faster rate (Haldimann 2006). This cooling stage allows the glass to gain advantageous residual stresses along the glass thickness, which are now compressive residual stresses near the surface and a tensile stresses enveloped in the core of the glass as shown in Figure 2-9. Meaning even with initial surface flaws, as long as the induced tensile stress is less than the residual compressive stress in the glass surface, there will be no cracking involved since the effective tensile stress is very little at that point.

Therefore, heat-tempered glass becomes about twice as strong as annealed glass, with an ASTM C1048 required surface compressive residual stress range of 24 MPa (3500 psi) up to 52 MPa (7500psi), while fully tempered glass becomes about four times stronger than annealed glass, with an ASTM C1048 required surface compressive residual stress minimum of 69 MPa (10,000 psi) (Architectural Engineering Institute 2013; E06 Committee 2016b; Haldimann 2006). Finally, even though heat-tempered glass does fracture in relatively large fragments as shown in Figure 2-9, it does so at a higher tensile stress than annealed glass and has better post-breakage structural capacity performance than fully tempered glass (Haldimann 2006). Fully tempered glass does have the highest tensile strength compared to both annealed and heat-tempered glass. However, fully tempered glass has the worst post-breakage structural capacity due to how it fractures into much smaller glass fragments as shown in Figure 2-9 (Haldimann 2006).

2.2.3 Stick-Built and Unitized Curtain Wall Construction

Glass curtain wall (CW) systems typically used in practice are constructed in one of two ways, either stick-built or unitized construction, and therefore can have a different structural performance depending on which is chosen. Glass CW that are stick-built have all their framing and glazing components manufactured in shops and then are assembled together at the construction site (Architectural Engineering Institute 2013). As previously mentioned for stick-built CW's, the vertical mullions are anchored to the structure before the horizontal transoms are attached, and this is followed by the glazing of the structural glass panel into the frame with the use of sealants or rubber gaskets and pressure plates. In contrast, unitized CW system's components are all fabricated and pre-assembled into curtain wall units in the shop before they are shipped out to the site to be erected onto the structure as shown in the. As seen in Figure 2-10, both types of systems have different semi-rigid mullion to transom connections since the stick-built version uses an aluminum shear block to connect the members, while the unitized version simply screws the framing mullions/transoms directly to each other without the use of the shear block. In addition to the different connections, the unitized system has different mullion profile extrusions to allow the CW units to be slipped/snapped into place as they are erected on site. As seen in some experimental test studies, such as in Figure 2-11, these "snap-in-place" extrusions allow the CW units to have more drift capacities than stick-built CW. Therefore, careful consideration of modeling these systems should be taken into account during any engineering analysis procedure.

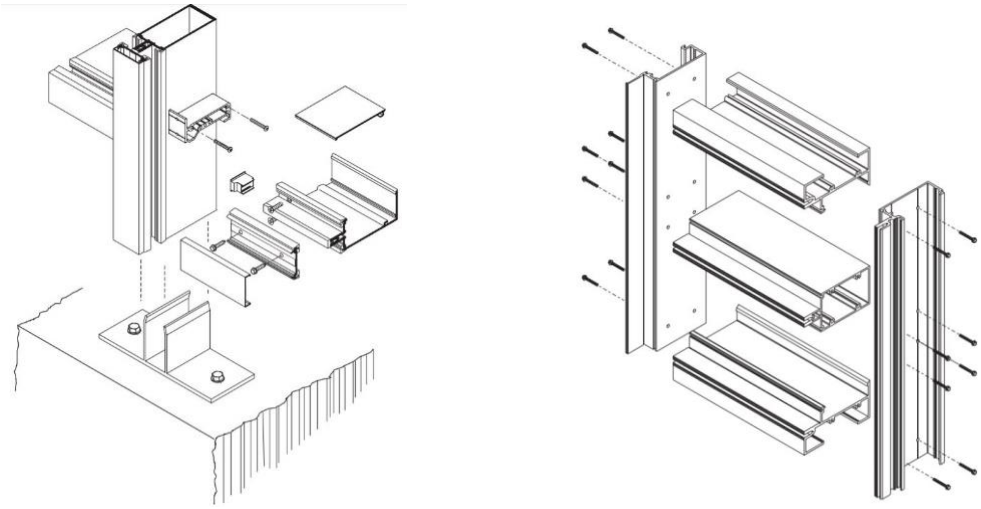

a) Kawneer 1600 Curtain Wall Framing System (Stick-built)

b) Kawneer 1600 SS Curtain Wall Framing System (Unitized)

Figure 2-10: Examples of stick-built vs unitized curtain wall framing systems with transom-mullion connection configurations

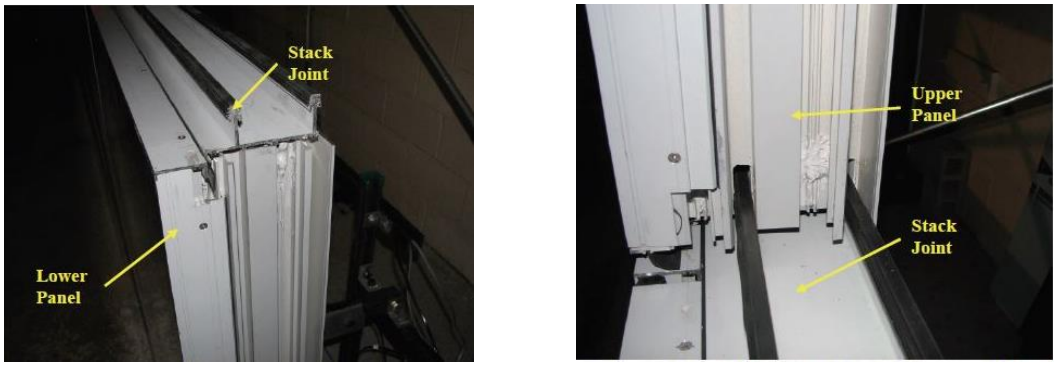

Figure 2-11: Unitized curtain wall framing stack joints from experimental racking test (Memari et al. 2011a)

2.2.4 Dry- and Wet-Glazed Curtain Walls

When structural glass panels are glazed into the framing pocket of the curtain wall units they use either dry or wet glazing components, such as EPDM rubber gaskets or structural sealants (silicone), respectively. Therefore, dry-glazed glass curtain walls use

rubber gaskets along the perimeter of both sides of the structural glass panel between the aluminum mullion and pressure plates, and compression helps keep the glass in place as well as prevents water intrusion and air infiltration as shown in Figure 2-12. The structural sealant glazed (SSG) curtain wall configuration, which uses structural sealants instead of the rubber gaskets as shown in Figure 2-13, can be used to improve the water intrusion resistance of the CW and to help restrict glass panel movement within the framing pocket (Vigener and Brown 2016a). Therefore, it is clear that both can have some performance difference when considering out-of-plane and in-plane effects depending which material is used.

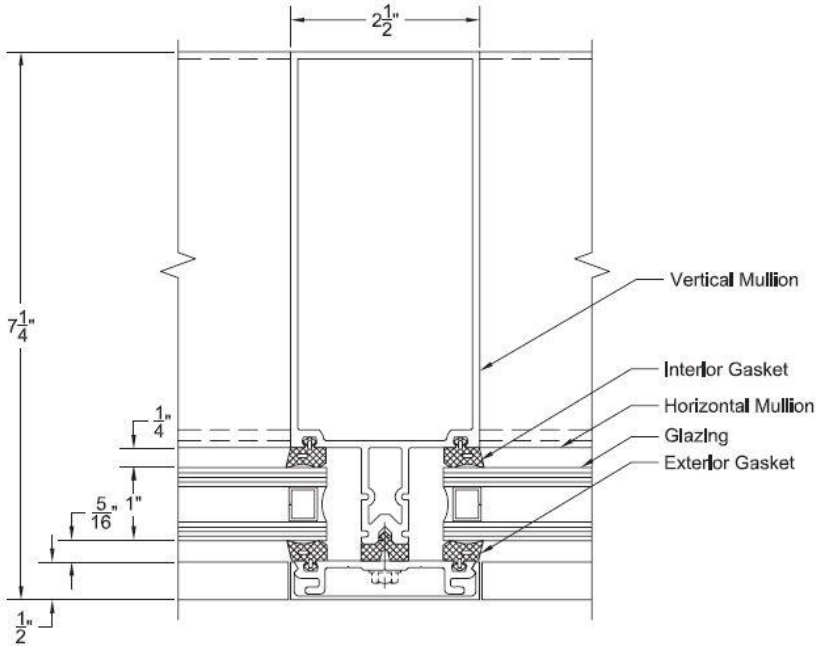

Figure 2-12: Plan-view of a dry-glazed Oldcastle BuildingEnvelope® system which implements rubber gaskets (Architectural Engineering Institute 2013)

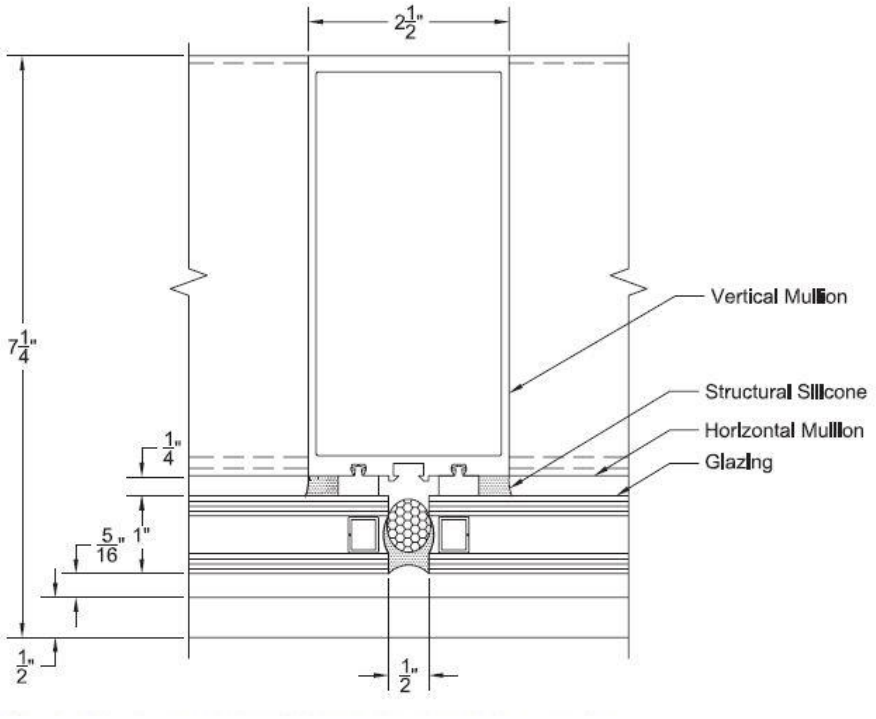

Figure 2-13: Plan-view of a structural silicone (SSG) Oldcastle BuildingEnvelope® system (Architectural Engineering Institute 2013)

2.2.5 Glass Curtain Wall Anchorage Configurations

In addition to having a variety of curtain wall configurations, glass CW's can have various anchorage attachments to the building system. The engineer must consider factors that would control the sizing, shape, and placement of these attachment anchors. These factors include span lengths, temperature and controlling design loads (i.e. seismic or wind) in addition to the curtain walls on self-weight (dead loads) (Architectural Engineering Institute 2013; Vigener and Brown 2016a). Therefore, with different attachment configurations based uniquely for each job, the flexibilities associated with the varied

anchorage connections can give differences in responses to wind or seismic events (Architectural Engineering Institute 2013; Memari et al. 2011a; Vigener and Brown 2016a). For wind loads, the anchors are designed primarily to accommodate movement for out-of-plane motions, and may also have multiple designs for a structure due to wind loads varying along the structures height (Architectural Engineering Institute 2013). In terms of seismic design in practice, anchor connections are not fully rigid and generally may allow some relative rotations and translations with respect to the curtain wall and the structural framing system (Memari et al. 2011a). While it is assumed that the glass CW sees the same lateral displacements as the structural framing due to these connections, in-plane rotational flexibilities of these connections are of key concern (Memari et al. 2011a).

In relation to fragility curve development for seismic performance, which will be discussed later, flexibilities in anchor connections used in real world construction are actually more flexible than the rigid connections used in testing facilities subjecting glass curtain walls to seismic racking tests. As is pointed out in an ATC-58 Project Report completed by (Memari et al. 2011a), it was observed that because of using more rigid connections (having no rotational/translational flexibilities), laboratory testing results can give more conservative glass CW drift capacities than what can be seen in the field. Thus, the glass panel corners would have frame contact at a much later drift if using these connections that allow some rotation as shown in Figure 2-14.

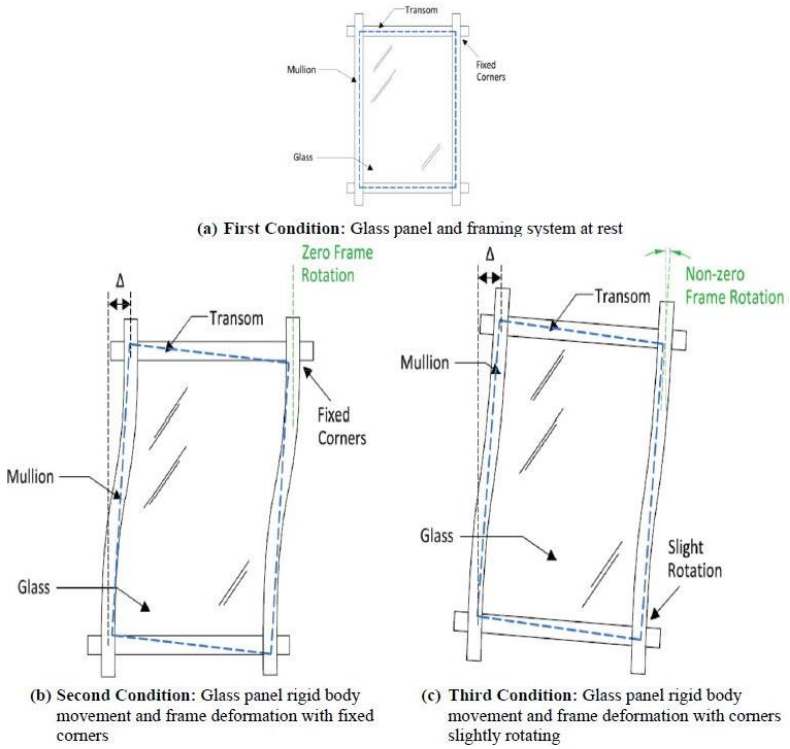

Figure 2-14: Illustration of the different effects to the structural response of CW configurations with either a fixed or flexible corners due to lateral forces being applied (Memari et al. 2011a)

2.3 Earthquake Related Damage States for Glass Curtain Walls

With respect to seismic performance of glazing systems, such as for glass curtain walls, storefront units and window walls, observations have been well documented through reconnaissance reports stating the damages that have occurred to these non-structural systems after seismic events. After large earthquakes, such as the 1964 Great Alaska Earthquake, 1990 Loma Prieta Earthquake, 1985 Mexico City Earthquake, 1995 Northridge Earthquake, to name a few, it became necessary for professionals and

researchers to further understand how to properly design for and analyze such glazing systems to improve the safety and performance during such events. Therefore, a number of glazing system experimental test studies have been completed to create/improve design standards, testing apparatus' and testing procedures that would aid engineers and researchers in today's seismic practice. A small portion of these experimental studies have been used for fragility curve developments. As for the number of numerical studies used in approximating seismic performance of glass curtain walls completed, thus far only a few have been completed. Even fewer have combined these summarized analytical methods with the fragility curve development frameworks established so far. Therefore, this section will discuss the different types of experimental and numerical studies completed in the past six decades and the most common damage states observed during these studies that can be used for fragility curve development later in this paper.

2.3.1 Common Experimental Test Apparatus and Testing Protocols for Curtain Walls

Most of the following experimental tests subject glazing system specimens to an in-plane horizontal displacement racking tests of some variation to replicate a seismic racking event.

The earliest approach of this horizontal displacement concept was established in a Bouwkamp (1961) study, which looked at how single window wall panels with various configurations, including different panel dimensions, panel attachments, sash materials, putty hardness, and glass-to-sash clearances behaved when subjected to racking displacements. The steel frame apparatus had pinned connections at corners to allow for

in-plane drifts imposed onto the panels as shown in Figure 2-15 (Bouwkamp 1961). Using a hydraulic loading jack at the top corners, either a static displacement, reversed (cyclic) displacement at increasing intervals, or impact displacement was applied to observe glass or glazing system failure.

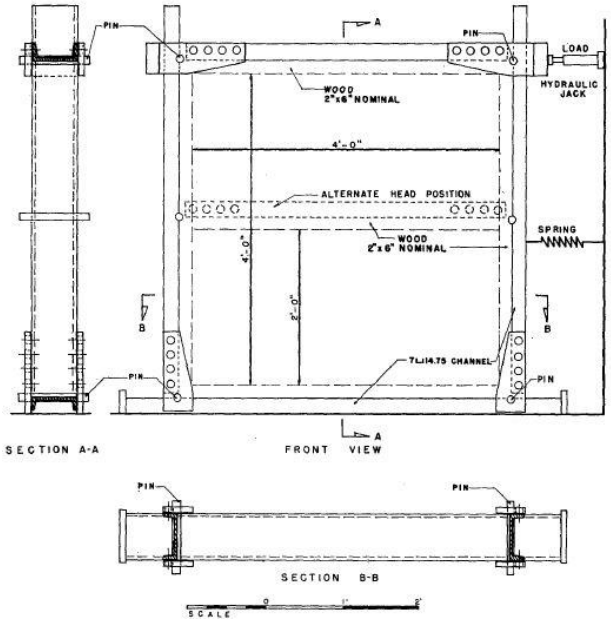

Figure 2-15: Layout of hinged loading frames used for application of racking loads onto window panel systems (Bouwkamp 1961)

At the Missouri University of Science and Technology (Missouri S&T) facility, Deschenes et al. (1991) completed another in-plane racking experiment using a different testing apparatus for a large section of glass curtain wall panels (Deschenes et al. 1991). Robertson Cupples conventional, stick-built glass curtain wall panels provided were attached to the testing apparatus which contained two horizontal structural steel tubes, one of which was fixed while the other was allowed to slide, mounted onto rigid steel columns as shown in Figure 2-16, while the displacements were provided by a hydraulic actuator

connected to bottom steel tube. A 3 phase dynamic cyclic protocol was established in which the first phase approximated drifts of a typical 15 story high-rise building frame subjected to ground motions, and the last two phases were additional interval cycles of increasing frequency for observing post breakage behavior.

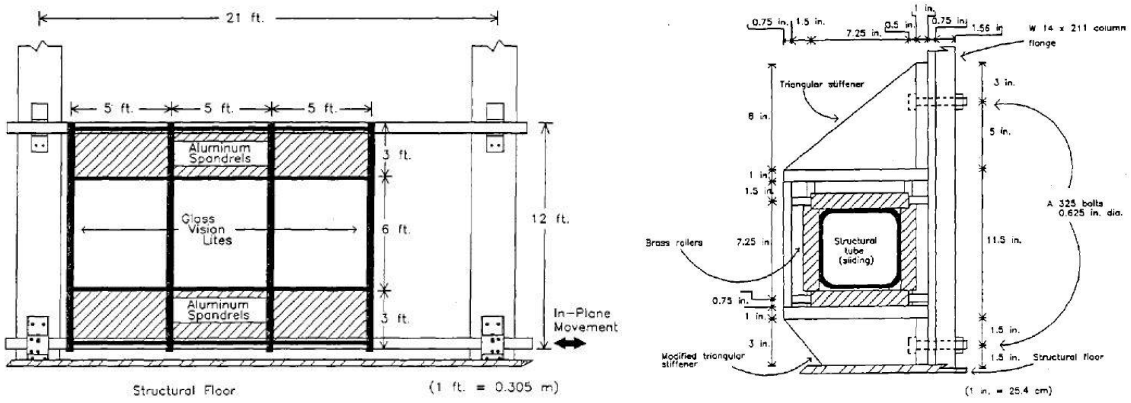

Figure 2-16: Layout of racking test apparatus with horizontal sliding tubes at the base and constrained tubes at the top. Illustrates an elevation view of the roller support implemented for the base sliding tubes.

More in-plane racking test were performed in New Zealand for the BRANZ group by Lim and King (1991) for five different glass curtain wall configurations such as a dry glazed (rubber gaskets) system; a patch fitting system; a 2-sided SSG system; a unitized, 4-sided SSG system; and a window panel system using a larger racking apparatus. As shown in Figure 2-17, this apparatus contains three horizontal steel tubes mounted onto two vertical columns, which allow for different boundary conditions to create 2 different interstory mode shapes when two of three tubes are fixed during racking. Additionally, this apparatus allowed for different story configurations to account for different glass panel sections and a 30 mm out-of-plane skewness was implemented on corners for when testing for in-plane/torsional effects in separate tests. The dynamic cyclic loading protocol applied

for this study was a cyclic saw tooth function which had variations of displacement rates, incremental displacement amplitudes, and number of cycles at a given amplitude to observe serviceability and ultimate limit states of the various curtain wall specimens.

Further tests were completed at the same New Zealand facilities for the BRANZ group by Thurston and King (1992), however, this time to investigate in-plane/out-of-plane behaviors due to corner configurations of curtain wall systems such as: a stick-built, dry glazed system; a unitized, 2-sided SSG system; and a unitized, 4-sided SSG system. The testing apparatus was configured in an L shape containing 4 steel tubes (top 2 being fixed while bottom 2 free to slide together) mounted onto 3 support columns as illustrated in Figure 2-17. Boundary conditions and story configurations similar to what is seen in the Lim and King (1991) study were used, as well as the same dynamic cyclic racking protocol to determine serviceability and ultimate drift limits (Thurston and King 1992).

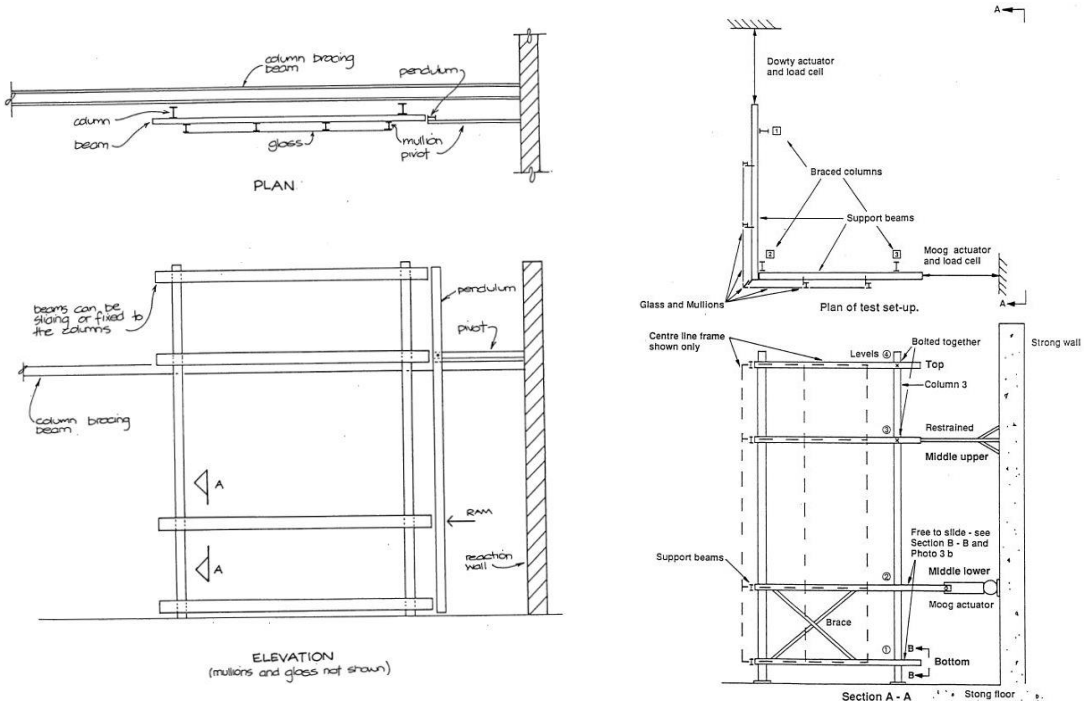

a) Plan and elevation views of CW racking displacement test apparatus for in plane and in-plane/torsional responses (Lim and King 1991)

b) Plan and elevation views of CW racking displacement test apparatus for in plane/out-of-plane responses (Thurston and King 1992)

Figure 2-17: Layouts of two separate test apparatus for CW racking tests carried out in New Zealand by BRANZ research group

Shanmugam (1993) completed additional studies at the same Missouri S&T facility used by Deschenes et al. (1991) to further investigate the same curtain wall systems now subjected to both in-plane/out-of-plane and in-plane/torsional motions. The group used the same test apparatus, but additional angular steel plates were added to the sliding bottom steel tube to achieve both out-of-plane or torsional motions when in-plane loading was applied. The same dynamic cyclic racking protocol by Deschenes et al. (1991) was used to observe damage states related to these motions. Additionally, Shanmugam (1993) worked on a linear elastic finite element model to determine glass movement within glazing pocket

and estimate in-plane displacements using this numerical analysis approach (Shanmugam 1993).

Another study by Behr et al. (1995) at the same Missouri S&T facility investigated the in-plane racking performance of common storefront glazing systems to observe more specified serviceability and ultimate damage states. While the same Missouri S&T testing apparatus described earlier was used, a pivot/fulcrum device was added to the apparatus to allow for both steel tubes to slide to achieve the same story drift. Another type of dynamic cyclic displacement protocol was used, as it was derived from the El Centro Earthquake, to create new serviceability and ultimate displacement loading histories used for assessing the damage states associated with each test (Behr et al. 1995a).

All of these previous test apparatus/protocols completed at the Missouri S&T facilities helped Behr and Belarbi (1996) establish what is now the most common testing apparatus and displacement protocol used for performance assessment of glazing systems, such as glass curtain walls, subjected to racking displacements, and the basis for the AAMA 501.4 and AAMA 501.6 standards discussed earlier. The finalized testing apparatus is the same used in Behr et al. (1995) experiments, containing both sliding steel tubes attached to a pivot/fulcrum mechanism and mounted onto two rigid columns as shown in Figure 2-18. Behr and Belarbi (1996) finalized the dynamic, cyclic crescendo loading protocol which contains sinusoidal waves with ramping up and constant amplitude sections, in an increasing incremental fashion, to achieve serviceability and ultimate damage limit states (Behr and Belarbi 1996). A compilation of further studies for various curtain wall configurations has been completed using this protocol, predominantly at Pennsylvania State University's Building Envelope Research Laboratory, to help with the

further assessment of various glass curtain wall configurations under this seismic racking displacement (Behr 1998b; Broker et al. 2012; Brueggeman et al. 2000; Dean et al. 2006; Memari et al. 2003, 2004, 2006, 2011a, 2012, 2011b; O'Brien et al. 2012; Shirazi 2005).

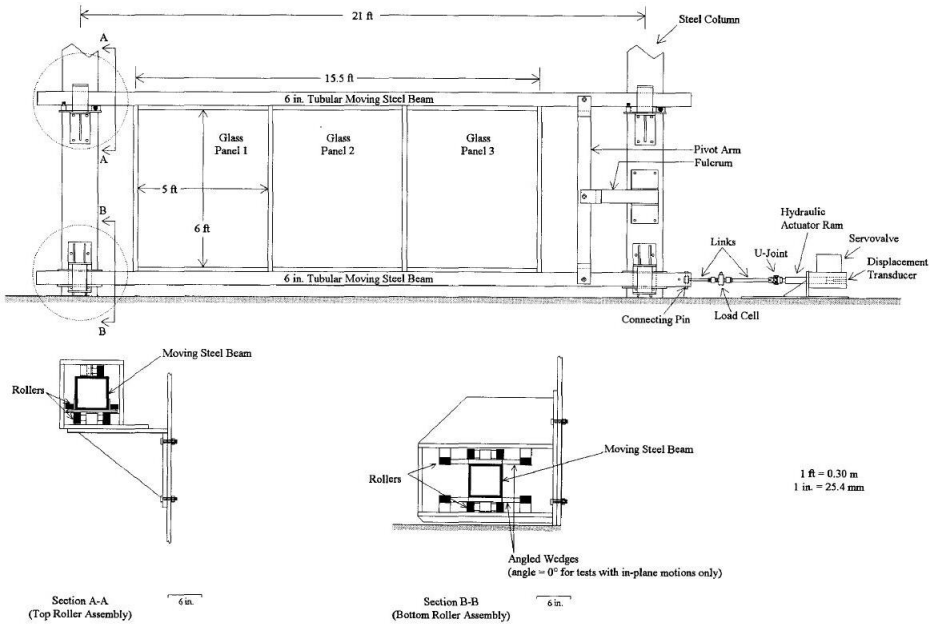

Figure 2-18: Dynamic Racking Test Apparatus at Missouri S&T (Behr and Belarbi 1996)

2.3.2 Observed Damage States to Curtain Walls Related to Earthquakes

Regarding the experimental test studies starting from Bouwkamp (1961) to the present time, this section will go into detail the most common earthquake related damage states (associated with increasing displacements) observed to glass curtain wall configurations during these studies. Definitions presented herein are provided by reports, such as the ATC 2011 Architectural Glass Seismic Behavior Fragility Curve Development

Report (Memari et al. 2011a), and standards, such as AAMA 501.4/501.6 (AAMA 2009a; b), but have been observed in most experiments thus far.

Furthermore, if the reviewed literature provided more details on the classification on any of the listed damage states, they were categorized as either a sequential, mutually exclusive or simultaneous damage state as defined in the FEMA P-58-1 Seismic Performance Assessment of Buildings report (Applied Technology Council (ATC) 2012). Sequential damage states are classified as one damage state occurring before another damage state can possibly occur in a sequential order as the demand (i.e. seismic drift) increases. Mutually exclusive damage states occur when one of the damage states precludes another damage state from occurring. And if a series of potential damage states can occur at the same time but not required to do so, meaning they are independent and unrelated, then the series of damage states are identified as simultaneous damage states.

The predominant earthquake related damage states that are characterized in the following sections are glass cracking, glass fallout, gasket/seal degradation, frame damage, and miscellaneous damage states (i.e. glass pullout and frame dislodging).

2.3.2.1 Glass Cracking

Glass cracking is a serviceability damage state that occurs after the glass panel rotates and translates enough to overcome the initial glass-to-frame clearance within the curtain wall's glazing pocket. It is defined as either through thickness cracking or crushing of the glass in the vision areas (glass area not covered by pressure plates/framing) and non-vision areas (glass area covered by pressure plate/within glazing pocket) of the curtain wall

unit as shown in Figure 2-19 (Behr et al. 1995a; Deschenes et al. 1991; Memari et al. 2006, 2011a; O'Brien et al. 2012). Usual points of cracking origin occur at the glass corners; wherever glass to setting/side block contact occurs; glass edges due to different corners or edge cuts; and either the exterior and/or interior glass panes in an IGU and laminated glass units (Behr et al. 1995b; a; Broker et al. 2012; Memari et al. 2006, 2011a, 2012; O'Brien et al. 2012; Pantelides and Behr 1994).

a) Glass spalling and cracking occurring at the corner regions (vision areas) (Memari et al. 2011a)

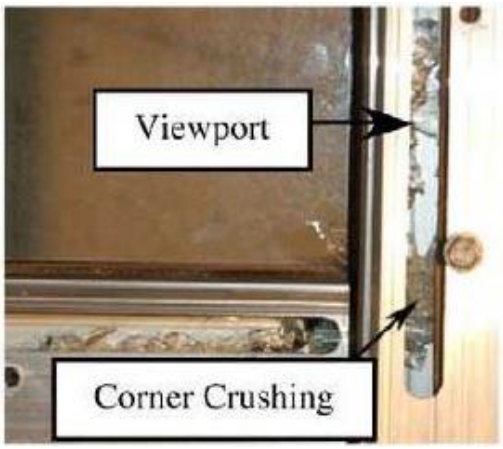

b) Glass spalling, crushing and cracking at the corner regions within the viewport areas (non-vision areas) (O'Brien et al. 2012)

Figure 2-19: Glass cracking damage state in the vision and non-vision areas of a glass CW specimen

2.3.2.2 Glass Fallout

As shown in Figure 2-20, glass fallout occurs at a drift where glass fragments greater than 1 in^2 fallout from glazing unit (AAMA 2009b; Memari et al. 2011a; O'Brien et al. 2012). This is considered an ultimate limit state due to the life safety hazard this causes to pedestrians and building occupants, and therefore calls for the immediate replacement of the glazing systems. As pointed out, various fragment sizes for glass fallouts can occur and can cause some uncertainty during visual observations for those especially small glass fallout situations (Memari et al. 2011a; O'Brien et al. 2012). While glass fallout usually occurs sequentially after the glass cracking damage state, these two can occur exactly at the same time for certain glass types and glass strengths (Memari et al. 2011a; O'Brien et al. 2012). If enough glass cracking or fallout takes place, a complete glass failure damage state can occur in which the entire structural glass panel shatters/falls out of the glazing panel or can no longer can resist loads (Bouwkamp 1961; Dean et al. 2006; Deschenes et al. 1991; Lim and King 1991; Memari et al. 2003, 2004, 2011a; Pantelides and Behr 1994; Shanmugam 1993).

Figure 2-20: Glass fallout damage state in vision area of glass CW specimen (Memari et al. 2011a)

2.3.2.3 Gasket/Seal Degradation

Another serviceability damage state seen in experimental tests is gasket degradation, which when reached and left unrepaired, can lead to air infiltration and water intrusion issues (Behr et al. 1995a; Memari et al. 2011a; O'Brien et al. 2012). As illustrated in Figure 2-21, four distinct gasket damage characteristics constitute this gasket damage state which are: (1) gasket distortion – the twisting or bulging of the gasket, while remaining between the glass and glazing pocket; (2) gasket pull-out – a gasket section being pulled out from the glazing pocket; (3) gasket push-in – a gasket section being pushed deeper into the glazing pocket; and (4) gasket shifting – a length of gasket section being displaced along it local longitudinal axis creating an open gap with the glazing pocket (Behr et al. 1995b; a; Memari et al. 2011a; O'Brien et al. 2012). Although gasket degradation can occur before glass cracking, it is considered mutually exclusive as it can occur before or after glass cracking or glass fallout and thus it is not sequential (Memari et al. 2011a; O'Brien et al. 2012). A subset of this damage state can occur for SSG, wet-glazed curtain walls which use structural silicone sealants in lieu of rubber gaskets. Therefore, tests that have used SSG curtain walls have also reported sealant degradation damage states that occur due to sealant elongation/distortions, tearing and cohesive/adhesive failures due to excessive racking displacements (Behr 1998a; Broker et al. 2012; Dean et al. 2006; Lim and King 1991; Memari et al. 2011a, 2012; Thurston and King 1992).

a) Gasket rolling/twisting (top) and pullout (bottom) damage states (Memari et al. 2011a)

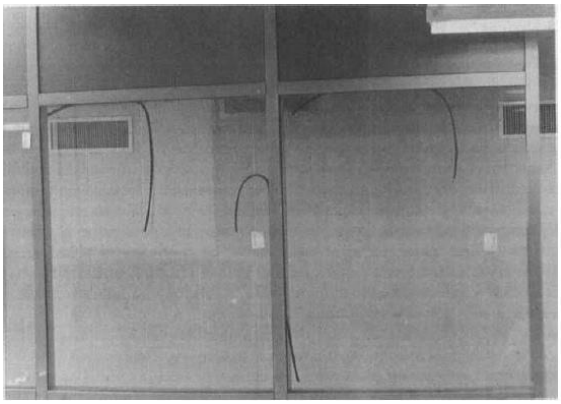

b) Gasket pullout damage state due to in-plane/out-of-plane racking test (Behr et al. 1995b)

Figure 2-21: Common gasket degradation damage states observed in glazing systems

2.3.2.4 Curtain Wall Frame Damage

Although not considered as a damage state in the initial ATC-58 fragility development report due to the difficulty of establishing the exact drift at occurrence, framing damage is still widely observed in previous glass curtain wall tests to date (Behr et al. 1995a; Deschenes et al. 1991; Lim and King 1991; Memari et al. 2003, 2011a; Pantelides and Behr 1994; Shanmugam 1993; Shirazi 2005). In some cases there is minor damage, such as at the mullion/transom connections (displacements or screws loose) or a minor decrease in framing stiffness throughout testing durations after repeated use (Deschenes et al. 1991; Lim and King 1991; Pantelides and Behr 1994; Shanmugam 1993). In other instances, plastic deformations and gouging within the frames glazing pocket can

occur (especially at mullion/transom corner regions) due to different glass edge configurations and/or heavier glass types (i.e. IGU's) as seen in Figure 2-22 (Behr et al. 1995a; Memari et al. 2003, 2011a; Shirazi 2005). In extreme cases, especially with heavier glass types (i.e. IGU's), frame damage can take the form of complete loses of horizontal pressure plates, extreme horizontal member rotations, and/or complete loss of horizontal members (Memari et al. 2011a; Shanmugam 1993).

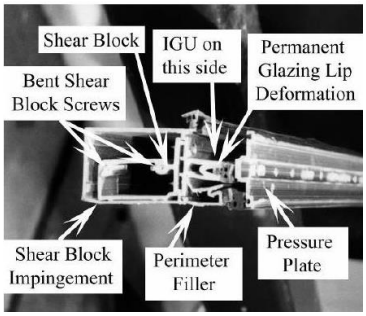

a) Section view of bottom horizontal transom of a CW frame with deformations caused after racking test is completed

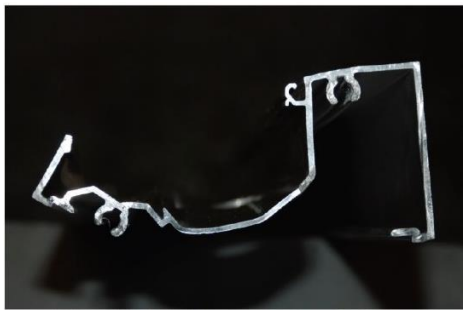

b) Horizontal mullion of a storefront system with framing deformation damages

Figure 2-22: Framing damage state of glazing systems subjected to racking motions (Memari et al. 2011a)

2.3.2.5 Miscellaneous Damage States

Two more damage states that can take place is glass pullout and frame dislodging, both of which are not fully considered in the current development of fragility curves. Glass pullout takes place when the glass comes out of the glazing pocket along any section of the glazing perimeter due to either glass buckling or loss of clamping force in pressure plates (Memari et al. 2011a) as shown in Figure 2-23. While glass fallout may not even occur prior to glass pull out, a clear envelope breach is apparent and requires repair/replacement.

Lastly, as shown in Figure 2-23 frame dislodging is a phenomenon that occurs to unitized curtain walls and storefronts because of how the framing units are pieced and clipped together at their framing joints (male/female extrusions) (Memari et al. 2011a). This occurs because unitized systems exhibit more of a swaying mode, instead of a racking mode, in which the panels slide in relation to one another during increasing lateral displacements because of the member joints, thus allowing for larger drift capacities (Memari et al. 2011a). Therefore, boundary conditions and racking/sway modes need to be considered when testing these units in the field and lab.

a) Glass pullout damage state observed in a laminate glass unit CW system (Memari et al. 2003)

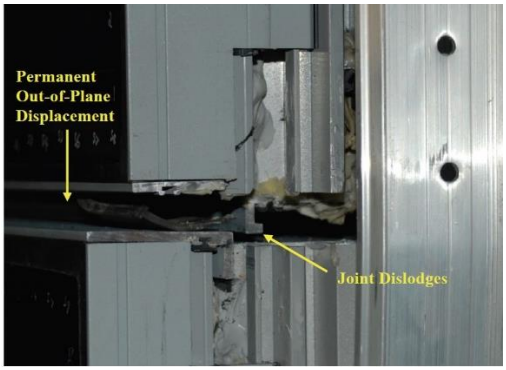

b) Frame dislodgement damage state observed at the horizontal stack joint of a unitized curtain wall configuration (Memari et al. 2011a)

Figure 2-23: Miscellaneous damage states observed in glazing systems subjected to racking displacement tests

2.3.3 Numerical Analysis of Glass Curtain Walls subject to Earthquake Related Events

This section highlights some of the most common finite element (FE) modeling techniques and simulations developed in the few studies that have applied a numerical analysis approach to simulate the seismic behavior of glass curtain wall systems subjected to in-plane horizontal racking displacements, similar to what has been produced in

experimental test studies mentioned in the previous section. Thus far, researchers have used several FE analysis software packages such as MSC/XL and MSC/NASTRAN (Shanmugam 1993), ANSYS (Memari et al. 2011b; Shirazi 2005), Straus7 (Galli 2012), Visual Analysis by IES (Broker et al. 2012; Memari et al. 2012), SAP2000 (Aiello et al. 2018; Caterino et al. 2017), and Abaqus (Bedon and Amadio 2018). While none of the models presented herein were used for the development of fragility curves, as is the focus of this paper, many showed promising results that demonstrated the effectiveness of using an FE analysis as an engineering analysis method for approximating the seismic performance of glass curtain walls.

To help maintain lower computational costs while still obtaining approximate solutions with a reasonable level of accuracy, numerical studies have used 2-node beam elements for modeling the framing members (mullions/transoms) for both unitized and stick-built systems (Aiello et al. 2018; Bedon and Amadio 2018; Broker et al. 2012; Caterino et al. 2017; Galli 2012; Memari et al. 2012, 2011b; Shanmugam 1993; Shirazi 2005). Most models have also modeled the horizontal transom to vertical mullion connections as a hinged connection by implementing moment releases (about the z-axis) for the horizontal transoms (Aiello et al. 2018; Broker et al. 2012; Caterino et al. 2017; Galli 2012; Memari et al. 2012; Shanmugam 1993). Only the model from Shirazi (2005) and Memari et al. (2011b), tried to implement a more semi-rigid connection by implementing smaller cross sectional properties in the beam elements directly in the connection regions to capture the framing lateral stiffness exhibited in the exact same experimental mock-up racking test. 3-node and 4-node elastic shell elements were implemented for glass panels in all the analyses to effectively capture stress distributions

and concentrations. Only the Bedon and Amadio (2018) study added a brittle cracking damage model to capture post-cracking behavior in Abaqus. Finally, setting blocks have either been modeled as roller supports at the base of the glass (Shanmugam 1993) or with shell elements with a bilinear elastic plastic material model (Memari et al. 2011b; Shirazi 2005).

In addition to the simplification of actual curtain wall components using shell and structural elements, models have used other alternative methods to deal with challenges related to the many interactions of all the curtain wall components that can occur due to their racking behavior. For the case of dry glazed curtain walls, studies have listed some of these common challenges such as: 1) the constantly changing boundary conditions of the glass panel due to glass-to-frame contacts; 2) the changing glass-to-gasket friction effects; 3) accounting for the framing members' bending stiffness and the transoms' twisting stiffness (due to glass contact along a mullions glazing lip); and 4) the transom-to-mullion connection stiffness (already discussed) (Memari et al. 2011b; Shirazi 2005). To overcome the first and third challenges, researchers have used compression only link elements (or "gap" elements depending on the FE software) connecting the boundary nodes between the glass panel edges and adjacent frame nodes to approximately model the effect of glass contacting the frame (within the glazing pocket) after the clearance closes (Aiello et al. 2018; Caterino et al. 2017; Galli 2012; Memari et al. 2011b; Shirazi 2005). This technique also accounts for the transom twisting stiffness and any local framing deformations made by the glass-to-frame contacts by modifying the elastic stiffness of these links once gap closure is evident. Early modeling by Shanmugam (1993) attempted to model these glass-to-frame clearance changes as well by using spring elements that effectively only

considered the stiffness between the gasket/glass combination, but it did not account for the gaskets frictional behavior. To implement glass-to-gasket friction behavior, models have also superimposed non-linear link elements, in parallel with the gap elements previously described, that can capture the gaskets changing mechanical behavior as the racking displacement increases (Aiello et al. 2018; Caterino et al. 2017; Memari et al. 2011b; Shirazi 2005). In this regard, the non-linear link elements used either an elastic-perfectly plastic relationship (Memari et al. 2011b; Shirazi 2005) or an elastic-plastic Wen model relationship to capture the before and after effects of glass slippage (Aiello et al. 2018; Caterino et al. 2017).

In all, every numerical analysis has implemented a displacement controlled analysis to simulate the racking displacement completed in the experimental tests. This was achieved by either directly applying the displacement condition directly to the frames corner nodes or by connection a rigid link/rod element to the frame corner. This allowed the simulation to provide results of how much force is applied for the associated drift applied.

2.3.4 Seismic Fragility Curve Development for Glass Curtain Wall Systems

With the combined effort of the Applied Technology Council (ATC) and the Federal Emergency Management Agency (FEMA), seismic fragility curve procedures based on experimental test results were developed in the FEMA P-58/BD-3.9.1 Background Document. This study was initiated to assist engineers in being able to evaluate glass curtain wall systems using a performance based engineering design

approach for building envelope performance assessment (Memari et al. 2011a). The generated fragility curves help estimate the damages that a glass CW system could sustain during a seismic event in terms of a probability of failure for different types of CW components (Applied Technology Council (ATC) 2012; Memari et al. 2011a; O'Brien et al. 2012). As a result of this framework, some experimental research has been completed to assist in the generation of seismic fragility curves for different configurations of glass curtain wall systems (Huang et al. 2017; O'Brien et al. 2012; Shirazi 2005). Only one study implemented FE model simulations in an effort to assist in generating a vulnerability rating system and a mathematical model which would derive seismic fragility curves (Shirazi 2005). Therefore, it is evident that more work is required into implementing FE models as an alternative engineering analysis method for seismic fragility curve development.

2.4 Hurricane Related Damage States for Glass Curtain Walls

As summarized by Tahir (2016), there is not a definitive approach in literature that establishes a well-developed connection between the necessary "pinch point variables" that are required in analysis when using performance-based engineering design for building envelopes resisting hurricane events. This is opposed to what has been established for earthquake PBE. For building envelopes in general, the established flow of these pinch points include the observed hazard aspects of the hurricane (i.e. wind pressure, uplift, windborne debris, wind driven rain, etc.); to the intensity measures (IM) defining the intensity of the hazard aspects (i.e. wind pressures/velocities, debris velocity, rain intensity,

etc.); to the engineering demand parameters (EDP) that represent the systems structural response to the IMs (deflections, roof drift ratios, volume of water, etc.); and then to the damage states at the component level due to the EDPs (i.e. crack, tear, displacement, failure, etc.) (Tahir 2016).

Now specifically in the scope of architectural glass CWs, there is a multitude of literature on the strength and structural behavior of just the structural glass panel itself. But based on a review of experimental tests and reconnaissance reports, there is also a gap between the pinch points for hurricane related IMs to EDPS to damage states for the entire glass CW system as a whole (i.e. glass panel, aluminum frame, gasket/sealant, anchorage, etc.). This is more evident in hurricane reconnaissance reports as glass CWs are susceptible to damage during hurricane events. The reason being that much of the presented reconnaissance reports for the observed damages stated in the following sections are not related to engineering demand parameters. Rather these damage states are reported to have occurred due to the intensity measures such as wind/debris velocities, either during or after the event, mainly the latter.

As previously stated, it is advantageous to have these connections from IMs to EDPs to damage states because the relationship between EDPs to damage states are required to develop fragility curves that would aid in the performance based engineering design of building facades (Tahir 2016). Regardless, this section will go over what has been collected in the literature regarding glass curtain walls subjected to hurricane related hazard aspects and the related damage states observed throughout. It will also overview common numerical analysis methods used thus far in attempting to simulate hurricane hazards.

2.4.1 Overview of Hurricane Reconnaissance Reports

Hurricane damages to a glass façade are very wide spread and difficult to measure/record during the actual hurricane event. Therefore, glazing failure damages are usually reported until after the event during reconnaissance reports that are coordinated by organizations such as FEMA (FEMA 488 2005; FEMA 489 2005; FEMA 548 2006), NIST (NIST 2006) or individual researchers (Beason et al. 1984; Behr and Minor 1994; Vega and Konz 2010). These reports summarized the different damage observations of glazing systems after Hurricane Alicia, Andrew, Charley, Ike, Ivan, Katrina, and Rita, all of which ranged between Category 3 to Category 5 levels with various maximum wind speed ranges. It was noted that inadequate glazing system designs due to outdated design codes were a factor to many of the observed glazing failures (Beason et al. 1984; FEMA 548 2006; NIST 2006). These reports also emphasized that the combination of wind pressures and windborne debris impacts were the main causes of glazing system failures. Additionally, while glazing fragments alone can pose a threat to people's life safety, it was evident that broken glass was an additional debris source that affected other glazing systems as well. Internal pressurization was another side effect of glazing failure, due to the effects on the structural internally and the opposite facing glass panels because of additional wind pressures (Behr and Minor 1994; FEMA 488 2005; FEMA 489 2005; FEMA 548 2006). Therefore, internal damages to a building can increase due to wind driven rain and the additional wind pressures/windborne debris caused by these envelope breaches. As such, a byproduct of these breaches is the increased repair costs for the internal damages which

are summarized in the reconnaissance reports. This is in addition to the cost of repairing/replacing damaged glazing systems widely needed after any hurricane event.

2.4.2 Common Experimental Test Apparatus and Testing Protocols for Curtain Walls

Over the past few decades, due largely in part to observed glass damages during hurricane events as was mentioned above, extensive experimental research for out-of-plane loading has been completed to better understand the strength and structural performance of structural glass panels, and to help with development of glass design aids and guidelines.

Current glass curtain walls usually go through extensive mock up testing before installation using several of the testing protocols mentioned earlier. However, in-depth results of these mock up tests are not readily available to the public other than some final result reports because many glass curtain wall systems are proprietary. Therefore, the available research on completed experiments with glass curtain wall configurations presented here is very limited (Behr et al. 1996; Horst 1991; Pantelides et al. 1991).

A majority of glass testing was initially taken on by researchers at Texas Tech University (Abiassi 1981; Bailey et al. 1990; Beason 1980; Behr et al. 1985; Kanabolo and Norville 1985; Linden et al. 1983, 1984; Reznik 1986), while other testing was either completed in facilities at Missouri S&T (Behr et al. 1996; Horst 1991; Pantelides et al. 1991; Venkata 2004) and within Canada (Gavanski 2010; Johar 1981). Closely based on ASTM standards provided earlier, test apparatus' used during glass testing include a vacuum air pressure chamber, an air system capable of controlling uniform air pressures

applied onto specimens, and a special testing frame to hold the glass specimen as shown in Figure 2-24.

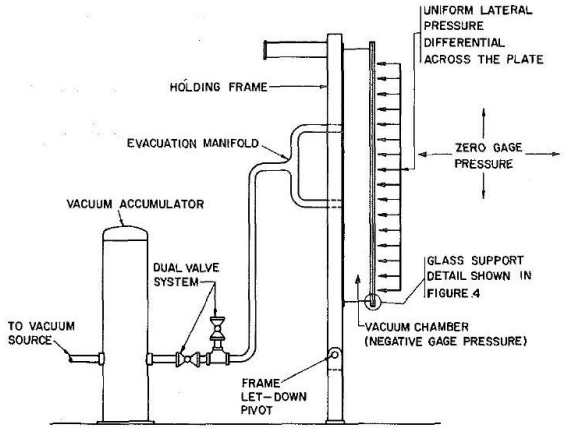

Figure 2-24: Test facility at Texas Tech University for applying lateral uniform pressure onto glazing specimens (Behr et al. 1985)

The test frames typically used were made out of various standard structural steel shapes with neoprene rubber gaskets placed in notches to provide a simply supported boundary condition along the glass perimeter as shown in Figure 2-3. Researchers prohibited out-of-plane displacements and allowed for in-plane displacements and rotations with different frame edge clamping loads (different screw tensions used between all studies) and setting blocks at the quarter points of glass panel base. As stated earlier, there is a limited amount of experimental tests in the literature that included an entire glass curtain wall system unit, which were either a dry-glazed system (using just rubber gaskets) (Horst 1991; Pantelides et al. 1991) or a combination of a wet-/dry-glazed system (silicone sealant with rubber gaskets) (Behr et al. 1996; Horst 1991; Pantelides et al. 1991). An example of one of these systems which was actually pressure tested is shown in Figure 2-25.

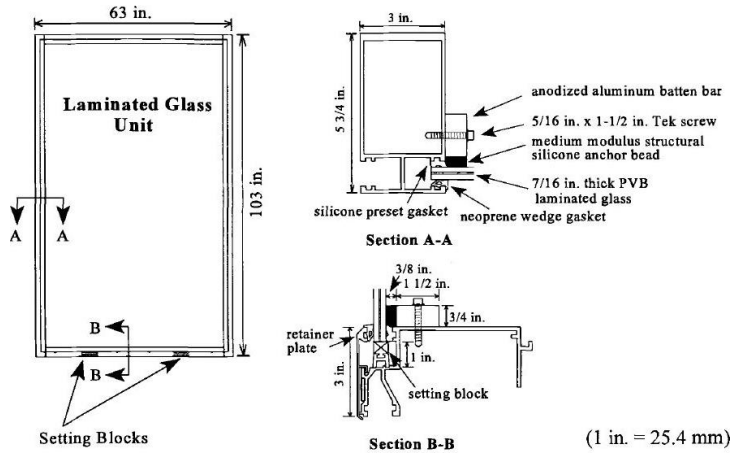

Figure 2-25: Laminate glass curtain wall configuration subjected to missile impacts and lateral uniform pressure (Behr et al. 1996)

Researchers employed additional apparatus when testing for the effects of increased temperature (Behr et al. 1985; Linden et al. 1983, 1984; Reznik 1986), debris impact (Behr et al. 1996; Horst 1991; Pantelides et al. 1991; Reznik 1986), or weathering effects (Behr et al. 1996) on the lateral performance of glazing specimens when subjected to uniform pressure. Therefore, environmental chambers were attached to test frames to increase the glass temperature. Compressed air cannons were employed to shoot small steel projectiles at specimens, at varied velocities, in symmetrical grid formations. And accelerated weathering chambers were enlisted to facilitate weathered and aged specimens in a time accelerated manner with adjustments to humidity and temperature.

After being subjected to temperature, weathering and/or projected missile impact effects, glass specimens were subject to uniform pressures up to failure by applying linearly increasing air pressures (Abiassi 1981; Bailey et al. 1990; Beason 1980; Behr et al. 1985; Gavanski 2010; Johar 1981; Kanabolo and Norville 1985; Linden et al. 1983, 1984; Reznik

1986) or utilizing cyclic air pressure spectrums that resemble windstorm events more closely (Behr et al. 1996; Gavanski 2010; Horst 1991; Pantelides et al. 1991). Additionally, evaluations for the effect of applying the linearly increasing pressures at different load durations and loading rates were completed throughout some of the specified experiments.

With the use of these various test apparatus and loading protocols, researchers were able to determine how various parameters effected the glass specimen performance such as their failure loads, maximum principal stresses, maximum deflections, fracture patterns, and damage mechanisms, which are illustrated in the next section. Overall, these studies have shown that various configurations of laminate and IGU specimens performed better than monolithic glass types when subjected to simulated hurricane hazard aspects (Behr et al. 1985, 1996; Horst 1991; Linden et al. 1983, 1984; Pantelides et al. 1991; Reznik 1986).

2.4.3 Observed Damage States to Curtain Walls Related to Hurricane Hazards

This section will give an overview of the damages recorded in reconnaissance reports and/or experimental test studies gone over in the previous two sections. Unlike the damage states defined in earthquake related events described earlier, most of the damages are not explicitly linked to engineering demand parameters or intensity measures required for fragility curve development. This is because most damages were either recorded based on visual observations after hurricane events or not related to the failure load and max displacements recorded at the end of a test. As a result of all these factors the damage states presented for out-of-plane loading may not match or be defined similarly as the in-plane racking displacements. The main out-of-plane damage states presented in next section

include glass cracking, glass fallout, complete glass failure, gasket/sealant damages, and a few miscellaneous damages states (i.e. frame/anchor damages, glass pullout, and delamination of PVB interlayers in LGUs.

First damage state seen in both hurricane surveys and experimental reports is glass cracking. In reconnaissance reports such as in Beason et al. (1984), windborne debris impacts were observed to be the main source of glass cracking based on the cracking shapes seen on glass still left in glazing systems as shown in Figure 2-26, and more likely linked to the combination of wind pressures/debris impacts. For experiments, Abiassi (1981) has the only mention of cracking or fracture seen due to just applied lateral pressures, however, the recorded fracture origin is not linked to a pressure for when the crack began. The hybrid tests (using missile impacts followed by air pressure cycles or ramp ups) state that cracking is observed at time of debris impact, but it is not further mentioned except for its origin and propagation after failure is already reached (Behr et al. 1996; Horst 1991; Pantelides et al. 1991; Reznik 1986).

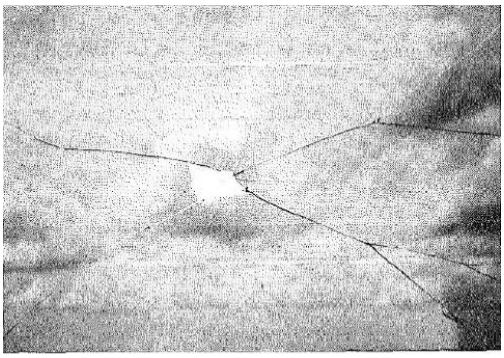

Figure 2-26: Glass cracking as a result of debris impacts observed during a hurricane event (Beason et al. 1984)

Glass fallout is another damage state that is linked primarily with windborne debris/wind pressure combination. In FEMA surveys, tempered glass was recorded to have shattered into smaller pieces than annealed monolithic glass and fallen out of the glazing units (FEMA 488 2005; FEMA 489 2005). During testing studies, fallout was also observed in just the hybrid testing of glass in which fallout rates or fallout percentages were recorded and illustrated in the results as shown in Figure 2-27 (Behr et al. 1996; Horst 1991; Pantelides et al. 1991). As most of these impact tests involved laminated glass specimens, majority of the fallout occurred only after the PVB interlayer and/or the inner glass lite had failed. This showed the advantage of using laminated glass in hurricane prone regions since broken outer glass lite sticks onto interlayer (Behr et al. 1996; Horst 1991; Pantelides et al. 1991; Reznik 1986)

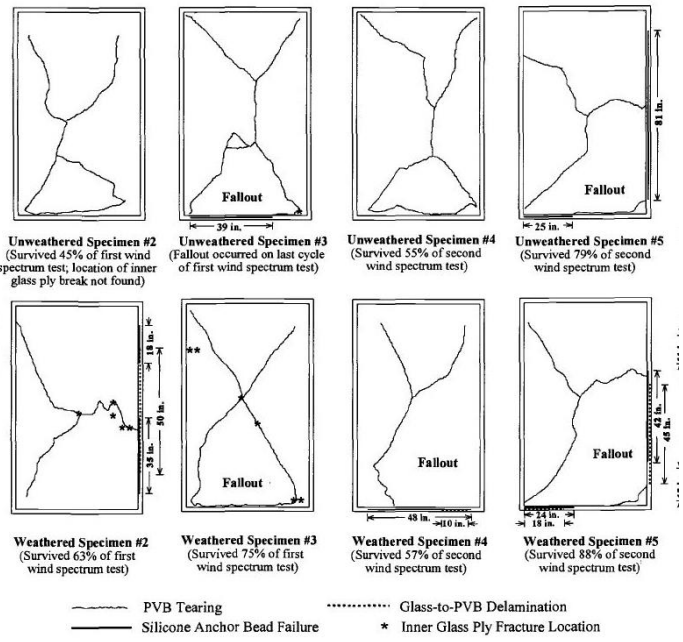

Figure 2-27: Glass fallout patterns and fallout rates observed in weathered and un-weathered laminated glass curtain wall specimens due to combination of missile impacts and wind pressures (Behr et al. 1996)

Due to the brittle nature of glass, fallout is very closely linked to the state of complete glass failure in many tests and surveys since both could happen at the same time or immediately in sequence when subjected to out-of-plane loadings. During reconnaissance reports, complete glass failure was reported to have occurred due to again the combination of debris and wind pressures. In surveys it is defined as either glass being broken or complete glass “blowouts” of the glazing units (Beason et al. 1984; Behr and Minor 1994; Cauffman 2006; FEMA 488 2005; FEMA 489 2005; FEMA 548 2006; NIST 2006; Vega and Konz 2010). For experiments using just uniform pressure or a hybrid of pressure/missile impacts, glass failure was mainly categorized as the event at which failure pressures and max displacements were recorded, at which point the glass specimen is assumed to have completely shattered/fractured as shown in Figure 2-28, entire panel falls out of the holding frame or can no longer resist loads applied within the chamber (Abiassi 1981; Beason 1980; Behr et al. 1996; Gavanski 2010; Horst 1991; Johar 1981; Kanabolo and Norville 1985; Linden et al. 1984; Pantelides et al. 1991).

Figure 2-28: Fracture pattern of a complete glass failure observed after a lateral uniform pressure was applied (Johar 1981)

For IGU units, sequential glass failures could actually occur to individual glass panes (outer or inner) as was observed in some IGU glazing systems, which only had the outer glass panes fail during Hurricane Andrew (Behr and Minor 1994). In experimental testing, laminate glass units also showed complete glass failure did not occur until failure of both glass lites and the PVB interlayer failed (Behr et al. 1985, 1996; Horst 1991; Linden et al. 1984; Pantelides et al. 1991; Reznik 1986). Therefore, as long as the inner glass pane was not damaged, complete glazing failure was not evident as pressure was applied.

Definitions for both gasket and sealant damage during experimental testing were not explicitly defined as was the case for earthquake related events, while no mention of either damage was recorded in hurricane reconnaissance reports. Gasket pullout was the only damage state observed during testing of the dry glazed and dry-/wet-glazed systems

which led to immediate glazing failures (Pantelides et al. 1991). For the case of sealant damage, either a loss of adhesion to the glass and/or cohesive tears within the silicone sealants were observed after the glass failures (Behr et al. 1996; Horst 1991; Pantelides et al. 1991).

Miscellaneous damage states that were not primarily observed or extensively recorded during this review include frame/anchor damages, glass pullout and delamination of laminated glass lites from the PVB interlayer evident in laminate glass units. Frame and anchor damages were only recorded in Behr and Minor (1994) and believed to have occurred because of poor installation and/or inadequate design. Glass pullout from the testing frames was evident primarily in Pantelides et al. (1991) due to excessive glass deflection and glass buckling which was seen primarily at the top of specimen. PVB interlayer tears and delamination in laminate units was observed and recorded during tests completed by Behr et al. (1996) study.

2.4.4 Numerical Analysis of Glass Curtain Walls subject to Hurricane Related Events

This section will present the most common numerical analysis methods used to simulate out-of-plane pressures applied to glass plates of various types used in glazing systems, such as curtain walls. A few theoretical methods will also be presented since they have been proven methods for approximating stress distributions and displacements in earlier studies. While the simulation of debris impacts on glass using numerical methods is evident in the literature, these methods will not be focused on here due to this paper's

focus on glass performance within glazing systems subjected to only out-of-plane pressures.

In Beason (1980), a theoretical analysis was conducted as part of the development of a failure prediction model that helped determine glass plate strength, and which takes into account surface flaws and other parameters such as load durations, relative humidity and temperature (Beason 1980). Beason's numerical analysis used both von Karman's non-linear plate theory equations and a developed finite difference model to solve the differential equations to obtain stress distributions and maximum displacements in the monolithic glass plate. This model gave the user the ability to input simply supported boundary conditions along the perimeter of the glass as it is being subjected to uniform pressure. This also captures geometrically non-linear effects in glass due to glass having much larger displacements relative to the plates thickness.

Similar endeavors using the geometrically non-linear von Karman equations and variations of the finite difference method produced by Vallabhan and Wang (1981) have been used for analyzing different glass types such as layered and laminated glass with a PVB interlayer; analyzing 4-sided SSG systems to approximately compute forces/deformations in the sealants; and comparing results in experimental studies (Beason 1980; Behr et al. 1985; Nagalla et al. 1985; Vallabhan et al. 1997). All of which still used simple boundary conditions prohibiting out of plane deflections at the edges but still allowing in-plane movements of the glass.

More recent studies have adopted finite element modeling methods with various software packages that are capable of analyzing glass with geometric non-linear effects, due to the large deformations exhibited during linearly increasing uniform pressures. For

instance, in the Duser et al. (1999), the finite element software, ABAQUS, was utilized to model laminated glass. The analysis was simplified by only modeling a quarter of the glass panel using axisymmetric analysis (Duser et al. 1999). Glass was modeled with 8-node solid elements with incompatible mode formulations to prohibit locking associated with bending and used linear elastic material properties. The PVB interlayer was modeled similarly with an additional hybrid formulation, to account for incompressible material properties, and contained a linear visco-elastic constitutive material behavior. Additionally, simply supported and axisymmetric boundary conditions were implemented at the necessary glass edges.

The same idea of modeling only a quarter of the glass with simply supported and axisymmetric boundary conditions was followed in other analytical studies that implemented SAP 2000 (Gavanski 2010), LUSAS FEA v14 (Overend and Zammit 2012) and ANSYS (Puga et al. 2015). Monolithic glass in these models commonly implemented elastic shell elements, with the exception of Overend and Zammit (2012) using 8-node quadrilateral thin shell elements. The maximum principal stresses obtained with models in the Puga et al. (2015) study were eventually used as input in a life time prediction model which subsequently created various fragility curves based on different glass sizes.

A geometrically non-linear analysis conducted in Abaqus by Svensson (2015) modeled the entirety of an IGU glass panel in an effort to understand and capture the effects of bulging observed in these units due to the pressure changes in the gaseous volume within the IGU cavity during applied uniform pressure (Svensson 2015). The boundary conditions implemented used a combination of simply supported and fixed conditions at just the corner nodes of the glass to get the maximum center of glass deflection. Lastly, the glass

lites in the IGU were modeled using 8-node quadrilateral continuum shell elements with first-order interpolation and reduced integration formulations and using linearly elastic material model. These shell elements prove advantageous over normal shell elements when contact is involved. Lastly, the gas cavity within the IGU units was modeled with hydrostatic fluid elements.

As illustrated in this section, these models were capable of approximating stress distributions and deflections across the glass unit. However, they have not fully implemented changing boundary conditions, curtain wall framing/glazing components and interactions that can occur within a curtain wall system when subjected to an applied uniform pressure. All of these factors need to be included in models to be able to fully observe other damage states and mechanisms that can occur and help with fragility curve development.

2.5 In-Depth Overview of Prioritized In-Plane and Out-of-Plane Experimental Testing of Glass Curtain Wall Systems

This section highlights two experimental test studies which have completed mock-up testing on glass curtain wall systems or structural glass panels used within glass CW systems. The additional importance of both of these experimental studies will be further discussed in the following chapters of this thesis.

First, an in-plane related study which performed typical seismic racking displacement protocols onto a commonly used glass curtain wall system. Test results were subsequently used to help generate finite element models and derive coefficients required

in the mathematical model to create an analytical methodology which predicts seismic vulnerability of typical glass CWs (Shirazi 2005).

An out-of-plane related study which compared the key structural behaviors of laminated glass and monolithic glass subjected to a statically increasing uniform pressure is summarized as well. In addition to testing the effects of elevated temperature changes, the experimental results were also compared to theoretical stress analyses to see if these also captured the structural behaviors of both laminated and monolithic glass (Linden et al. 1983).

2.5.1 Overview of In-Plane Experimental Test

The thesis of Shirazi (2005), completed at the Building Envelope Research Laboratory (BERL) at Pennsylvania State University (PSU), is summarized in detail herein to present a prime example of a mock-up testing of glass curtain walls for seismic performance. The main reason being the experimental protocols completed in the Shirazi (2005) research was entirely modeled after the static and dynamic in-plane displacement racking procedures developed for glass CWs in the AAMA standard test protocols. Shirazi (2005) also recorded relevant damage states observed during the racking tests, and documented the relationship between the damage states and the EDP (i.e. interstory drift ratio) throughout the racking test required for earthquake fragility development as established in the FEMA P-58 Background Document (Memari et al. 2011a).

The glass CW system chosen by Shirazi (2005) was common in the industry and represented the general CW configurations seen in construction. The Kawneer 1600 Wall

System™ 1 Curtain Wall, a dry-glazed and stick-built system, was selected for his experimental research which embodies a typical glass curtain wall system for mid-rise to high produced in the marketplace today. Based on the details provided by both Kawneer (Kawneer 2019b) and Shirazi (2005), the 5-1/4 inch (63.5 mm) frame depth system, used commonly for a 1/4 inch (6 mm) glass infill, was identified as the featured configuration.

This UT thermal version provides a smaller glazing lip on the mullions, as shown in Figure 2-29, and a 1/4 inch (6 mm) thermal break gasket between the lip and pressure plates which improves the system's thermal performance. Within the glazing pocket, a 1/4 inch (6 mm) thick glass is supported between two fixed EPDM rubber gaskets and an 11 mm glass-to-frame clearance is upheld. To maintain the glass clearances, two setting blocks are placed at the base of the glass panel at quarter points relative to the glass width, and two side blocks are placed (one on each side) at the glass mid-point relative to height.

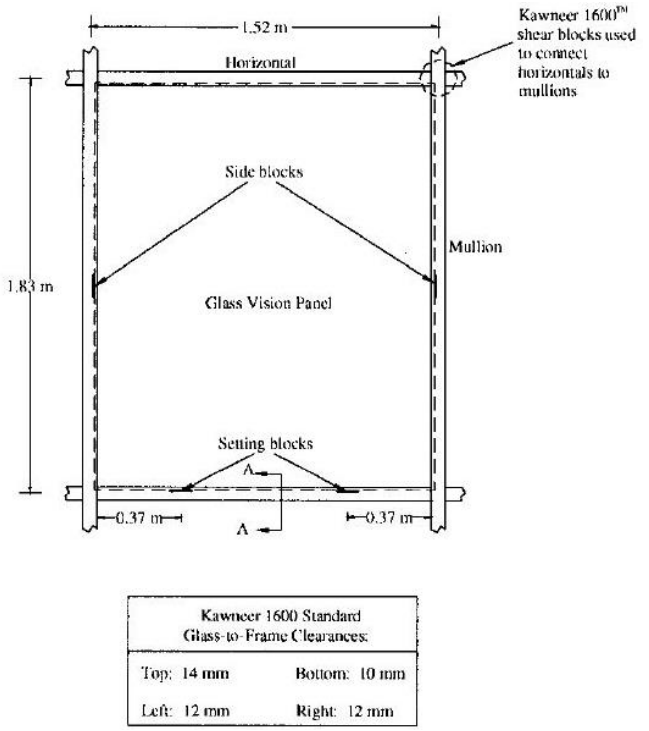

a) Elevation view of Kawneer 1600 Wall System™ 1 Curtain Wall specimen and standard glass-to-frame clearances commonly used

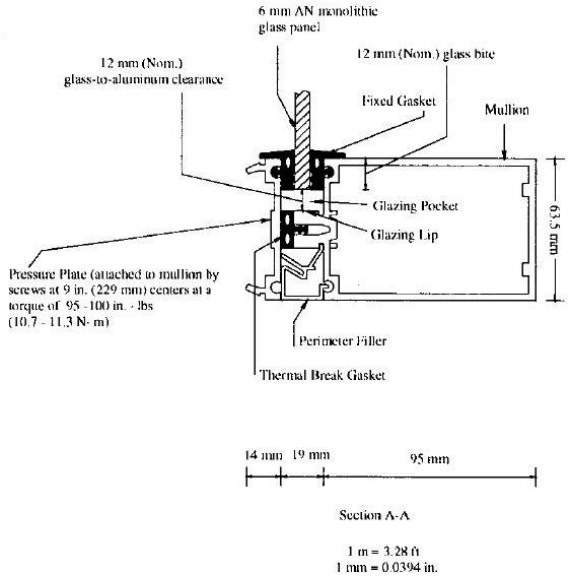

b) Section A-A view (bottom horizontal transom) of Kawneer 1600 CW frame which contains intermediate "flat" pressure plate configuration

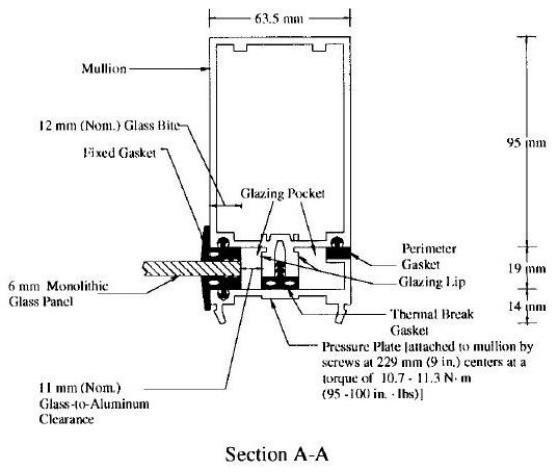

c) Section A-A view (right vertical mullion) of Kawneer 1600 CW frame which contains perimeter "L" pressure plate configuration

Figure 2-29: General glazing details of the Kawneer 1600 Wall System™ 1 Curtain Wall specimen subjected to static and cyclic racking displacements during experimental study (Shirazi 2005)

For a perimeter glazing profile, as shown in Figure 2-29, a perimeter pressure plate is attached with perimeter rubber gaskets. For the intermediary glazing profile, as shown in Figure 2-29, a flat pressure plate can be attached with a perimeter adapter. Both pressure plate profiles are attached to the mullion with screws spaced at a 9 in center-to-center spacing and with a required screw torque of 95-100 lb-in (10.7-11.3 N-m) to clamp glass in place. Additionally, for the mullion-to-transom connection shown in Figure 2-29 and Figure 2-30, specified shear blocks connect them together.

For the experiments, 6 ft high x 5 ft wide (1829 mm x 1524 mm) annealed, monolithic glass panel sizes were used. Finally, pressure plates had viewing slots cut along corner regions of unit in order observe more accurately when glass-to-frame contacts occurred.

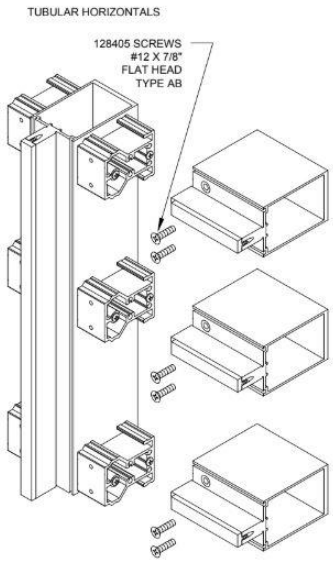

Figure 2-30: Isometric view of transom-mullion connections with shear block attachments (drawing provided by Kawneer installation manual)

2.5.1.1 In-Plane Test Apparatus and Test Protocol

Experimental racking protocols were completed within the same test facilities used in many previous experimental curtain wall tests at the BERL (Memari et al. 2003, 2004, 2006, 2011a; b, 2012; O'Brien et al. 2012). Shirazi (2005) implemented the same dynamic and static testing procedures defined in current AAMA racking mock up test standards (AAMA 2009a; b). These AAMA protocols are based on crescendo tests developed by Behr and Belarbi (1996) which were described in the previous literature review sections. Therefore, in the experiment the curtain walls were attached to the test apparatus shown in Figure 2-31 with two sliding steel tubes connected to a pivot/fulcrum mechanism and mounted onto two rigid columns to simulate in-place racking motions glass CW's may experience during a seismic event. The required vertical mullion to steel anchorage connections used in attaching the CW to the apparatus closely follows connections detailed within AAMA 501.4 (AAMA 2009a). It is important to note that the maximum displacement the actuator could apply to the system through the bottom steel tube was ±3 inches (±76 mm). However, the pivot/fulcrum mechanism allowed the top and bottom steel tubes to have a total drift of ±6 inches (±152 mm).

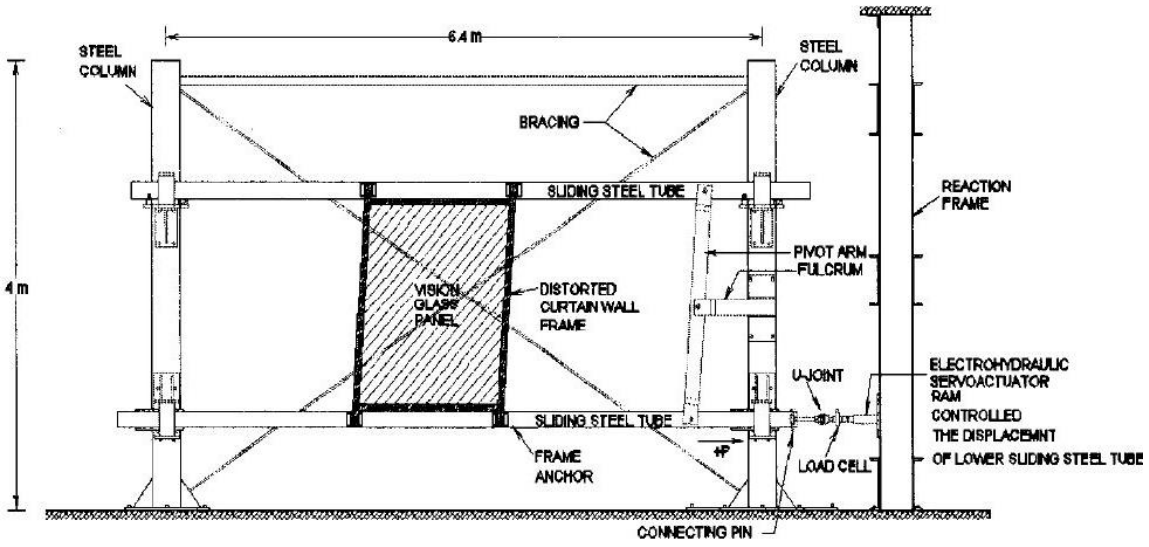

Figure 2-31: Layout of racking test facility at PSU used for imposing a story drift onto the Kawneer 1600 CW system (Shirazi 2005)

Shirazi (2005) sought to observe the relationship between an increasing lateral drift applied to a glass CW and the stresses accumulated at certain locations on the glass panel. Therefore, rosette strain gages were strategically placed on the glass panel near areas of glass-to-frame contact to gather useful stress distributions throughout the duration of the experiment. Additionally, a load cell and displacement transducer were attached to the hydraulic actuator ram, as shown in Figure 2-31, to measure the in-plane racking loads applied to the specimen and the racking displacement of the specimen, respectively.

To investigate the relationship between applied drift and the generated stress on the glass, Shirazi (2005) completed four sets of tests which can be categorized as either a cyclic or static pushover test. In the first set, a cyclic test was performed using the derived continuous dynamic crescendo tests implemented in the AAMA 501.6 protocols. Shirazi modified this initially continuous crescendo protocol into separate intervals of dynamic and static steps to be performed in a stepwise manner, steadily increasing at ¼ in. (6mm)

increments from 0 to 1.25 in. For the primary results, Shirazi (2005) prioritized the static interval where an applied displacement up to 1.25 in. amplitude at a 0.01 Hz frequency was implemented.

For the second test set, a static pushover test was implemented where the actuator was programmed to displace the bottom steel to apply a racking displacement at a monotonically, static rate of 0.01 cm/sec. This would subject the CW specimens to a linearly increasing static drift.

In the third testing set, the same static pushover test was applied to the glass CW but without pressure plates on to determine the contribution the pressure plate has on the generated stress on the glass during the applied drift.

And lastly, the fourth set completed both a cyclic and static pushover test, using the same protocols described in the first two test sets, to investigate the contribution of the lateral stiffness of the unglazed frames (i.e. only the bare frame) to the total lateral stiffness of the dry-glazed CW system.

2.5.1.2 Cyclic Test Results for Dry-Glazed Curtain Wall Specimen

The results included in Shirazi (2005) study were graphs that plotted load-displacement relationship and drift-strain relationships. Looking at Figure 2-32, different states of glass curtain wall behavior were observed at certain drift levels during the cyclic racking displacement. Shirazi (2005) reported that the initial stiffness response in the plot is due to a combination of the elastic lateral stiffness of the CW's aluminum frame (i.e.

semi rigid transom-mullion connections) and the rubber gasket/block-to-glass surface friction.

Lastly, the first and second principle strains at the glass corners were determined based off of the strain gages as the cyclic drift was applied. As an example, just the first principle strain-drift relationship at gage #1 is shown here in Figure 2-33. Based off this plot, a big drop in the strain magnitudes is evident once cracking has initiated.

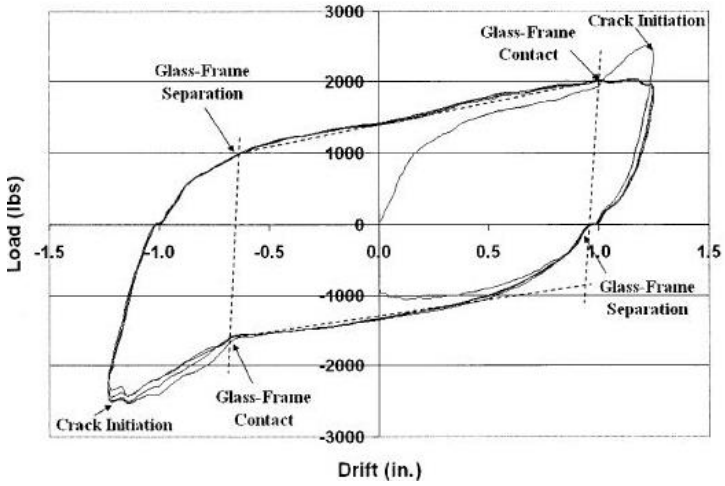

Figure 2-32: Load-displacement relationship for cyclic protocol (Shirazi 2005)

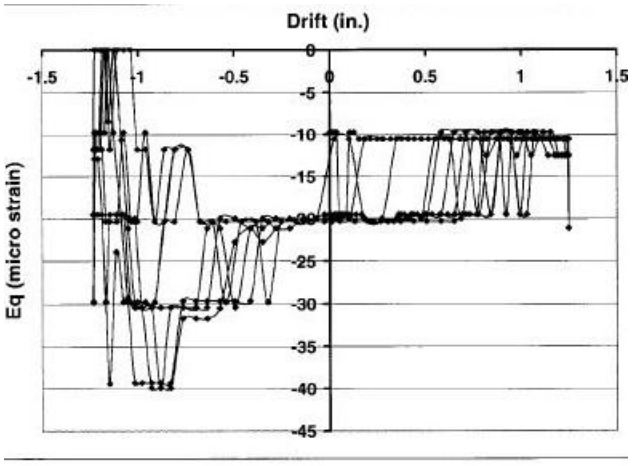

Figure 2-33:First principal strain-drift relationship from rosette strain gage #1 during cyclic protocol (Shirazi 2005)

2.5.1.3 Static Pushover Test Results for Dry-Glazed Curtain Wall Specimen

For the dry-glazed specimen, the recorded results include graphs which illustrate the load-displacement relationship, drift-strain relationship, and glass panel movements (rotations and displacements of the glass panel). Looking at Figure 2-34, different states of glass curtain wall behavior were observed at certain drift levels during the increasing racking displacement. Shirazi (2005) reported that the initial stiffness response in the plot is due to a combination of the elastic lateral stiffness of the CW's aluminum components and rubber gasket/block-to-glass surface friction. The magnitude of frictional forces caused by the gasket-to-glass contact became constant at the start of Point 1. From Points 1 to 2, a decrease in slope is observed due to the frame's lateral stiffness once the friction forces caused by the gasket-to-glass interactions are no longer effective in resisting the applied loading. Once glass-to-frame contact occurs at the top left corner of the glass at Point 2, another stiffness increase is observed from Points 2 to 3. At Point 3, the glass has translated

and rotated enough within the glazing pocket to have another glass-to-frame contact occur in the bottom right corner. Shirazi (2005) recorded localized crushing/flaking of the glass occurring at the bottom right corner of the glass which caused the slight drop in load resistance at Point 4. Another sharp increase in CW stiffness was observed from points 4 to 6 because the glass started to resist racking loads in addition to the framing components once both opposite corners of the glass came into contact with the frame. Local crushing/flaking of the top left corner of glass occurred at Point 5, defined as a small crack. At Point 6 a significantly large through thickness crack occurred in the glass which caused no increase in load resistance occurring after. Shirazi (2005) did not show data results past this point because the focus of this test was just on reaching the serviceability limit state of cracking.

The first principal strain-drift relationships are shown in Figure 2-35, and the first principal strain-load relationship is shown in Figure 2-36. These principal strains were measured at the top left and bottom right corners. As seen in Figure 2-35**,** it was observed that at 0.8 in. and 1.8 in. drift the top left corner and the bottom right corner of the glass had come into contact with the mullion lip, respectively. Due to the fact that these contacts did not occur simultaneous, it makes sense that the strain-drift and strain-load relationships are not identical. The horizontal, vertical and rotational movement of the glass was also measured using LVDTs attached to the center of the glass panel throughout the applied drift. These relationships are shown in Figure 2-37 and Figure 2-38.

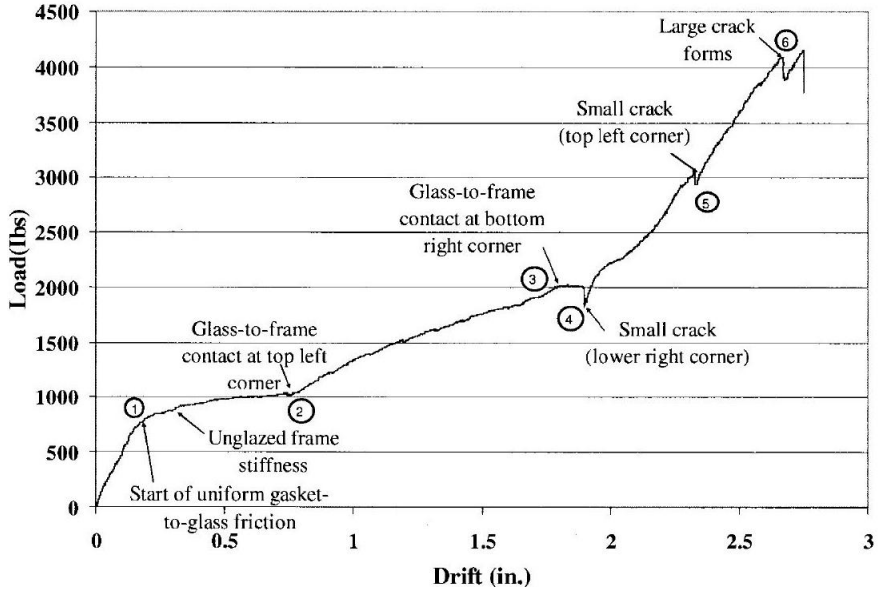

Figure 2-34: Load-displacement relationship of Kawneer 1600 CW during static racking test (Shirazi 2005)

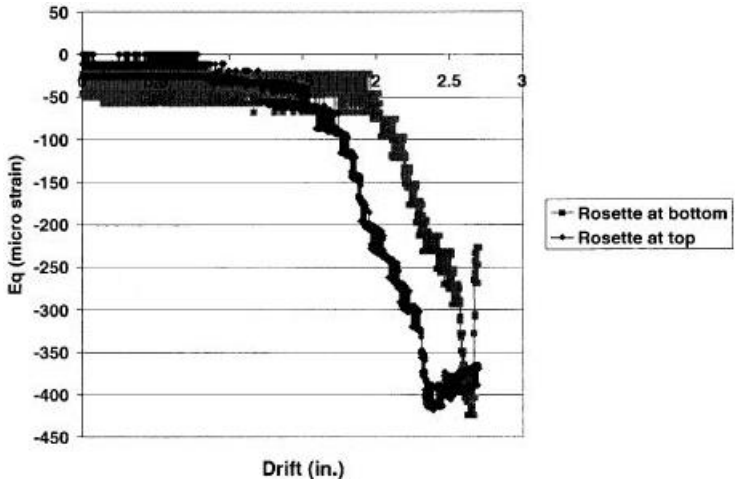

Figure 2-35: First principal strain-displacement relationship for dry-glazed CW static pushover test (Shirazi 2005)

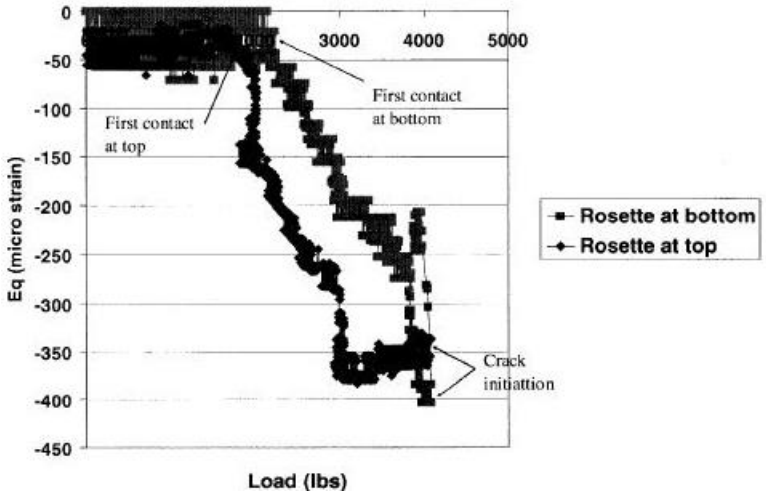

Figure 2-36: First principal strains-load relationship for dry-glazed CW static pushover test (Shirazi 2005)

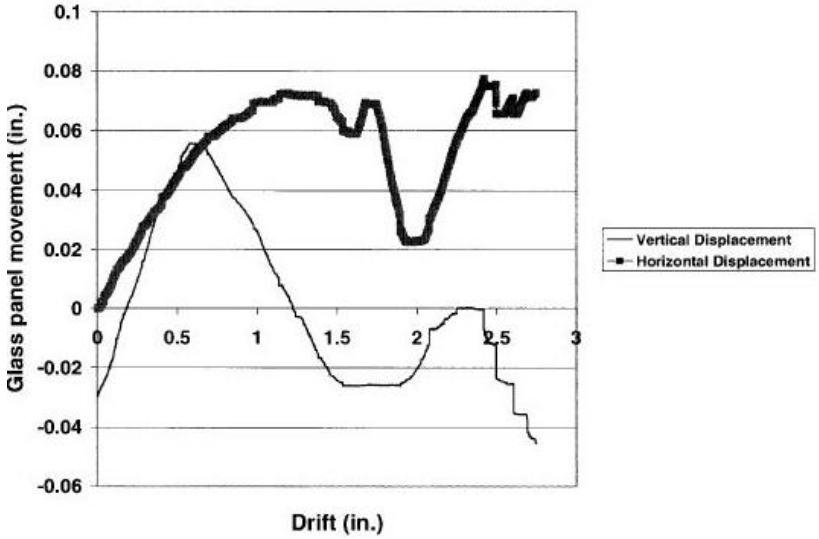

Figure 2-37:Translations of glass-displacement relationship for dry-glazed CW static pushover test (Shirazi 2005)

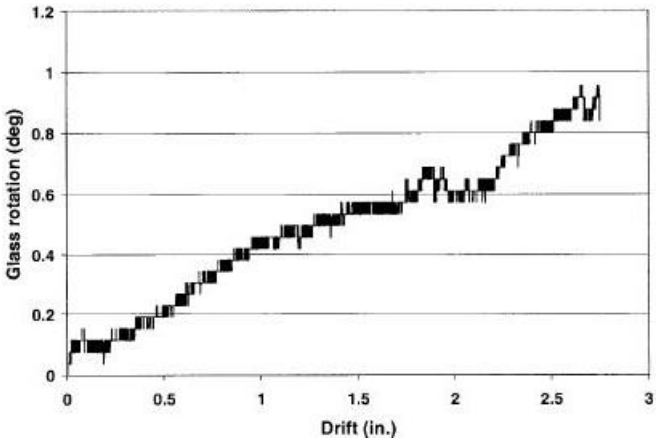

Figure 2-38: Rotations of glass-displacement relationship for dry-glazed CW static pushover test (Shirazi 2005)

2.5.1.4 Static Pushover Test Results for Curtain Wall without Pressure Plates

In this test set essentially no gasket friction was evident in the results which included load-drift relationship and principal strain-drift relationships. The load-drift relationship, as shown in Figure 2-39, is plotted to illustrate key contact stages and damages throughout the drift application. Only the first and second principal strain-drift relationships at the top right corner are plotted in Figure 2-40 and Figure 2-41, respectively. As shown in Figure 2-40 it was also observed that because there is no friction involved, there is a linear relationship between the first principal strain and drift.

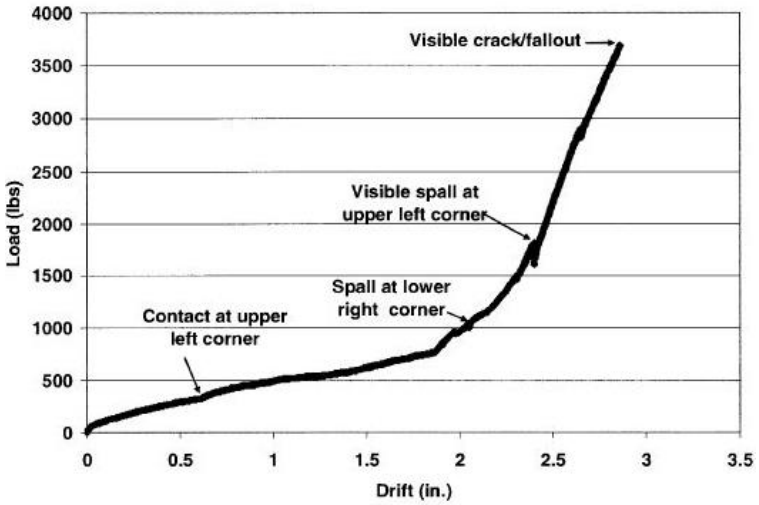

Figure 2-39: Load-displacement relationship for static pushover test of CW system with no pressure plates (Shirazi 2005)

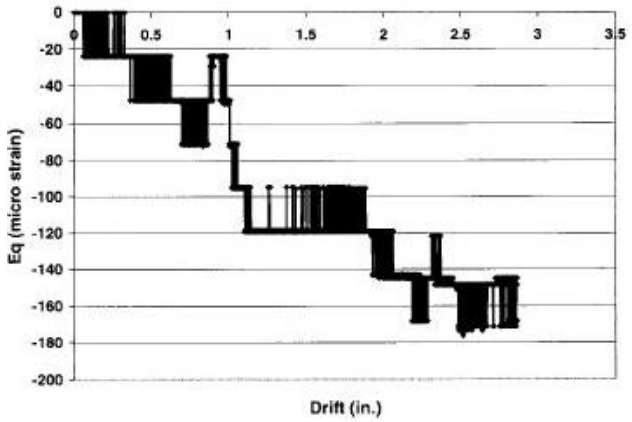

Figure 2-40: First principal strain-displacement relationship for static pushover test of CW system with no pressure plates (Shirazi 2005)

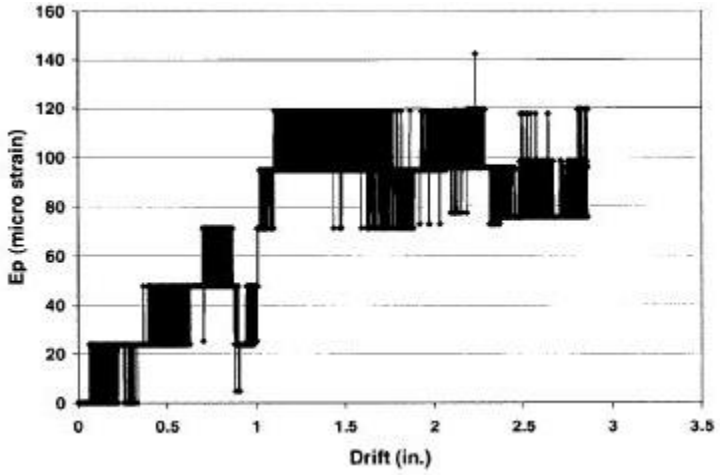

Figure 2-41: Second principal strain-displacement relationship for static pushover test of CW system with no pressure plates (Shirazi 2005)

2.5.1.5 Cyclic and Static Pushover Test Results for Unglazed Curtain Wall

In this test set, Shirazi (2005) sought to find the amount of lateral stiffness the frame itself contributed to the total lateral stiffness of the fully glazed curtain wall specimen during racking. The bare frame obtains this lateral stiffness due to the semi-rigid transom-to-mullion connections which are achieved with the use of the shear blocks as shown in Figure 2-30. The load-drift relationship for the cyclic protocol, using a static crescendo with a drift amplitude of 1.25 in. at a frequency of 0.01 Hz, is shown in Figure 2-42. As for the static pushover test which applied a static drift at a rate of 0.01 cm/sec, the resulting load-drift relationship measured and the corresponding line-of-best fit curve is shown in Figure 2-43. The results from Figure 2-43was subsequently used in the calibration of the hinged connection that was implemented in Shirazi's FE model.

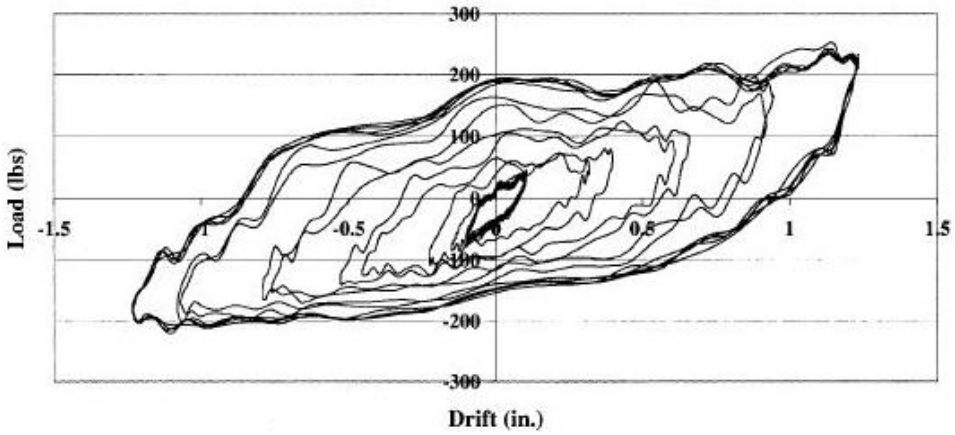

Figure 2-42: Load-displacement relationship of unglazed (bare) Kawneer 1600 CW frame subjected to cyclic racking test (Shirazi 2005)

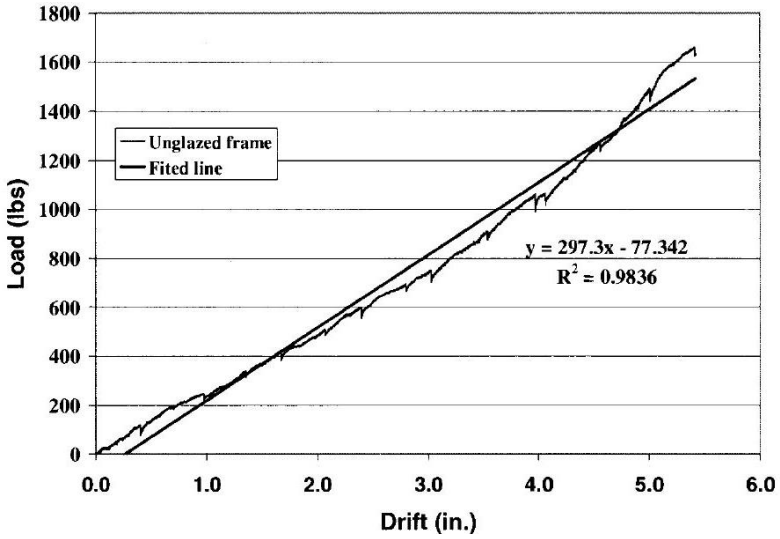

Figure 2-43: Load-displacement relationship of unglazed (bare) Kawneer 1600 CW frame subjected to static racking test (Shirazi 2005)

2.5.2 Overview of Out-of-Plane Experimental Test

At Texas Tech University, Linden et al. (1983) completed lateral uniform pressure testing of laminated glass panels as part of a window glass research program set on establishing improved glass design procedures and understanding glass behaviors during extreme windstorms. The behavior of the laminated glass was compared to structural behaviors of a monolithic glass and a layered glass specimen, all of which were subjected to a uniform pressure. Additionally, the monolithic glass and layered glass results were compared to their respective theoretical analysis models to validate these models. Then the verified theoretical model of the layered glass was used to compare with the laminated glass test results. The dimensions of the monolithic, layered and laminated glass panels were 96 in. height x 60 in. width (2,438 mm x 1,524 mm) with a total thickness of 1/4 inch (6 mm).

2.5.2.1 Out-of-Plane Test Apparatus and Test Protocol

As discussed in section 2.4.2, most tests follow similar testing protocols and utilize test apparatus' that can perform uniform pressure loadings commonly based on ASTM standards provided earlier. Therefore, test apparatus' used during Linden et al.'s (1983) monolithic glass testing included a vacuum air pressure chamber, vacuum accumulation tanks with dual valve system, and a specimen holding frame, all of which is illustrated in Figure 2-44. Simply supported boundary conditions were established within the holding frame to restrict out-of-plane displacements along the glass boundaries, but allowed for in-plane translations and rotations of the glass. A detailed drawing of the test frame using this

simply supported boundary condition is illustrated in Figure 2-44. This shows how Teflon beads were placed in grooves along the frame channels and cover plates allowing the glass to rest between the two opposing beads and prohibit out-of-plane displacements. Additionally, screws along the test frame were tightened enough to secure the cover plates along the frame and maintain a 0.001 inch (25.4 μm) gap between the outside glass surface and the cover plate's Teflon bead surface. Therefore, while out-of-plane displacements are effectively prohibited, this maintained gap implies that no clamping force exists and thus allows for in-plane translations and rotations along the glass boundary during loading. Finally, strain gages were strategically placed on the glass surfaces for the measurement of strains, and a deflection transducer device set up at the center of the glass specimen to acquire displacements during loading.

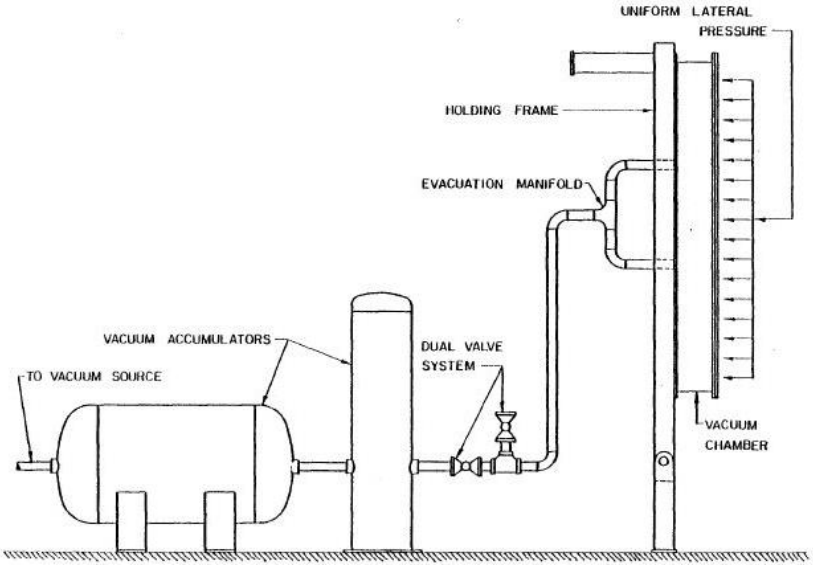

a) Layout of test apparatus at Texas Tech University used to carry out lateral uniform pressure tests on monolithic and laminated glass panels

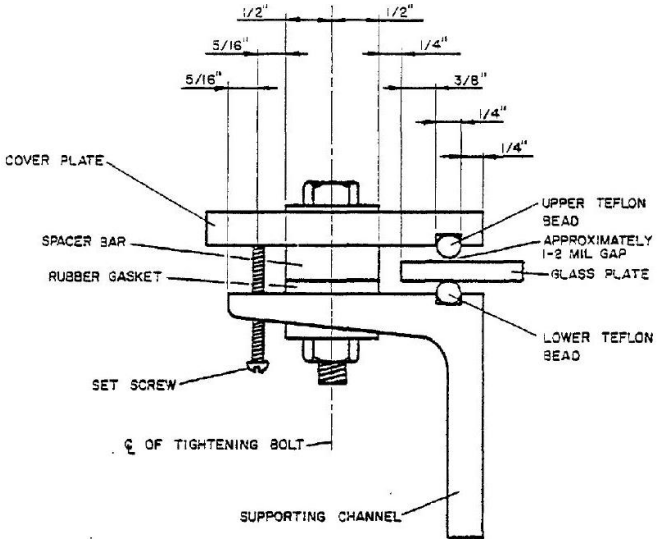

b) Detail cross-section drawing of glazing closure device (steel holding frame)

Figure 2-44: Test apparatus setup for lateral uniform pressure testing of glass panels used in glazing systems (Linden et al. 1983)

The testing plan executed in the research was divided into 4 separate parts for the different incorporated glass types: 1) monolithic glass at 72 °F (22 °C); 2) layered glass (two 1/8 in. glass on top of each other) at 72 °F (22 °C); 3) laminated glass at 72 °F (22

°C); and 4) Laminated glass at 32 °F, 100 °F, 120 °F, 170 °F. Each of these tests sets were loaded laterally with a linearly increasing uniform pressure up to 0.40 psi, with the exception of the monolithic set which was up to 0.75 psi (5.17kPa), in 15 seconds. A more detailed description of each test is provided by Linden et. al (1983). The loading procedure in these experiments was more of a non-destructive protocol because Linden et al. (1983) mainly wanted to validate the theoretical models used for each of the glass specimen types. Therefore, failure was not reached in these test and so no identifiable cracking or failure mechanisms were reported or even looked for. Additionally, the last set of results will not be summarized in the following sections but readers may view such results within the report by Linden et al. (1983).

2.5.2.2 Lateral Uniform Pressure Results for Monolithic Plate Specimen

While failure loads were not reached and acquired, the maximum principal stresses and their respective orientation angles were measured as a function of the applied uniform pressure at the corner regions and center of the glass panel as depicted in Figure 2-45, respectively. Additionally, the lateral displacements of the glass center were also measured as a function of the applied uniform pressure as illustrated in Figure 2-46. It is observed that the maximum principal stresses are much higher at the corners of the glass than at the center region. Looking at the all graphs it is clear that the theoretical analysis is validated due to similar results in the experiment. In all the graphs, the theoretical model was able to capture the change in orientation angle at the maximum principal stress of 0.35 psi. As for the maximum deflection, values in both sets of theoretical and experimental results

obtained maximum lateral glass center deflection of 1.5 inch at an applied pressure of 0.75 psi. It is clear that the pressure vs. lateral deflection at the center of glass displays a geometrically non-linear behavior due to max displacement being greater than the thickness of the glass panel.

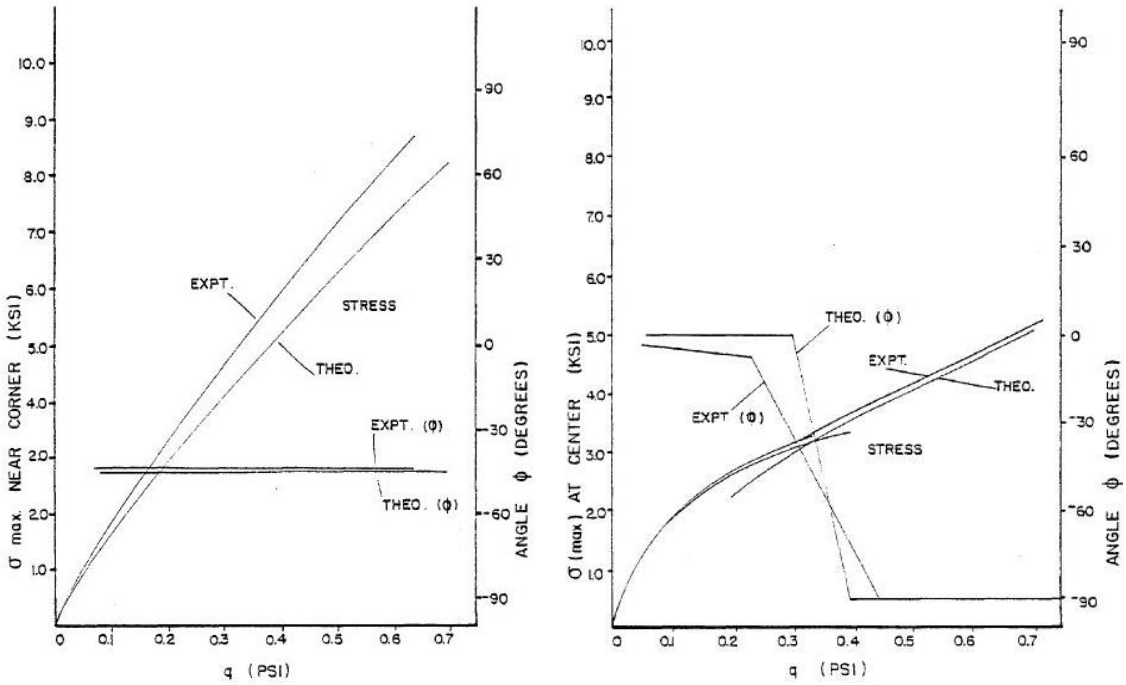

a) Magnitude and orientation of max principal stresses at the corner of monolithic glass during applied lateral uniform pressure (theoretical and experimental results)

b) Magnitude and orientation of max principal stresses at the center of monolithic glass during applied lateral uniform pressure (theoretical and experimental results)

Figure 2-45: Maximum principal stress and their respective orientation angles at the corner and center of monolithic glass due to applied uniform pressure (theoretical and experimental results) (Linden et al. 1983)

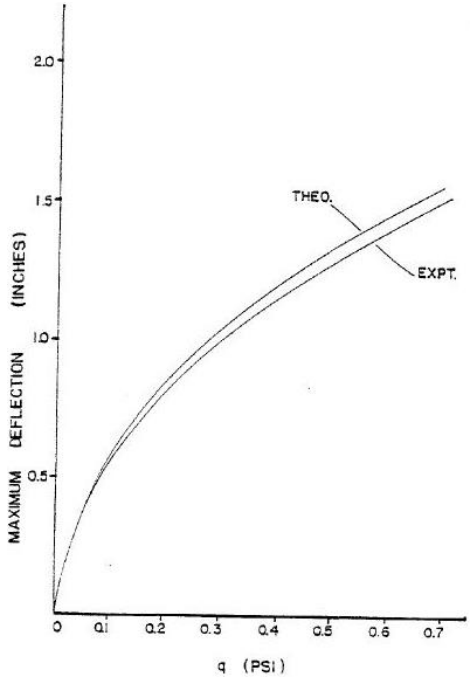

Figure 2-46: Maximum deflection at the center of monolithic glass panel due to the applied uniform pressure (theoretical and experimental results) (Linden et al. 1983)

2.5.2.3 Lateral Uniform Pressure Results for Layered Glass Plate Specimen

The maximum principal stresses and their respective orientation angles from the experiment were measured as a function of the applied uniform pressure at the corner regions and center of the glass panel as depicted in Figure 2-47, respectively. Additionally, the lateral displacements of the glass center were also measured as a function of the applied uniform pressure as illustrated in Figure 2-48. Overall, results have validated that the theoretical layered model is an acceptable analysis method for layered glass subjected to lateral pressures. This is because most of the errors between experimental and theoretical results were within 5 to 15 percent.

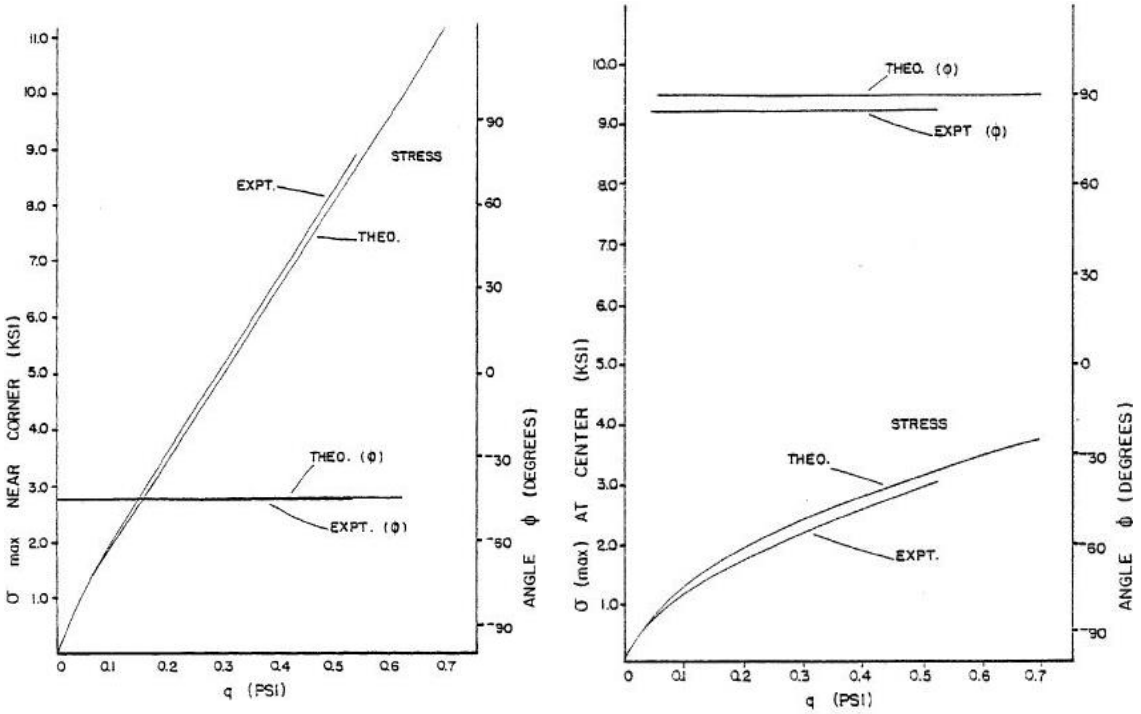

a) Magnitude and orientation of max principal stresses at the corner of layered glass during applied lateral uniform pressure (theoretical and experimental results)

b) Magnitude and orientation of max principal stresses at the center of layered monolithic glass during applied lateral uniform pressure (theoretical and experimental results)

Figure 2-47: Maximum principal stress and their respective orientation angles at the corner and center of layered glass due to applied uniform pressure (theoretical and experimental results) (Linden et al. 1983)

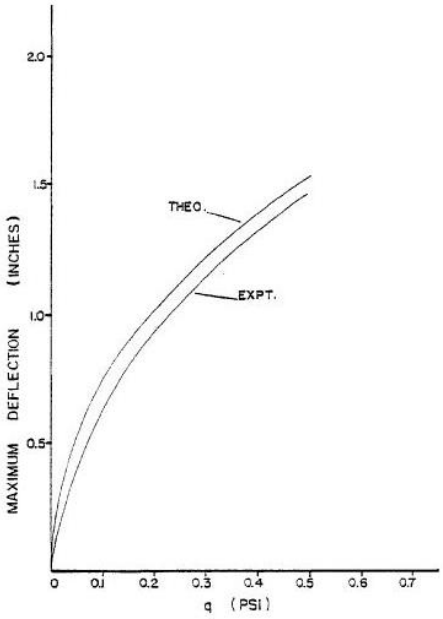

Figure 2-48: Maximum deflection at the center of layered glass panel due to the applied uniform pressure (theoretical and experimental results) (Linden et al. 1983)

2.5.2.4 Lateral Uniform Pressure Results for Laminated Glass Plate Specimen

The maximum principal stresses and their respective orientation angles form the laminated glass experiment were measured as a function of the applied uniform pressure at the corner regions and center of the glass panel as depicted in Figure 2-49, respectively. Additionally, the lateral displacements of the laminated glass center were also measured as a function of the applied uniform pressure as illustrated in Figure 2-50. This time the experimental results were compared to both the validated theoretical analysis results from the monolithic and layered glass units as well to view which model captured the behavior most accurately of the laminated glass. Overall, based on the observed comparisons within

the results, it was concluded that the laminated glass behaved more like a monolithic panel as all results were more similar to the validated monolithic glass model, as opposed to the layered model.

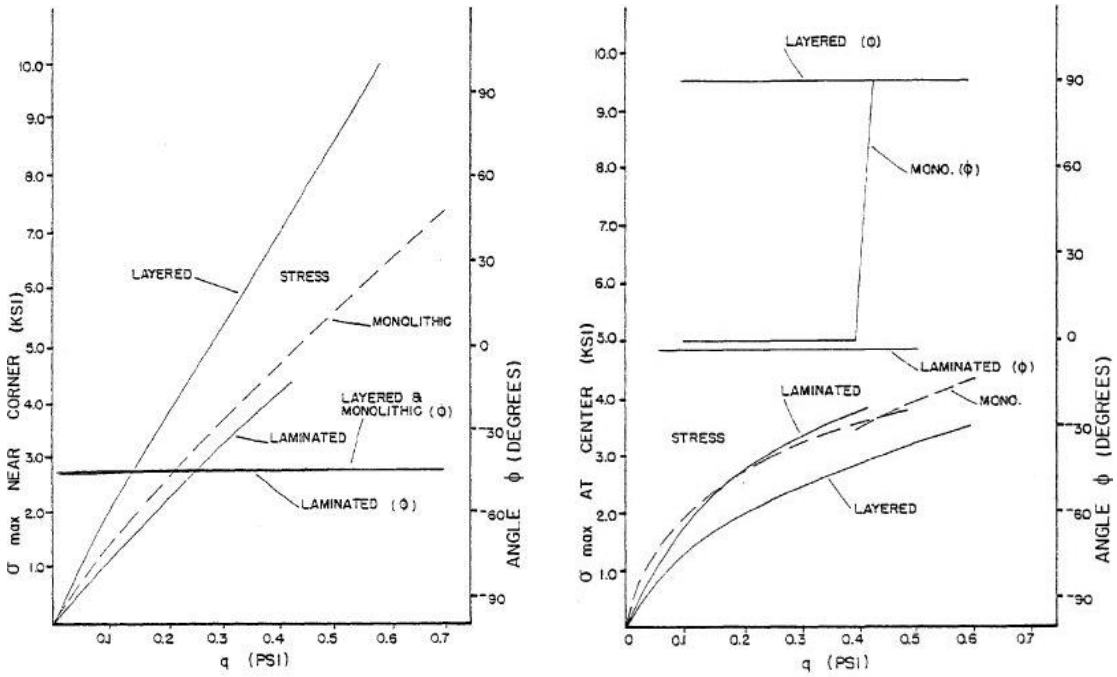

c) Magnitude and orientation of max principal stresses at the corner of laminated glass during applied lateral uniform pressure (theoretical and experimental results)

d) Magnitude and orientation of max principal stresses at the center of laminated glass during applied lateral uniform pressure (theoretical and experimental results)

Figure 2-49: Maximum principal stress and their respective orientation angles at the corner and center of laminated glass due to applied uniform pressure (theoretical and experimental results) (Linden et al. 1983)

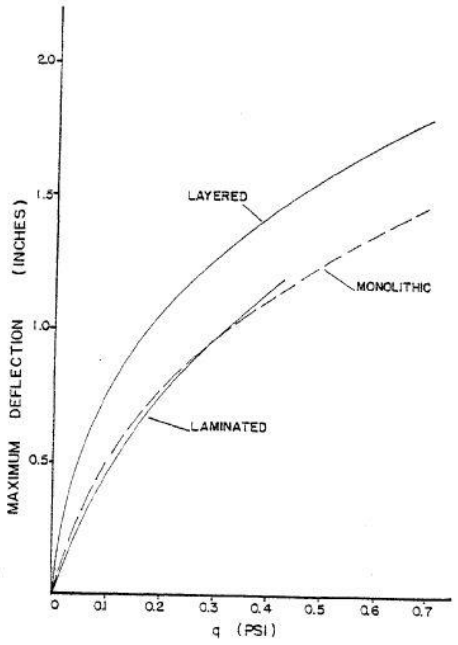

Figure 2-50: Maximum deflection at the center of laminated glass panel due to the applied uniform pressure (theoretical and experimental results) (Linden et al. 1983)

Chapter 3

Small-Scale Glass Curtain Wall Experimental Test for Determination of Equivalent Clamping Load

3.1. Purpose

From the selected in-plane experimental racking test study summarized in the literature review section, it was concluded by Shirazi (2005) that the Kawneer 1600 Wall System™ 1 Curtain Wall was representative of the CW systems designed and constructed in today's built environment. This CW system, and the in-plane experimental study from Shirazi (2005), would therefore be chosen for the validation of the FE computational modeling utilized for the fragility curve development study herein.

It was clear through Shirazi's (2005) experimental work with the Kawneer 1600 CW system that the observed gasket-to-glass friction had a key contribution in the CW specimen's resistance to the applied in-plane racking displacements. The Kawneer 1600 CW system has glass panels installed between the pressure plates and aluminum framing members (i.e. mullions/transoms) along the panel's perimeter surfaces as shown in Figure 2-29. Compression forces acting along the glass perimeters keeping the panel in place are then established by the 9 inch (229mm) center-to-center spacing of screws, which are tensioned up to a screw torque of 95-100 lb-in (10.7-11.3 N-m) required by Kawneer. The clamping force (i.e. compression force) at every screw location is then distributed through the attached fixed glazing gaskets on either side of the glass panel. The modeling of this

clamping force was deemed important to incorporate within the FE models in this computational study since it is directly tied to the gasket-to-glass frictional forces produced when the CW specimen is subjected to drift. Based on the modeling method chosen to generate the Kawneer 1600 curtain wall FE model in Chapter 4, a small scale experimental study was executed to find the equivalent clamping load provided at each screw tensioned to a torque of 95 lb-in (10.7 N-m).

This chapter describes the approach of determining the equivalent clamping loads using an acquired sample of the Kawner 1600 CW system. This approach involved running two uniaxial compression tests to apply a concentrated applied compression force at one of the screw locations. The first test involved a compression force applied until the measured displacements at the CW's glazing pocket, shown in Figure 2-29, were approximately equal to the measured displacements at the same locations when the screws along the assembled sample CW framing system are fully torqued to the required 95 lb-in (10.7 N-m) torque. The force at which the compared measured displacements were the same was approximately the equivalent clamping load. The second compression test involved the same procedure but without the thermal gasket shown in Figure 2-29, to determine how much of the approximated equivalent clamping load is distributed to each fixed glazing gasket on either side of the mullion lip. A more detailed description of this testing plan is presented in the following sections.

3.2. Test Specimen and Test Apparatus

To determine the equivalent clamping load provided by the tensioning of the screws with the required torques suggested by Kawneer, a small portion of the same Kawneer 1600 CW system used in the Shirazi (2005) experiment was obtained. A 24 inch (610 mm) portion of the Kawneer 1600 CW was provided by Kawneer. As shown Figure 3-1, the components provided include: 24 inch (610 mm) intermediate pressure plate, 24 inch (610 mm) thermal break gasket, 24 inch (610 mm) fixed rubber glazing gaskets (a set of 4), and a packet of screws and setting blocks. Plexi-glass panels of 1/4 in. (6 mm) thickness were used instead of the annealed monolithic glass type used in the Shirazi (2005) tests. This was deemed acceptable since the load distribution to the gaskets and the plexi-glass specimen will not be effected. For these tests the intermediate (flat) pressure plate Kawneer 1600 configuration as shown in Figure 3-1 was used.

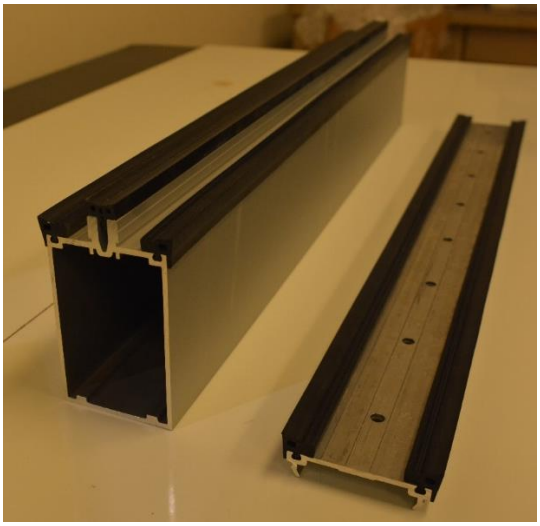

Figure 3-1: Components of the sample Kawneer 1600 CW frame specimen provided by Kawneer : Mullion, pressure plate (flat configuration), fixed glazing gaskets, and thermal gasket

3.2.1. Torque Wrench

To achieve the required screw torque, a torque wrench with a torque capacity range of 5-100 lb-ft (6.78-135.58 N-m) was used. The wrench had an electronic preset feature which allows the user to input a desired torque to be reached. This torque preset feature gives the user the ability to know that the desired torque has been reached within a level of accuracy of ±3%. The feature was used to preset the desired torque limit to 95 lb-in (10.7 N-m) which was within the Kawneer torque requirement listed earlier. This experiment therefore used common methods performed at the construction site with torque meters provided by Kawneer to the installers."

3.2.2. Dry-Glazing Setup Table

A setup table as shown in Figure 3-2 was utilized to help stabilize and minimize movement of the plexi-glass panel whenever the screws were tightened with the torque wrench. Additional weights were placed on the sides of the mullion member to restrict movement of the mullion itself. This setup table made it easier to measure and maintain the glass-to-frame clearance of 11 mm (0.43 in) during this dry-glazing procedure.

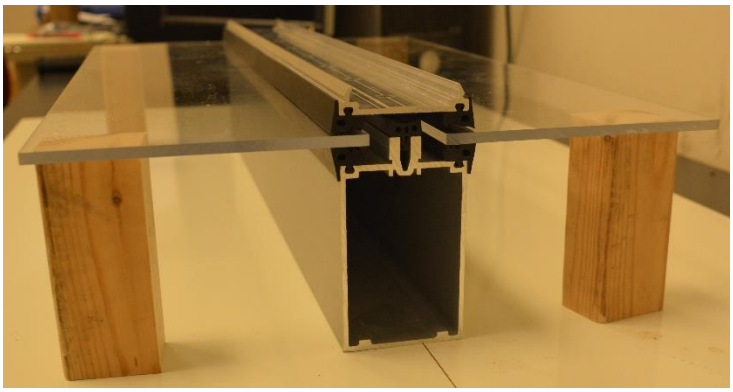

a) Profile view of setup table

b) Plan view of setup table

Figure 3-2: Views of dry-glazing setup table

3.2.3. MTS Electromechanical Loading Frame

An MTS electromechanical universal testing system was utilized for the monotonic compressive loading protocol. The MTS loading frame, which is depicted in Figure 3-3, had the capability of applying compressive forces up to 150 kN (33,721 lbs) onto a specimen. Connected to the MTS loading frame was a lab computer that controlled the applied loads with the use of the accompanying MTS TestSuite software. Furthermore, this software allowed the user to control the direction of the load applied, the loading rate and

measure in real-time the applied loading from the load cell integrated within the loading frame. As shown in Figure 3-3, a steel block was placed on top of the bottom wedge action grip to act as a flat surface for the front half of the CW specimen to rest on. Some concrete and wooden blocks were stacked behind the loading frame, approximately up to the same height as the steel block on the wedge grip, to support the back half of the CW specimen.

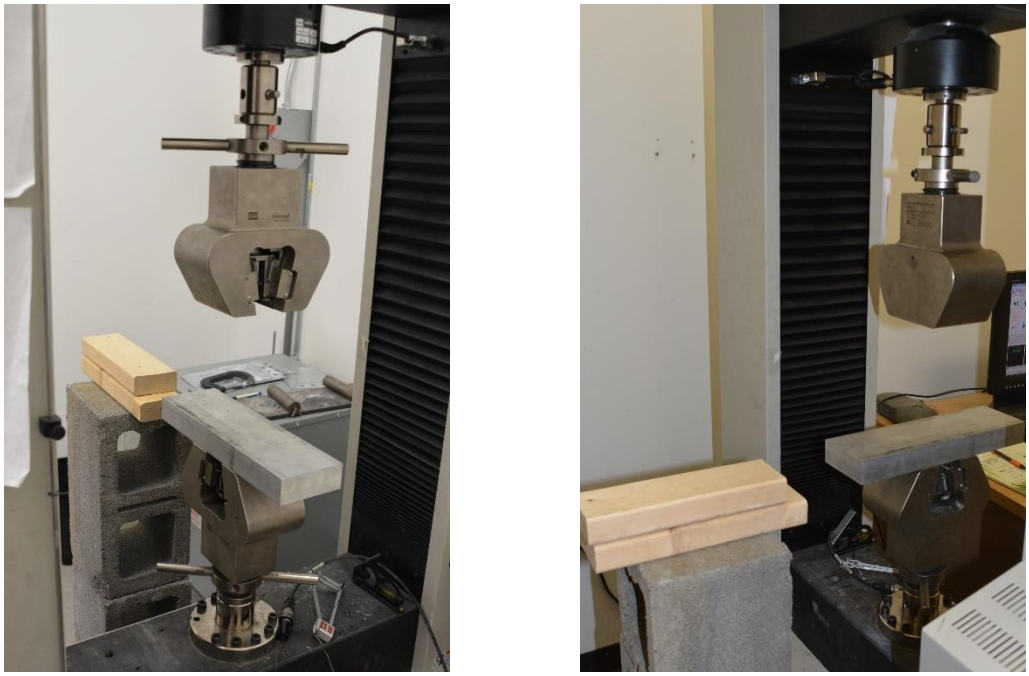

Figure 3-3: Front (left) and back (right) views of the MTS electromechanical universal testing frame layout

Additionally, to concentrate the applied compression force through the top wedge action grip to the pressure plate, wood blocks were cut out and assembled to channel the generated load. As shown in Figure 3-4, the larger wood block makes contact with the bottom of the top wedge action grip surface, and the smaller block would contact the pressure plate directly over the screw hole near the front of the CW specimen such that the surface area of the smaller block would cover the general area of the screw, if it were being

utilized. The final specimen layout within the loading frame for the determination of the equivalent clamping force is shown in Figure 3-5.

Figure 3-4: Wooden block component placed between wedge action grips and top of pressure plate

Figure 3-5: Front (left) and back (right) views of sample CW frame specimen layout within the MTS loading frame

3.3. Data Acquisition

The Displacements were determined from distance measurements taken with a caliper tool at three locations. These locations, labeled A through C, were taken along the glazing pocket cross section as shown in Figure 3-6. Measurements were taken near the front face of the glazing pocket cross section because it was closest to the first screw location, labeled as CC in Figure 3-7. This helped obtain better approximate displacement measurements observed at the screw location during the application of a screw torque or compression load. Caliper measurements taken as the glazing pocket distance decreased, between the top surface of the pressure plate and the bottom surface of the top flange of the mullion frame shown in Figure 3-6, were recorded into an excel table. These measurements were taken during different applied screw torque stages and various increments of compression loads.

The applied compression loads were also obtained and measured with the load cell integrated within the MTS machine. Readouts of the applied loads displayed on the lab computer were then recorded into an excel table. The forces were recorded at the same time the glazing pocket measurements were made in order for a relationship between the applied compression forces and the decreasing glazing pocket distances to be determined later.

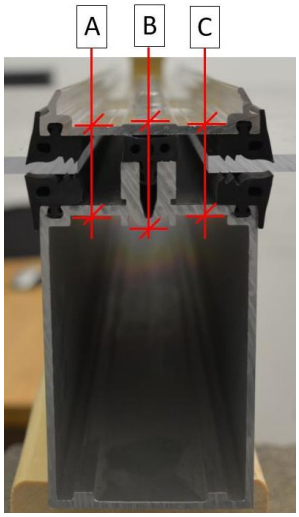

a) Cross-section view of the glazing pocket measurement locations A through C where distance measurements will be made using caliper device

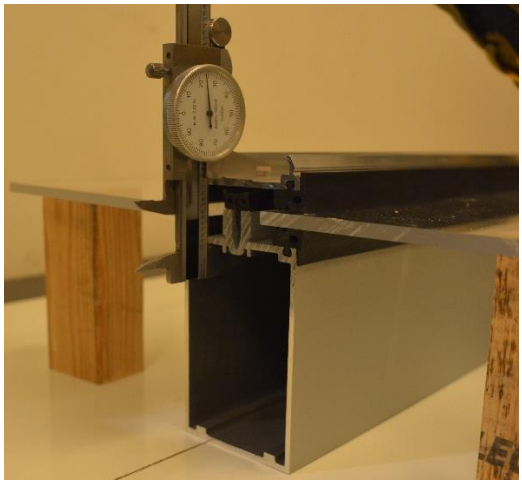

b) Glazing pocket distance being measured with caliper device while on the dry-glazed setup table

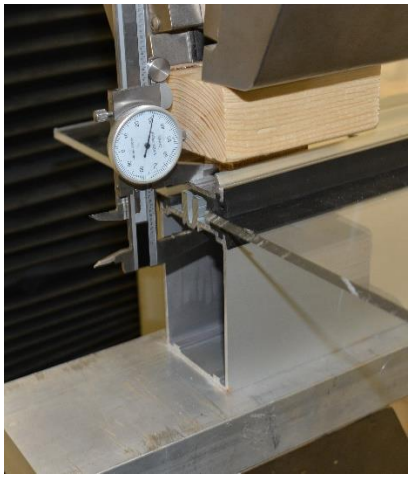

c) Glazing pocket distance being measured with caliper device while in the MTS loading frame

Figure 3-6: Glazing pocket measurement locations for the duration of the equivalent clamping load tests

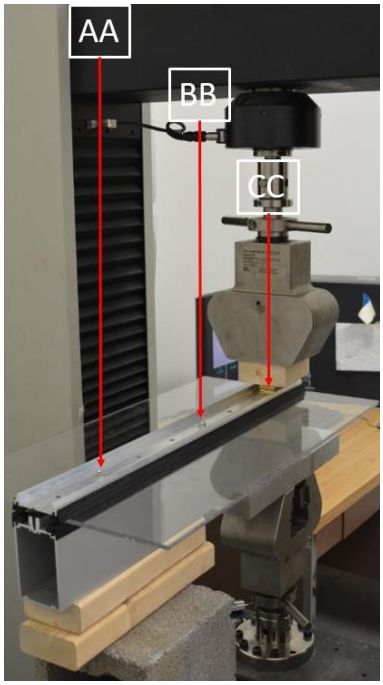

Figure 3-7: Screw locations and naming conventions for the equivalent clamping load tests

3.4. Test Protocol

This section will describe the three test procedures completed to assist in approximating the equivalent clamping load that each screw provides due to a 95 lb-in (10.7 N-m) torque. The first test determined the glazing pocket displacements acquired when the torque requirement was reached on a fully dry-glazed CW specimen. The second test applied a static increasing compressive load to the fully dry-glazed CW specimen until the same displacements obtained in the first test were reached to determine the total equivalent clamping load. Finally, the third test applied the same static increasing compressive load until the initial displacements found in test one are reached. However, this time a partially dry-glazed CW specimen without the thermal rubber gasket was tested

to find the distribution of total equivalent clamping load to the fixed glazing gaskets. These results will help in the calibration and validation of the FE models generated in the next section.

3.4.1. Test #1 Procedure

This test series deals with obtaining the glazing pocket displacements which coincide with both an applied 65 lb-in (7.34 N-m) and 95 lb-in (10.7 N-m) torque at screw CC, which were necessary for the next set of tests. The initial glazing pocket distances at Point A, Point B and Point C of the fully dry-glazed sample curtain wall specimen were measured at the front cross sectional edge near screw CC as depicted previously in Figure 3-6 and Figure 3-7. However, these initial measurements were taken while the sample Kawneer 1600 CW specimen was laid out on the dry-glazing setup table as shown in Figure 3-7. This fully dry-glazed configuration, includes the plexi-glass held between fixed glazing gaskets and pressure plate. No screws were used in this initial stage, however, to record the initial glazing pocket distances under no compression from screw tension. It was observed that the pressure plates did not come into full contact with the thermal gaskets as it rested on only the top layer of fixed glazing gaskets in the initial dry-glazed stage.

Once these initial measurements were recorded, tensioning of the screws with the torque wrench commenced in two stages. In the first stage, all three screws (screw AA, BB and CC) were placed inside the pre-cut holes along the pressure plate at 9 in. (229 mm) center-to-center spacing. Once in place, the torque wrench was preset to the desired torque of 65 lb-in (7.34 N-m), which was determined to be the “snug tight” torque when the

pressure plate initially comes into full contact with the thermal gasket, as well as above the minimum torque which can be readout on the LCD display. All three screws were then tightened until the “snug tight” toque was met. The order the screws were tightened to was first the two outside screws (screw AA and CC) and then the inside screw (screw BB), to minimize any additional glass/components movement and maintain the 11 mm glass-to-frame clearance. Finally, the newly decreased glazing pocket distances, which coincided with this 65 lb-in “snug tight” torque, were measured and recorded.

In the second stage, the torque wrench is preset to the required 95 lb-in and the screws are fully torqued in the same order as in the first stage of this test. Once the wrench beeps and displays the full 95 lb-in torque, the newly decreased glazing pocket distances, which coincided with the full torque, are measured and recorded. Glazing pocket displacements were then computed from the glazing pocket distances at “snug tight” and full torque. Therefore, the last two tests will then use both sets of displacements that relate to the “snug tight” and full torques, to acquire the equivalent clamping loads.

3.4.2. Test #2 Procedure

In this test series, the same Kawneer sample specimen in the fully dry-glazed configuration was held in the dry-glazing setup table for screw tensioning. However, in this series only two screws, specifically screw AA and BB, were ever tensioned for the duration of the test, and the compression load would be applied in lieu of screw CC. This series was completed in two stages.

In the first stage, while the specimen was still on the setup table layout, only the last two screws (screw AA and BB) were tensioned to the “snug tight” torque of 65 lb-in using the same torque wrench process in test #1 series. Once the desired torque was reached, the fully dry-glazed curtain wall specimen was placed in the MTS loading frame on top of the blocks directly above the bottom wedge grip such that the top wedge grip was directly above where screw CC would be. The top wedge grip was lowered until it rested just on top of the wood block cut outs as shown in Figure 3-5, representing a zero compressive load. Using the MTS TestSuite software on the lab computer, a statically increasing, downward force was then applied onto the screw CC location at approximately 10 pound increments. Using the computer’s load cell readout to help with approximating the loading increments, the decreasing glazing pocket distances along the specimen’s cross section, and the load readouts, were measured and recorded at every load increment. This continued until all three of the glazing pocket distances (at Points A through C) measured were approximately equal to the glazing pockets measured distances recorded from test #1 for the “snug tight” torque stage. The glazing pocket displacements for Points A through C during the “snug tight” torque stage are then calculated from the difference of the initial pocket distances measured before any torque is applied, as determined in test #1, and the decreasing pocket distances measured throughout the “snug tight” torque stage in this test series.

Stage two, described as the full torque stage, is then carried out. While the glazed specimen is still loaded in the MTS loading frame, screws AA and BB are fully torqued to the 95 lb-in required torque. Once the full torque had been achieved, the downward force procedure carried out in stage one was continued, however, this time in increments of

approximately 20 lbs. Again, at every increasing load increment the glazing pocket distances at Points A through C were measured and recorded. This continued until the distances acquired were approximately equal to the distances recorded back in test #1 which coincided to the desired full torque. The same process of deriving and recording the glazing pocket displacements at Points A through C back in stage one was carried out throughout this full torque stage. However, this time the recorded glazing pocket distances that coincide with the fully torqued specimen in test #1 were used.

3.4.3. Test #3 Procedure

For this test final series, the thermal gasket was taken out of the Kawneer curtain wall sample specimen to approximate the distribution of the total equivalent clamping load to the fixed glazing gaskets, and consequently to the thermal gasket. With this partially dry-glazed specimen, the same procedure utilized for test #2 was carried out to obtain equivalent clamping loads, glazing pocket distances and glazing pocket displacements during the “snug tight” and fully torqued stages of incremental compression loading.

3.5. Results and Discussion of Tests

This section will overview the test results obtained in test series 1 through 3, as well as the applied compressive load-glazing pocket distance relationship and the applied load-glazing pocket displacement relationship derived. Both relationships were utilized in the

approximation of the total equivalent clamping load due to the required full torque of 95 lb-in (11.3 N-m), and the distribution of the total equivalent clamping load to each gasket.

3.5.1. Test #1 Results

The initial measurements of the fully dry-glazed Kawneer sample specimen along Points A through C which were taken at the pre-torque phase, when screws were not tightened, are shown in Table 3-1. This also included the actual 0.215 in. (5.46mm) thickness of the plexi-glass plate and the glass-to-frame clearance of 11 mm which was maintained throughout test series. The thermal gasket was observed to not come into full contact with the pressure plate because of an extrusion cut made in the cross section of the thermal gasket. Some small differences were measured in the glazing pocket distance at Points A and C, but these were very minimal and attributed to the tolerances in the components and the fixed gasket profile shapes.

Table 3-1: Summary of Initial Measurements of Fully Dry-Glazed Sample CW Specimen Prior to Any Screw Torque

Nominal Glass Thickness	0.215 in.	5.46 mm
Glass-to-Frame Clearance	0.433 in.	11.0 mm
Point A Initial Distance	1.107 in.	28.1 mm
Point B Initial Distance	1.252 in.	31.8 mm
Point C Initial Distance	1.102 in.	28.0 mm

The glazing pocket distance measurements taken after all three screws were tightened to the “snug tight” torque of 65 lb-in are shown in Table 3-2. The calculated glazing pocket displacements at the “snug tight” torque were also recorded in Table 3-2. An average glazing pocket displacement of 0.124 in. (3.14 mm) was observed during this

"snug tight" stage. Subsequently, the same glazing pocket distances and displacements when screws were fully torqued to 95 lb-in are shown in Table 3-3. And an average total glazing pocket displacement of 0.166 in. (4.22 mm) took place during the fully torqued stage.

Table 3-2: Summary of Test #1 - Glazing Pocket Distances & Displacements After a Screw Torque of 65 lb-in (7.34 N-m) [Fully Dry-Glazed Configuration]

Point A Distance	0.984 in.	25.0 mm
Point B Distance	1.126 in.	28.6 mm
Point C Distance	0.98 in.	24.9 mm
Point A Displacement	0.123 in.	3.12 mm
Point B Displacement	0.126 in.	3.20 mm
Point C Displacement	0.122 in.	3.10 mm
AVG:	0.124 in.	3.14 mm

Table 3-3: Summary of Test #1 - Glazing Pocket Distances & Displacements After a Screw Torque of 95 lb-in (10.7 N-m) [Fully Dry-Glazed Configuration]

Point A Distance	0.948 in.	24.1 mm
Point B Distance	1.078 in.	27.4 mm
Point C Distance	0.936 in.	23.8 mm
Point A Displacement	0.159 in.	4.04 mm
Point B Displacement	0.174 in.	4.42 mm
Point C Displacement	0.166 in.	4.22 mm
AVG:	0.166 in.	4.22 mm

Observations noticed that after each screw torque stage the small glazing pocket distance at Points A and C, and their related displacements, were still not equal after gasket compression occurred. However, these differences in distances seem to have been consistent throughout the screw tensioning process as the glazing pocket displaces.

Therefore, the load resistance to the compression during screw torqueing at this point was assumed to be distributed equally between the fixed glazing gaskets.

After the full screw torque is reached, the gaskets exhibit both in-plane and out-of-plane (thru thickness direction) distortion. This caused the gasket-to-glass surface area to increase along the length of the glass edge as the gaskets spread out, in-plane of the glass, the tighter the screws became. Based on the gasket distortions and changes in contact, the frictional forces may vary along the length of glass-to-gasket contact regions and this will need to be incorporated/captured in the ensuing FE models.

3.5.2. Test #2 Results

With the applied compression loads and glazing pocket distance measurements recorded throughout both “snug tight” and full torque stages, the applied load-glazing pocket distance relationship and applied load-glazing pocket displacement relationship were studied at each Points A through C on the glazing pocket. The load-distance relationship for each glazing pocket point was graphed in Figure 3-8. Based on this figure, the decreasing glazing pocket distances shows an approximately linear load-distance relationship across all points. It is evident that the small difference between the glazing pocket distance at Points A and C is held constant as load is increased. The gap between the curves on Figure 3-8 is relatively kept the same except for in the higher compressive loads region. This relatively constant difference correlates well with what was observed in test #1 results and validates the assumption that the applied compressive load due to the screw torque is distributed evenly to the fixed glazing gaskets at Point A and Point C.

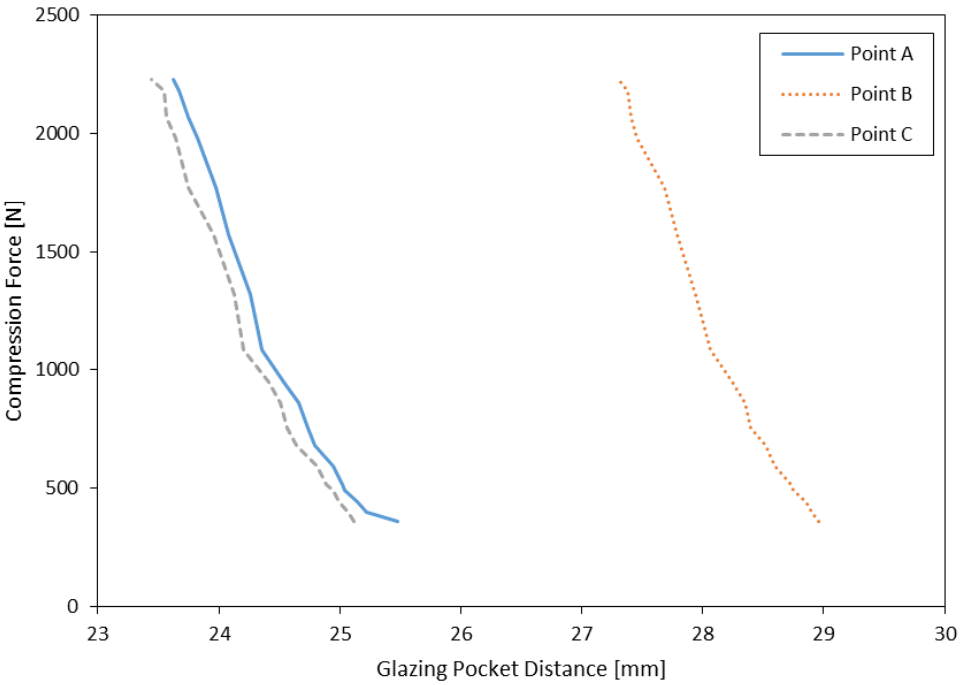

Figure 3-8: Compression load-glazing pocket distance relationship for Test #2

Utilizing the glazing pocket displacements calculated with the process described in test #2's procedure, the load-displacement relationship at each glazing pocket point location was graphed in Figure 3-9. This plot showed a nearly linear load-displacement relationship as the compressive loads reached an equivalent glazing displacement that coincided with the Kawneer torque requirement.

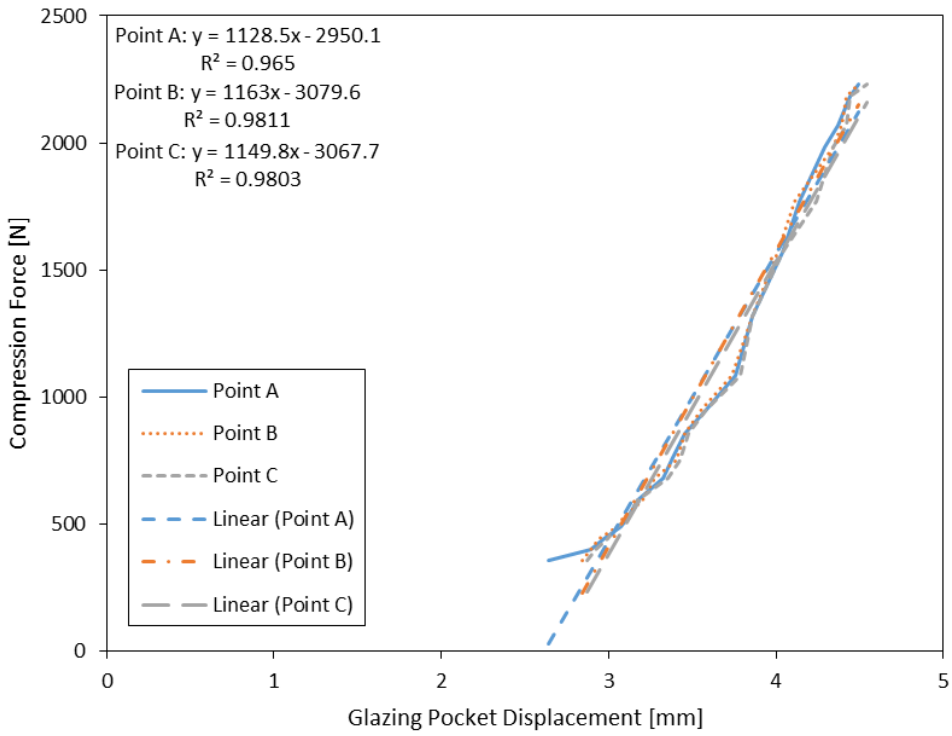

Figure 3-9: Compression load-glazing pocket displacement relationship for Test #2

As shown in Table 3-4, the three displacements found in this test for Points A through C, which relatively matched with the displacements at "snug tight" torque in test #1, occurred at relatively the same compression force in the loading frame. However, this was not the case for the displacements acquired during the full torque stage, since the three displacements at Points A through C, which relatively matched with the displacements at full torque in test #1, did not occur at the same compression forces. Therefore, a slight modification to the assumption of an equal distribution of total equivalent clamping load to the fixed gaskets at Points A and C previously stated must be made. Based on the data, the distribution of the total equivalent clamping loads could be assumed to be equal during low torque levels, such as during the "snug tight" torque stage, but unequal at higher torque

levels, such as during the full load torque stage. This uneven distribution of forces can be attributed to the observed distortions of the gaskets and the material's non-linear behavior during increased compression. Additionally, while the load-distance and load-displacement relationships are assumed to be linear, the curves produced in Figure 3-8 and Figure 3-9 still showed signs of a non-linear relationship.

Table 3-4: Glazing Pocket Displacements and Respective Compression Loads Matched to Initial Glazing Pocket Displacements at Different Torque Stages [Test #2]

	Displacement [mm]	Compression Load [N]	Torque Stage
Point A	3.10	516	"Snug Tight"
Point B	3.20	594	"Snug Tight"
Point C	3.10	516	"Snug Tight"
Point A	4.04	1570	Full
Point B	4.42	2182	Full
Point C	4.24	1770	Full

Two methods were employed to determine the total equivalent clamping load that equated to the desired 95 lb-in (11.3 N-m) torque. The first method involved using the set of the three glazing pocket displacements (at Points A through C), and their respective applied compressive load, from test #2 as shown in Table 3-4. These test #2 displacements were approximately equal to the measured displacements at the full torque stage measured in test #1. The applied compressive loads at each point as shown in Table 3-4 were then averaged to obtain the total equivalent clamping loads at each torque stage as shown in Table 3-5. Therefore, the total equivalent clamping load at the full torque stage (i.e. 95 lb-in (10.7 N-m)) was 414 lbs. (1,841 N). This procedure was repeated for the "snug tight" torque stage (i.e. 65 lb-in (7.34 N-m)) which approximately resulted in a total equivalent clamping load of 122 lbs. (542 N).

Table 3-5: Average Compression Loads Along the Glazing Pocket Points (Fully Dry-Glazed Configuration) During Different Torque Stages [Matching Displacement Data Method]

	Compression Load [N]	Torque Stage
Points A-C Average	542	"Snug Tight"
Points A-C Average	1841	Full

The second method involved using the load-displacement relationship curves generated for test #2 in Figure 3-9. Linear regression lines were created through the excel toolset to get a linear line of best fit for each of the load-displacement curves generated for Points A through C. Three line of best fit equations were displayed on Figure 3-9 and listed in order from top to bottom to match with the corresponding linear regression lines generated for Point A, B and C load-displacement curves, respectively. With the glazing pocket displacements associated with the full torque recorded in Table 3-3, the total equivalent clamping loads were determined by inputting each displacement into their appropriate line of best fit equation for Points A through C. The three equivalent clamping loads at each glazing pocket point were determined from each equation and then averaged to produce the final total equivalent clamping load associated with the desired full torque stage as shown in Table 3-6. Therefore, the total equivalent clamping load at the full torque stage (i.e. 95 lb-in (10.7 N-m)) using method two was determined to approximately be 408 lbs. (1816 N). This same method two procedure was used to find the total equivalent clamping load at the “snug tight” torque stage (i.e. 65 lb-in (7.34 N-m)) which led to an approximate load of 128 lbs. (571 N) as shown in Table 3-6.

Table 3-6: Average of the Compression Loads Along the Glazing Pocket Points (Fully Dry-Glazed Configuration) During Different Torque Stages [Linear Regression Lines Method]

	Compression Load [N]	Torque Stage
Point A	576	"Snug Tight"
Point B	642	"Snug Tight"
Point C	495	"Snug Tight"
AVG	571	"Snug Tight"
Point A	1607	Full
Point B	2060	Full
Point C	1780	Full
AVG	1816	Full

Based on these two methods implemented, the approximated total equivalent clamping loads produced were very similar. Therefore, to be implemented into the FE models generated later, it was decided to use 405 lbs. (1,800 N) as the total equivalent clamping loaded associated with the 95 lb-in (10.7 N-m) full torque required. Rounding down to the nearest hundred Newton was done such that SI units could be implemented within the FE software used later.

3.5.3. Test #3 Results

Once the test #3 series was completed with a partially dry-glazed Kawneer CW specimen, where the thermal gasket was not used, similar results that occurred during test #2 were observed in terms of component behaviors and load-distance/load-displacement relationships. With the applied compression loads and glazing pocket distance measurements recorded throughout both “snug tight” and full torque stages in this test series, the applied load-glazing pocket distance relationship and applied load-glazing

pocket displacement relationship were studied at each Points A through C of the glazing pocket. The load-distance relationship for each glazing pocket point was graphed in Figure 3-10. Based on this figure, the decreasing glazing pocket distances still showed an approximately linear load-distance relationship across all points, which was evident in test #2 series. However, the load-displacement curves had more aggressive slope changes when a compressive load of approximately 900 N (202.38 lbs) was reached. Since this occurred during the full torque stage, this behavior was mainly attributed to the fixed glazing gaskets behaving more non-linearly than in test #2 series because the thermal gasket was absent, and only the fixed glazing gaskets were resisting the compression forces. Likewise, the in-plane and out-of-plane (thru thickness direction) gasket distortions observed during this test were more evident than what was observed in test #2.

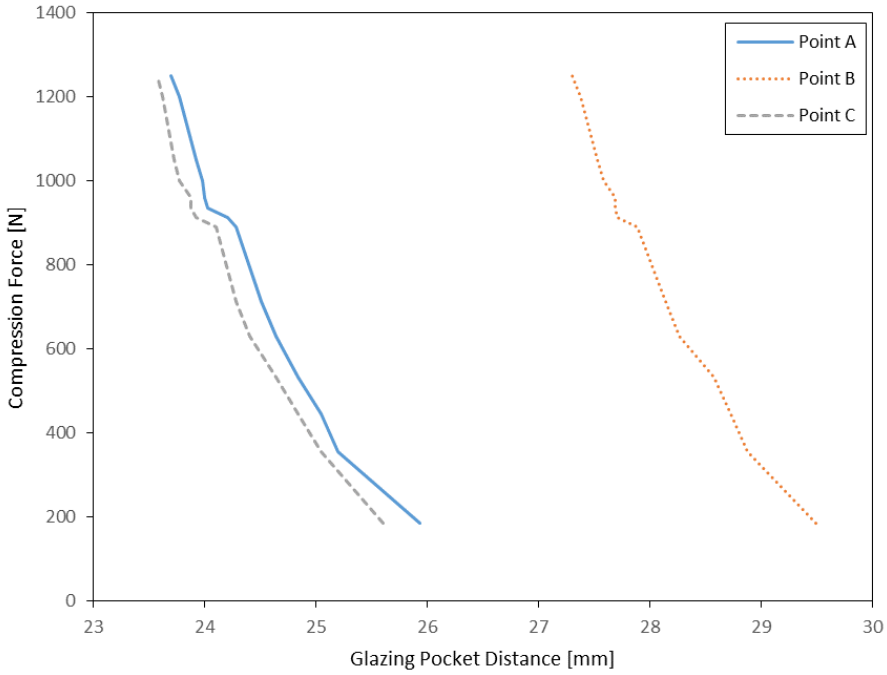

Figure 3-10: Compression load-glazing pocket distance relationship for Test #3

Furthermore, it was still observed that the small difference between the glazing pocket distance at Points A and C was relatively constant as the load was increased. This constant difference correlates well with what was observed in test #1 results and for now validates the assumption that the applied compressive load due to the screw torque is distributed evenly to the fixed gaskets at Point A and Point C.

Utilizing the glazing pocket displacements calculated with the process described in test #3's procedure, the load-displacement relationship at each glazing pocket point location was graphed in Figure 3-11. The plotted curves showed a nearly linear load-displacement relationship as the compressive loads reached an equivalent glazing displacement that coincided with the Kawneer torque requirement.

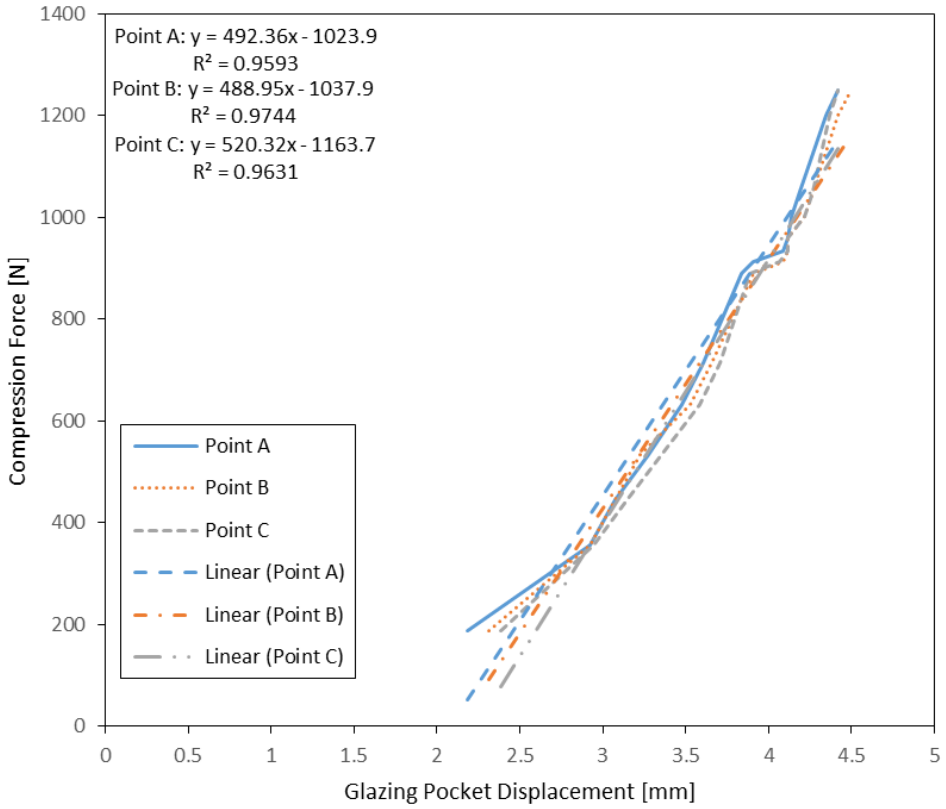

Figure 3-11: Compression load-glazing pocket displacement relationship for Test #3

As shown in Table 3-7, the three displacements found in this test for Points A through C, which relatively matched with the displacements at "snug tight" torque in test #1, occurred at relatively the same compressive force in the loading frame. However, this was not the case for the displacements acquired during the full torque stage, since the three displacements at Points A through C that relatively matched with the displacements at full torque in test #1 did not occur at relatively the same compressive forces. So just as was discussed in test # 2 results section, a slight modification to the assumption of an equal distribution of total equivalent clamping load to the fixed gaskets at Points A and C previously stated must be made. Therefore, based on this data, the distribution of the total

equivalent clamping loads could be assumed to be equal during low torque levels, such as during the “snug tight” torque stage, but unequal (or rather the distribution changes back and forth between the glazing gaskets at Points A and C) at higher torque levels, such as during the full load torque stage. This uneven and changing distribution of forces can be attributed to the observed distortions of the gaskets and the material’s non-linear behavior during increased compression, which again was more apparent in this test #3 series because of the absence of the thermal gasket. During this test #3 series, the changing distribution of forces was also more evident because when looking at the load-displacement curves of Points A and C in Figure 3-11 the curves were not always aligned throughout the compressive loading protocol, whereas the load-displacement curves of Point A and C in Figure 3-9 were more aligned throughout compression.

Table 3-7: Glazing Pocket Displacements and Respective Compression Loads Matched to Initial Glazing Pocket Displacements at Different Torque Stages [Test #3]

	Displacement [mm]	Compression Load [N]	Torque Stage
Point A	3.07	445	"Snug Tight"
Point B	3.23	534	"Snug Tight"
Point C	3.15	445	"Snug Tight"
Point A	4.09	934	Full
Point B	4.42	1201	Full
Point C	4.22	1001	Full

Next, the distribution of the total equivalent clamping load, found in the test #2 results section, to the fixed glazing gaskets at Point A and C was determined. Consequently, the portion of clamping load that goes into the thermal gasket at Point B was found as well. The same two methods used in section 3.5.2 were used to find the combined equivalent clamping loads at the fixed glazing gaskets. Therefore, for method one, the set of the three

glazing pocket displacements (at Points A through C) was used, as was their respective applied compressive load from test #3 as shown in Table 3-7. These test #3 displacements were approximately equal to the measured displacements at the full torque stage measured in test #1. The applied compressive loads at each glazing pocket point, as shown in Table 3-7, were then averaged to obtain the combined equivalent clamping load that goes into both of the fixed glazed gaskets at each torque stage as shown in Table 3-8. Therefore, the combined equivalent clamping load at the full torque stage (i.e. 95 lb-in (10.7 N-m)) was 235 lbs. (1,045 N). This procedure was repeated for the "snug tight" torque stage (i.e. 65 lb-in (7.34 N-m)) which approximately resulted in a total equivalent clamping load of 107 lbs. (474 N)."

Table 3-8: Average Compression Loads Along the Glazing Pocket Points (Partially Dry-Glazed Configuration) During Different Torque Stages [Matching Displacement Data Method]

	Compression Load [N]	**Torque Stage**
Points A-C Average	474	"Snug Tight"
Points A-C Average	1045	Full

The second method involved using the load-displacement relationship curves generated for test #3 in Figure 3-11. Linear regression lines were again generated through the excel toolset to get a linear line of best fit for each of the load-displacement curves generated for Points A through C on the partially glazed specimen. Three line of best fit equations were displayed on Figure 3-11 and listed in order from top to bottom to match with the corresponding linear regression lines generated for Point A, B and C load-displacement curves, respectively. With the glazing pocket displacements associated with the full torque recorded in Table 3-3, the total equivalent clamping loads were determined

by inputting each displacement into their appropriate line of best fit equation for Points A through C. The three equivalent clamping loads at each glazing pocket point were determined from each equation, and then averaged to produce the combined equivalent clamping load going into the fixed gaskets associated with the desired full torque stage as shown in Table 3-9. Therefore, the combined equivalent clamping load at the full torque stage (i.e. 95 lb-in (10.7 N-m)) using method two is determined to approximately be 234 lbs. (1,039 N). This same method two procedure was then used to find the combined equivalent clamping load at the "snug tight" torque stage (i.e. 65 lb-in (7.34 N-m)) which led to an approximate load of 112 lbs. (497 N) as shown in Table 3-9.

Table 3-9: Average Compression Loads Along the Glazing Pocket Points (Partially Dry-Glazed Configuration) During Different Torque Stages [Linear Regression Lines Method]

	Compression Load [N]	Torque Stage
Point A	514	"Snug Tight"
Point B	527	"Snug Tight"
Point C	449	"Snug Tight"
AVG	497	"Snug Tight"
Point A	965	Full
Point B	1123	Full
Point C	1030	Full
AVG	1039	Full

Based on these two methods implemented, the approximated combined equivalent clamping loads produced by each method were very similar. Therefore, the final value of the combined equivalent clamping load at the full torque of 95 lb-in (10.7 N-m) was changed to be approximately 225 lbs. (1,000 N). This value from both methods was rounded down to the nearest hundred Newton since SI units were to be implemented within the FE software used later. This consequently meant that the portion of the total equivalent

clamping load found in the test #2 results that went directly into the thermal gasket at Point B was equal to 180 lbs. (800 N). Therefore, a majority of the total equivalent clamping load is distributed to the fixed glazing gaskets at Points A and C evenly.

3.6. Summary

A series of small-scale tests were completed with a Kawneer 1600 curtain wall sample specimen to determine the equivalent clamping load a screw produced when it was tensioned to the required torque of 95 lb-in (11.3 N-m). The first test sought to find the displacements of the glazing pocket cross section after the screws were tensioned along the pressure plate to a “snug tight” torque of 65 lb-in, and a full torque (the required Kawneer torque) of 95 lb-in. The second test then used a steadily increasing compressive load, in lieu of screw CC, on the frame to reach the same glazing pocket displacements recorded in test #1 series. These displacements resulted in a total equivalent clamping load of 405 lbs. (1,800 N) due to the full torque. The third test series was completed to find the distribution of the total equivalent clamping load to the fixed gaskets and thermal gasket as Points A through C. Therefore, it was concluded that the thermal gasket would see 180 lbs. (800 N) of the total clamping load, and the fixed glazing gaskets would resist 225 lbs. (1,000 N). Additionally, in-plane and out-of-plane gasket distortions were observed to occur when full torque of screws was reached.

.

Chapter 4

Finite Element Model

4.1. Introduction

As discussed in Chapter 1, there is a shift towards implementing performance-based engineering design methods and tools to improve the resiliency of a building façade, specifically the architectural glass curtain wall (CW) system, when subjected to natural hazards such as earthquakes and hurricanes. The fragility curve is one such useful tool that allows engineers to estimate the probability of failure for various damages states that may occur during an event. The primary method to obtain the data required for fragility development is to execute multiple experimental or mock-up tests. As previous engineering analysis attempts have shown, finite element modeling offers a cheaper, effective engineering analysis alternative to approximate a few key damage states. Based on the literature, work has not been done to include simulation techniques for both in-plane displacements and out-of-plane uniform pressures using one FE model. Using one model has the benefit of assisting engineers with analyzing CW systems using both loading scenarios to support multi-hazard performance based engineering of these glazing systems.

This chapter presents a new FE modeling approach which sought to explicitly model more of the glass CW components and the structural interactions/behaviors between the generated components. The advantages of modeling more of the CW component behaviors/interactions included: accounting for additional structural damage states (i.e.

glass-to-frame contact, glass cracking, glass/frame breaches) that may occur due to each simulated loading scenario; accounting for non-structural damage states (i.e. water intrusion and air infiltration damage states) as a direct result of the structural damage states occurring; and having the ability to model different CW system configurations.

To achieve these main objectives, ABAQUS was the FE software package utilized to generate these FE models in this study. The FE model generated in this study will be based on the Kawneer 1600 Wall System™ 1 Curtain Wall which was subjected to experimental tests by Shirazi (2005). To validate the generated FE models for both the in-plane and out-of-plane simulations, analysis results were compared to experimental results acquired from the two selected studies summarized in detail within Chapter 2.

4.2. Issues in Current FE Modeling Approaches

One common modeling approach used in previous research attempts reviewed in the literature was to model the glass CW system (or only the glass panel) for either earthquake-related or hurricane-related intensity measures separately. Therefore, the models only focused on the in-plane or out-of-plane responses separately. Even so, these previous FE techniques were still effective in approximating some important CW system's structural behaviors. For instance, the in-plane FE models referenced in Chapter 2 could capture in-plane behaviors such as: in-plane displacement/rotation of the glass, in-plane flexural response of the framing members and semi-rigid connections, rubber-to-glass friction, glass-to-frame contacts and glass cracking (due to generated stress/strains in the glass panels). The out-of-plane FE models could capture out-of-plane behaviors

such as: out-of-plane displacement/rotation of glass (includes geometric non-linearity behaviors due to excessive displacements), generation of stresses on the glass panel and glass cracking/failure (i.e. either with generated stresses or post-failure modeling). While the models certainly approximated key behaviors/interactions required for analysis of glass curtain wall systems, it is not effective to have to generate two separate models using separate modeling techniques if required to complete a multi-hazard analysis.

Likewise, some of the implemented FE modeling approaches oversimplified some structural behaviors/interactions to help decrease computational time during analysis. As described in Chapter 2, some of these simplifying techniques for the in-plane models included implementing: structural elements for the framing members; linear gap elements to model glass-to-frame contact and the bending/twisting stiffness of the framing members; non-linear gap elements to model changing rubber-to-glass friction; and reduced cross sectional properties of framing members to model semi-rigid transom-mullion framing connections. The out-of-plane simplified methods modeled just the glass panels and used simply supported boundary conditions along the panels edges to. These simplified modeling methods also limited the type of variations of CW configurations that can be changed and modeled within both simulations.

No models explicitly modeled the structural behaviors/interactions of all the CW components in one model such as the rubber gaskets/blocks, steel anchor connections, and other framing members. In the case of in-plane models, twisting of the frame members could not be observed since beam elements were used. For the out-of-plane models, the flexural behavior of the framing members and their contribution to out-of-plane flexural resistance was not considered since framing members were not modeled.

For both model types, gap openings/closing or envelope breaches along the perimeter of the CW system could not be explicitly modeled throughout the analysis because actual glass-to-frame clearances and glazing components were not modeled. Finally, variables which caused contact non-linearity (i.e. changing boundary conditions), such as rubber-to-glass friction and glass panel movement within glazing pocket, were not explicitly modeled. Explicitly modeling for these changing boundaries would be useful if changes were made to how the CW was installed since this would affect when the glass-to-frame contacts would occur (in-plane simulation), and how much glass panel displacements/rotations would occur (in- and out-of-plane simulations).

Modeling of the aforementioned additional CW behaviors/interactions were deemed necessary in this FE computational study to approximate additional key CW component damages seen in the field or experiments. Also, using the approach of generating one model which could simulate both in- and out-of-plane simulations would be advantageous to the engineers during multi-hazard PBE analysis and design. In summary, the FE modeling approach used in this analytical study included: 1) the explicitly modeling of CW components (i.e. mullions/transoms, pressure plates, EPDM rubber gaskets/blocks, and glass panel); 2) the explicitly modeling of the contact interactions/constraints between CW components (i.e. aluminum-to-rubber, rubber-to-glass, and glass-to-frame contacts); and 3) the modeling of the transom-mullion semi-rigid connections.

4.3. Overview of Selected Experimental Test Studies for Validation of FE Model

Validations of the FE model in two orthogonal directions were carried out using studies which simulated either earthquakes (i.e. in-plane racking displacements) or hurricanes (i.e. out-of-plane uniform pressures). Therefore, this section will overview the selected experimental studies and their respective results used for validation of the FE model.

4.3.1. Selected In-Plane Experimental Test Study

The experimental research completed by Shirazi (2005) described in Chapter 2 was selected to support the in-plane validation of the FE models created in this computational study. The glazing system chosen for Shirazi (2005), and subsequently for this FE modeling study, was the Kawneer 1600 Wall System™ 1 Curtain Wall, a dry-glazed and stick-built system as shown in Figure 4-1. Based on the details provided by both Kawneer (Kawneer 2019) and Shirazi (2005), the 5-1/4 inch (63.5 mm) frame depth system, used commonly for a 1/4 inch (6 mm) glass infill, was identified as the featured configuration to be modeled in this study. As shown in Figure 4-1, this configuration also includes: 11 mm glass-to-frame clearances, 1/4 in. (6 mm) thermal break gaskets, and setting/side blocks at the mid-points of the glass sides and quarter points of the glass base. The annealed, monolithic glass panel experimented with in the CW system had dimensions of 6 ft high x 5 ft wide (1829 mm x 1524 mm). Finally, pressure plates were attached to the mullion with screws spaced at a 9 in center-to-center spacing and with a

required screw torque of 95-100 lb-in (10.7-11.3 N-m) to clamp glass in place within the glazing pocket.

While Shirazi (2005) obtained results for the Kawneer 1600 CW subjected to cyclic displacements, this computational study only focused on using the static pushover results for validation. The static pushover protocol was applied using the curtain wall test apparatus constructed at the Pennsylvania State University's Building Envelop Research Laboratory as shown in Figure 4-2. A detailed description of how the Kawneer CW was attached to this apparatus and how it applied the static racking displacement is included in Chapter 2.

Results from two static pushover tests are included from the fully dry-glazed Kawneer configuration and the bare frame configuration which were described in Chapter 2. For the fully dry-glazed CW tests, the results that were compared to the FE simulation results included: 1) the load-displacement relationship plot as shown in Figure 2-34 and 2) the drift-strain relationship plots as shown in Figure 2-35. For the bare frame static pushover tests, the results used included just the load-drift relationship plot as shown in Figure 2-43. Some of the material properties implemented in the Shirazi (2005) FE models were also incorporated into the FE models within this study.

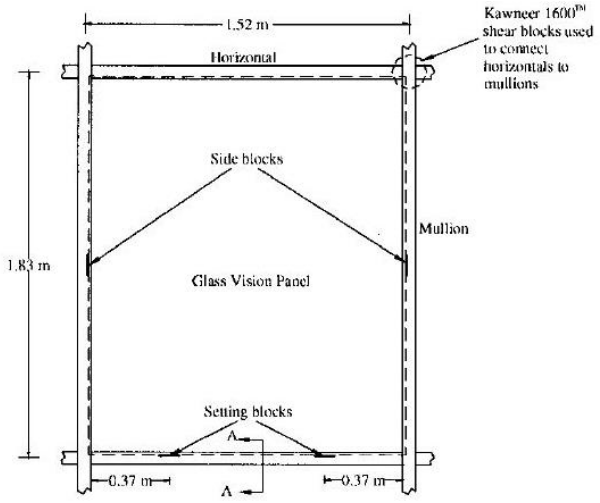

Kawneer 1600 Standard Glass-to-Frame Clearances:	
Top: 14 mm	Bottom: 10 mm
Left: 12 mm	Right: 12 mm

a) Elevation view of Kawneer 1600 Wall System™ 1 Curtain Wall specimen and standard glass-to-frame clearances commonly used

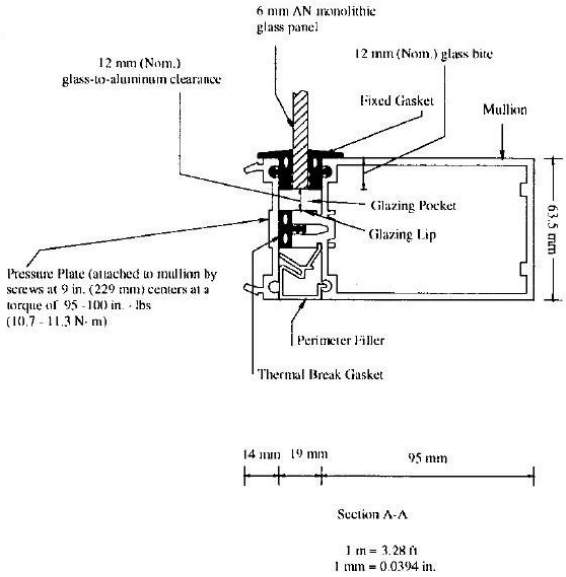

b) Section A-A view (bottom horizontal transom) of Kawneer 1600 CW frame which contains intermediate "flat" pressure plate configuration

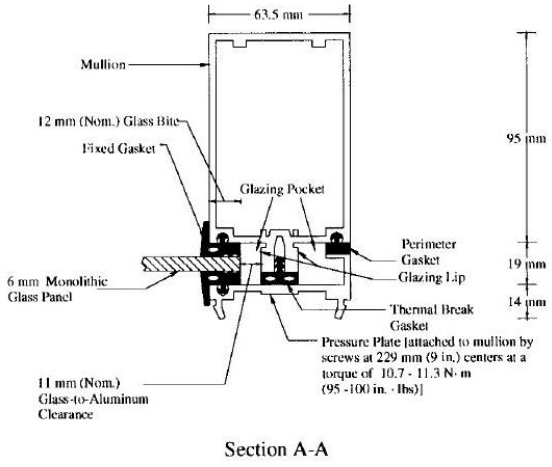

c) Section A-A view (right vertical mullion) of Kawneer 1600 CW frame which contains perimeter "L" pressure plate configuration

Figure 4-1: General glazing details of the Kawneer 1600 Wall System™ 1 Curtain Wall specimen subjected to static and cyclic racking displacements during experimental study (Shirazi 2005)

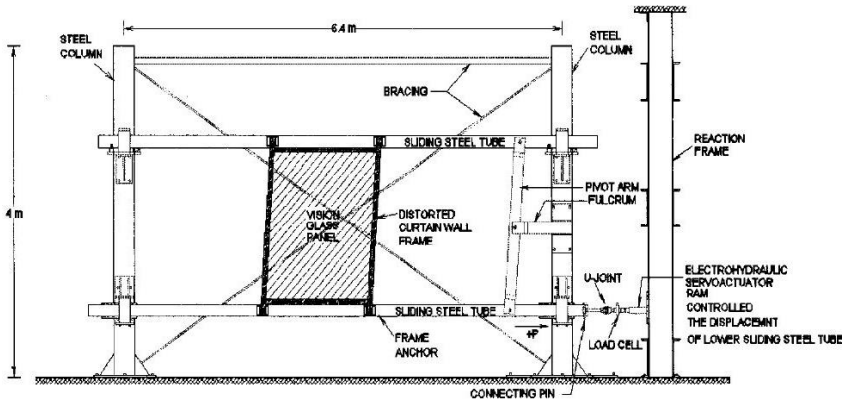

Figure 4-2: Layout of racking test facility at PSU used for imposing a story drift onto the Kawneer 1600 CW system (Shirazi 2005)

4.3.2. Selected Out-of-Plane Experimental Test Study

The experimental study used for the out-of-plane validation study was selected from Linden et al. (1983). This study was chosen because it replicated ASTM tests protocols for monolithic glass panels subjected to uniform wind pressures. Additionally, this study had continuous recorded data throughout the applied static pressures test which is useful for this study.

The Linden et al. (1983) experiments involved monolithic glass panels with 1/4 in. (6 mm) thickness the full dimensions of 8 ft. high x 5 ft. wide (2,438 mm x 1,524 mm) were used. This difference in glass dimensions between the in- and out-of-plane selected studies was deemed acceptable since capturing the behavior of the glass panel when subjected to out-of-plane pressures was of main concern. If the explicit modeling of the CW components (i.e. framing members, connections, pressure plates, and rubber gaskets)

and the relevant CW component interaction was validated with the in-plane model, then these explicit modeling techniques should be able to model the out-of-plane behaviors.

The test facility involved within the Linden et al. (1983) included a vacuum air pressure chamber, vacuum accumulation tanks with dual valve system, and a glass specimen holding frame which is illustrated in Figure 4-3 and described in Chapter 2. The glass was then loaded laterally with a linearly increasing uniform pressure up to 0.75 psi (5.17kPa) in 15 seconds at a room temperature of approximately 72 °F (22 °C) (Behr et al. 1985; Linden et al. 1983). The loading procedure in the experiment was a non-destructive protocol because primary goal was to validate their theoretical models. Therefore, failure was not reached in these test and so no identifiable cracking or failure mechanisms were reported.

The results described in Chapter 2 which will be used to validate the generated FE model herein include: 1) the maximum principal stress-applied pressure relationships at the center and corners of glass as shown in Figure 2-45 and 2) the maximum deflection-applied pressure relationships at the center of glass as shown in Figure 2-46.

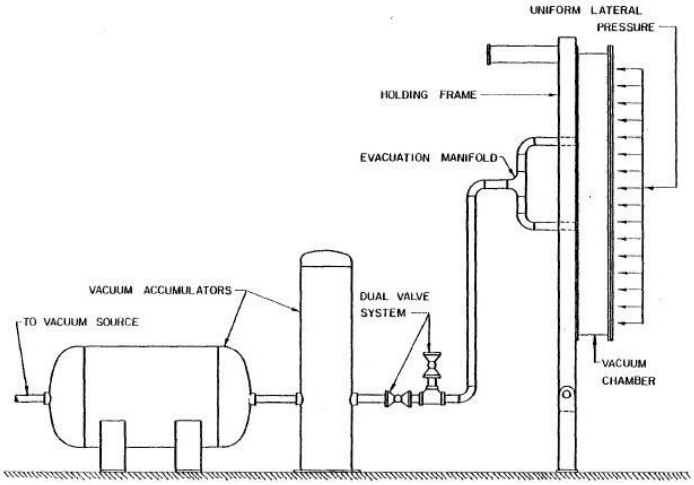

a) Layout of test apparatus at Texas Tech University used to carry out lateral uniform pressure tests on monolithic and laminated glass panels

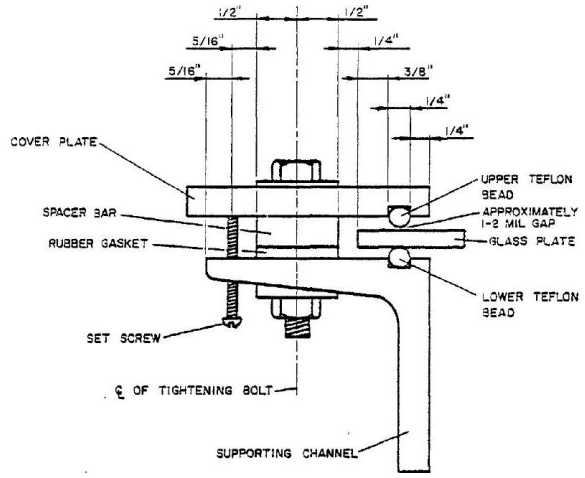

b) Detail cross-section drawing of glazing closure device (steel holding frame)

Figure 4-3: Test apparatus setup for lateral uniform pressure testing of glass panels used in glazing systems (Linden et al. 1983)

4.4. Description of Curtain Wall Component Modeling

This section will describe the modeling procedure for each of the components used in the Kawneer 1600 CW system, which is illustrated in Figure 2-29, that were deemed necessary for the FE analysis. For each modeled part, an overview of the cross-sectional

dimensions, the materials and section properties, the elements chosen and the meshing procedure will be described. Since ABAQUS has no units built into the software, it was decided to use SI units to keep everything consistent throughout the FE model.

4.4.1. Mullion/Transom Model

Both the vertical mullions and horizontal transoms were modeled as 3D extrusion parts in ABAQUS based on the cross-sectional dimensions obtained from Kawneer and the Shirazi (2005) thesis as shown in Figure 4-4. The final mullion cross-section dimensions are shown in Figure 4-4 with some of the intricate extrusions left out to simplify the modeling. These simplifications include using a constant thickness of 3 mm for the mullion side wall and modeling the mullion lip as completely solid without the screw holes through the mullion's length. Due to modeling primarily being based on Shirazi (2005) drawings before actual Kawneer detail drawings were obtained, some dimensions had slight differences in the FE model such as the mullion lip having a slightly wider cross section (about 1.5 mm width difference). Overall, these simplifications and dimensional differences were not extensive and did not affect the cross-sectional properties, such as the moment of inertia, during analysis.

The nominal aluminum mullion properties used in ABAQUS are listed in Table 4-1 and are based on the aluminum 6063-T6 material specified by Kawneer for the 1600 CW system. An isotropic, elastic-plastic material model was implemented to capture the plastic yielding of the aluminum as shown in Table 4-1. The use of a bi-linear elastic-perfectly plastic model was not used to reduce issues with modeling such a stringent material

behavior when the first yield was reached. Therefore, to minimize material convergence issues, a small hardening effect was added to the material model by including a slightly higher second yield stress as shown in Table 4-1.

Table 4-1: Nominal Aluminum 6063-T6 Material Properties

Modulus of Elasticity [MPa]	6.90E+04
Poissons's Ratio	0.33
Density [tonne/mm^3]	2.70E-09
Stress [MPa]	**Plastic Strain**
215	0
250	0.1
565	1

To generate a computationally efficient FE model, using 3D solid hexahedral (continuum) elements for the entire mullion became unfeasible. The reason being, to properly capture bending in the walls of the mullion, it would have been necessary to use at least four 3D continuum elements through the thickness to prohibit hourglass modes. Therefore, the final mullion part contained partitions through the cross section such that different sections of the part could be modeled with either a 3D continuum shell element or a 3D solid “brick” (continuum) element as shown in Figure 4-5. Additional partitions along the length of the mullions were created to represent the locations of the screw holes at 9 in. (229 mm) center spacing as shown in Figure 4-5. With these partitions along the mullion, the equivalent clamping load at each screw location could be distributed into a group of concentrated loads at each set of nodes created by the partitions. This equivalent clamping load procedure is described in more detail in later sections. All the partitions to the part’s cross-section and along the mullion member are shown in Figure 4-5.

The mullion lip portion was modeled separately with C3D8R elements (3D continuum “brick” element), and the rest of the thin mullion walls were modeled with SC8R elements (3D continuum shell element). The SC8R elements are implemented on the thin walled sections of the mullion part since they are capable of accounting for finite membrane strains, large rotations, and changes in thickness which make it advantageous during a geometric non-linear analysis A more detailed description of these two types of elements is described in Appendix A.1.

A global mesh size of 12 mm x 12 mm was chosen for the entire meshing of the mullion part within ABAQUS. Additionally, local mesh size of 4 elements through the thickness of the mullion lip section was used while only one element through the thickness was used for the thin walls of the mullion. Each SC8R element had 5 gauss points selected for the section integration. The final mesh of the mullion is shown in Figure 4-5.

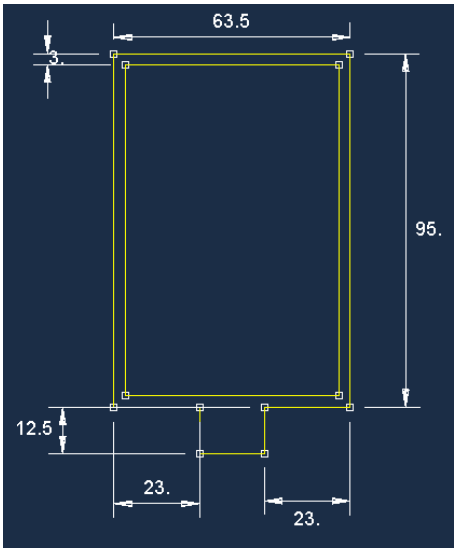

a) Mullion cross-section dimensions in ABAQUS

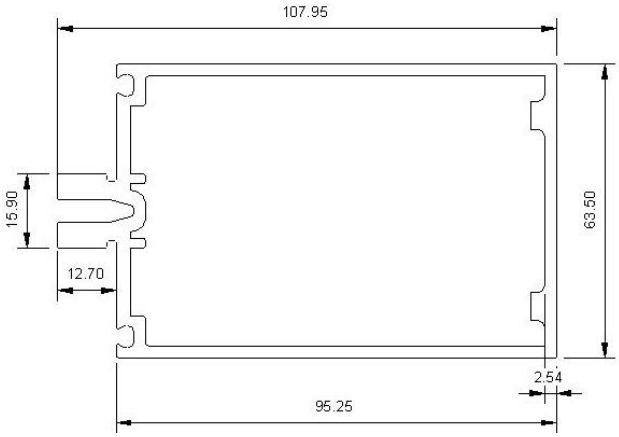

b) Mullion cross-section dimensions provided by Kawneer

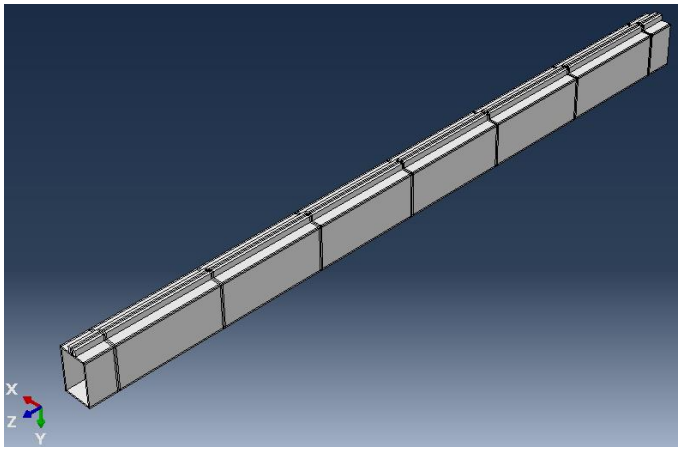

c) Isometric view of extruded mullion member in ABAQUS

Figure 4-4: Views of extruded mullion/transom members in ABAQUS

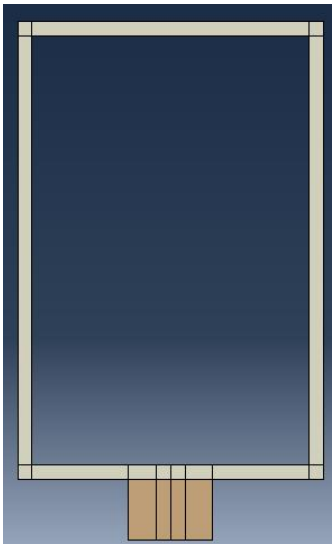

a) Illustration of the cross sectional partitions used to separate the continuum shell and solid sections for the mullion

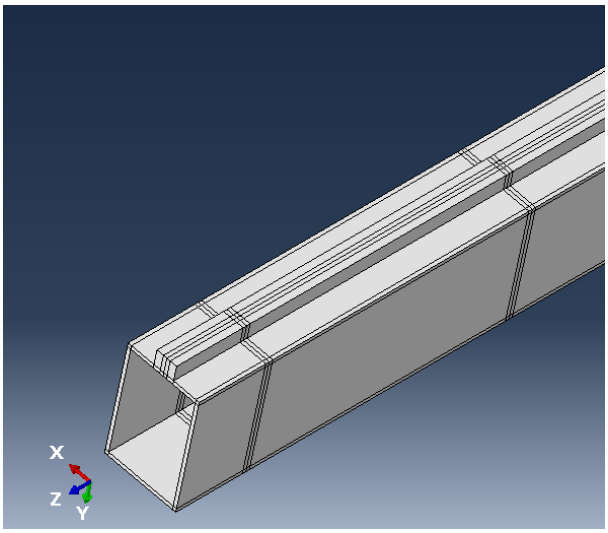

b) Partitions along mullion generated to represent screw hole locations

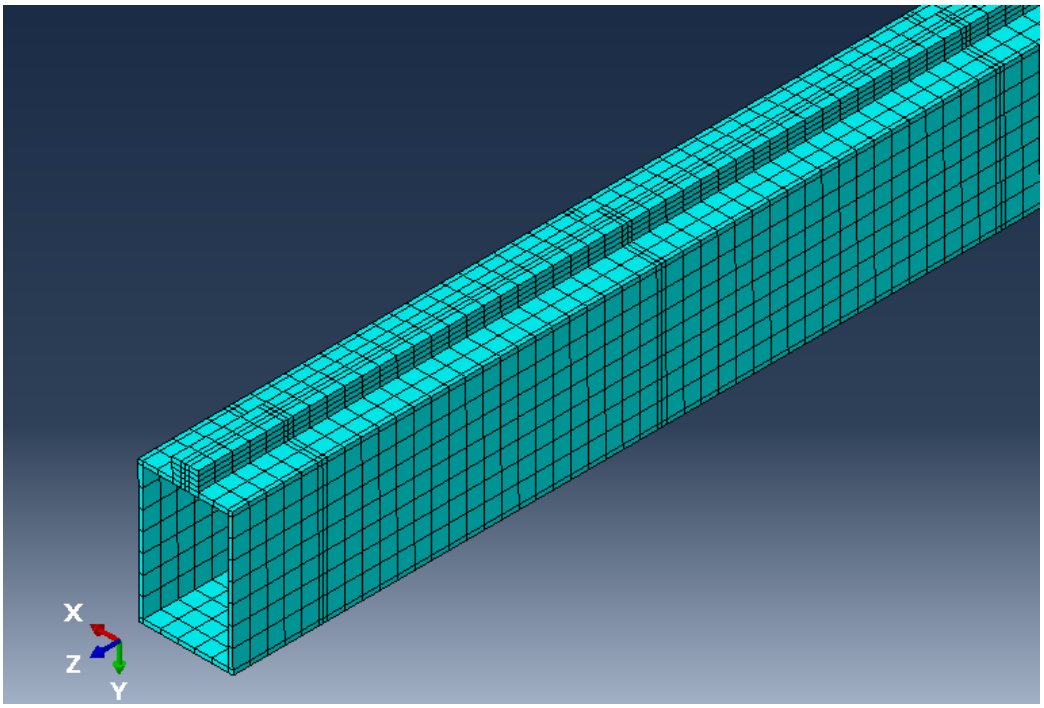

c) Mesh generated for mullion/transom members in ABAQUS

Figure 4-5: Views of partitioned and meshed mullion/transom members in ABAQUS

4.4.2. Pressure Plate Model

For the pressure plate, only the “L” shaped configuration will be modeled and described in this section. However, the intermediate flat configuration was also modeled using similar techniques in the next chapter of this computational study. The same method of simplifying the cross sectional extrusion shape of the mullions was completed for this pressure plate part once detailed drawings provided by Kawneer and Shirazi (2005) were obtained. This method led to the final pressure plate, which was also modeled as a 3D extrusion part, with a constant plate thickness of 2.3 mm as shown in Figure 4-6. Once again, the issue of differences in dimensions between the model and actual pressure plate were due to primarily using detail drawings from Shirazi (2005) study. However, overall these simplifications and dimensional differences, as shown in Figure 4-6, were not extensive and should not affect the cross-sectional properties, such as the moment of inertia, much during analysis. Furthermore, no screw holes or screws were explicitly modeled because concentrated loads along the pressure plates were implemented to represent the equivalent clamping load derived in Chapter 3. This method is described in analysis section later.

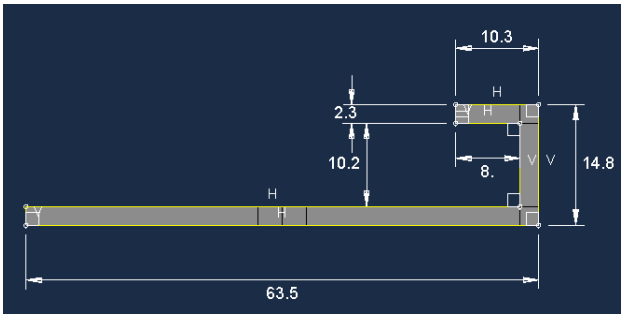

a) Pressure plate cross-section dimensions in ABAQUS

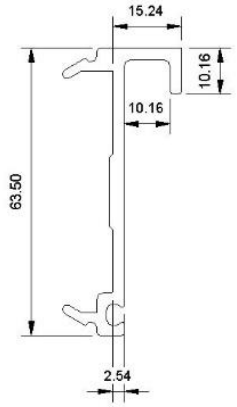

b) Pressure plate cross-section dimensions provided by Kawneer

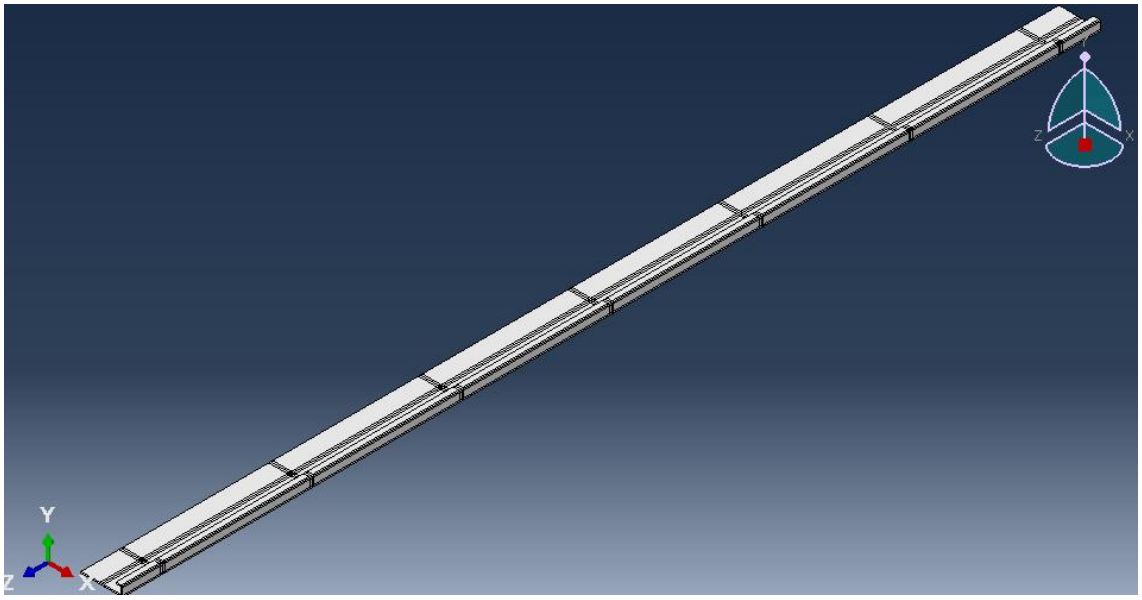

c) Isometric view of extruded pressure plate member in ABAQUS

Figure 4-6: Views of extruded pressure plate member in ABAQUS

The pressure plate used the same aluminum 6063-T6 material as the mullions. Therefore, the aluminum properties used in Table 4-1 were implemented for the pressure plate material behavior as well.

Final partitions were generated through the cross section of the pressure plate as shown in Figure 4-7. Likewise, partitions were generated along the length of the pressure

plate which replicated the screw locations and allowed for concentrated loadings to be used in lieu of actual screws (as will be discussed later).

Again, because the thickness of the pressure plate wall is much smaller than the other pressure plate dimensions, the use of a solid brick element was not considered due to inefficiency and expensive computational cost. Therefore, the entire pressure plates were modeled with SC8R elements with five Gauss points through the thickness used for the section integration. A global mesh size of 12 mm x 12 mm was generated as shown in Figure 4-7. Furthermore, only one continuum shell element through the thickness of the thin walls was required with the generated mesh.

a) Cross sectional partitions of pressure plate illustrated

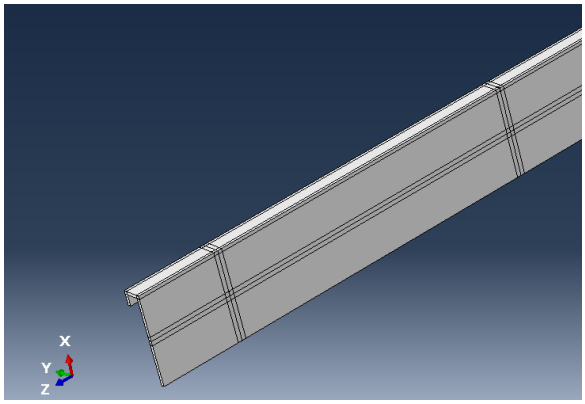

b) Partitions along pressure plate generated to represent screw hole locations

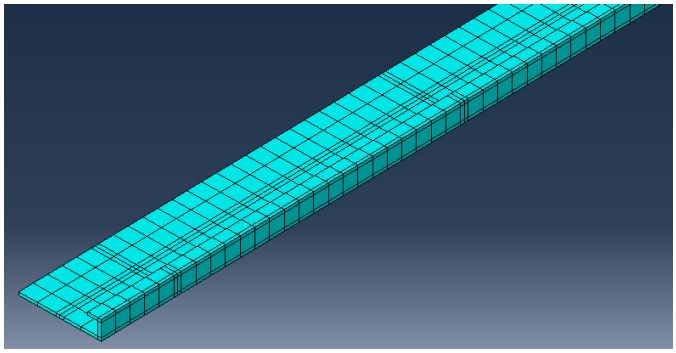

c) Mesh generated for pressure plate members in ABAQUS

Figure 4-7: Views of partitioned and meshed pressure plate members in ABAQUS

4.4.3. Rubber Gasket Model

The models of three different types of gasket extrusions used within the glazing pocket of the dry-glazed Kawneer 1600 curtain wall system were generated. These included the perimeter gasket, the fixed glazing gaskets, and the thermal break gasket which were all used for the perimeter “L” shaped pressure plate configuration. Once again, the cross-sections were approximated primarily on the Shirazi (2005) drawings. As stated previously, these cross-section differences are not excessive and should not affect the component behavior during the analysis simulations. All three gasket extrusions are modeled in ABAQUS as a 3D extruded part and the final cross-section dimensions are shown in Figure 4-8.

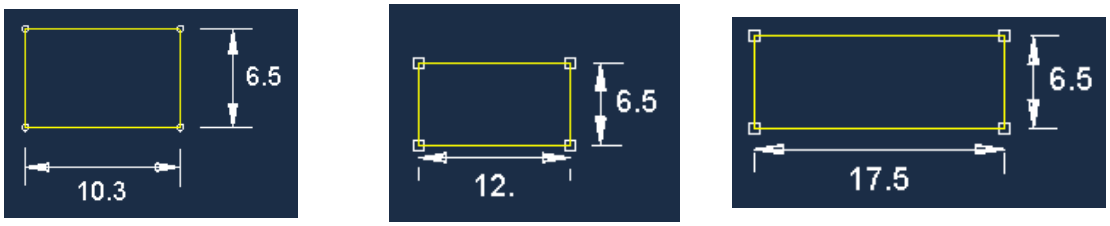

a) Perimeter (left), fixed glazing (middle) and thermal break (right) gasket cross-section dimensions in ABAQUS

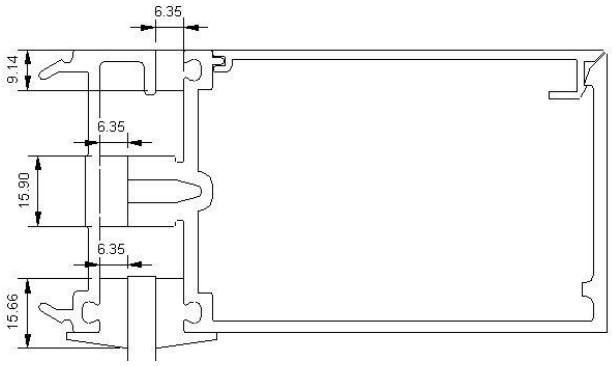

b) Gasket cross-section dimensions provided by Kawneer

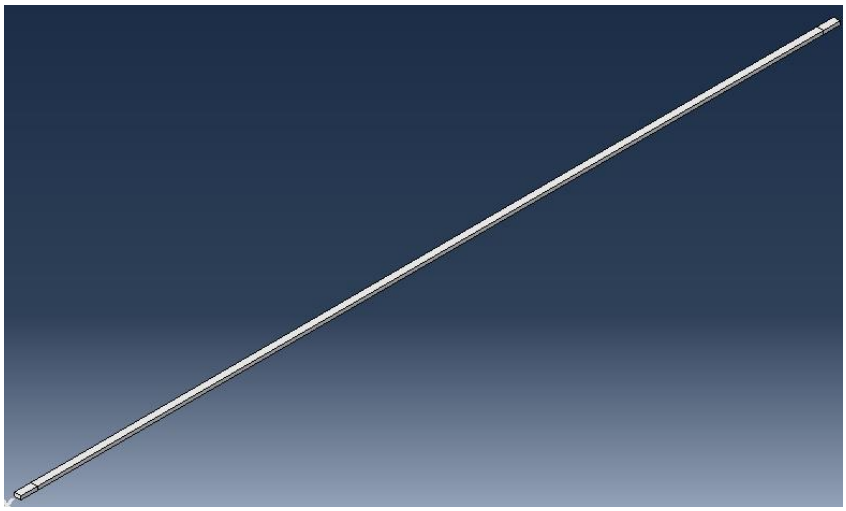

c) Example isometric view of extruded fixed glazing gasket component in ABAQUS

Figure 4-8: Views of extruded gasket components in ABAQUS

These gaskets used in the Kawneer 1600 system are made out of an EPDM Shore A60 rubber material which can be manufactured to have different properties depending on the job. After discussions with Kawneer, it was determined that two options were plausible

to implement in the rubber material model to represent the gaskets used in the 1600 CW system. The first choice was to model the rubber based on the Tremco manufacturer EPDM rubber product material sheet and use a simple linear elastic behavior since certain deformations and responses of the rubber were not exactly the main focus of this project. The second option was to model the rubber with a hyperelastic material model using Mooney Rivlin coefficients which are based on tests on similar EPDM rubber extrusions by the Semperit manufacturer provided to Kawneer. The first option was picked, using Tremco's EPDM Shore A60 rubber material data, to help capture at least approximate rubber behavior responses without having to add another degree of non-linearity to the model. Thus, an isotropic, linearly elastic material model was chosen with the nominal EPDM rubber material properties shown in Table 4-2. The modulus of elasticity was derived from the materials Shore A hardness factor of 65, using the Gent relation equation commonly used in the rubber industry to relate the Shore A Hardness to the modulus of elasticity (Gent 1958),

$$E = \frac{0.0981(56+7.62336S)}{0.137505(254-2.54S)} \qquad (4\text{-}1)$$

where the units of E are MPa. Additionally, the Poisson's ratio was set to υ=0.3 instead of the usual rubber Poisson's ratio of υ=0.5 which normally constitutes an incompressible material. During initial iterations of this FE model, the Poisson's ratio was set to υ=0.495 as recommended to minimize convergence and analysis issues when modeling an incompressible material with υ=0.5. However, due to excessive element

distortions observed during analysis runs, it was decided to stay with υ=0.3 to allow for some compressibility in the rubber.

Table 4-2: Nominal EPDM Rubber Gaskets Material Properties

Modulus of Elasticity [MPa]	4.425
Poissons's Ratio	0.3
Density [tonne/mm^3]	1.30E-09

While the cross-sections of each of the three gasket types are slightly different from one another, similar meshing sizes were used to balance computational savings and overcome shear locking issues. This led to using the final global meshing size of 6 mm x 6 mm, and a local edge seed size of 2 elements through the thickness of the gaskets cross section. The rubber gaskets were modeled with C3D8 solid "brick" elements which are described in detail in Appendix A.1.This final mesh for each type of gasket can be viewed in Figure 4-9.

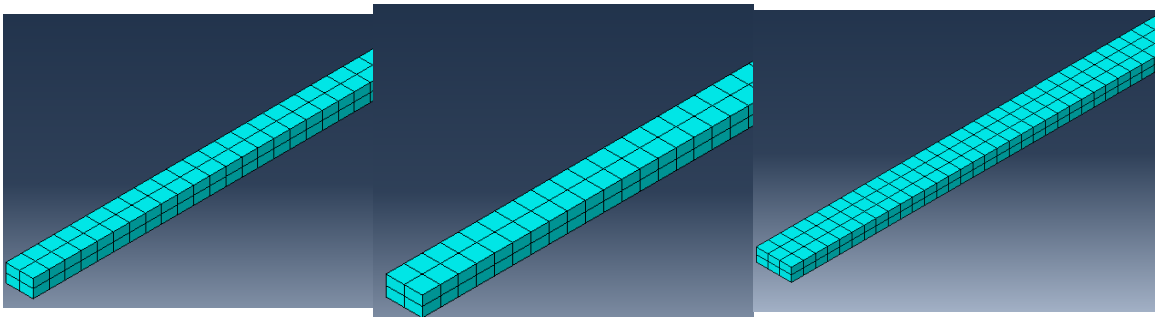

Perimeter (left), fixed glazing (middle), thermal break (right) gasket mesh

Figure 4-9: Views of meshed gasket components in ABAQUS

4.4.4. Setting/Side Blocks

Actual dimensions of the setting/side blocks were not provided by Shirazi (2005) but they were determined through a review of the Kawneer installation guides. The setting/side blocks used to maintain the glass-to-frame clearance of 11 mm, typically varied depending on the glass thickness used in the field. The blocks also must be wide enough such that at least ½ of the outboard glass panel is covered by the block as per Kawneer instructions, which are based on GANA regulations. Based on Kawneer 1600 detail drawings, setting/side blocks provided to the installer are usually much wider to meet this requirement, as shown in Figure 4-10. However, for this FE model it was decided to model the width of the setting/side blocks to 1/4 in. (6mm), the same width as the glass thickness for the 1/4 in. infill configuration used in the Shirazi (2005) tests. As for the length of the setting/side blocks, these were kept at the standard 4 inches (102 mm).

Since the blocks were used to establish the glass-to-frame clearances, the heights of the blocks were usually set to equal to these glass-to-frame clearances. The heights for the setting blocks at the base of the glass panel were set at 11 mm. This was also the height for the side block at the right side of the glass panel. However, the final height for the side block at the left side of the glass panel was set at 8.5 mm. This final height for the left side block was calibrated to help the generated FE model herein to better match the load-drift relationships recorded in the Shirazi (2005) experiments. Discussion of how this was calibrated, along with necessary glass height changes and glass-to-frame clearances is presented in the assembly sections of this chapter. Therefore, the final cross-section

dimensions used in this model are shown in Figure 4-10. The blocks were both modeled in ABAQUS as a 3D solid extrusion part.

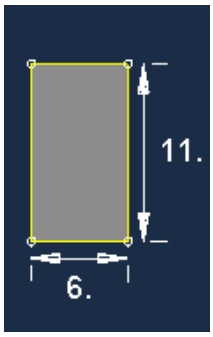

a) Setting block and right side block cross-section dimensions in ABAQUS

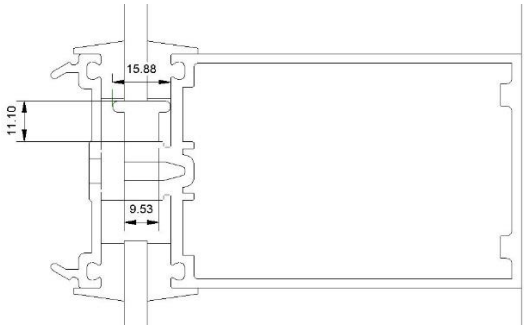

b) Side/setting block cross-section dimensions provided by Kawneer

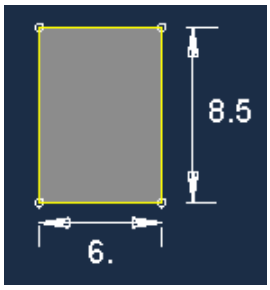

c) Left side block cross section dimensions in ABAQUS

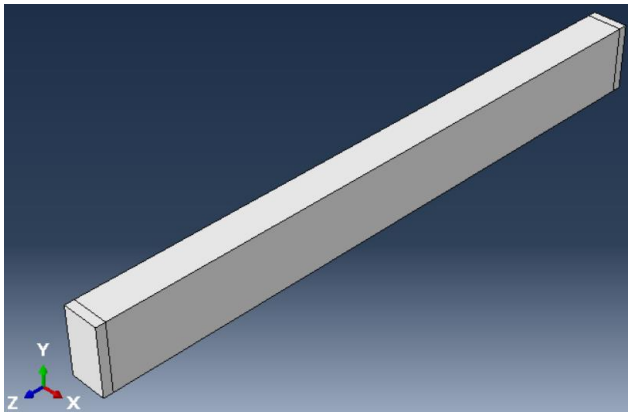

d) Isometric view of extruded Side/setting block component in ABAQUS

Figure 4-10: Views of extruded side/side block component in ABAQUS

Based on discussions with Kawneer, the setting blocks were thought to have been made of the same EPDM rubber material as the rubber gaskets discussed in the previous section. However, when the EPDM rubber gasket material properties were used in initial simulation runs, the blocks deformed heavily, especially the setting blocks. This was evident because once the glass panel starts to rotate and translate within the framing system

as racking drifts are increased, the compression forces acting along the setting/side blocks increases and deforms the blocks heavily as the glass-to-frame clearances are overcome.

To bypass this excessive distortion issue while not affecting the response of the overall glass panel movement within the glazing pocket, the EPDM rubber material stiffness implemented for the setting/side blocks was increased by a factor of 5. This was deemed a reasonable material change since the setting/side blocks sent in the sample CW system for the small scale experimental tests were noticeably stiffer than the rubber gasket components. Therefore, the EPDM rubber material properties for the setting and side blocks are shown in Table 4-3.

Table 4-3: Nominal EPDM Rubber Setting/Side Block Material Properties

Modulus of Elasticity [MPa]	22.125
Poissons's Ratio	0.3
Density [tonne/mm^3]	1.30E-09

In addition to the material stiffness increased, a kinematic coupling constraint was applied to constrain the degrees of freedom on the side face surfaces of the setting blocks to an adjacent referent point on the same surface as shown in Figure 4-11. This was done to control in-plane deformations of the setting blocks by coupling the motions of the setting block outer surfaces to the rigid body motion of the reference point created. A summary of how kinematic coupling constraints work in ABAQUS is contained in Appendix A.2. Partitions offset by 1.5 mm from the side faces of the setting blocks were made as shown in Figure 4-10. This kinematic coupling constraint method was not necessary for the side

blocks since using just the new material properties was enough to continue adequate simulations.

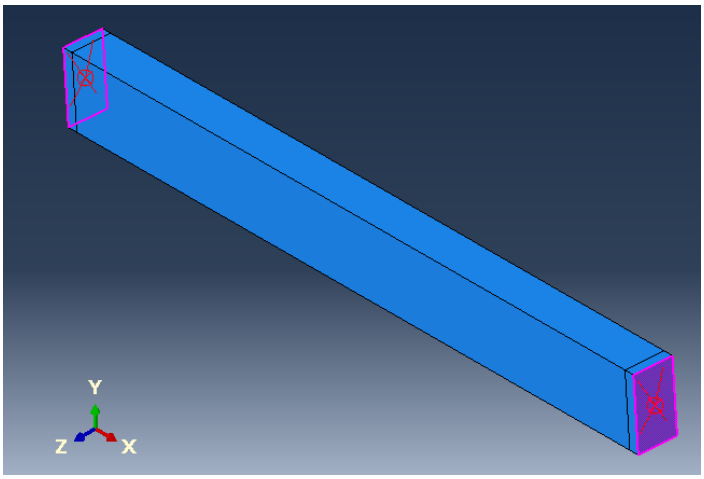

Figure 4-11: Kinematic coupling constraint applied to setting blocks

Consequently, the setting/side blocks had a more refined mesh compared to the other rubber gaskets because these would be subjected to much more bending and compression, especially for the in-plane racking displacement analysis, since the glass sits directly on the blocks. Therefore, the C3D8 solid "brick" full-integration elements were implemented in the discretization of the block parts. A global mesh size of 1.5 mm x 1.5 mm was generated along with implementing local edge mesh seed controls such that 4 elements are generated through the thickness of the blocks as shown in Figure 4-12. This refined mesh would help minimize any shear locking effects that could arise during FE simulations.

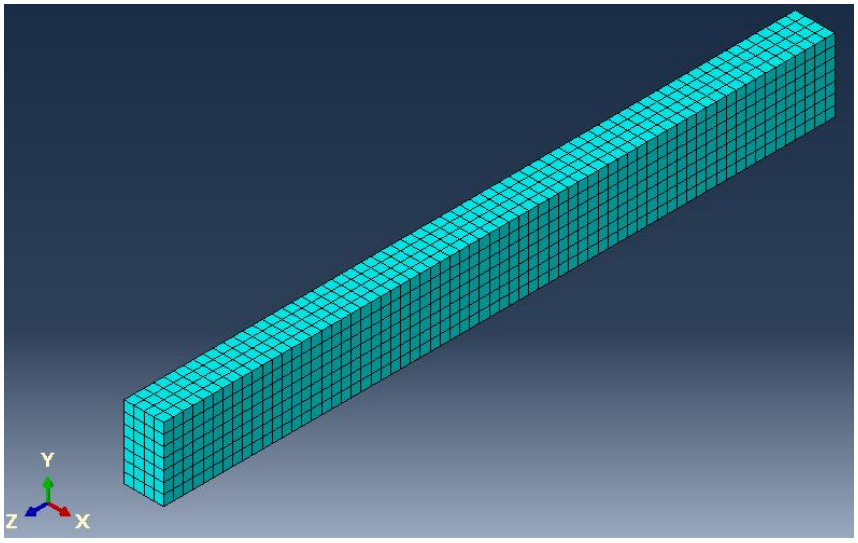

Figure 4-12: Mesh generated for setting/side block components in ABAQUS

4.4.5. Glass Model

There were no details of the actual measured glass dimensions for the glass panel installed within the CW system used in the Shirazi (2005) experiments. Shirazi (2005) described completing the racking tests on 6 ft high x 5 ft wide x 1/4 inch thick (1,829 mm x 1,524 mm x 6 mm) annealed, monolithic glass panels. But the glass dimensions illustrated in the detail drawings within the Shirazi (2005) study were 1,830 mm x 1,520 mm as shown in Figure 4-1, which appears to be based off rounding to the nearest tens place. Neither of these described glass dimensions worked in the FE model analysis because the occurrence of the glass-to-frame contacts approximated by the FE model herein did not match what was observed in the experimental load-drift relationships. To help match these experimental results the final glass dimensions generated in the FE model herein were 1,835 mm height x 1,520 mm width as shown in Figure 4-13. Discussion of how the glass

was calibrated, along with necessary side block height changes and glass-to-frame clearances, is presented in the assembly sections of this chapter. Additionally, the glass plate was modeled as a 3D extruded part using these dimensions.

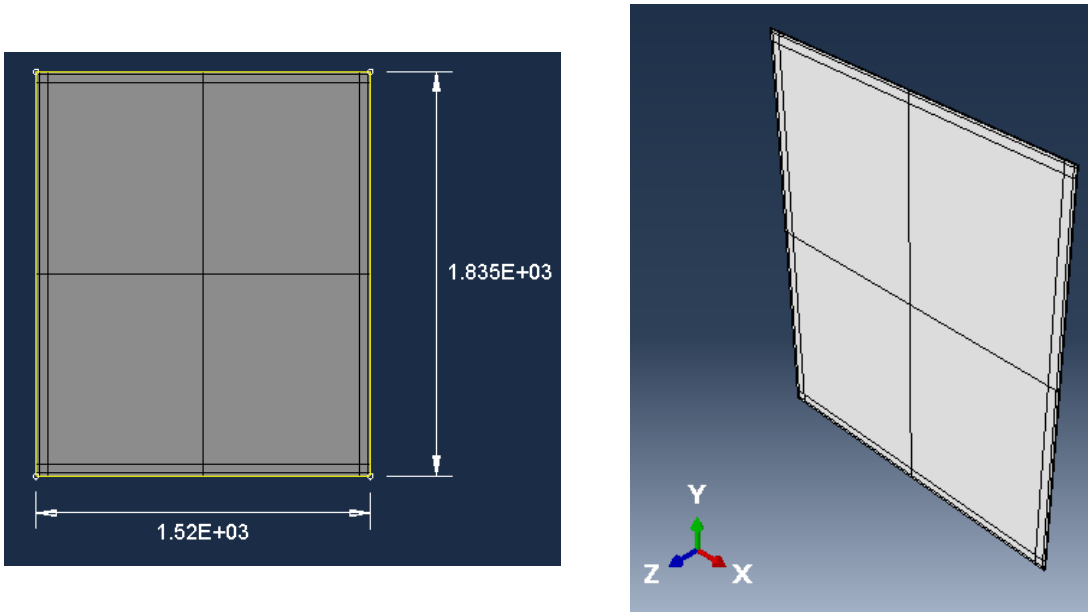

a) Glass panel (monolithic) cross-section dimensions in ABAQUS

b) Isometric view of extruded glass panel (monolithic) in ABAQUS

Figure 4-13: Views of extruded glass panel in ABAQUS

The nominal material properties implemented for the annealed, monolithic glass in the FE model herein were the same as what Shirazi (2005) implemented into his own FE model which is listed in Table 4-4. Just as was done with Shirazi's (2005) model, this study used a linear elastic behavior model for the glass model to help with capturing the distribution of stress observed on the glass and the relative translations and rotations of the glass within the glazing pockets of the 1600 CW system. This linear elastic model was deemed acceptable up to the racking displacement where glass cracking was observed in the Shirazi (2005) experiment. At this point, as observed in Shirazi's experiments, larger

glass cracking and initial glass fallouts occurred at after glass-to-frame contact on two diagonal corners occurred within the glazing pocket. Since glass is very brittle in nature, modeling of the cracking/fracture behavior would capture the decrease in stiffness seen after glass cracking occurs in the experimental load-drift relationships. However, modeling of glass fracture was beyond the scope of the computational research herein. Therefore, the linear elastic model was used to validate the in-plane and out-of-plane model. This was deemed appropriate for approximating the displacement and stress associated with the glass cracking in this computational study.

Table 4-4: Nominal Glass (Annealed) Material Properties

Modulus of Elasticity [MPa]	7.20E+04
Poissons's Ratio	0.25
Density [tonne/mm^3]	2.50E-09

When subjected to increasing in-plane racking displacements and out-of-plane pressures, glass will experience both bending and axial forces in both events. To capture both these bending and axial stresses for both events, the SC8R continuum shell element was again used because of the capability to capture bending and membrane stresses developed within the element. As described in Appendix A.1, this element works well with 3D solid parts and also makes it advantageous for modeling contact. This is key in this computational study when having glass-to-rubber and glass-to-frame interactions during applied loadings. Additionally, these general purpose continuum shells can capture finite membrane strains/deformations, large rotations, and changes in thickness which make it

advantageous during geometric non-linear analysis. This is important when the glass experiences out-of-plane displacements much larger than the thickness of the glass.

Partitions were made to allow for mesh refinement near the perimeter and corners of the glass, and to assist in obtaining deflections at the center of the glass (mainly for out-of-plane simulations). Strategical mesh refinement was implemented to better approximate the stresses in the modeled glass near the same locations measured in both in- and –out of plane experiments. These locations were about 2-3 inches (50-75 mm) from the corners of the glass in both experiments. With the help of these mesh refinements near these corner regions, stress approximated from the model assisted in determining the glass cracking stress from the racking simulations and pressure simulations. Therefore, partitions along the perimeter were made with a 50 mm offset on all four sides of the glass, and through the middle of the height and width of the glass as shown in Figure 4-13. Additional partitions along the perimeter of the glass, not shown in Figure 4-13, were generated during the out-of-plane simulations to help apply wind pressures on just the vision portions of the glass (i.e. glass that is not hidden within the glazing pocket behind the pressure plates).

The glass model was meshed with a global mesh size of 25 mm x 25 mm as shown in Figure 4-14. The local mesh sizes implemented along the glass perimeters and corners were set to 6.25mm as shown in Figure 4-14. This final local mesh sizes for mesh refinement was based off a mesh refinement study presented in the validation section of this chapter. As mentioned, only one continuum element through the thickness was generated with the use of SC8R elements.

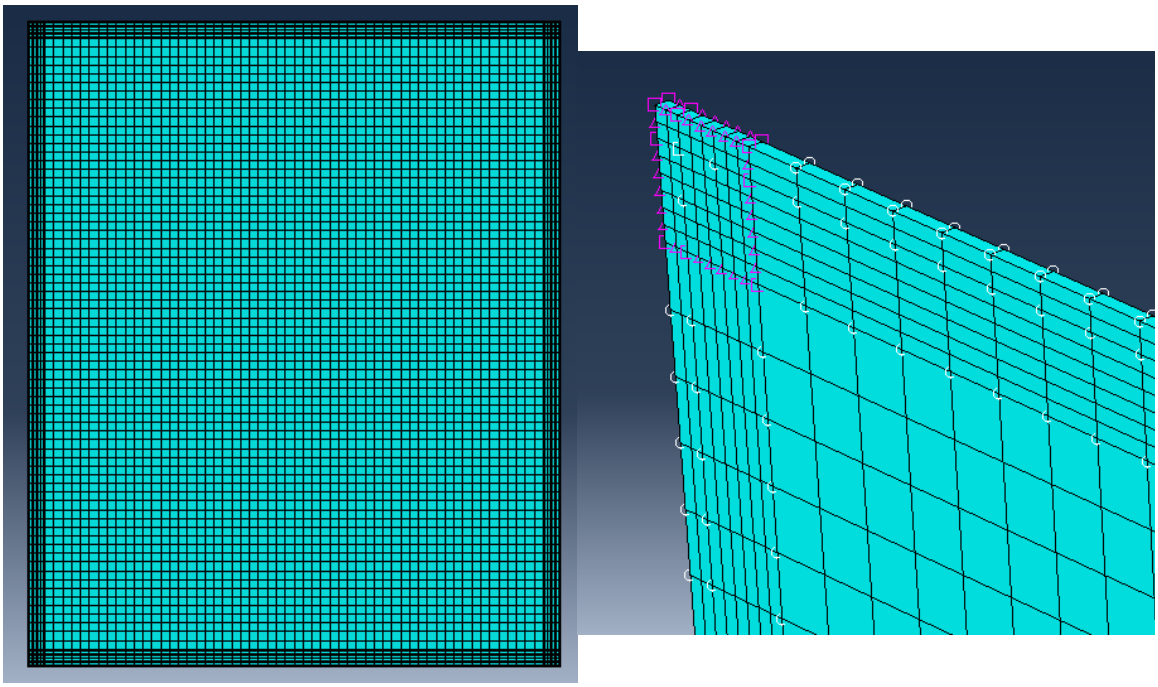

a) Front view of glass panel's refined mesh with global mesh of 25 x 25 mm

b) Isometric view of 6.25mm local mesh seeds implemented for mesh refinement at corners and perimeters of glass panel

Figure 4-14: Views of the glass panel's refined mesh in ABAQUS

4.5. Curtain Wall Assembly Model Description

This section pertains to the assembly of all the previously generated parts for the Kawneer 1600 curtain wall panel specimen. Likewise, the modeling methods implemented to capture component interactions and structural behaviors are discussed. Where needed, calibration of the aforementioned modeling methods and final CW system configuration was completed to further help capture the actual structural response and matching with the in-plane and out-of-plane experiments.

4.5.1. Curtain Wall Assembly

Based on the specimen descriptions and the detail drawings obtained from Shirazi (2005), only a single CW system panel unit configuration was generated for the FE model. While the testing apparatus used in the BERL at the PSU facility was not modeled, all the CW framing member components were modeled such that it could resemble the actual curtain wall specimen held within the racking test apparatus described in Chapter 2. This was done so the racking displacements could be applied in a similar manner that was provided by steel anchors attached to the sliding steel tubes. The vertical mullions had a length of 2,333 mm to account for the maximum mullion extension of 200 mm above/below the outside edge of the horizontal mullions. While no mention of this was seen in the Shirazi (2005) thesis, it was a requirement in the AAMA 501.6 test which the experimental test was based on.

As stated earlier, there were a few calibration changes regarding the glass panel heights, glass-to-frame clearances and side block heights implemented in the FE model generated. The original 11 mm glass-to-frame clearances thought to have been present in the experiments were implemented in the initial generated FE model. However, the load-displacement relationships obtained from the FE simulations did not match the in-plane experimental results when the model was assembled with the original 11 mm glass-to-frame clearances, 11 mm heights of the setting/side blocks, and the original 1,830 mm x 1520 mm glass panel dimensions. These results did not match because the glass to frame contacts at the top left corner and bottom right corner of the glass were occurring much later than expected. Therefore, it was assumed that the reasons for these response

differences could be attributed to the actual glass size, the actual side block thickness, the actual glass-to-frame clearances used in the mock up curtain wall specimen, as well as the flexibilities within the experimental test apparatus.

Due to time constraints and not having the actual measured dimensions of all the components/clearances used in the mock-up test performed by Shirazi (2005), engineering judgment was used to assume that a combination of the actual glass and side block sizes (which also effect the glass-to-frame clearances on the left, right, and top glass sides) were what caused the glass-to-frame contact drifts to occur much earlier in the experimental tests. This is justified because in order for the glass-to-frame contact to occur earlier at the top left corner, the glass-to-frame clearance at the top and left side of the glass panel needs to be smaller than the assumed 11 mm on all four sides of the initial FE model. This would prompt the top left glass corner to contact the frame sooner and cause more rotation of the glass such that the bottom right corner could have frame contact earlier as well, which is what is believed to be what might have occurred during Shirazi (2005) experiments. Rubber-to-glass friction (which is presented in later section) was not considered since the initial stages of the load-drift relationship results were deemed to have matched.

Therefore, the combination of increasing the glass height, and decreasing the left setting block thickness (in tandem with shifting the glass panel to the left so that the left side would rest on the smaller left side block) would be implemented to decreased the glass-to-frame clearance on both the top and left sides. Consequently, this left a small gap between the right side of the glass and the right side block which subsequently increased the right side glass-to-frame clearance. All of these geometric changes would eventually

lead to a better approximation of the load-displacement relationship exhibited by the experimental mock up curtain wall specimen.

After several iterations of these geometric changes, the final geometric calibration included the final glass height of 1,835 mm (an increase of 5 mm), a left side block thickness of 8.5 mm (a decrease of 2.5 mm) and a gap of 2.5 mm present between the right side block and right glass side. These would consequently change the glass-to-frame clearances along the glass perimeter to 6 mm on the top side, 8.5 mm on the left side, and 13.5 mm on the right side, respectively. The bottom glass-to-frame clearance was kept at 11 mm. All of these configuration changes (increased glass height, decreased left side block height, and glass-to-frame clearance changes) were made based on the illustrated CW specimen in Figure 4-1 of the Shirazi (2005) experiments.

As such, for the generated FE model the remaining final CW configurations assembled, which were based on the pre-calibrated model configurations previously described, are presented. The horizontal mullion lengths were set at 1,496 mm and positioned such that the horizontal mullions had 1,869.5 mm center-to-center spacing. The vertical mullions subsequently had a 1,559.5 mm center-to-center spacing. The rest of the horizontal CW components (gaskets and “L” shaped pressure plates) all shared the same length as the horizontal mullion, while the rest of the vertical components (gaskets and “L” shaped pressure plates) were extruded to length of 1,933 mm to line up with the outside edge of the transoms. However, the fixed glazing gaskets used on the vertical framing components were only extruded to have the same length as the height of the pre-calibrated glass at 1,830 mm. Finally, two setting blocks were positioned at the base of the glass panel at the quarter points, and side blocks were positioned at the glass mid-height point on either

side. Due to the calibration changes of the glass heights and shifting within the glazing pocket, the setting blocks were actually kept at the original quarter and midpoints of the pre-calibrated model (from the 1,830x1,520mm glass and 11 mm glass-to-frame clearances on all sides). The

With all the components in place, the final vertical and horizontal CW frame cross-sections are shown in Figure 4-15. A few of the calibrated geometric changes made to the final generated FE model are shown in Figure 4-16. The curtain wall model was positioned such that the in-plane response is captured in the global X-Y plane and the out-of-plane response is captured along the global Z axis (global Y-Z plane).

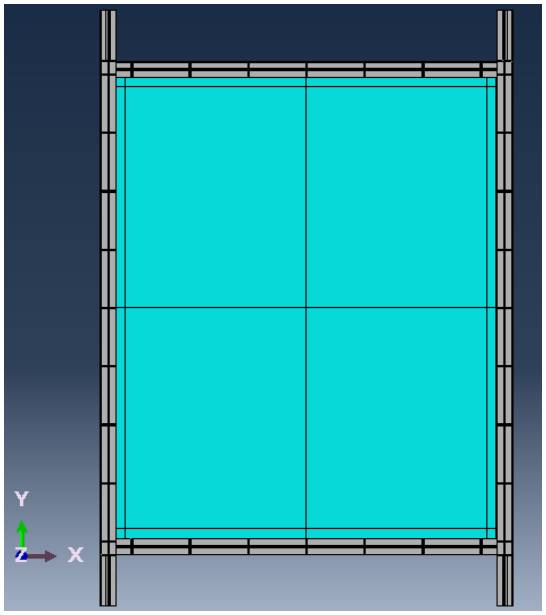

a) Front view of curtain wall model assembly

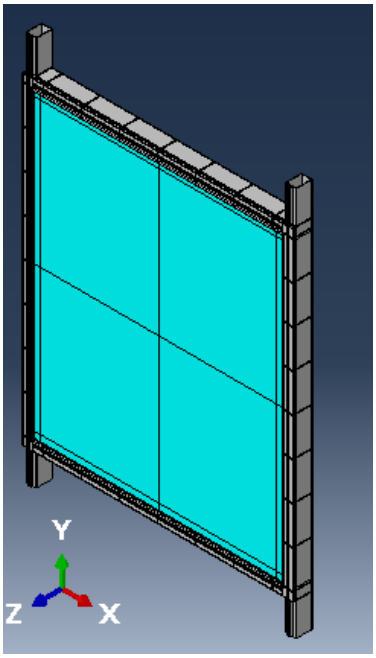

b) Front isometric view of curtain wall model assembly

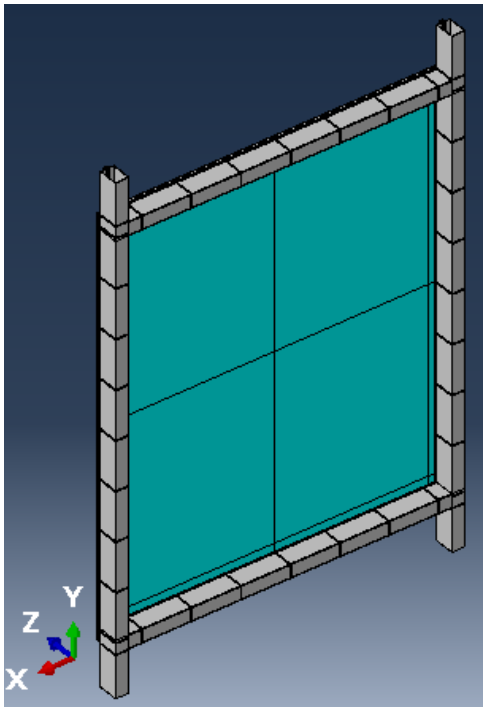

c) Back Isometric view of curtain wall model assembly

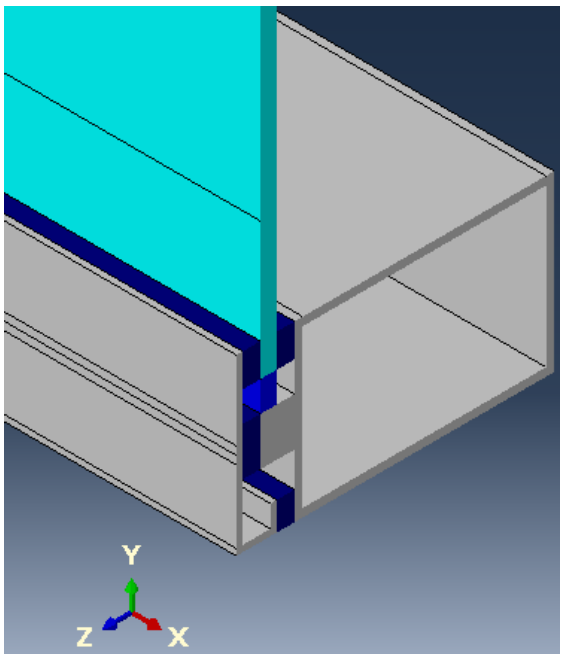

d) Isometric cross section view of curtain wall assembly at the bottom horizontal mullion

Figure 4-15: Views of generated glass curtain wall model assembly in ABAQUS

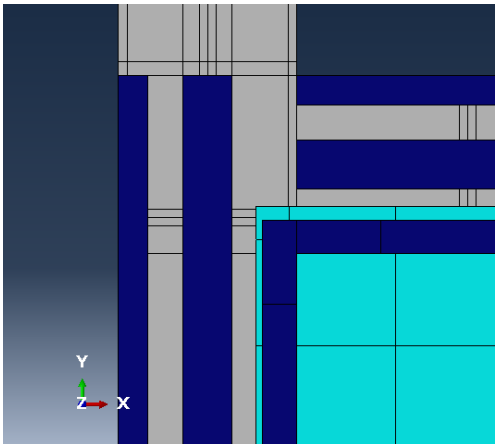

a) Front view at top left corner of CW model with geometric calibrations included (i.e. increased glass height and panel shift to the left)

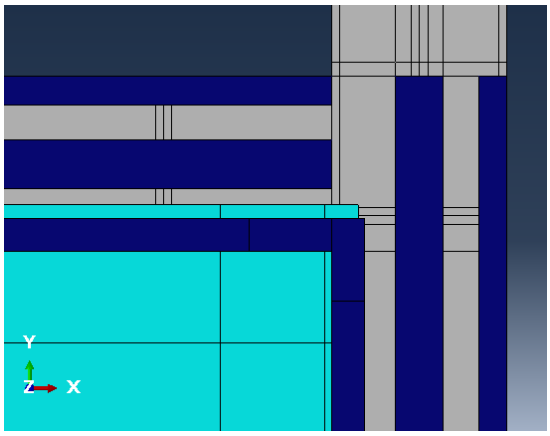

b) Front view at top right corner of CW model with geometric calibrations included (i.e. increased glass height and panel shift to the left)

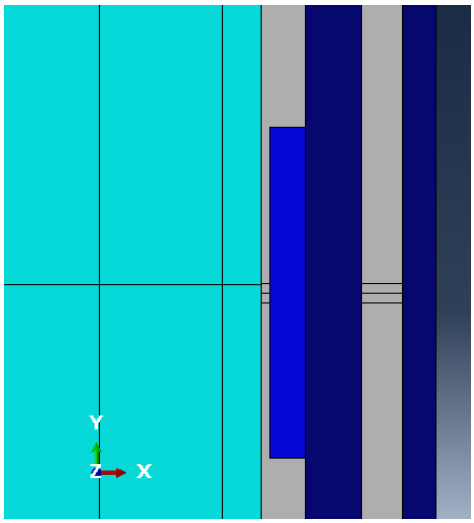

c) Front view at middle left side of CW model with geometric calibrations included (i.e. panel shift to the left 2.5mm gap between side block and glass)

Figure 4-16: Views of geometric calibrations implemented in generated curtain wall model assembly

4.5.2. Contact Interactions and Contact Constraints for CW Components

In ABAQUS, every part that comes into contact with another part must have either interactions or constraints defined between the surfaces in contact, otherwise, no stresses will develop on the parts as they are allowed to penetrate into each other. The following

section will overview the methods employed for both constraints and interactions in the FE model herein. For contact interactions specifically, two types of contact simulation methods that ABAQUS implements for modeling the interactions between surfaces in contact, either at the start or throughout the analysis, were implemented (i.e. contact pairs and general contact). Both of these interaction methods allow for contact separations (and re-contact) during the analysis as well. Care must be taken however on implementing these interactions in either ABAQUS/Standard or ABAQUS/Explicit solver which may have small differences in contact formulations during these two types of analysis. Herein, the models will focus mainly on the methods for ABAQUS/Standard, and the options applied were strategically chosen such that if using either Standard or Explicit analysis, the interaction formulations won't have many differences when switching between the two analyses.

4.5.2.1.Aluminum-to-Rubber Gasket Constraints

As seen in the detail drawing of the Kawneer 1600 system and during the small scale experimental test, all the rubber gaskets (perimeter, fixed glazing and thermal break gaskets) have dart extrusions which are fitted through the slot cut outs on either the pressure plate or mullion face until they are snug in place. Now while it is evident that gasket degradation (i.e. pullout, push-in, shifting or twisting) can occur during racking tests, simplifications were made to the gaskets and framing cross-sections such that constraints were needed to at least capture this snug fit behavior. The decision was made to model the gaskets as fixed to the aluminum surfaces throughout the duration of the analysis because

the focus of this study was not necessarily to capture all of the gasket degradations observed in the racking tests (i.e. pullout, pushing). Also, none of the slots in the framing members' extruded cross sections were modeled. Fixing the gasket to the aluminum surfaces would replicate the gaskets being fitted snug inside the slot cut outs seen along the pressure plate and mullion extrusions.

Therefore, tie constraints were implemented in the model to enforce this fixed constraint behavior between the aluminum to rubber gasket surfaces. Examples of these tie constraint surfaces are illustrated in Figure 4-17. These surfaces again include any contact between the three gasket types (i.e. perimeter, fixed glazing, and thermal break gasket) and the either the aluminum mullion or pressure plate surfaces. These tie constraints essentially constrain the translational degrees of freedom to have the same displacements on both surfaces in the aluminum-to-gasket contact pair. A detailed discussion of how ABAQUS implements this tie constraint method in the models is presented in Appendix A.3.1. It is important to note that the perimeter and thermal break gaskets have tie constraints on two faces since they are between pressure plate and mullion surfaces. The fixed glazing gaskets are only tie constrained on one face since the opposing face is in contact with the glass.

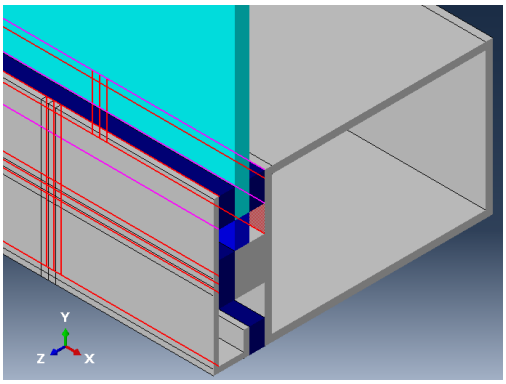

a) Example of mullion-(or pressure plate-) to- fixed glazing gaskets surface tie constraints

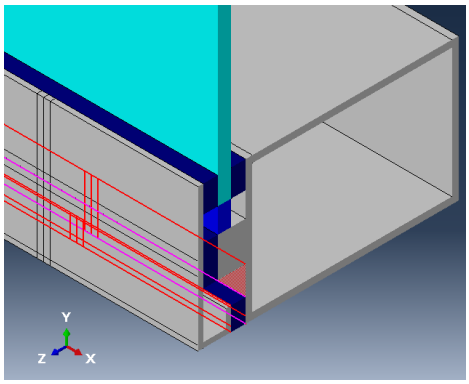

b) Example of mullion-(or pressure plate-) to- perimeter gasket surface tie constraints

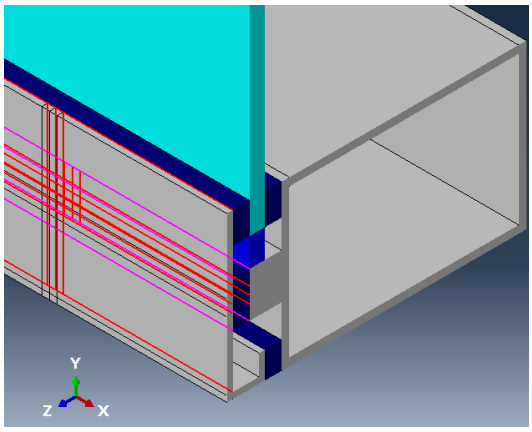

c) Example of mullion-(or pressure plate-) to- thermal break gasket surface tie constraints

Figure 4-17: Aluminum-to-rubber gasket surface tie constraint illustrations

4.5.2.2.Aluminum-to-Rubber Side/Setting Block Constraints

The setting and side blocks were also tie constrained to the mullion glazing lips in their respective locations along the framing members (i.e. bottom transom, left/right mullion). In the installation of the CW system, no glue is used to restrain the blocks from moving or falling once the glass rotates/translates enough during the racking motions. However, fixing the blocks to the mullion lips throughout the simulation helped prevent

rigid body motions and contact stabilization issues with the generated blocks, and thus implementing tie constraints was deemed appropriate for the FE models generated.

As shown in Figure 4-18, the entire bottom surface of both side blocks were the slave surfaces and the mullion's mullion lip surfaces are the masters for the tie constraint pairs. However, as also shown in Figure 4-18, only the middle section at the bottom surface of each setting block was used as the slave surface, and the transom's mullion lip the master. This middle section was only included in the tie constraint pairs because the bottom edges at the left and right face were already included within a slave surface in another constraint (i.e. kinematic coupling constraint) as shown in Figure 4-18. As a general rule, a slave node cannot be a part of two different constraints (i.e. kinematic coupling constraint and tie constraint).

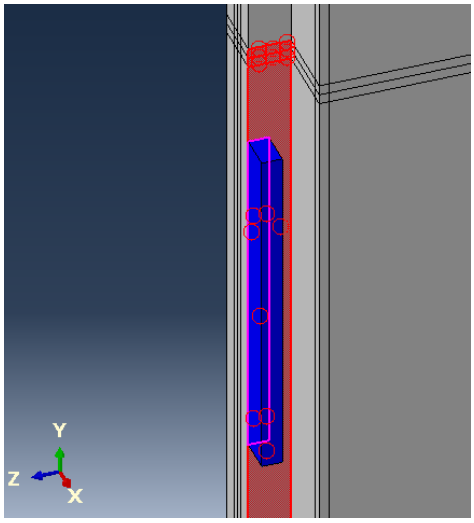

a) Example of mullion-to-side block surface tie constraints

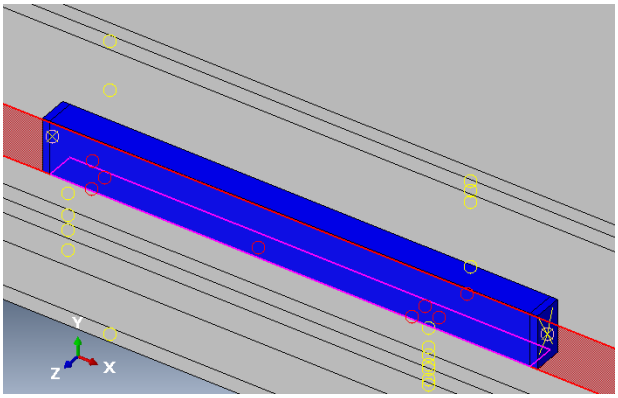

b) Example of transom-to-setting block surface tie constraints

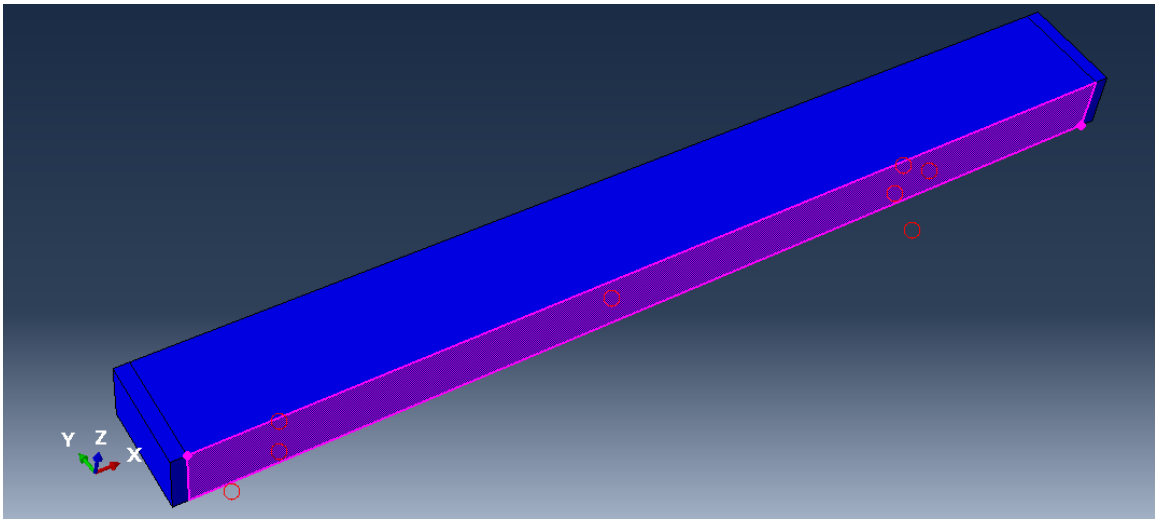

c) The middle section of the setting block's bottom surface selected as the slave surface in the tie constraint

Figure 4-18: Aluminum-to-rubber side/setting block surface tie constraint illustrations

4.5.2.3. Rubber Gasket-to-Glass Interactions

In this model, the contact between the fixed glazing gaskets and the glass panel is explicitly modeled such that the model can handle the changing contact observed during

an in-plane racking displacement analysis, and subsequently an out-of-plane pressure analysis. Therefore, within the ABAQUS model the contact pair algorithm was implemented to model the rubber gasket-to-glass contact interactions throughout the FE analysis simulation. Two main contact properties which were defined for the contact pair approach to work were two mechanical behaviors: 1) the normal behavior which implements the pressure-overclosure relationship once normal contact occurs (contact between two surfaces perpendicular to each other) and 2) tangential behavior which captures the effects of sliding friction between two surfaces gasket-to-glass surfaces. While ABAQUS has multiple contact property models for both mechanical behaviors, only two were chosen.

The contact property model used to define the normal behavior between the gasket-to-glass interaction was the "Hard" contact pressure-overclosure relationship. As for the tangential behavior, the property model used was the Coulomb friction model. A more detailed discussion about both of these property models and how they work in combination with the contact pair algorithm is presented in Appendix A.3.2.

With the Coulomb friction model, a coefficient of friction between the gasket-to-glass surfaces could be defined. Since the equivalent clamping load was already determined earlier, it was necessary to only calibrate this coefficient of friction value to help match the experimental load-displacement relationship. Using this coefficient of friction, the frictional forces generated along the glass edges as a result of the interaction between the fixed glazing gaskets needed to be calibrated such that their contribution to the curtain wall resistance was captured at the initial stages of the experimental load-displacement relationship, specifically in the initial drift stages up to approx. 4-5 mm as shown in Figure

2-34. As observed in the experimental load-displacement curve, the frictional forces were primarily resisting the applied drift as the forces kept increasing until this approximate 4 mm drift was reached (at an approx. constant frictional force of 3,340 N). After this drift was reached the frictional forces were held constant throughout the rest of the test and the glass starts to rotate/slip with respect to the gaskets in the glazing pocket as the drift increases. During this drift stage after constant frictional forces had been reached (i.e. approx. 4mm up to 20mm), both the rubber gasket-to-glass friction forces and the bare frame's lateral stiffness were now resisting this increasing drift (at this stage primarily due to the frames lateral stiffness). Therefore, to help the model better capture the experimental results, several coefficient of friction values were analyzed with during the simulated displacement protocol in ABAQUS until the model's load-displacement curve matched the experimental curve up to the first load-displacement stage (i.e. approx. 4-5mm). At the end of these iterations, a coefficient of friction value μ=0.65 was determined as appropriate to generate the approximate frictional forces due to the gasket-to-glass interaction. The load-displacement validation while using this coefficient of friction and contact pair method is discussed in the in-plane validation section.

All of the surfaces for the rubber gasket-to-glass interaction contact pairs are illustrated in Figure 4-19.

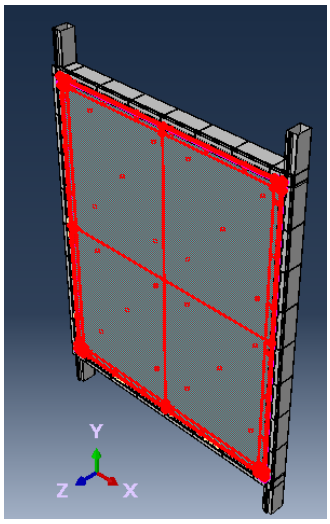

a) Overall isometric view of all rubber gasket-to-glass interaction surface pairs

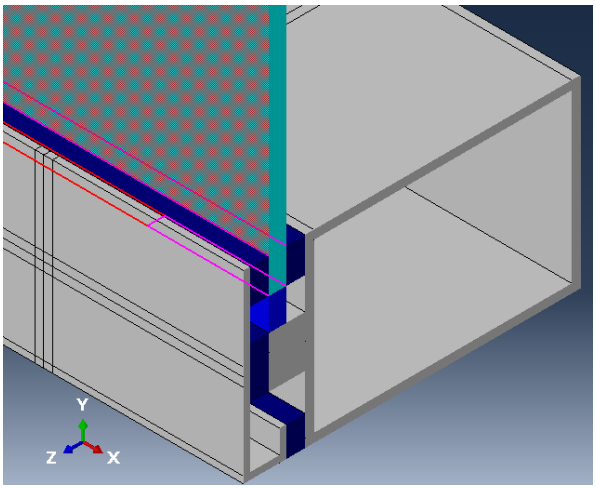

b) Isometric cross sectional view of interaction pairs between the glass and the fixed glazing gaskets surfaces

Figure 4-19: Rubber gasket-to-glass interaction surface (contact pairs) illustrations

4.5.2.4.Rubber Setting/Side Block-to-Glass Interactions

Similar to the rubber gasket-to-glass interactions, the contact pair algorithm was implemented to model the rubber setting/side block-to-glass contact interactions. However, this time the frictionless model was used for the tangential behavior which allowed the two selected surfaces to slide against one another during contact without friction. It was determined that it was not necessary to allow frictional forces to generate when these surfaces were in contact. Therefore, only “Hard” contact was needed for the normal behavior. The frictionless contact property was helpful in limiting the distortions of the blocks by eliminating frictional forces that could generate during contact with the glass sides once the panel began to rotate/side. The entire top surfaces of the setting/side blocks

were selected for the slave surface in this contact pair. Illustrations of the setting/side block-to-glass interaction contact pairs are shown in Figure 4-20.

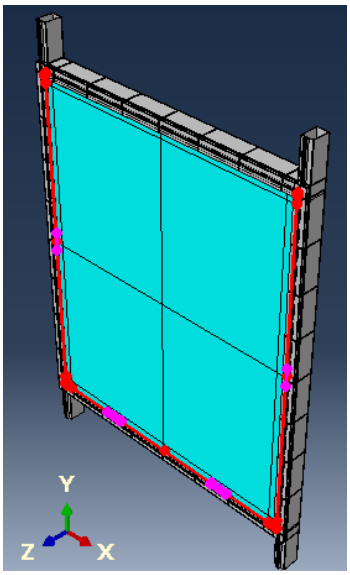

a) Overall isometric view of all rubber setting/side block-to-glass interaction surface pairs

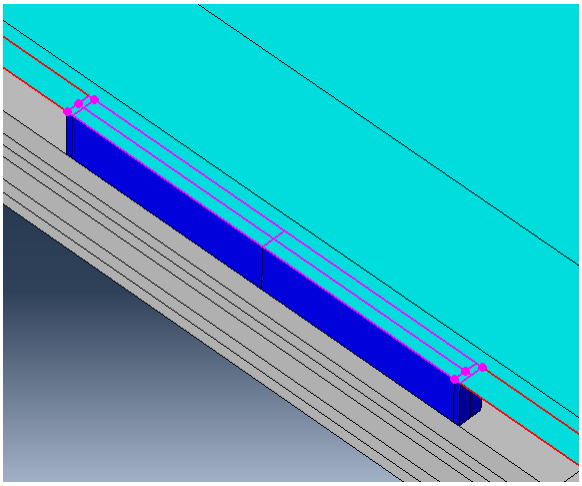

b) Isometric cross sectional view of interaction contact pairs between the glass and the setting block surfaces

Figure 4-20: Rubber setting/side block-to-glass interaction surface (contact pairs) illustrations

4.5.2.5.Glass-to-Frame Interactions

Unlike other FE modeling attempts, the glass-to-frame contact interaction that occurred once the clearance had been overcome was explicitly modeled herein. These interactions mainly occur between the glass corner regions and the mullion's glazing lip near the frame connections as highlighted in Figure 4-21. While these surfaces are initially separated because of the glass-to-frame clearances, contact interactions could still be established within ABAQUS using similar interaction methods implemented with the

previous contact pairs approach. This would help to model the glass-to-frame contacts that occurred with increasing in-plane displacements applied within the model simulation. Only difference was that the general contact algorithm will be implemented in combination with the interaction contact properties defined between these surfaces.

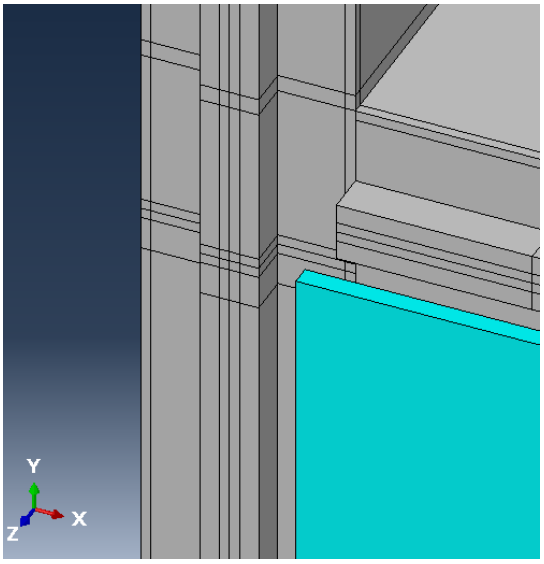

a) Top left glass corner within the CW model which includes the initial 11 mm glass-to-frame clearance

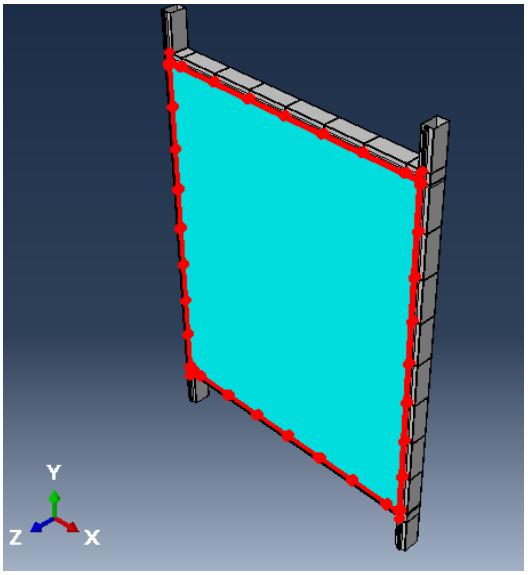

b) Overall isometric view of all selections of glass-to-frame interaction surface pairs

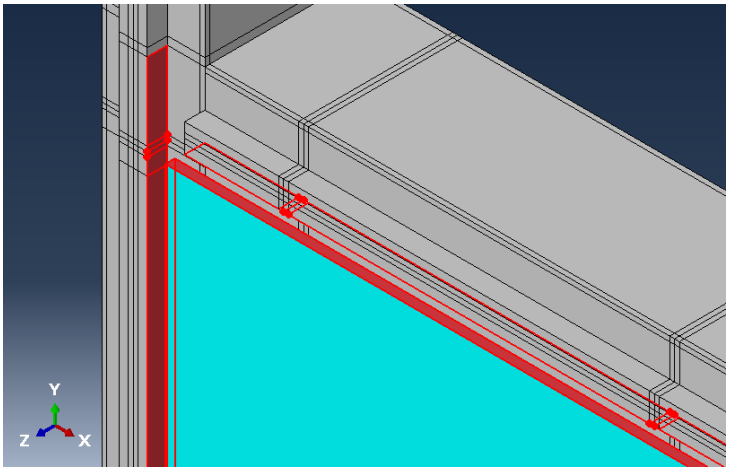

c) Close up of all glass-to-frame interaction surfaces at the top left glass curtain wall model within the glazing pocket

Figure 4-21: Glass-to-frame interaction surface (general contact pairs) illustrations

It was considered appropriate to allow contact/separation between the glass and frame in order for stress to generate along both the glass corners and frame, and to propagate through both components. But it was not a major concern to allow frictional forces to generate between the two surfaces since it was not observed to contribute to the resistance against the applied drift during the experiments. For the normal behavior, the same “Hard” contact was used to define the pressure-overclosure relationship for when contact does occur between the glass and mullion lip. For the tangential behavior, a frictionless formulation was chosen between the glass sides/edge and mullion lip surfaces. This was because it can be assumed that the frictional forces generated between both surfaces was insignificant when compared to stresses generated due to the normal forces seen once contact occurs.

As such, these contact properties were then implemented throughout the analysis using what ABAQUS calls the general contact algorithm. A more detailed discussion of how ABAQUS implements the general contact method with the defined mechanical contact properties and why it was chosen to model the glass-to-frame contact interactions is presented in Appendix A.3.3.

While glass contact with the frame can occur (i.e. pressure plates or other parts of the frame within the glazing pocket) during applied out-of-plane pressures to the CW model, it was not necessary to include these additional surfaces as part of the frame surface selections. The pressure applied to the CW during this study was never high enough to facilitate enough out-of-plane rotation/translation of the glass to allow this type of contact to occur. Therefore, only the glass side surfaces and the mullion lips were selected for the glass-to-frame contact interaction using general contact as shown in Figure 4-21.

4.5.3. Frame Connection Model

As illustrated in the Kawneer drawings, the transom-mullion connections for the curtain wall frame are achieved with use of the shear blocks attachments. These provide semi-rigid connections to the frame which have been previously modeled using some form of a hinge connection in Shirazi's (2005) finite element model. For the FE model generated herein, a combination of coupling constraints and wire connector elements were used instead to achieve this semi-rigid connection. This semi-rigid connection would allow for some in-plane rotations at the bare frame connections during increasing lateral drift. Therefore, the rotational stiffness' of the wire connectors were calibrated such that the generated load-displacement relationship of the bare frame subjected to drift approximately matched the load-displacement relationship curve recorded in Shirazi's (2005) pushover test of the unglazed frame, as is discussed in the literature review.

Partitions were already made on the vertical mullions where the horizontal transoms were in contact with so that mullion surfaces that aligned with the transom's cross section could be defined as shown in Figure 4-22. A reference point was generated at the centroid of the partitioned mullion surface and at the centroid of the transom cross section. A kinematic coupling constraint was then applied to constrain the degrees of freedom (DOF) on a defined vertical mullion surface to its adjacent referent point. This was repeated for the opposing transoms cross section (minus the mullion lip cross section since it does not come into contact with vertical mullion) and its adjacent reference point. This kinematic coupling constraint approach, which is shown in Figure 4-23, is then repeated for the rest

of the defined mullion surfaces and transom surfaces. A summary of what the kinematic coupling constraint does within ABAQUS can be found in Appendix A.2.

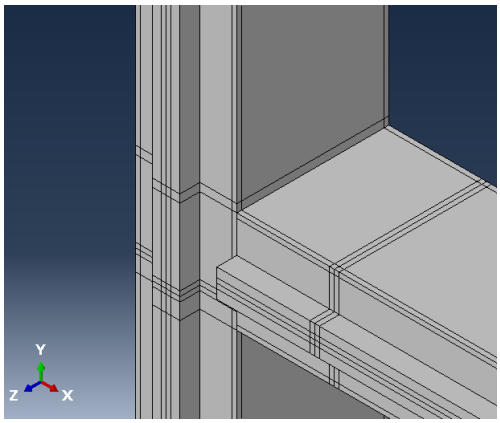

a) Isometric view of partitions generated on the vertical mullion which are perpendicular to transom surface

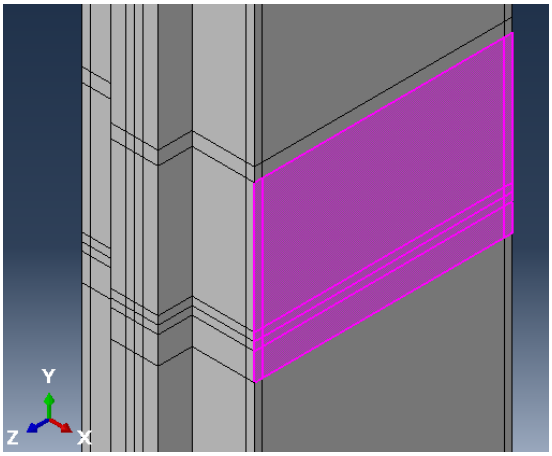

b) Selection of partitioned vertical mullion surface involved in transom-mullion frame connections

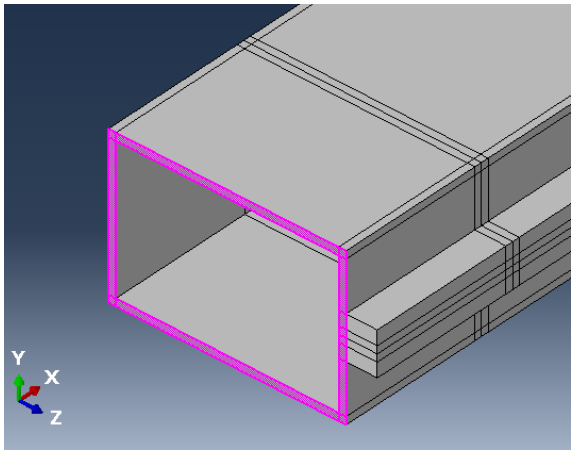

c) Selection of horizontal transom surface involved in transom-mullion frame connections

Figure 4-22: Views of necessary partitions on the vertical mullions and surface selections of relevant frame connection surfaces

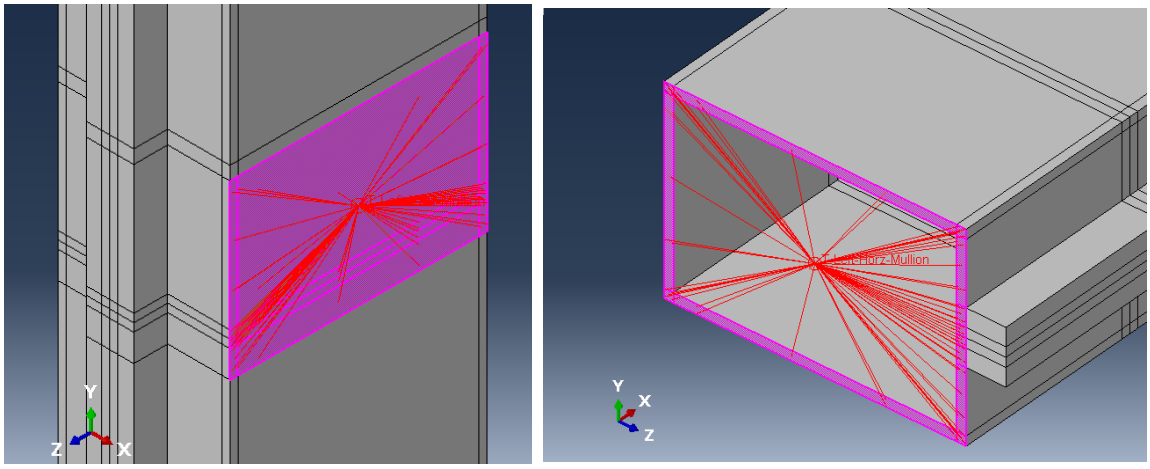

a) Example of kinematic coupling constraint approach and surface selection along vertical mullion at frame connection locations

b) Example of kinematic coupling constraint approach and selection along horizontal transom surface at frame connection locations

Figure 4-23: Illustration of the kinematic coupling constraints implemented at all transom-mullion frame connections

After the kinematic coupling constraints were established, a 3D wire (connector element) was generated to connect the two reference nodes (points) previously created at each transom-mullion connection on the curtain wall frame. These 3D connector elements provided by ABAQUS allow for 3 relative displacements and 3 relative rotations that are local to the elements, since each connector element contains 2 nodes each with 6 DOF's (ABAQUS 2017). The relative displacements and rotations between the two nodes of the connector are subsequently defined as components of relative motion which can either be constrained or unconstrained to one another based on the user definition. The user can then utilize ABAQUS' predefined connection-types which have different constrained components of relative motion already set and various available components of relative motion which can be further defined. For this semi-rigid connection application, the U-Joint assembled connection type was implemented to define the connector behavior. Essentially it fixed all translational DOF's, and the rotational DOF's with respect to the

global y-axis, to each other on both reference nodes connected by the wire at a given transom-mullion connection. This left the remaining components of relative motions for the unconstrained rotational DOF's available, the rotation about the global x-axis and the global z-axis, to be defined using elastic spring-like connector behavior. This U-Joint was deemed an appropriate connection type for permitting flexibility relative to the moment about the global z-axis since the lateral stiffness of the bare frame was attributed to both the flexural stiffness of the framing members and the rotational stiffness of the shear block connections. Based on how the shear block connections were installed to the bare frame members, it is assumed that only relative rotations about the z-axis are occurring while the other remaining relative translational and rotational motions are mainly fixed. Therefore, to constrain the components of relative rotations about the global x-axis, a rigid elastic spring behavior was imposed to essentially constrain these rotations between the transom and mullion connections leaving only the z-axis rotations left to define.

The behavior for the final component of relative z-axis rotations was defined based on trying to match the load-displacement behavior recorded in the Shirazi (2005) bare frame pushover test as shown in Figure 2-43. As observed in Figure 2-43, the lateral stiffness of the bare frame increases once a drift of 3.5 in. (89 mm) has been reached. Therefore, it was necessary to capture this stiffness increase by defining a non-linear elastic spring stiffness for the final components of relative z-axis rotations. With this non-linear spring stiffness, the user is able to define moments as functions of the relative rotations about the z-axis between the transom-mullion reference nodes at the ends of wires. An example of this moment-relative rotation (along the z-axis) relationship which can be defined in ABAQUS is shown in Figure 4-24.

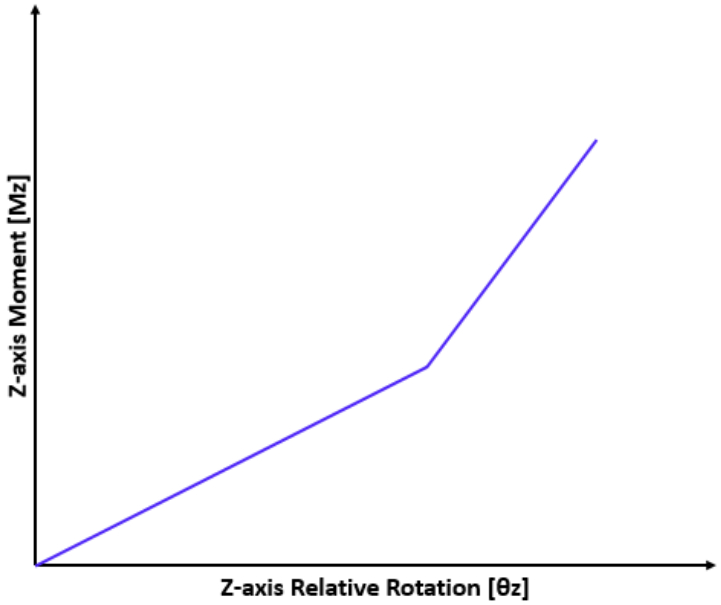

Figure 4-24: Example of moment-relative rotation (along z-axis) relationship utilized for defining wire connector behaviors

Three pairs of moment-rotation (along the z-axis) parameters were then identified after several bare frame simulation iterations that best captured the change in lateral stiffness. To assist with matching the experimental and FE analysis results, a linear regression analysis was completed to generate two linear lines of best fit to approximately define the two slopes of stiffness segments on the experimental results as shown in Figure 4-25. The calibrated z-axis moment-rotation parameters used to define the non-linear elastic behavior of the connectors is presented in Table 4-5. The last moment is very high to capture the connection becoming more rigid as further drift is applied to the experimental CW framing system.

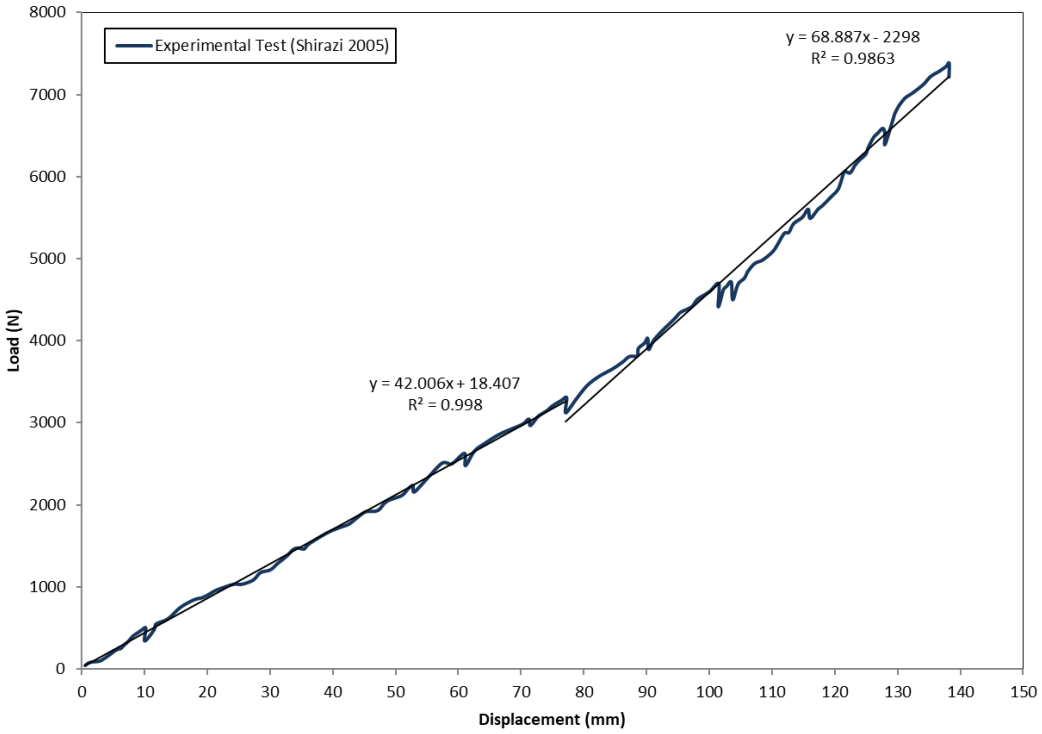

Figure 4-25: Load-displacement relationship of unglazed curtain wall frame from Shirazi (2005) experimental tests subjected to static racking displacement at a rate of 0.01cm/sec

Table 4-5: Non-Linear Elastic Connector Section Behavior: Moment-Rotation (Global Z-axis) Relationship

Data #	Moment [N-mm]	Rotation [radians]
1	0	0
2	7.13E+05	0.0612
3	1.00E+10	0.088

4.6. Non-linear Finite Element Analysis Simulations in ABAQUS

This section will overview the required analysis setup implemented to complete a non-linear FE analysis within ABAQUS so that in-plane and out-of-plane simulations

could be run to validate the generated single CW system model when compared to the in- and out-of-plane experimental studies. These include: 1) non-linear static stress analysis using ABAQUS/Standard; 2) non-linear analysis step definitions; 3) boundary conditions; and 4) loading conditions.

For the in-plane simulation, the assembled single CW system with the 6'x5' glass panel will be analyzed. For the out-of-plane simulation, only the 8'x5' glass panel will be modeled and analyzed since the ability to capture the out-of-plane behavior of the glass was required to be validated during the pressure simulations. While these simulations were run using different models, the goal was to make sure that a single CW model (which incorporates both simulation techniques into one model) can be validated. This process was developed since no out-of-plane experimental results were found for a CW system and therefore had to settle on using a glass panel experiment for the out-of-plane validation of the glass model.

4.6.1. Non-Linear Static Stress Analysis using ABAQUS/Standard

Based on the model generated for the in-plane racking displacement simulations, three sources of non-linearity were present which needed to be accounted for in the ABAQUS model. Material non-linearity was present due to material behaviors being defined with elasto-plastic relationships. Geometric non-linearity, which is identified when large displacements and deformation occurs, was present due to the large displacements applied to the curtain wall frame but also to the deformations in the rubber and aluminum components. And lastly, boundary/contact non-linearities arose because of the changing

contact conditions occurring between most of the curtain wall components and the glass panel. Since the Shirazi (2005) experimental mock-up tests applied a monotonically, static displacement to induce racking motions, a similar displacement-controlled approach needed to be defined using ABAQUS/Standard. Additionally, loads had to be applied along the pressure plates to allow for enough compression to hold in place the glass plate within the glazing pocket throughout the racking simulation. Similarly, for the out-of-plane simulation modeled after the Linden et al. (1983) experiments, static uniform pressures had to be applied on the glass panels and CW components (once incorporated in the validated model).

Therefore, within the ABAQUS/Standard module a static stress/displacement analysis was chosen to solve this highly non-linear FE model. With this analysis method, ABAQUS implements an iterative Newton-Raphson algorithm to solve for the non-linear response of the curtain wall model. A detailed description of how the iterative Newton-Raphson numerical analysis method is implemented in ABAQUS/Standard is presented in Appendix A.4.1.

4.6.2. Non-linear Analysis Steps

Within ABAQUS, users may create different analysis steps, which follow the model's initial conditions step, so changes in loads and boundary conditions throughout the simulations can be implemented. Therefore, in this section, an overview of each analysis step required to run the simulations (i.e. in- or out-of-plane) is presented herein.

4.6.2.1.In-Plane Analysis Steps

The curtain wall racking FE simulation in ABAQUS/Standard was divided into several analysis steps to account for geometric non-linearity, the different applied loading protocol simulations, and to prohibit rigid body motions at the start of the analysis. There were 5 steps generated in this ABAQUS simulation as shown in Table 4-6. This includes the default initial step where initial conditions/interactions developed for the model are applied, and 4 analysis steps which define the different loading/displacement protocols necessary for in-plane racking simulation. As stated previously, the NLGEOM option was turned on for all analysis steps to account for large displacements and deformation as a result of the geometric non-linear analysis. The Pre-contact step was the first analysis step created to use boundary conditions that restrain the entire curtain wall model to prohibit any rigid body motions which continuously developed in initial simulation runs as a result of turning on the geometric non-linear analysis feature (NLGEOM) throughout all analysis steps. The second analysis step, named Pre-tension, followed to apply equivalent clamping loads along the pressure plates to generate the necessary compressive forces along the glass edges before the complete removal of boundary conditions used to restrain the glass panel's rigid body motions within the glazing pocket during the previous steps. During the third analysis step, BC-Change, the boundary conditions holding up the glass are removed as enough compression has been generated such that the glass can now be fully supported in glazing pocket in the dry-glazed configuration. Finally, the fourth analysis step was the simulation step in which either the in-plane displacement or out-of-plane pressure protocol would be applied. For the in-plane validation case, the simulation step, named Static-Rack-

Displacement, applied the racking motions to the dry-glazed curtain wall specimen as was done in Shirazi's (2005) experimental tests.

Table 4-6: ABAQUS Analysis Step Definitions for Static In-Plane Racking Displacement Simulation

Analysis Step	Time Period [sec]	Max. No. Increments	Initial Time Increment [sec]	Min. Increment [sec]	Max. Increment [sec]	NLGEOM On/Off
Pre-Contact	1	1000	1.00E-15	1.00E-50	1	ON
Pre-Tension	1	100000	1.00E-20	1.00E-100	1	ON
BC-Change	1	10000	1.00E-04	1.00E-50	1	ON
Static-Rack-Displacement	1	1000000	0.0001	1.00E-50	0.01	ON

4.6.2.2.Out-of-Plane Analysis Steps

Only one analysis step (after the initial conditions step) was needed since this out-of-plane validation model only represented the glass panel. In this analysis step, the same uniform static pressure applied in the experiments by Linden et al. (1983) was applied onto the generated glass panel. The boundary conditions used on the modeled glass were continued in this analysis step from the previous initial conditions step. Likewise, the NLGEOM option within ABAQUS was turned on for all analysis steps to account for large displacements and deformation as a result of the geometric non-linear analysis. The single analysis step and relevant step definitions input in this FE model are shown in Table 4-7.

Table 4-7: ABAQUS Analysis Step Definitions for Static Pressure Simulation (Glass Panel Only)

Analysis Step	Time Period [sec]	Max. No. Increments	Initial Time Increment [sec]	Min. Increment [sec]	Max. Increment [sec]	NLGEOM On/Off
Static-Pressure	1	1000	1.00E-04	1.00E-50	1	ON

4.6.3. Boundary Conditions

These are the boundary conditions implemented during each analysis step for the in-plane displacement simulation and the out-of-plane pressure simulation.

4.6.3.1.In-Plane Boundary Conditions

The boundary conditions (BC) utilized on several components of the curtain wall system and when they were applied throughout the analysis steps are shown in Table 4-8. The Base1 and Base2 BC's, as shown in Figure 4-26, are only applied to the outer edges of the vertical mullions at the base of the curtain wall to approximately simulate the fixed boundary conditions when the curtain wall is attached to the steel anchors on the racking test apparatus in Shirazi (2005). All translational DOF's were restrained, U1= U2 = U3 = 0 mm, throughout all steps in the simulation. These boundary conditions were created at the initial step and then propagated through all the analysis steps. The edges of the mullions were only selected to limit the amount of restraining boundary conditions on the surfaces of the mullion. Additionally, a partition was made to the base of both mullions at a 5 mm

offset from the outside edge of the horizontal transom so no overconstraints occurred at the already defined vertical surface used for the kinematic coupling constraints used in the semi-rigid connections.

Table 4-8: ABAQUS Boundary Condition Definitions Implemented for Static In-Plane Racking Displacement Simulation

	Analysis Step				
Boundary Condition	**Initial**	**Pre-Contact**	**Pre-Tension**	**BC-Change**	**Static-Rack-Displacement**
Base1	Created	Propagated	Propogated	Propogated	Propogated
Base2	Created	Propagated	Propogated	Propogated	Propogated
GlassBC	Created	Propagated	Modified	Inactive	Inactive
Racking-Displacement	-	-	-	-	Created
Gasket-Distortion-BC	-	-	-	-	Created
Setting-Block-BC	-	-	-	-	Created
Side-Block-BC	-	-	-	-	Created
PreContactBC	Created	Propagated	Inactive	Inactive	Inactive
PreContactBC-Wire	Created	Propagated	Modified	Modified	Inactive

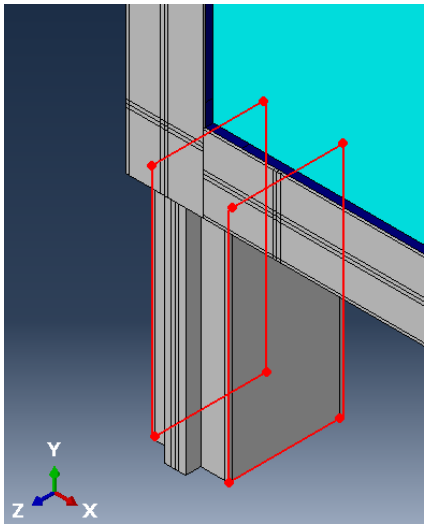

a) Base1 boundary conditions selection at bottom left vertical mullion

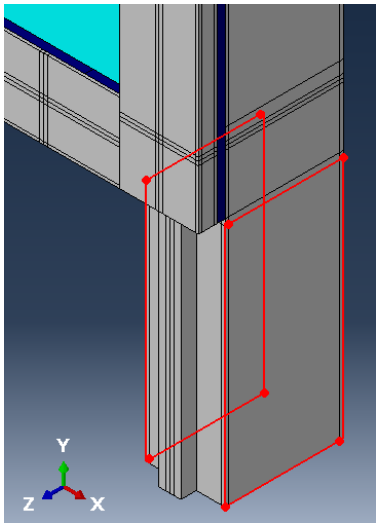

b) Base2 boundary conditions selection at bottom right vertical mullion

Figure 4-26: Base1 and Base2 boundary conditions illustrated

For the GlassBC boundary condition, the glass panel's entire bottom and right side surfaces/edges were selected as shown in Figure 4-27. This boundary condition was

modified throughout all analysis steps as summarized in Table 4-8. All the translational DOF's were restrained, U1= U2 = U3 = 0 mm, from the Initial step and propagated through the Pre-contact step. Then only the x- and y-axis translational DOF were restrained, U1= U2 = 0 mm, so that glass panel was able to freely translate along the z axis during the Pre-tension step when clamping loads were applied. All boundary conditions were deactivated (unrestrained) for the BC-Change step as the glass is now able to be held and set within glazing pocket by the clamping forces and frictional forces. The glass was still left unrestrained during the Static-Rack-Displacement step, because while still being held within the glazing pocket, the panel is now free to translate and rotate throughout the applied racking motions.

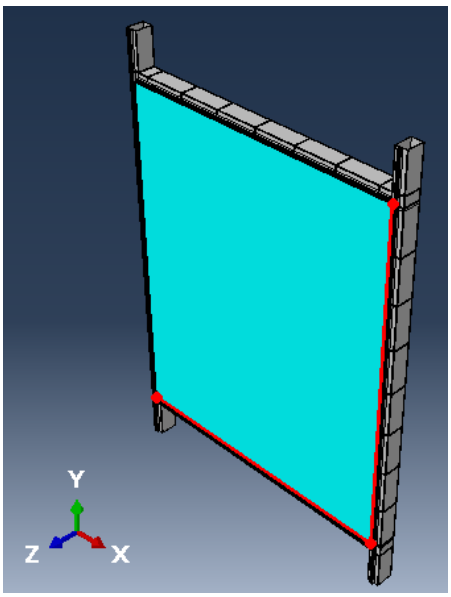

Figure 4-27: GlassBC boundary condition along right and bottom edge surfaces

For the Racking-Displacement boundary condition, a kinematic coupling constraint was used to constrain the top left outer surface of the left vertical mullion to the motion of

a reference point (node) as shown in Figure 4-28. In this coupling constraint, all translational DOF's (U1, U2, U3) of the mullion surface were constrained to all the translational DOF's of the reference node to simulate the frame being fixed within the steel anchors attached to the sliding tube in the racking test apparatus. With this kinematic coupling constraint generated, a static displacement would be applied to the reference node which in turn would displace the top left frame corner to simulate the increasing story drift and the CW fixities to the steel anchors inside the test apparatus. Therefore, during the Racking-Displacement step, the y- and z-axis translation DOF's were restrained, U2 = U3 = 0 mm and only +x-axis translational DOF was displaced at U1 = 70 mm since this was about the max displacement reached before the large crack was observed at the end of the static pushover test in Shirazi (2005). This made the FE in-plane simulation primarily a displacement-controlled analysis during this step.

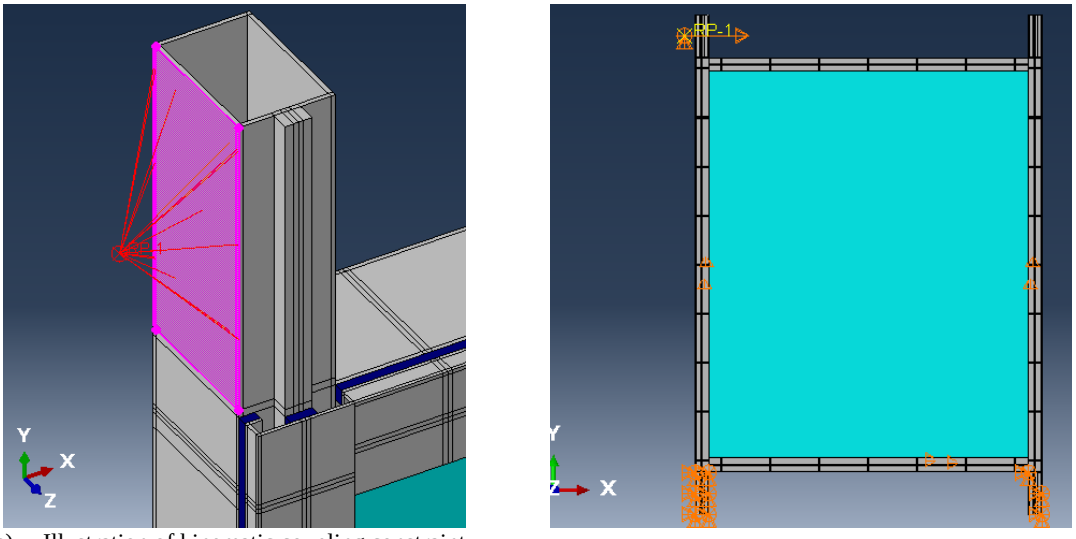

a) Illustration of kinematic coupling constraint implemented for applying the displacement at top left corner of vertical mullion

b) Plan view of Racking-Displacement boundary condition and direction of applied displacement

Figure 4-28: Racking-Displacement boundary condition illustrated

From initial iterations of simulation runs, excessive element distortion was observed to many of the rubber components in contact with the glass during the applied drift before a majority of displacement was reached. Therefore, to prohibit excessive distortions, but still allow gaskets and setting/side blocks to deform in a practical manner along the in-plane direction, boundary conditions were strategically applied on the surfaces. It is important to note that all the rubber related boundary conditions will not be used during an out-of-plane analysis since these issues were not observed.

For the Gasket-Distortion-BC boundary condition, the z-axis translational DOF was restrained, U3 = 0 mm, along the fixed glazing gasket surfaces touching the glass panel as shown Figure 4-29 during the displacement step. While this does stop the gaskets from distorting/rolling out-of-plane into the glass panel surface it won't entirely effect to much the frictional forces acting on the glass as it translates/rotates in-plane within the glazing pocket. For both the Setting-Block-BC and Side-Block-BC conditions the front and back face surfaces (along the z-axis) of the blocks had the z-axis translations restrained, U3 = 0 mm, throughout the entire displacement step as shown in Figure 4-30. Separate boundary conditions (one for the setting blocks and one for the side blocks) were made in case further excessive deformation issues arose individually.

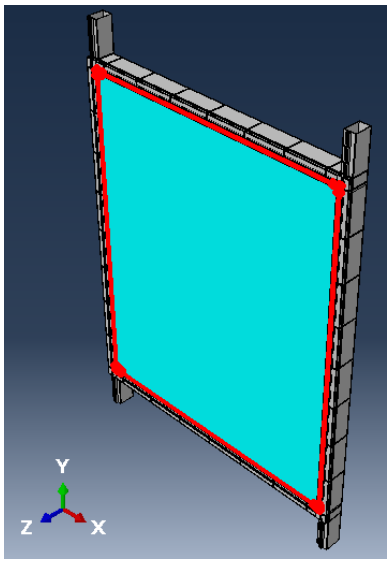

a) Overall selection for Gasket-Distortion-BC boundary condition

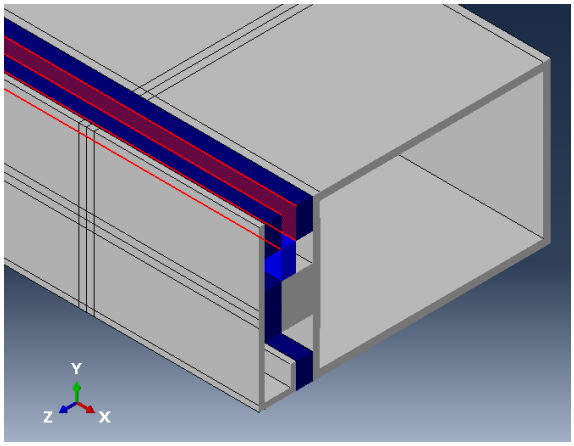

b) Close up of fixed glazing surfaces selected for Gasket-Distortion-BC boundary condition

Figure 4-29: Gasket-Distortion-BC boundary condition illustrated

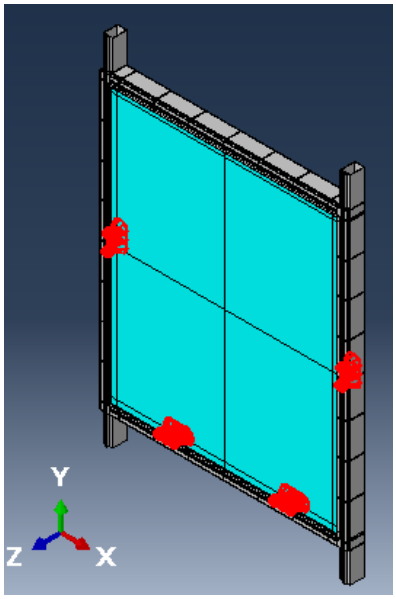

a) Overall selection for the boundary conditions Setting-Block-BC and Side-Block-BC

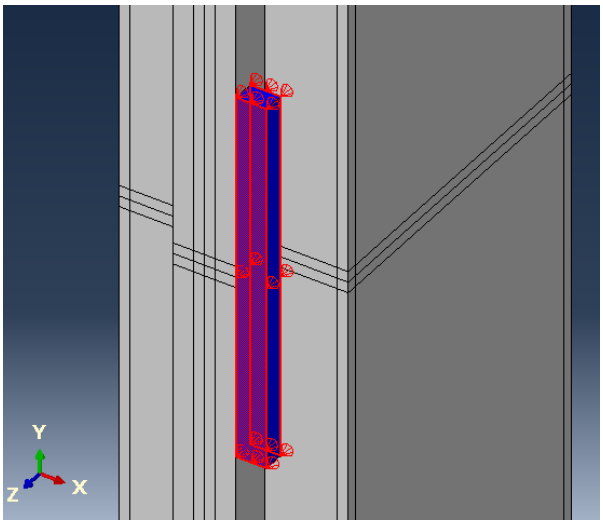

b) Close up example of the front and back face selection in the Setting Block boundary condition

Figure 4-30:Setting-Block-BC and Side-Block-BC boundary conditions illustrated

Finally, additional boundary conditions were added to the entire model and wires separately to restrain rigid body motions that occurred when the NLGEOM feature was turned on to allow for geometric non-linear analysis to be implemented. Therefore, as shown in Figure 4-31 for PreContactBC, all the translational DOF's for all the parts in the model (except the wires) were restrained, U1 = U2 = U3 = 0 mm, from the initial step through the Pre-Contact step. But then deactivated at the start of the Pre-tension step for the rest of simulation. Now for boundary condition PreContactBC-Wire as shown in Figure 4-31, the wires were all restrained for all translational and rotational DOF's, U1 = U2 = U3 = 0 mm and UR1 = UR2 = UR3 = 0 radians, from the initial step through the PreContact step. But it was modified in the Pre-tension step to allow for the z-axis translational DOF to freely displace as clamping loads were applied. Then this wire boundary condition was deactivated for the remaining steps as it was no longer required. These modifications at each step for both of these pre-contact boundary conditions are summarized in Table 4-8.

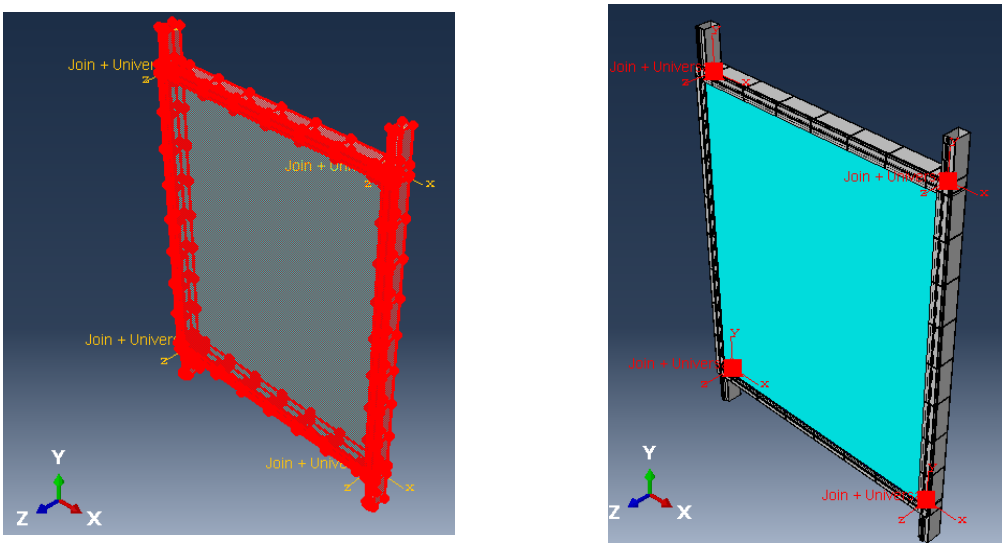

a) Selections made for PreContactBC b) Wire selections made for the PreContactBC-Wire

Figure 4-31: PreContactBC and PreContactBC-Wire boundary conditions illustrated

4.6.3.2.Out-of-Plane Boundary Conditions

Similar to the simple boundary condition approach implemented in Linden et al. (1983) for their theoretical models and experimental setup, a set of boundary conditions were created along the edges of the glass panel to primarily restrain just the out-of-plane translations/rotations as shown in Figure 4-32. Boundary conditions were also strategically added at the glass corner vertices, as shown in Figure 4-32, to restrict any in-plane rigid body motions during the analysis which minimized the in-plane translations/rotations, and still allowed for the maximum out-of-plane displacements to develop during the Static-Pressure analysis step. The details of what DOF's were restrained in this set of boundary conditions applied are described in Table 4-9 and illustrated in Figure 4-32.

It is important to note that these applied boundary conditions to the glass model here were not exactly the same as the experimental boundary conditions from the glass panel holding frame in Figure 4-3. In the experimental test, no clamping load was applied to the glass within the holding frame as the screws were not fully tightened. This meant a slight gap was present between the perimeter surfaces of the glass panel and perimeter rubber gaskets as shown in Figure 4-3. So while the experimental holding frame primarily held the glass in place using simply supported conditions, this slight gap meant these boundary conditions were more flexible and allowed for more out-of-plane translations/rotations at the edges, as well as in-plane translations/rotations. Due to this fact, it can be assumed that the boundary conditions implemented in the glass model were more restrained than the boundary conditions used in the experiments. Also, the location

at which the boundary conditions were applied in the experimental tests were not exactly at the edge of the glass panel, but rather at a location offset from the glass edge as shown in Figure 4-3.

Table 4-9: ABAQUS Boundary Condition Definitions Implemented for Static Out-of-Plane Pressure Simulation (Glass Only)

	Analysis Step	
Boundary Condition	**Initial**	**Static-Pressure**
Glass-Side-Edges [U3=0mm]	Created	Propagated
Glass-Top-Left-Corners [U1=0mm]	Created	Propagated
Glass-Bottom-Left-Corners [U1=U2=0mm]	Created	Propagated
Glass-Bottom-Right-Corners [U2=0mm]	Created	Propagated

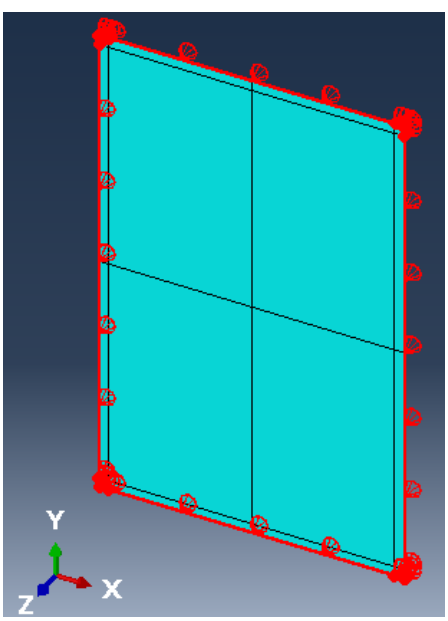

a) Glass panel edges (front and back) selected

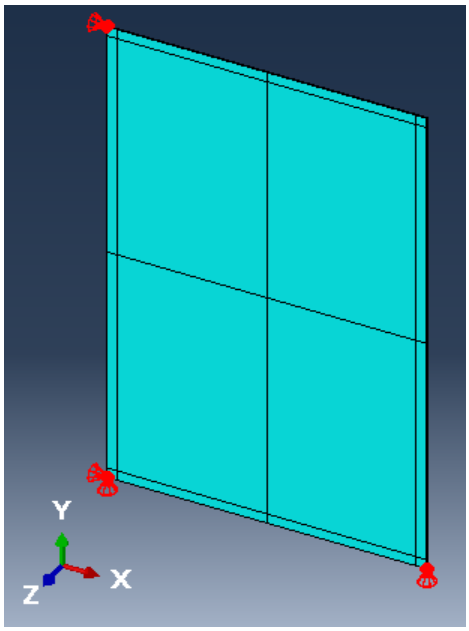

b) Glass panel corner vertices (except at top right) selected

Figure 4-32: Illustration of glass panel boundary conditions applied during out-of-plane simulation (glass only)

4.6.4. Loading Conditions

This section overviews the application of the equivalent clamping loads (for in-plane CW simulation only) and the out-of-plane static uniform pressure (for the out-of-plane glass simulation only). After validation of the out-of-plane glass panel simulation, the equivalent clamping load case could be added to the out-of-plane single CW system model. But this equivalent clamping load was implemented in the out-of-plane CW simulations generated for Chapter 5 and are not described in this section as a result.

4.6.4.1.In-Plane Loading Conditions: Applying the Equivalent Clamping Load

Since the screws used to attach the pressure plates to the mullions were not explicitly modeled, an alternative approach was implemented to apply the equivalent clamping loads to the pressure plates which simulate the same compression achieved by the screw tension. Therefore, strategic partitioning was generated along the mullion and pressure plates as previously mentioned at positions where screws and screw holes would have been located. These partitions created regions that approximately covered the same surface area as the bolt sizes used in the curtain wall installation process. Concentrated loads were therefore applied to the nodes at the intersection points created by the partitions on both the front surface of the pressure plates and the inner surface directly behind the mullion lips to achieve this equivalent clamping force. The total equivalent clamping load of 1,800 Newton, determined empirically by the small CW experiment previously, was divided equally amongst the 9 nodes at these intersection points to evenly distribute this force on the cross section. Therefore, at each of these nodes a concentrated force of -200

N was applied along the –z-axis for points on the front pressure plate surfaces, and a +200 N force applied along the -+z-axis for points on the inner surfaces behind the mullion lip as illustrated in Figure 4-33. These concentrated loads were initially created in the Pre-tension step (2nd analysis step) where it was linearly increased up to the total defined load by the end of the step. The equivalent clamping loads are then propagated throughout the rest of the analysis steps including the displacement step.

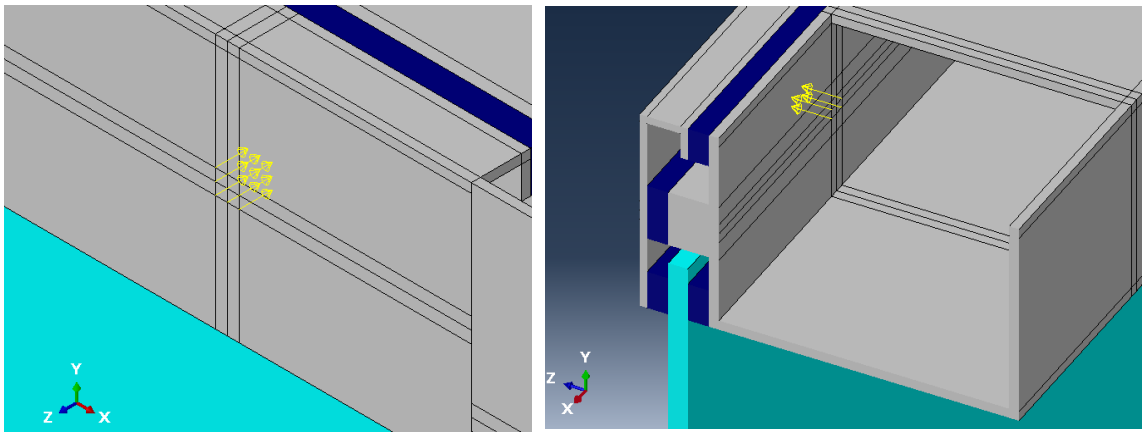

a) Group of concentrated loads applied directly on partitioned nodes on the outside surface of pressure plates which represent screws locations

b) Group of concentrated loads applied directly on partitioned nodes on the inside surface of the mullions directly behind the mullion lip which represent screws locations

Figure 4-33: Application of the equivalent clamping loads using concentrated loads on the partitioned pressure plates and mullions

4.6.4.2.Out-of-Plane Loading Conditions: Applying the Static Uniform Pressure

A static uniform pressure was applied to the entire front surface of the glass panel to simulate the experimental tests. The uniform pressure applied to the glass panel model was up to 0.00517MPa (0.75psi), the same pressure applied to the monolithic glass plates used in the Linden et al. (1983) experiments. This pressure was applied linearly during the

Static-Pressure analysis step which simulates the same linear ramping pressure protocol used in the experiments as well. The application of the static uniform pressures onto the 8 ft. x 5 ft. (2,438 mm x 1,524 mm) glass panel is shown in Figure 4-34.

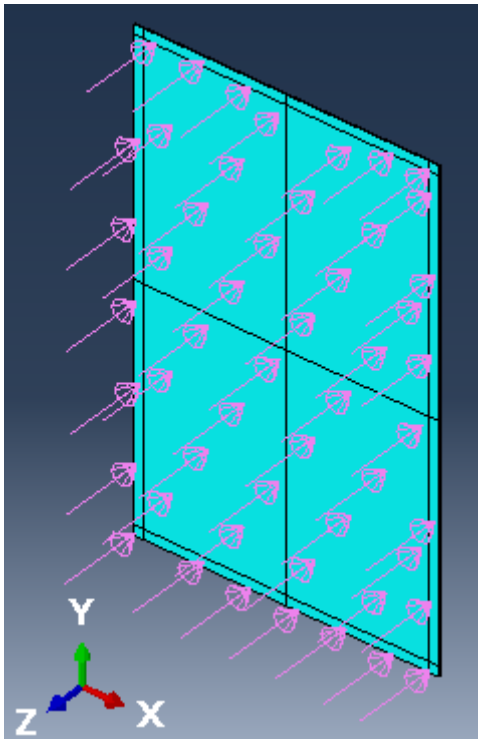

Figure 4-34: The static uniform pressure of 0.00517MPa applied onto front surface of 8'x 5' glass panel

4.7. Validation of the Generated FE Models

This section highlights the validation of the in-plane CW model simulation and the out-of-plane glass panel model simulation. As will be presented, the FE models generated within this study for this chapter were validated since the analysis results had a good agreement with the in-plane and out-of-plane experimental results from Shirazi (2005) and Linden et al. (1983), respectively.

4.7.1. In-Plane Validation of Curtain Wall FE Model

Results obtained from the FE analysis included the load-displacement relationship derived from the x-direction force and displacement history output obtained from the reference node at which the in-plane displacement was applied through. The load-displacement relationship from the FE analysis was compared to the load-displacement relationship from the experimental pushover test completed by Shirazi (2005) as shown in Figure 4-35. Differences in results and in curtain wall responses will be discussed in this section, as well as agreements between the simulation and experimental tests.

As an overview, the FE model included the calibrated semi-rigid transom-mullion connection; the calibrated coefficient of friction equal to 0.65 for the rubber gasket-to-glass interaction surfaces, and the calibrated geometric/configuration changes made to the glass panel (1,835 mm x 1,520 mm) and left side block height (8.5 mm) to capture the experimental test results as best as possible. The model also included concentrated loads applied to potential screw locations (at 229 mm center-to-center spacing) which equaled a total equivalent clamping load of 1,800 N at each location.

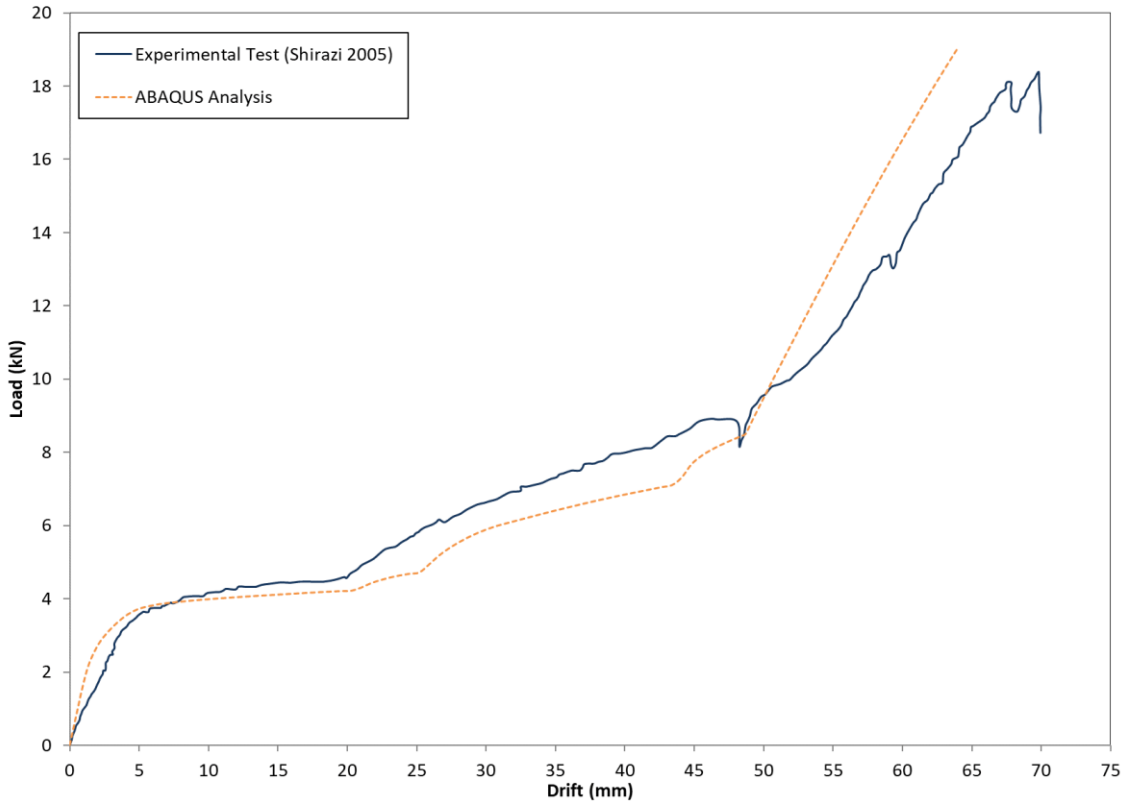

Figure 4-35: Load-displacement relationship of final calibrated glass curtain wall model and experimental results

Overall, the load-displacement curve from the FE analysis had a good agreement with the experimental results. In the case of the first drift stage (i.e. from 0 to approx. 20 mm) the model seems to have reached a constant frictional force of approximately 3,633 N when the drift has reached approx. 4.52 mm in the analysis. The constant frictional force was approximately 3,340 N when about 4.3 mm was reached in the experimental test meaning the modeled captured this within a magnitude of 7% error. Once the constant frictional force was reached in the analysis, the glass panel was observed to translate/rotate with respect to the fixed glazing gaskets as further drift was applied in the simulation. This

means that modeling both the equivalent clamping force to 1,800 N, and the calibrated coefficient of friction to 0.65 was sufficient in approximating when glass starts to slip relative to the fixed glazing gaskets.

From 0 to 3.91 mm of drift, the resistance curve of the FE model is much stiffer. Based on initial iterations of modeling the rubber gasket material behaviors and figuring out the optimum element type for the gaskets, a better fit to this initial resistance slope was could have been achieved when using a Poisson's ratio of 0.495, a hyper-elastic material model, and using incompatible modes in tandem with the fully integrated brick elements. However, these earlier methods resulted in higher computational costs and issues with convergence so they were not used in the final calibrated model.

Between the 4.52 mm and 20 mm drift range of the in-plane simulation, the CW bare frame lateral stiffness and the constant frictional forces are both contributing to the CW's total lateral resistance. Since constant friction has already been met, the bare frame's lateral resistance has a much larger contribution in this range as noted by the Shirazi (2005) experiments. To check if the FE model captured this, an in-plane simulation of the unglazed framing model (just the vertical mullions and horizontal transom members) with the calibrated semi-rigid connections in ABAQUS was analyzed. The resultant load-displacement curve of the bare frame due to a static displacement applied to the FE model is shown in Figure 4-36. In Figure 4-36, the last half of the applied drift shows some yielding in the modeled frame. This was attributed to accounting for large displacements/deformations using the geometric non-linear analysis option. But the analytical results still showed a good match with the unglazed experimental results. While the unglazed frame model matched the experiment, the analysis results in Figure 4-35 show

that the fully glazed CW model had slightly less lateral stiffness than what is observed in the mock-up tests in the 4.52mm to 20mm drift range. Since the modeled unglazed CW model had a successful match to the experiments, this slight difference in resistance could be attributed to how the fully dry-glazed CW system was fixed to the testing apparatus in the experiments. Taking a look at the actual fixities used in the experiments could help further explain why a stiffer resistance is seen in the experimental results.

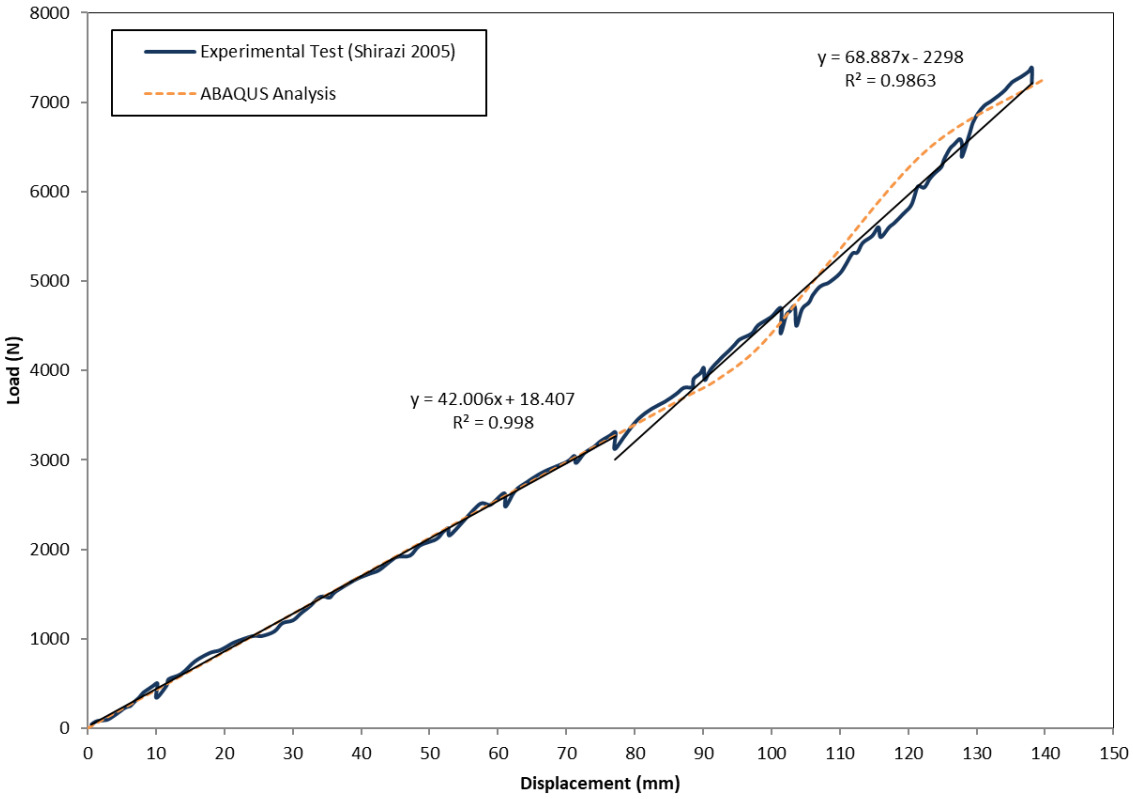

Figure 4-36: Load-displacement relationship of the unglazed frame model using the calibrated semi-rigid connections and the experimental unglazed mock-up test completed by Shirazi (2005)

For the next drift stage (approx. 20-49mm), the first glass-to-frame contact for the analysis occurred at approximately 20.3 mm. Likewise, the bottom right glass corner came into initial contact with the mullion lip at approximately 43.4 mm. Both of these initial contacts closely matched the experimental results. However, while reviewing the experimental results more closely, an argument can be made that the bottom right corner glass contact occurred at roughly 42-43 mm instead of the identified 45 mm drift, which would improve the FE results. This is because at the proposed 42-43 mm drift, there is a noticeably sharper increase in stiffness, and at the original 45 mm drift there is a decrease in stiffness. As shown in Figure 4-35, both the increase and decrease in stiffness within the 43.4 to 48.74 mm drift range was observed in the analysis as well. However, with model visualization capabilities, it was observed that the bottom right corner made contact at the 43.4 mm drift during the first stiffness increase stage and not during the second decreasing stiffness phase as was identified in the experimental results (at about the 45 mm mark). So while it was unclear if Shirazi based this bottom corner contact drift on the load-displacement graph or based on visual observation, this argument (i.e. that the experimental second glass-to-frame contact actually occurred at 42-43mm) could be justified based on visual observations within the FE model in combination with the analysis' load-displacement response.

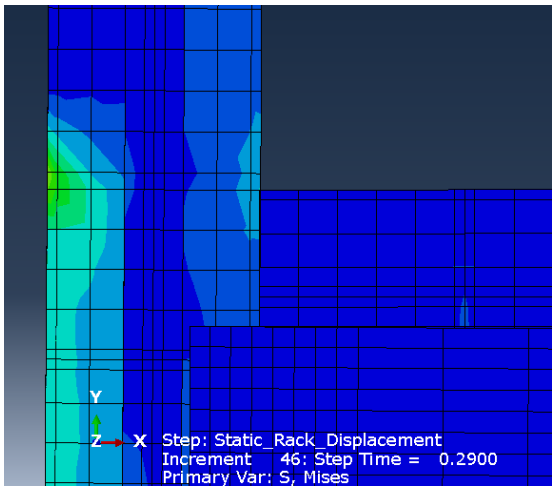

a) Top-hand side of top left corner glass-to-frame contact (1st glass-to-frame contact)

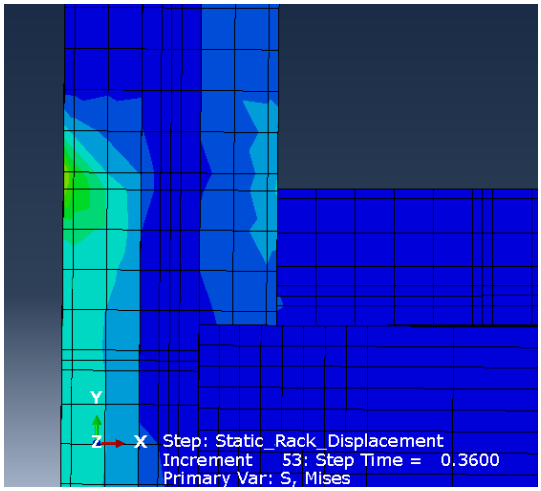

b) Left-hand side of top left corner glass-to-frame contact (2nd glass-to-frame contact)

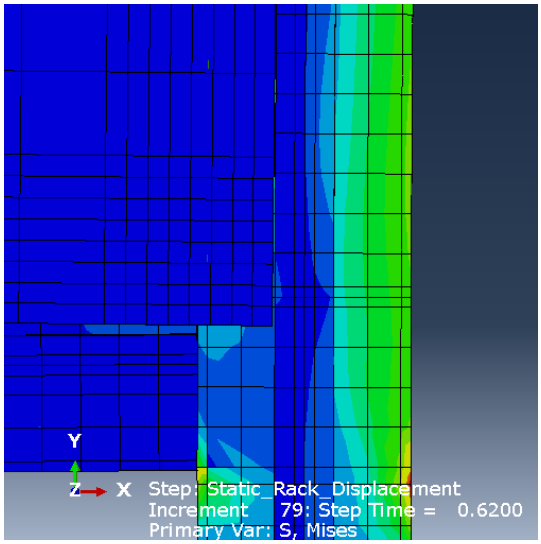

c) Right-hand side of bottom right corner glass-to-frame contact (3rd glass-to-frame contact)

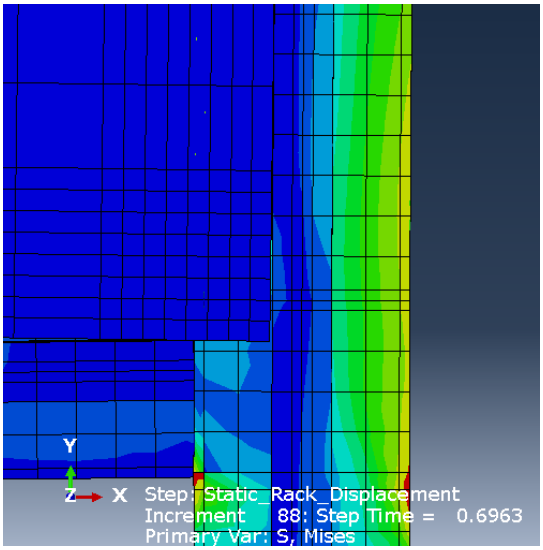

d) Bottom-hand side of bottom right corner glass-to-frame contact (4th glass-to-frame contact)

Figure 4-37: Different stages of glass-to-frame contacts that occur in the ABAQUS model during in-plane simulation

Although it was not entirely discussed by Shirazi (2005), additional glass-to-frame contacts on the glass corners were also identified based on the visualization capabilities within ABAQUS post-processing module, in combination with the load-displacement results, as shown in Figure 4-37. For instance, glass-to-frame contact first occurred at the

top-hand side of the top left glass corner and the mullion lip at 20.3 mm. Then the left-hand side of the same top left glass corner came into contact at approximately 25.2 mm. For the bottom right glass corner, the right-hand side came into contact at 43.4 mm, while the bottom-hand side came into contact at approximately 48.74 mm. While these four specific glass-to-frame contacts were not described in the experiments, they do at least follow the main experimental observations that the first contact is at the top left corner and the last contact is at the bottom right corner.

Now as shown in Figure 2-34 from the experimental test, there was an immediate drop in load at the 48 mm drift due to an initial small crack in the lower right glass corner. This was followed by another stiffness increase which led to another small crack in the top left glass corner at approximately 59 mm, and then a larger crack at approximately 67 mm. As shown in Figure 4-35, the FE analysis showed a good agreement with where the increased stiffness change initiated at about 48.74 mm of drift. However, since the model did not capture the sharp drops in load resistance, it was assumed that the small crack at the lower right corner would occur at the same 48.74 mm drift (at the stiffness change) due to both glass corners coming into full contact with the frame at this point in both the analysis and experiment. Therefore, with this assumption, the model and experiment show good agreement in regard to when the small initial cracks/spalling would occur, and when the increase in stiffness due to both corners coming into contact occurs.

The reason for this approximately sharp linear stiffness increase continued after 48.74 mm in the analysis, without drops in load resistance, was attributed to the glass being modeled with only a linear elastic behavior. It was assumed that if the brittle cracking behavior had been modeled, which considers a failure stress and a Mode I fracture energy

in ABAQUS, then the model would have seen less of a stiffness increase and some noticeable drops in load resistance/stiffness once the glass cracking stress had been reached.

However, another glass cracking identification approach was used to validate that the experimental large cracking stress (onset of glass cracking) was captured in the FE model using experimental minimum principal stress/strain results. Based on the minimum principal strain-load/drift relationships shown in Figure 2-35 and Figure 2-36, the experimental glass cracking stress was approximately 28.8 MPa (minimum principal stress). Since experimental cracking stress was reached at different glass-to-frame contact drifts, it was determined that the glass in the FE model must reach the 28.8 MPa at both the top left and bottom right corners for it to be considered as cracked. A mesh refinement study was completed to obtain accurate stress results during the analysis at the same locations strain gages were installed in the experiments. The mesh was only refined near the corners and perimeters of the glass (up to a 50mm offset on all sides). Several trials with different local mesh sizes (i.e. 25mm, 12.5mm, 6.25mm, 3.125mm and 1.5625mm) were completed to analyze the stress at a location offset from the top left and bottom right corners during different drift stages where the glass-to-frame contact had occurred as shown in Figure 4-37. The minimum principal stress-displacement relationships during each glass-to-frame contact stage at the top left and bottom right corners are shown in Figure 4-39 and Figure 4-40, respectively. The approximated minimum principal stresses, which were obtained using the elements highlighted in Figure 4-38, converged once the 1.5625mm local mesh size was used. To save computational time, the local mesh size of 6.25mm was appropriately used for the rest of the FE models in this study because the

minimum principal stresses recorded were about the same. Based on this mesh refinement, and the glass cracking stress identification approach, the glass cracking was only reached in the top left corner. The bottom right corner came close to the 28.8 MPa glass cracking stress, but since the simulation stopped at 63.9mm it was not reached. However, other models that were generated in the next stage of this study using the same FE modeling techniques in this chapter were able to have both corners reach this glass cracking stress thereby validating this approach.

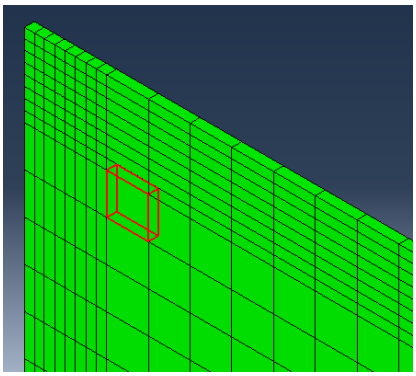

a) Element selected at top left corner for minimum principal stress output in mesh refinement study

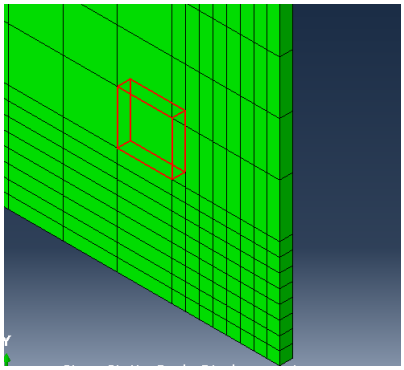

b) Element selected at bottom right corner for minimum principal stress output in mesh refinement study

Figure 4-38: Element selections for obtaining minimum principal stress outputs

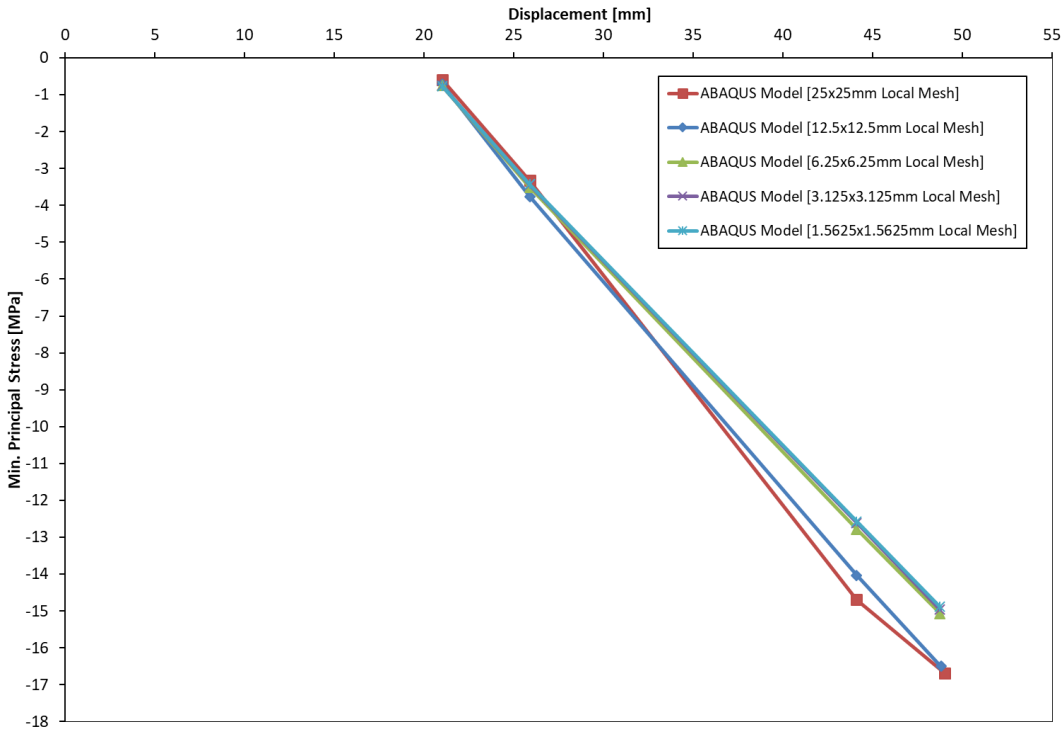

Figure 4-39: Glass-to-frame contact minimum principal stress-displacement relationship at top left corner for glass mesh refinement study

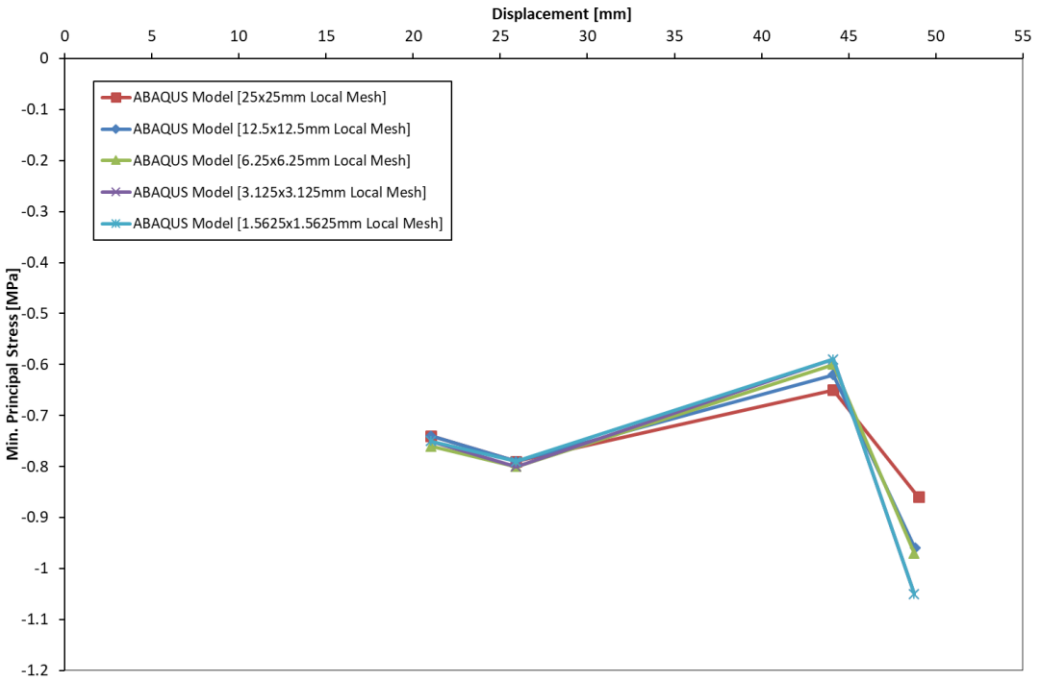

Figure 4-40: Glass-to-frame contact minimum principal stress-displacement relationship at bottom right corner for glass mesh refinement study

The fact that the model stopped at a drift of about 63.9 mm due to the generation of extreme residuals within the analysis (causing non-convergence), which is relatively similar to the large cracking drift of 67 mm observed in the experiment, further verifies that the model can simulate similar mock-up curtain wall structural responses. Based on this, the model still was adequate in capturing the curtain wall response up to and past the first large glass cracking drift near 48mm. Overall, the FE modeling approach taken in generating the dry-glazed CW model subjected to the displacement simulations has proven to be validated.

Further structural responses of the CW model during the applied drift simulation were observed which were considered useful in identifying structural damage states for the

next phase in the study. As shown in Figure 4-41, when enough drift was applied, in-plane gap openings (glass/frame breach) were present between the glass and fixed glazing gaskets as a result of the glass rotations/translations. Also, both the horizontal transom and vertical mullion members showed stress concentrations and deformations at the corner mullion lip regions where glass contacts occurred, much like what was reported in other experimental racking tests. Additionally, after full glass contact at both corners occurred, the horizontal members rotated about the x-axis as further drift was applied as shown in Figure 4-42. Yielding of the aluminum CW frame members was also observed as stress concentrations were apparent along the walls of the vertical mullions. As shown in Figure 4-43, these were more evident at the bases where the restraining boundary conditions were used, the top left surface region where the displacement was applied through kinematic coupling constraints, and around the regions where the semi-rigid transom-mullion connections were made. Lastly, gasket deformations were also observed throughout the analysis, but this was primarily limited to the fixed glazing gaskets. Even so, gasket degradations (i.e. pull-out, push-in, and shifting) could not be fully captured due to being tie-constrained to aluminum surfaces throughout the model. This is opposed to the actual CW installation which allows the gaskets to shift within the slotted holes in which they are fitted to in the actual aluminum pressure plates and mullions. However, since these gasket slots were not modeled and aluminum-to-rubber constraints were assumed, only twisting and bulging was mainly captured during simulations. This approach to modeling the rubber behavior (i.e. only allowing twisting and bulging deformations due to constraints) was deemed appropriate for the scope of this research since it still allowed for capturing some realistic performance of the rubber components during the loading simulations. However,

this means gasket degradation damage states were not primarily analyzed and used for seismic fragility curve development in the following chapters.

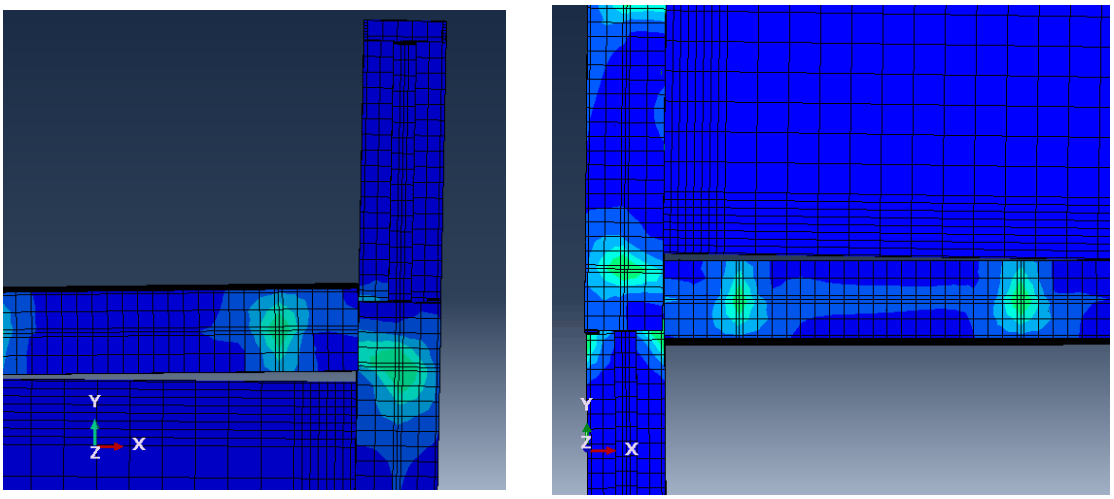

a) Example of in-plane gap opening (glass/frame breach) at top right corner of CW model

b) Example of in-plane gap opening (glass/frame breach) at bottom left corner of CW model

Figure 4-41: Illustrations of in-plane gap openings (glass/frame breach)

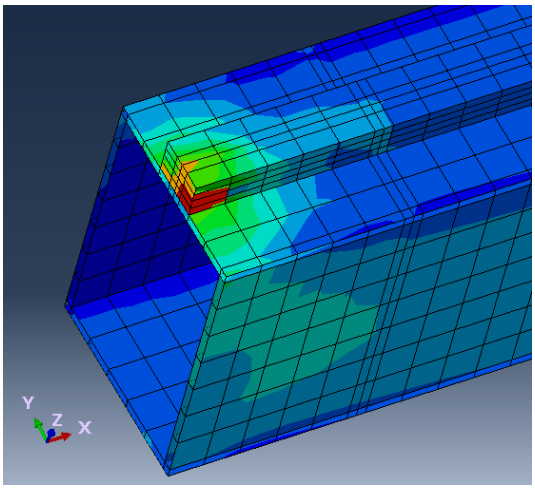

a) Example of stress concentrations where glass-to-frame contacts occur at top left corner of horizontal transoms

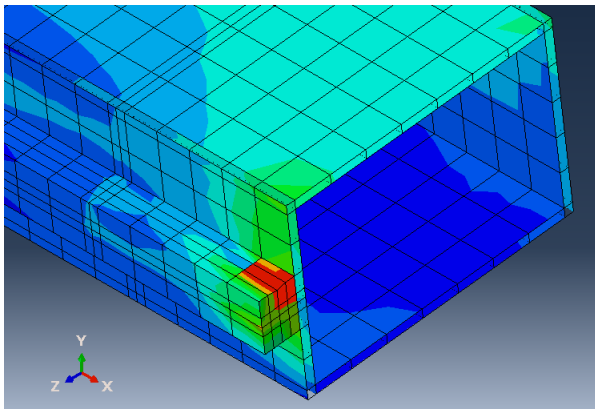

b) Example of stress concentrations where glass-to-frame contacts occur at bottom right corner of horizontal transoms

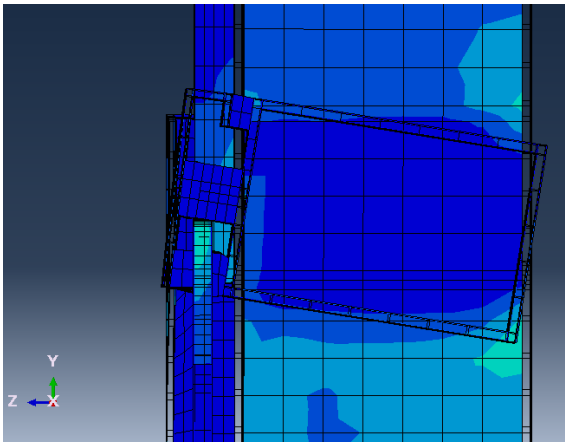

c) Example of out-of-plane rotation of the transom due to top left corner glass-to-frame contacts

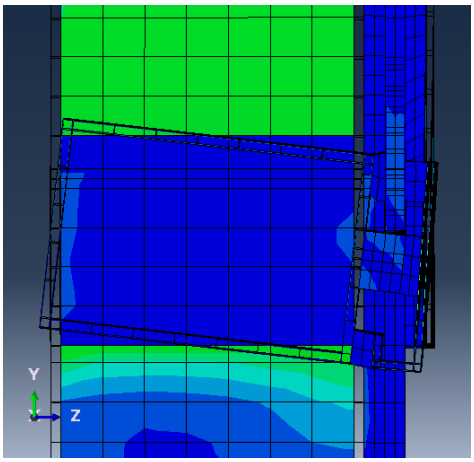

d) Example of out-of-plane rotation of the transom due to bottom right corner glass-to-frame contacts

Figure 4-42: Illustrations of stress concentrations and out-of-plane rotations along the horizontal transom members during glass-to-frame contacts

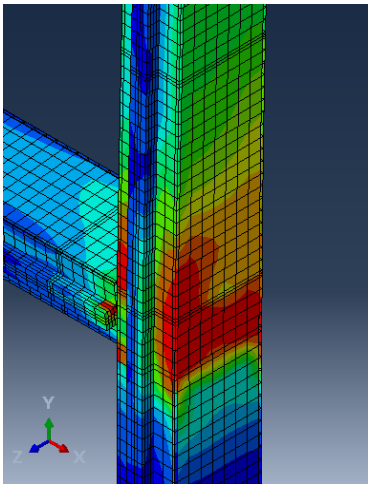

a) Example of stress concentrations and aluminum yielding near fixed boundary conditions at the bottom right mullion

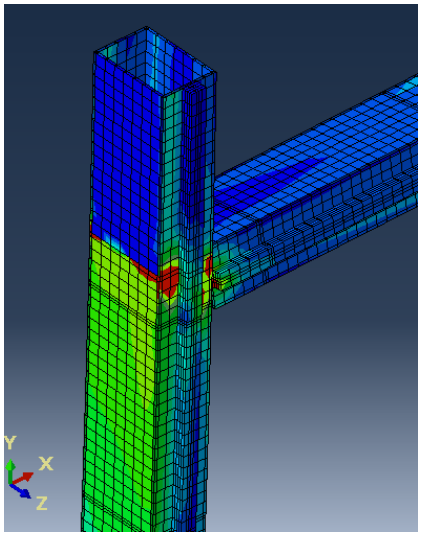

b) Example of stress concentrations and aluminum yielding near applied displacement using kinematic coupling constraint at the top left mullion

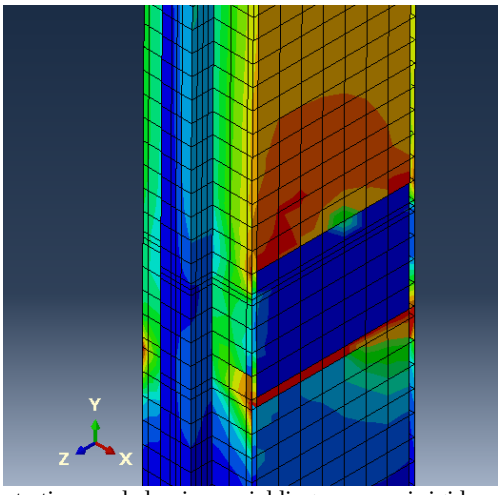

c) Example of stress concentrations and aluminum yielding near semi rigid connections region at the bottom left mullion

Figure 4-43: Illustrations of aluminum yielding and stress concentrations along vertical mullion members

4.7.2. Out-of-Plane Validation of Monolithic Glass Panel FE Model

For the out-of-plane simulation, a static uniform pressure of 0.00517 MPa was applied to the surface of an 8ft. x 5ft. (2,438mm x 1,524 mm) monolithic glass panel with a thickness of 0.233in (5.92mm). Using a combination of simply supported and catenary boundary conditions on the glass, the first set of results included experimental and analytical comparisons of the maximum principal stresses at the top left corner due to the applied pressure as shown in Figure 4-44. The maximum principal stress was obtained from the same top left element location selected from the in-plane simulation test as shown in Figure 4-38.Since the glass model was meshed with SC8R continuum shell elements, stress outputs can be obtained at each Gaussian integration point along the thickness of element. However, only the maximum principal stress located at the bottom of the element (along the z-axis of the element in question) was used since experiments measured for the tensile maximum principal stress near the same corner location. Based on Figure 4-44, it seems that the analyzed maximum principal stresses near the corner differ from the experimental results, since they are lower than what is observed in the experiments. While there is a relatively good match near the start of the pressure simulation, the differences in results increased as the applied pressure increased. These differences could be attributed to the fact that the maximum principal stress from the model was not obtained in the exact location as in the experiment. Another contribution could be the more rigid boundary conditions applied in the glass panel model as opposed to the more flexible boundary conditions used in the experimental testing apparatus. Or the fact that the boundary

conditions were applied directly at the edge of the glass panel in the model as opposed to the slight offset used in the experiments.

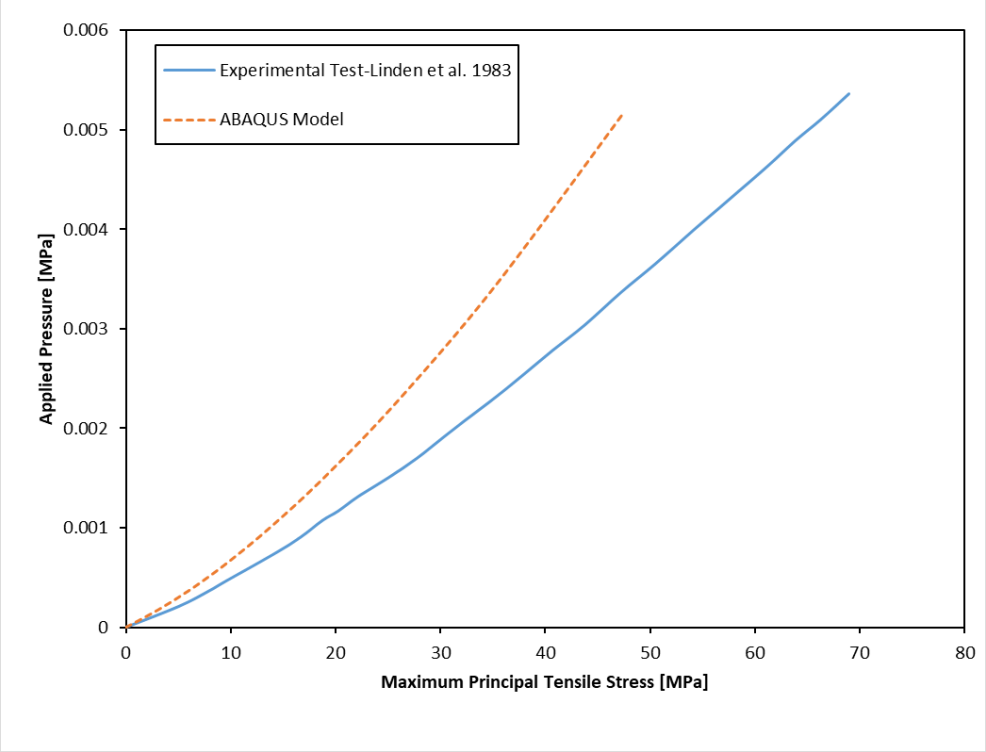

Figure 4-44: Applied pressure-maximum principal tensile stress relationship at the top left corner of a monolithic glass panel due to an applied static uniform pressure of 0.00517 MPa (Experimental and Analytical)

Next the maximum principal stresses at the center of the glass panel due to the applied pressure were obtained from the model as shown in Figure 4-45. Here, the model showed a much better match to the experimental results throughout the entire pressure applied. This shows that the glass model is sufficient at obtaining the glass stress near the center of the panel, since the model approximated a maximum principal stress of 33.1 MPa, which was close to the recorded 36.15 MPa in the experiment. Also, the maximum principal stresses near the center of the glass model were lower than the approximated

stresses near the corner of the glass, similar to what was observed in the experiments. Again, the slight difference in results throughout the simulation could be due to the boundary conditions applied in the model.

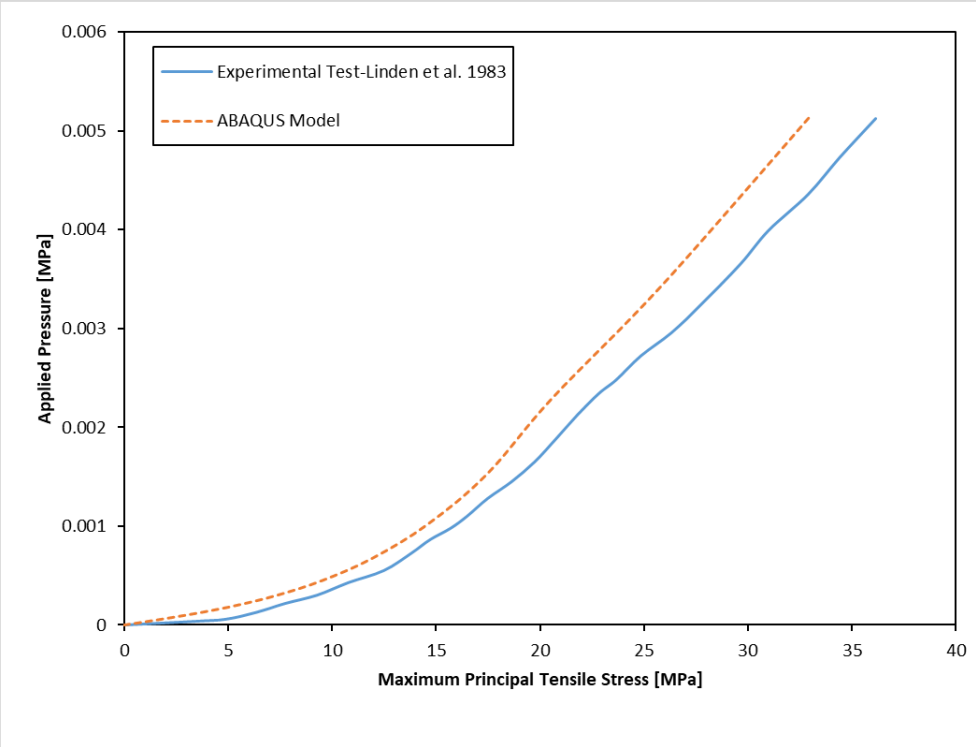

Figure 4-45: Applied pressure-maximum principal tensile stress relationship at the center of a monolithic glass panel due to an applied static uniform pressure of 0.00517 MPa (Experimental and Analytical)

Another good match observed between the analysis and experiments was with the applied pressure-deflection relationship at the center of the glass panel as shown in Figure 4-46. The results between the analysis and experiment are again very similar to one another as analytical results show that the model can obtain a max. deflection of about 38.7 mm at an applied pressure of 0.00517 MPa, quiet similar to the max. out-of-plane displacement of 38.4 mm obtained in the experiment. Therefore, from the three analytical results

obtained, it is clear that the glass model generated in ABAQUS was validated and can capture key structural responses (i.e. maximum principal stresses and maximum deflections) when subjected to an out-of-plane static uniform pressure simulation. Since these were validated near the corner and center of the glass, it is appropriate to assume that the approximated stresses and deflections along the entire glass model are accurate as well. This would be useful for identifying glass cracking stress when the CW model is subjected to out-of-plane pressures later on. As such, Figure 4-47 shows the maximum principal stress along the front and back surfaces (at the top and bottom integration point locations of the continuum shell elements, respectively) of the glass panel at the end of the pressure application.

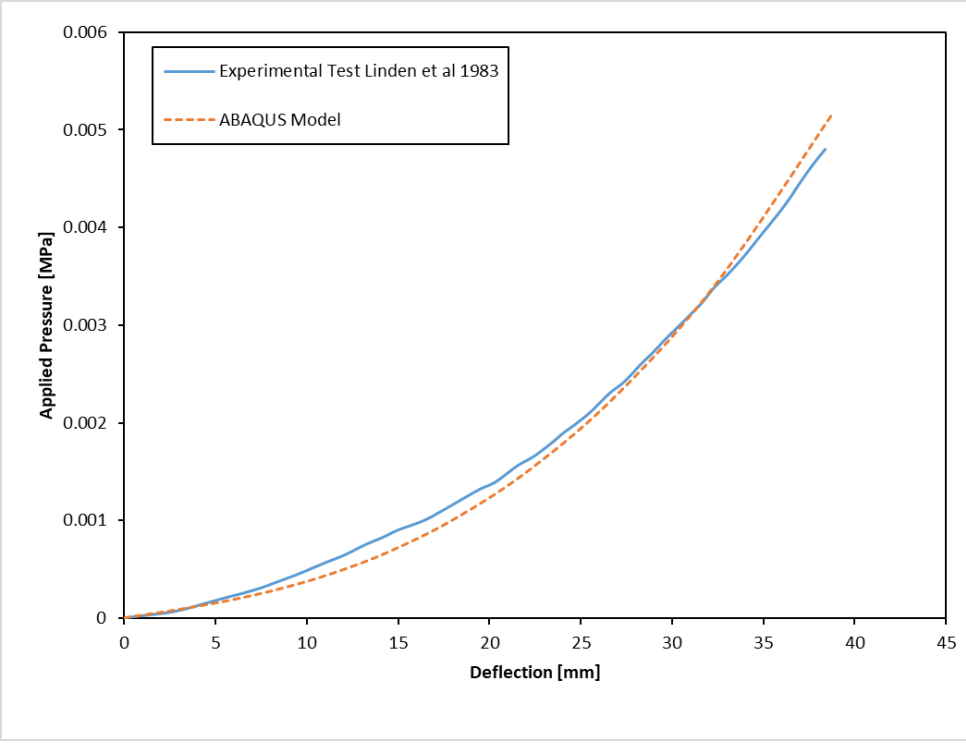

Figure 4-46: Applied pressure-deflection relationship at the center of a monolithic glass panel due to an applied static uniform pressure of 0.00517 MPa (Experimental and Analytical)

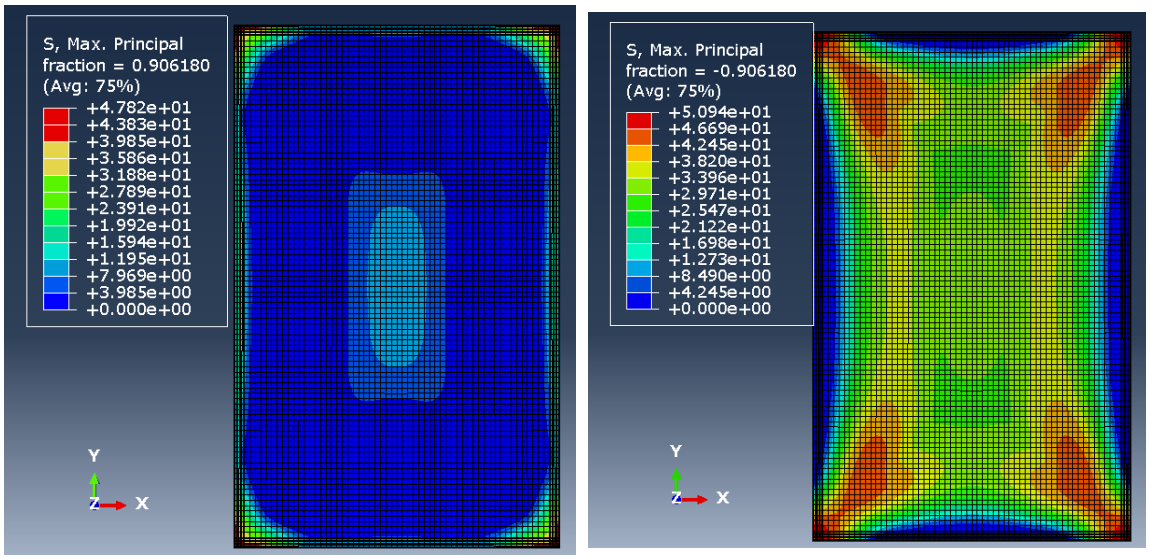

a) Contour plot of maximum principal stresses of the glass located at the top integration point

b) Contour plot of maximum principal stresses of the glass located at the bottom integration point

Figure 4-47: Contour plots of maximum principal stresses of the glass due to static uniform pressure of 0.00517MPa

4.8. Summary of FE Model Validations

In summary, the model generated for the in-plane racking displacement simulation shows a relatively good agreement when compared to the experimental results of Shirazi (2005). This is due to the load-displacement relationship derived from the non-linear analysis in ABAQUS/Standard matching well with that of the mock-up test during key drift stages. This means structural responses at certain drift levels from the analysis matched closely when compared to the experiment. These structural responses/observations include: 1) point of constant friction forces (or initial glass slipping); 2) the different glass-to-frame contacts at the glass corners; and 3) the initial glass cracking (large) stress. Likewise, because the model is sufficient enough to properly capture the glass movement within the

glazing pocket, post-processing observations of the model can be made to approximate certain structural damage states which would lead to non-structural damage states (i.e. water intrusion and air infiltration). These include: 1) glass cracking (due to glass cracking stress) and 2) in-plane gap openings (glass/frame breach). Additional structural responses which do not necessarily lead to the non-structural damage states that were observed include: 1) yielding of the aluminum framing members and 2) twisting of the framing members during glass-to-frame contact. While this model was validated for in-plane responses, it was noted that further refinement of the brittle cracking behavior within the glass model could be carried out to improve the in-plane, and subsequently the out-of-plane response, once glass cracking is reached. Likewise, better modeling of the rubber component behaviors should be studied in an effort to improve their performance during the racking simulation.

The glass panel simulation, which subjected the model to out-of-plane static uniform pressures, helped establish that the FE modeling approach taken to generate the glass model for the in-plane simulation is valid for simulating out-of-plane structural behavior as well. This was based on the glass model successfully capturing the out-of-plane behaviors observed in the Linden et al. (1983) tests such as: maximum principal stresses at the glass corners/center, and the maximum deflections at the glass center. While this out-of-plane validation process involved only modeling of the glass panel with simply supported/catenary boundary conditions (as opposed to the full dry-glazed CW system model), it effectively validated the use of the glass panel model within the CW system model for pressure simulations. Most importantly, the changing boundary conditions

observed within the CW glazing pocket during the applied pressure could be captured due to the explicit 3D FE modeling of the CW components and the component interactions.

Therefore, a successful FE modeling method was developed and validated within this study for both in-plane and out-of-plane simulations with one model of a single panel CW system. Now this validated model will be expanded upon to a much larger scale curtain wall section in the next chapter. This is done to assist in approximating structural damage states based on the structural responses that can now be approximated with this model on a much larger scale for fragility curve development.

Chapter 5

Large Scale Glass Curtain Wall Section Simulations

5.1. Introduction

The research thus far has led to the generation of a validated finite element model for a single unit of glass curtain wall system. The model has the ability to run analytical simulations which subject the CW unit to loading in two orthogonal directions, an in-plane static racking displacement and an out-of-plane static uniform pressure. Both of these simulations represented intensity measures which a CW system may see during an earthquake and a hurricane, respectively. Certain structural behaviors related to the performance of the CWs were also observed to be approximated for both simulations. For the next phase of this computational study, work was required to help further support the use of the alternative engineering analysis method established in Chapter 4 for the development of seismic and hurricane fragility curves. Being able to obtain such fragility curves based on FE models would be beneficial for engineers implementing a multi-hazard performance based engineering design/analysis for CW systems during the preliminary design phase of a project.

Therefore, to further support the use of the previously validated FE modeling approach, a model was generated containing a larger one story section of a curtain wall which included different glass panel sizes. A case study of a Virginia Tech research building containing glass curtain walls was reviewed to help design this larger CW section

to get a better representation of how these sections were designed and constructed in the field. The original Kawneer 1600 CW system configurations were still implemented in this model since it was the basis of the validated model in the previous chapter. Also included in the model were steel anchor connections because the effects of these CW system-to-structure system connections (i.e. connection fixities in the field as opposed to in the lab) were considered important to the performance of the CW system, as noted by other studies reviewed in the literature. Different configurations of the designed larger section of glass CW were generated and subjected to the same simulated in-plane and out-of-plane loading protocols to analyze how these would affect their performance against simulated seismic and hurricane events. Analyzed structural observations that the CW model could capture were then identified to help approximate structural damage states of the CW which are required for the fragility curve development stage in the next chapter. For in-plane and out-of-plane simulations, these structural damage states included: 1) initial glass-to-frame contact (only in-plane); 2) initial glass cracking; 3) glass/frame breach; 4) yielding of aluminum mullions; and 5) yielding of steel anchors. Based on the structural damage states being reached, non-structural damage states are also obtained which are related to water, air infiltration (condensation) and thermal performance damages.

5.2. Design of Large Scale Section of Glass Curtain Wall System

This section provides an overview of the design of a one story section of glass curtain wall incorporated for this fragility study. To assist with the design, a case study of a Virginia Tech research building containing glass curtain walls was chosen and reviewed.

From this, a baseline CW section was designed and became the control for a set of CW models developed to capture the effects of different CW configurations subjected to the two different simulations. These configurations will also be discussed.

5.2.1. Glass Curtain Wall Case Study: Virginia Tech Research Building

The structure chosen as the case study was the Rackspace Research Building at the Virginia Tech Corporate Research Center (VTCRC). From the building's architectural plans, a curtain wall section from the North Elevation side of the two-story building was selected as the primary influence for the CW section to be designed. The considered side elevation view and a close up of the selected curtain wall section are shown in Figure 5-1 and Figure 5-2, respectively. This curtain wall section contains 10 glass panels, two panels wide by five panels high, with various glass dimensions. Note that this CW section was not attached to structural members with anchor connections since it was attached at the perimeters. As shown in Figure 5-3, head, sill and jamb perimeter framing members were directly fixed to either the ground or surrounding stone façade system. To determine the final design of the steel connection for this study, a detail drawing of one of the steel anchor connections at another CW section included in the VT CRC Research Building was reviewed as shown in Figure 5-4. As shown in Figure 5-4 (connections), the bottom side of the transom member is directly in line with the floor slab, and the anchor is connected below this floor slab to a structural member. The framing system was installed such that a 2 in. offset from the structure was established throughout the height of the section.

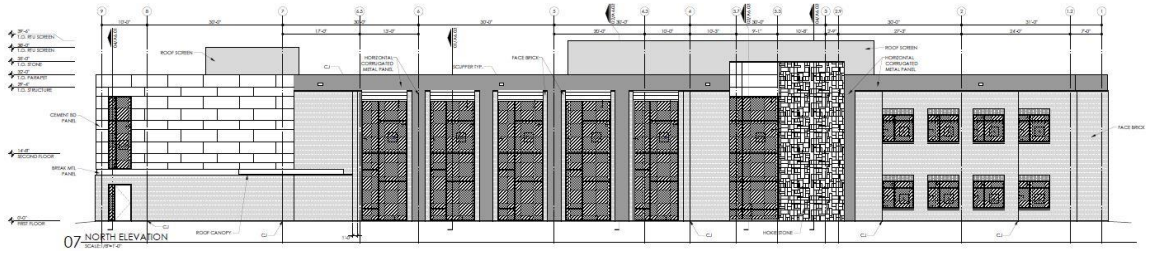

Figure 5-1: North elevation view of the VTCRC Rackspace Research Building

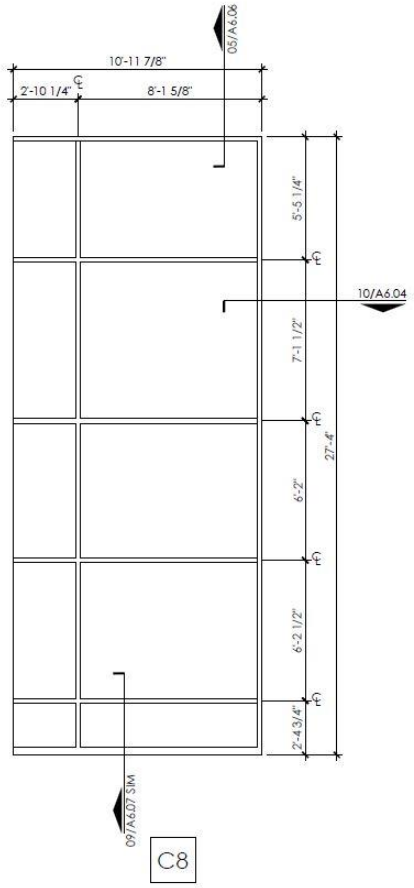

Figure 5-2: Detail drawing of selected curtain wall section on the VTCRC Rackspace Building

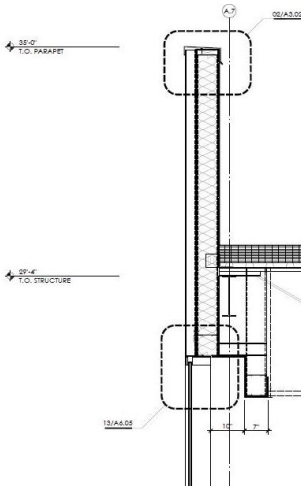

a) Top profile view of the selected curtain wall section

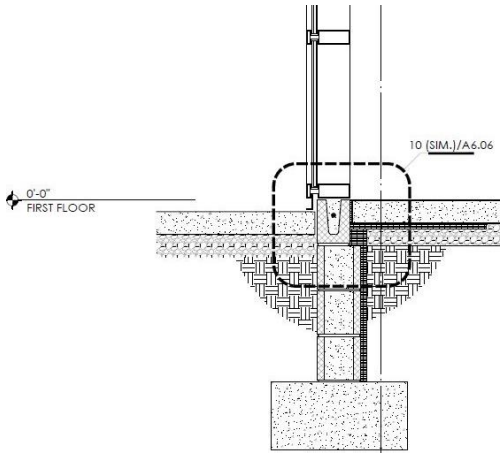

b) Bottom profile view of the selected curtain wall section

Figure 5-3: Profile views of perimeter connections from the selected curtain wall section

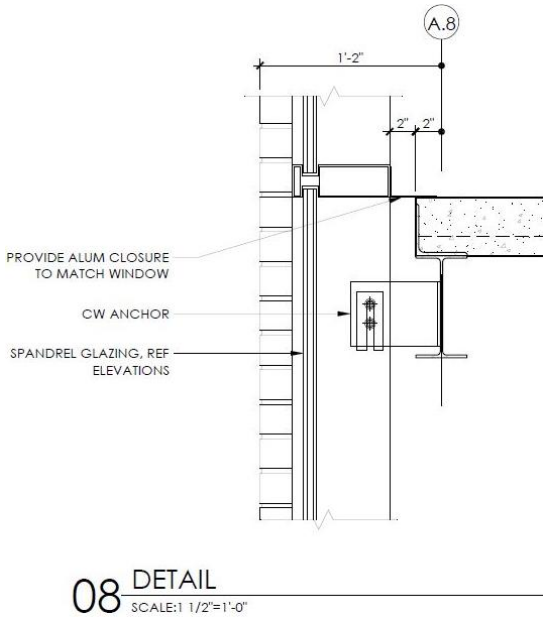

Figure 5-4: Profile view of steel anchor connections constructed on other curtain wall sections in VTCRC Rackspace Building

5.2.2. Description of Baseline Curtain Wall Design

Based on the VTCRC Rackspace Building's detailed drawings described above, a 14 ft. x 14 ft. (4,266 mm x 4,266 mm) section of glass curtain wall, using the Kawneer 1600 CW system, was designed as shown in Figure 5-5. This CW was designed to represent a mid-span section (i.e. not near a structure's perimeter/corners) at any story of a building (i.e. low-, mid-, or high-rise) with a story height of 14 ft. (4,266 mm). The design includes a 3 panel high by 3 panel wide CW section which contains 4 different glass sizes which are representative of what was shown in the case study curtain wall. The vertical mullions extended past the top and bottom transom members by 200 mm to replicate conditions used in the validated model and the AAMA racking test standards. But similar to the validated model, this added length was not added to the vertical pressure plates.

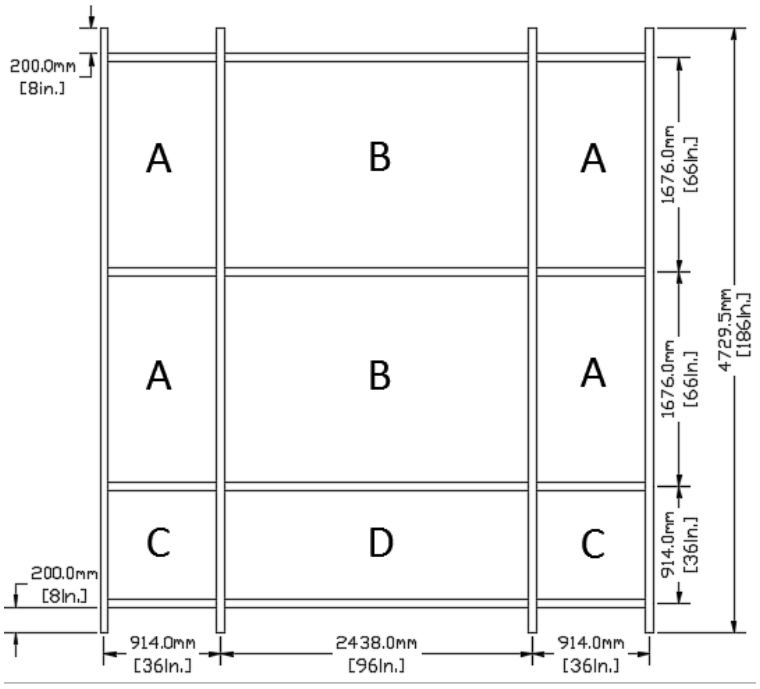

Figure 5-5: Elevation view of baseline curtain wall designed for fragility curve development study

Since the validated model was based on the Kawneer 1600 CW system, the baseline CW contained the same dry-glazed configurations as well. Because this was a multi-panel section, both perimeter ("L" shaped) and intermediate (flat) pressure plates from Kawneer 1600 CW were implemented as well. This means the perimeter pressure plate configuration (includes perimeter, fixed glazing, and thermal gaskets) were used along the perimeter mullions/transoms within the baseline CW. The intermediate pressure plate configurations (includes only thermal and fixed glazing gaskets) were used with the intermediate mullions/transom members holding glass panels on both sides, similar to what was done in the small scale experimental test study in Chapter 3. Furthermore, it was determined that the geometric/configuration calibrations (i.e. dimension changes made to glass panel and side blocks and changes made to glass-to-frame clearances) implemented with the validated CW model will not be included throughout the larger baseline CW design. These geometric calibrations were considered appropriate only for the validation of the 6'x5'CW unit configuration to better match the Shirazi (2005) experimental results. As such, the baseline CW design incorporated 11 mm glass-to-frame clearances on all four sides of each glass panel. This lead to the glass panel dimensions as shown in Table 5-1 for each panel illustrated in Figure 5-5.

Table 5-1: Dimensions of glass panels included in baseline CW design

	Dimensions [H x W x t]	
Glass Panel ID	mm	in.
A	1,636.5 x 874.5 x 6	64.42 x 34.42 x 0.25
B	1,636.5 x 2,398.5 x 6	64.42 x 94.42 x 0.25
C	874.5 x 874.5 x 6	34.42 x 34.42 x 0.25
D	874.5 x 2,398.5 x 6	34.42 x 94.42 x 0.25

Incorporating a larger CW section also brought about the opportunity to observe the effects that steel anchor connections have on the performance of curtain wall systems as constructed in the field. According to the literature, actual CW system-to-steel anchor connection performance has not been included in most experimental and analytical research, which used either fixed or pinned connections, respectively. This study therefore sought to analyze CW system-to-steel anchor connection performance with the larger CW model generated. As such, an anchored connection was designed and modeled which would connect the baseline CW framing system to the structural system (i.e. top and bottom floor slab in this case) at the top and base of each vertical mullion. The final design of the steel anchor connections includes 2L-5”x3”x1/4” steel angles at each mullion connection location (i.e. top and base of each vertical mullion). An example of the CW system-to-steel anchor connection at the base is shown in Figure 5-6. While not shown, the CW system-to-steel anchor connection at the top is similar in design. The steel angle design was checked using design criteria from the AISC Steel Construction Manual (AISC 2017) which included: bolt shear, net shear, and bolt limits (i.e. bearing, tear-out and bolt shear). The design criteria were used primarily to design the angle-to-CW frame connection. To obtain the required design loads, the “Exterior Non-Structural Wall Element Connections” example from the 2012 IBC SEAOC Structural/Seismic Design Manual, Vol. 1 (SEAOC 2013) reference was followed to obtain the seismic out-of-plane load (i.e. approx. 0.40 x weight of CW tributary to connection) and the in-plane dead load (i.e. weight of CW tributary to connection). Even though these would not be included in the model, the final design accounted for using 1/2” bolts with a 1.5 in. c-c spacing as shown in Figure 5-6. Lastly, based on conversations with Kawneer and review of the case study, the locations

of the steel anchor connections (i.e. at top and base of each vertical mullion) were all placed below the horizontal transoms in this baseline CW section as shown in Figure 5-6. This meant that the transom members were level with the structural system (i.e. floor slabs) in this design.

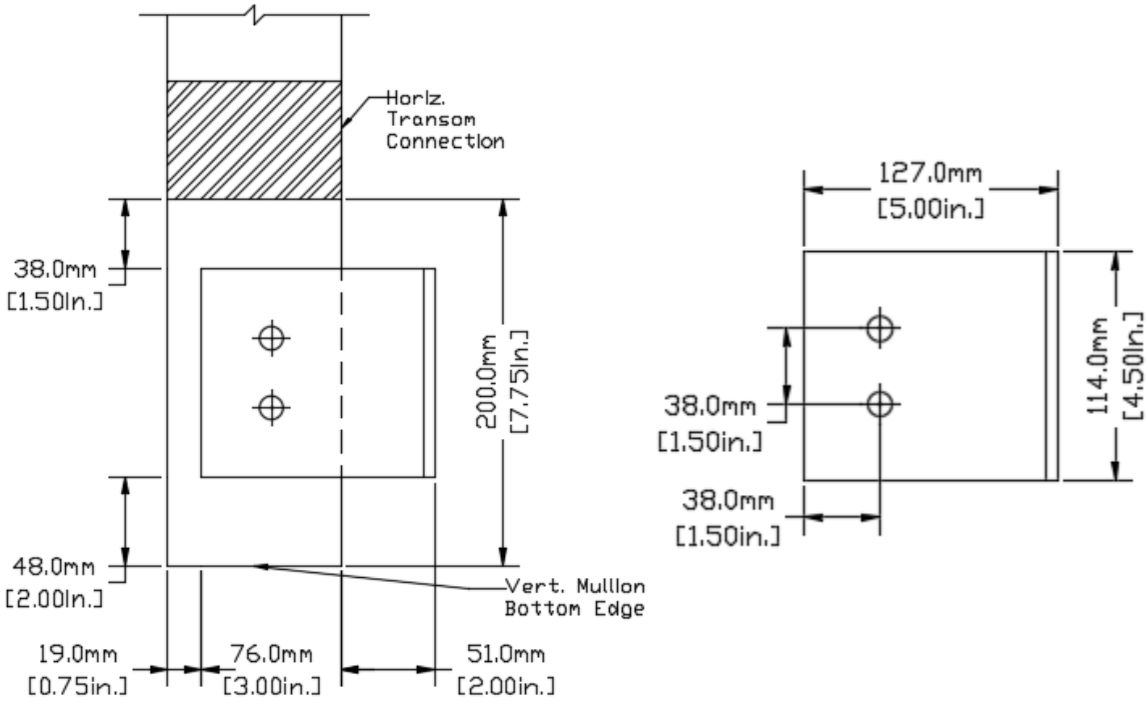

a) Example of an elevation view of CW frame system-to-steel anchor connection at the base of the baseline CW section

b) Elevation view of 5”x3”x1/4” steel angle shape designed for steel anchor connection

Figure 5-6: Detail drawings of designed CW system-to-steel anchor connections

5.2.3. Research Plan for Baseline CW Section Configuration Changes

A set of baseline CWs with configuration changes were also considered for the last stage of analysis to observe how different configurations perform when subjected to the

loading simulations. Three different configuration parameters were specifically changed to represent what an engineer may have originally designed for. And how the final constructed system may end up looking like due to either poor construction or different installation methods. These parameters included changes to: 1) the equivalent clamping load (due to changes in screw torque applied to the screws); 2) the glass panel thickness; and 3) the glass-to-frame clearances (still equal on all four sides). Including the original baseline CW model, there were 11 CW section configurations designed and modeled to be subjected to both loading simulations as shown in Table 5-2. CW models #2-#10 will have configuration changes based on the designed baseline CW model #1 described in the previous section. Some components of the original Kawneer 1600 CW system were also redesigned to accommodate these parameter changes to models #5-#11. As will be discussed in the next FE modeling section, these were considered likely and appropriate component design changes after discussions with Kawneer representatives.

Table 5-2: List of FE curtain wall models generated containing different configuration parameters

	Configuration Parameter		
Model #	**Equivalent Clamping Load (N)**	**Glass Panel Thickness (mm)**	**Glass-to-Frame Clearance (mm)**
1-Baseline	**1800**	**6**	**11**
2	1530	6	11
3	2070	6	11
4	2340	6	11
5	1800	13	11
6	1800	19	11
7	1800	25	11
8	1800	6	3
9	1800	6	6
10	1800	6	16
11	1800	6	19

5.3. Description of FE Models and Analysis Simulations for Large Scale CW Section

This sections presents the description of the FE model generated for the baseline CW section and the simulation protocol implemented for the in-plane and out-of-plane loadings. Descriptions were also made of each configuration change made to the baseline CW section to incorporate the different parameters summarized in Table 5-2 for each additional models.

5.3.1. Generated FE Model and Simulations Implemented for Baseline CW Section

Using the design for the one story baseline CW section as shown in Figure 5-5, the same FE modeling approach from the validated single unit CW model in Chapter 4 was also followed for the baseline CW model generated. However, no geometrical/configuration calibrations were used in this baseline model: a constant 11 mm glass-to-frame clearance was established on all four sides of every glass panel with 11mm setting/side blocks as well. The additional components in this model included the intermediate (flat) pressure plate as used in Chapter 3, and the steel angles for the anchor connections as designed in Figure 5-6. The intermediate pressure plates were modeled the same as the perimeter (“L” shaped) pressure plates (i.e. partitions necessary for equivalent clamping load application and element mesh type) but with a constant thickness of 2.3mm as shown in Figure 5-7.

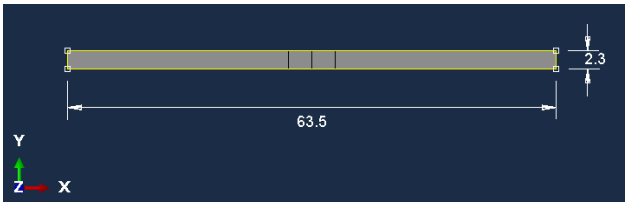

a) Intermediate pressure plate cross-section dimensions in ABAQUS

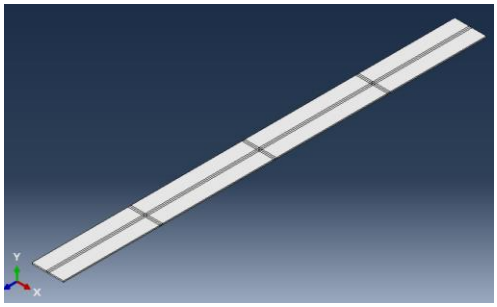

b) Example of intermediate pressure plate extrusion with partitions

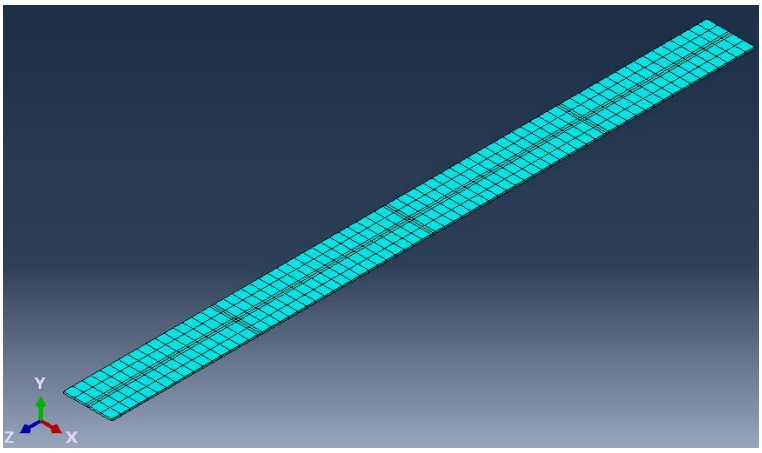

c) Example of isometric view of meshed intermediate pressure plate member in ABAQUS

Figure 5-7: Generated intermediate pressure plate model in ABAQUS for baseline CW section

The steel angles were modeled as a solid part with cross section dimensions shown in Figure 5-8. Partitions were made on the angle's legs which established the center line of each bolt hole location. Since no bolt holes were generated, these partitions help to divide the member into sections which will be used for constraints and contact interactions to represent a bolted connection. The angles were meshed with SC8R conventional shell elements and had a global element mesh size of 14 mm x 14 mm as shown in Figure 5-8. Five Gauss points through the thickness of each element was used because only one element through the thickness of the angle's legs was necessary. The nominal elastic-

plastic steel material properties for the angle members are presented in Table 5-3. All other components of the baseline CW were modeled using the same modeling procedures in Chapter 4.

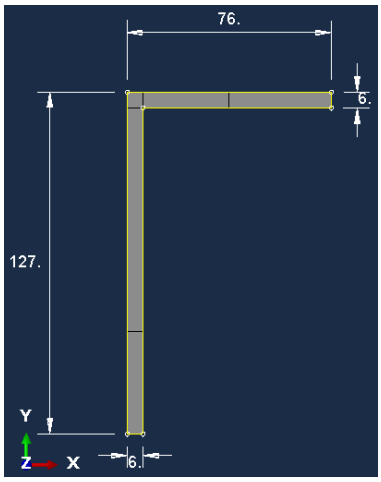

a) Steel angle (5”x3”x1/4”) cross-section dimensions in ABAQUS

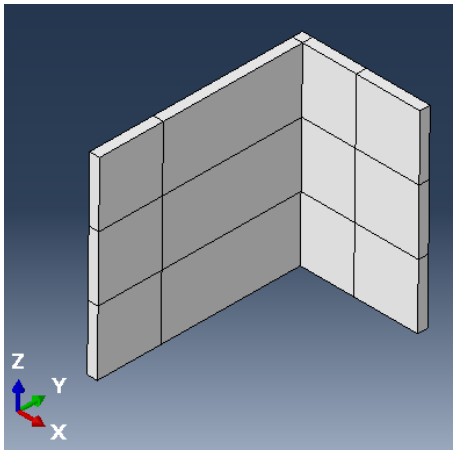

b) Isometric view of steel angle extrusion with partitions

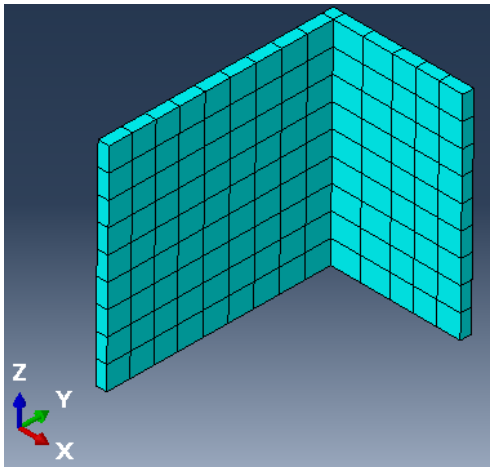

c) Isometric view of meshed steel angle in ABAQUS

Figure 5-8: Illustrations of generated steel angle (5”x3”x1/4”) designed for baseline CW

Table 5-3:Nominal ASTM A36 Steel Material Properties

Modulus of Elasticity [MPa]	2.00E+05
Poissons's Ratio	0.26
Density [tonne/mm^3]	7.80E-09
Stress [MPa]	**Plastic Strain**
250	0
1250	1

The rest of the components based on the designed baseline CW in Figure 5-5 were generated using the same FE modeling approaches described in Chapter 4. This led to the full scale baseline CW model as shown in Figure 5-9, which includes the new intermediate pressure plates and the steel angles located at the top/bottom of each vertical mullion as designed.

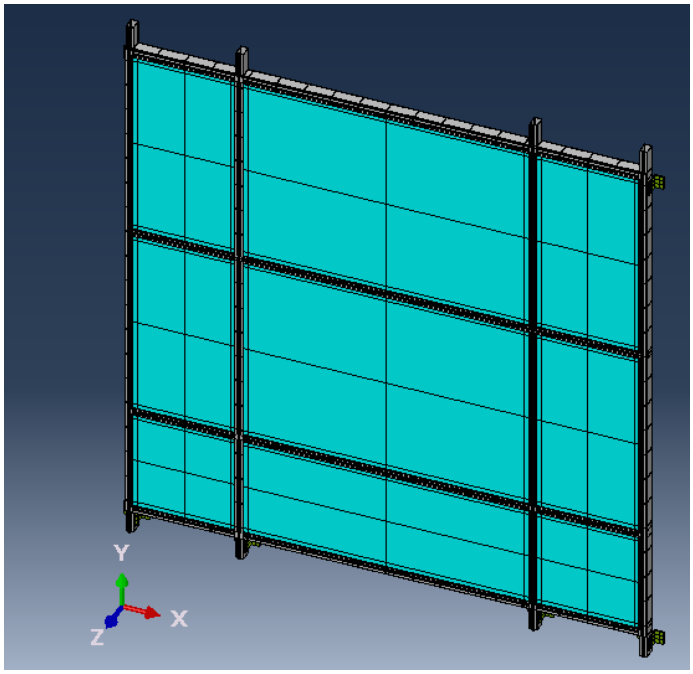

Figure 5-9: Isometric view of baseline CW model generated in ABAQUS

While all the same contact interactions and constraints methods used for modeling component interactions were the same in the baseline CW model, two new interactions/constraints were added for the mullion-to-steel angle interactions. To obtain a bolted connection that is similar to what is constructed in the field (i.e. semi-rigid connection), a tie constraint between the mullion and a section of the angle leg (between the center-to-center spacing of the bolt locations) were used as shown in Figure 5-10. For the angle leg surface region that was not selected for the tie constraint, an interaction contact pair was implemented as shown in Figure 5-10. For this mullion-to-angle interaction contact pair, the tangential and normal mechanical contact properties were defined as frictionless and "Hard" contact, respectively. These mechanical properties were similar to what were defined in the setting/side block-to-glass interaction contact pairs in Chapter 4 Section 4.5.2.4. The use of both tie constraints and interaction contact pairs for the mullion-to-angle connections would allow for connection flexibilities that were not typically modeled in previous analytical models or experimental tests.

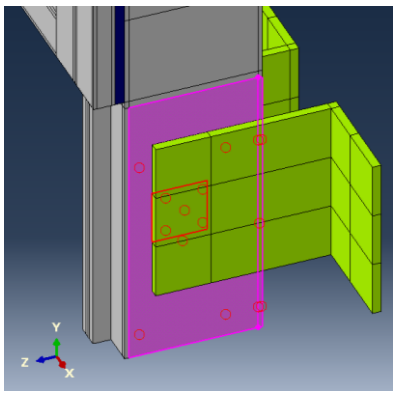

a) Example of mullion-to-angle tie constraints with master-slave (red-purple) surface regions selected

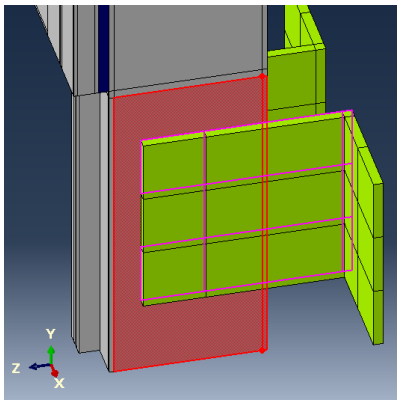

b) Example of mullion-to-angle interaction contact pairs with master-slave (red-purple) surface regions selected

Figure 5-10: Tie constraints and interaction contact pairs implemented at the mullion-to-angle surfaces to model bolted connections

5.3.1.1.In-Plane Simulations for the Baseline CW Model

With ABAQUS/Standard, the same non-linear static stress analysis procedure implemented for the single CW model in-plane simulation was similarly implemented for each loading simulation subjected on the baseline CW model in this chapter. However, there were some changes to this simulation procedure which are described here for both simulation scenarios.

For the in-plane displacement simulation, the same 5 analysis steps (i.e. initial conditions step and 4 analysis steps) summarized in Table 4-6 were generated. The same boundary conditions listed in Table 4-8 were also used on the same components with exception to the vertical mullion base restraints (since steel angles are used now) and the application of the racking displacement. Restraints to the translational DOF's (U1=U2=U3=0mm) were applied to the back leg surfaces of all the base steel angles through all 5 analysis steps as shown in Figure 5-11. A kinematic coupling constraint was used to couple the translational motions of the back leg surfaces on all the top steel angles to one reference node as shown in Figure 5-11. To simulate the flexible anchor connection fixities to the structural system of a building (as opposed to the fixed connections in the experiments) the racking displacement boundary condition applied to the reference node was as follows: 1) restrain all DOF's (U1=U2=U3=0mm; UR1=UR2=UR3=0rad.) from the initial step to the fourth step (i.e. BC-Change); 2) during the fifth step the restraints on DOF's U2, UR1 and UR3 were released and the racking displacement was applied in the

+x direction up to U1=152mm (6 in.) as shown in Figure 5-11. Additional boundary conditions (U2=0mm) were also strategically applied to the side face surfaces of some of the vertical fixed gaskets and side blocks, as shown in Figure 5-11, to prohibit excessive distortions during the racking displacement step.

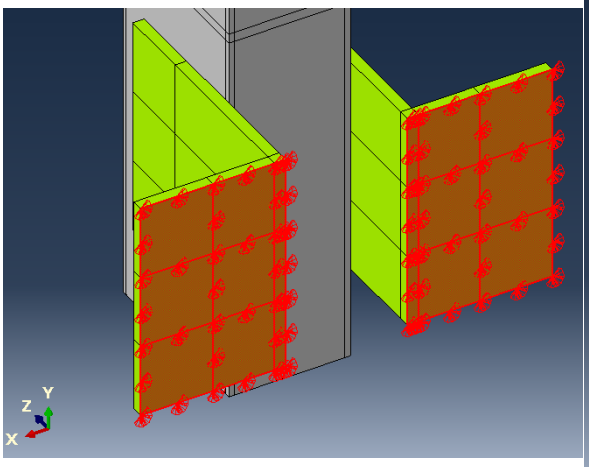

a) Example of surfaces selected for boundary conditions applied to each base angle

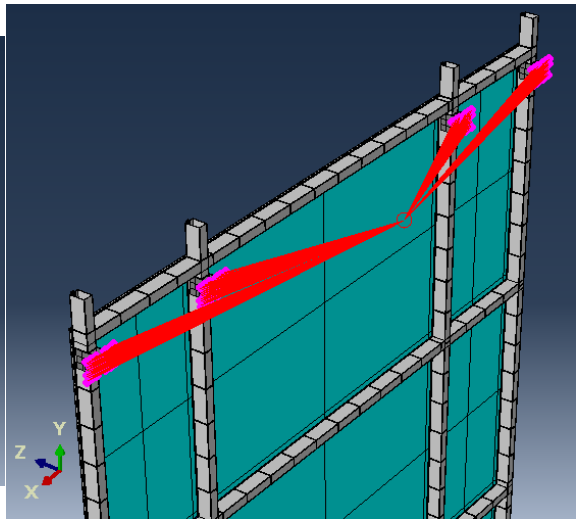

b) Example of kinematic coupling constraint applied to the back surfaces of top angles required for application of racking displacement

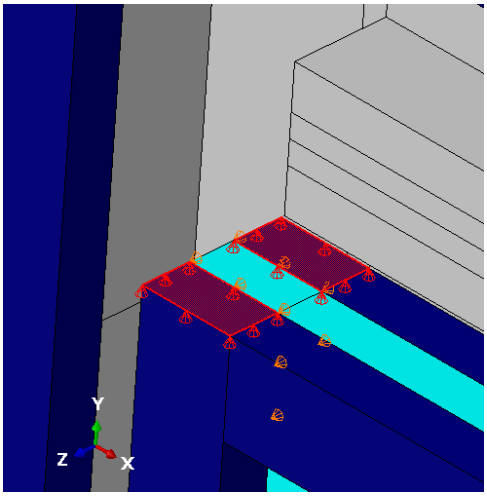

c) Example of additional boundary conditions added to the side surfaces of the vertical fixed glazing gaskets

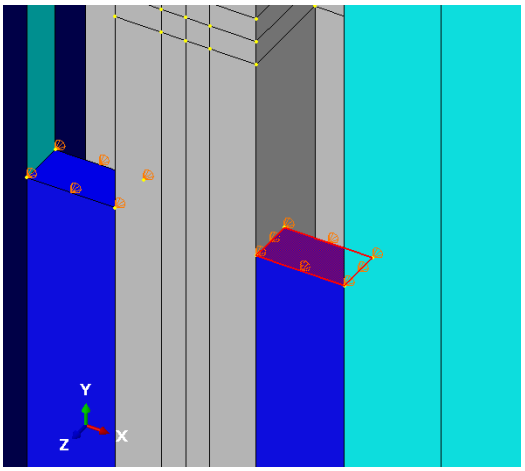

d) Example of additional boundary conditions added to the side surface of a side block

Figure 5-11: Boundary conditions changed/added for the in-plane simulations of the baseline CW model

5.3.1.2.Out-of-Plane Simulations for the Baseline CW Model

Since the single CW model was also validated for the out-of-plane simulations in Chapter 4, the baseline CW model will implement the following for the out-of-plane simulation. All 5 analysis steps generated for the in-plane baseline CW model described previously, and summarized in Table 4-6, were also generated for the out-of-plane simulation. However, the last analysis step will be affected because a static uniform pressure will now be applied instead of the racking displacement.

As such, certain boundary conditions applied to the baseline CW model during the in-plane simulation described previously were also affected. This meant removing all the boundary conditions that were applied to the rubber components (i.e. gaskets and setting/side blocks) to allow them to displace/rotate out-of-plane. Also, the boundary condition and kinematic coupling constraint used to apply the racking displacement to the top angles were removed. Instead, boundary conditions to restrain all the translational DOF's (U1=U2=U3=0mm) were applied to the back leg surface of each of the top angles, just like the base angles shown in Figure 5-11. This was done to simulate the curtain wall being attached to the structural system of a building which was assumed to have negligible out-of-plane drift during a static pressure application. Therefore, only the boundary conditions at the base angles, the pre-contact/pre-contact-wire selections and the glass panel sides were kept the same from the in-plane baseline model to this out-of-plane model.

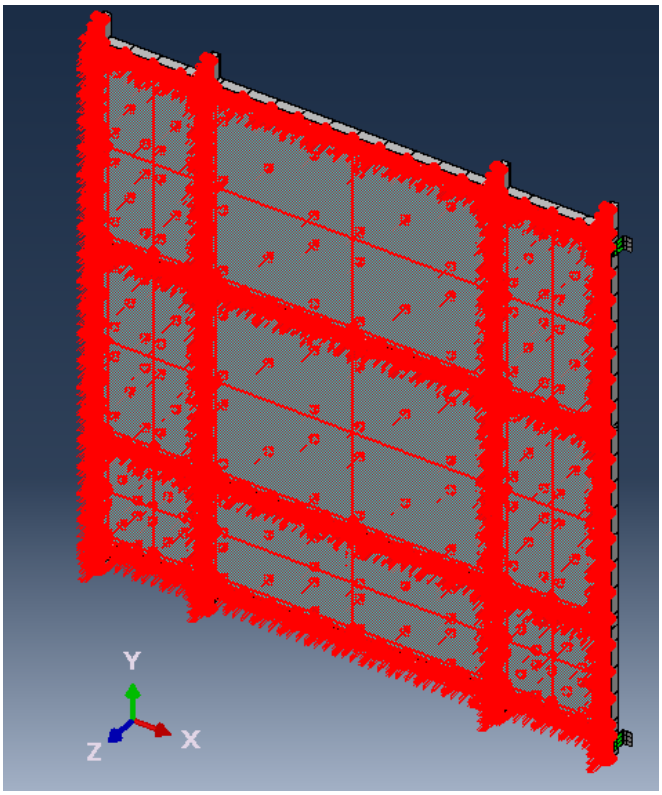

Figure 5-12: Illustration of surfaces selected for the application of the static uniform pressure of 0.005MPa

No other changes were made to the rest of the modeling approaches implemented for the in-plane baseline CW simulations in this out-of-plane simulation such as: component interactions/constraints, semi-rigid transom-mullion framing connections, and equivalent clamping load application. In the last simulation analysis step, a static uniform pressure linearly increasing up to 0.005MPa (0.725psi) was applied in the –z-axis direction to all the exterior surfaces of the baseline curtain wall model. As shown in Figure 5-12, these surfaces included the pressure plates, exposed vertical mullions, and the vision areas of the glass panels (i.e. glass surfaces not covered in the glazing pocket underneath the pressure plates).

5.3.2. Configuration Changes Implemented on Baseline CW Model

To proceed with generating the other set of CW models which apply the three different parameter changes summarized in Table 5-2, there were some changes made to the generated baseline model (the control model). These baseline CW configuration changes are described in this section for each of the 10 new large scale section CW models that were subjected to the in-plane displacement and out-of-plane pressure simulations overviewed previously.

5.3.2.1. Description of CW Models #2 - #4 for Change in Equivalent Clamping Loads

Three different total equivalent clamping loads were analyzed for these set of large CW models. As described in Chapter 4, the original total equivalent clamping load of 1,800 N was applied at screw locations along the pressure plates (at 229 mm center to center spacing) by being distributed equally among each set of nine nodes with concentrated loads. The same procedure was completed for the new total equivalent clamping loads identified in Table 5-2 for CW models #2 - #4.

5.3.2.2. Description of CW Models #5 - #7 for Change in Glass Thicknesses

Glass thicknesses were only increased for this study in CW models #5 - #7. No changes were made to the other components within the glazing pocket configurations such as the fixed glazing gaskets and perimeter gaskets. However, to accommodate gaps made due to the glass thickness being increased in each CW model, changes were made to the

cross section dimensions of the: perimeter pressure plates, thermal gaskets and setting/side blocks. In general, an increase to one of the legs on the perimeter pressure plates was incorporated such that it would still be in contact with the perimeter gaskets fixed to the mullions. For instance, if the glass was increased up to 13mm (CW model #5), then the difference between the new thickness to the original 6mm thickness (baseline CW model) was added to the length of this leg in the pressure plate as shown in Figure 5-13. This difference in thickness was also added to the height of the thermal gaskets also shown in Figure 5-13. Finally, the width of all the setting/side blocks were changed to match the thickness of the glass in each model. After these component dimension changes were made, the meshing and partitioning process used for the baseline CW was completed for each of the new CW models in this parameter set.

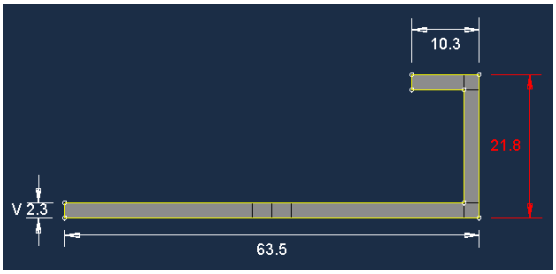

a) Example of length increase applied to leg of perimeter pressure plate in CW model #5

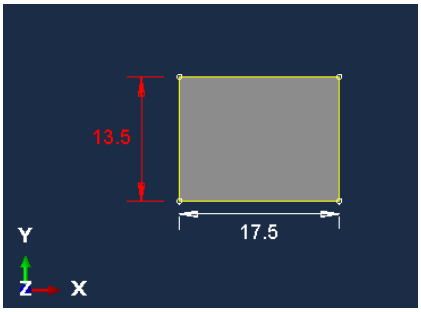

b) Example of height increase applied to thermal gaskets in CW model #5

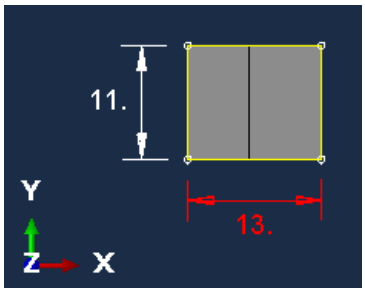

c) Example of width increase applied to setting/side blocks in CW model #5

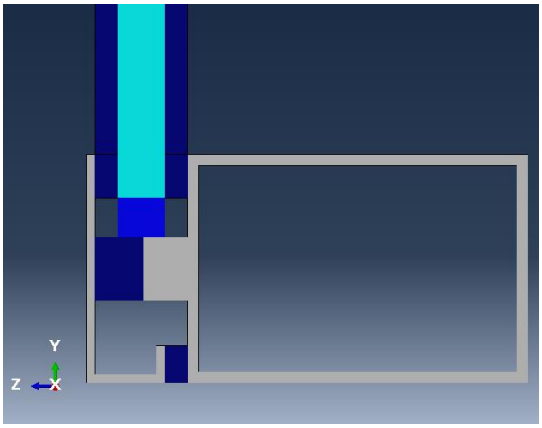

d) Example of new perimeter configuration profile view in CW model #5

Figure 5-13: Examples of component configuration changes made to the CW models generated for the glass thickness increase parameter

Using the CW model #5 configuration as an example, the new cross section for the CW framing members should have the setting/side blocks resting on both the thermal gaskets and mullion lip as shown in Figure 5-13. To make sure this did not affect the glass panel rotations/translations in the glazing pocket, all the setting/side blocks had a partition added through the center so that half of the middle bottom surface was tied constrained to the mullion lip as shown in Figure 5-14. The other half of the middle bottom surface had a rubber-to-rubber interaction created which simulated the mechanical contact properties of frictionless and “Hard” contact as shown in Figure 5-14.

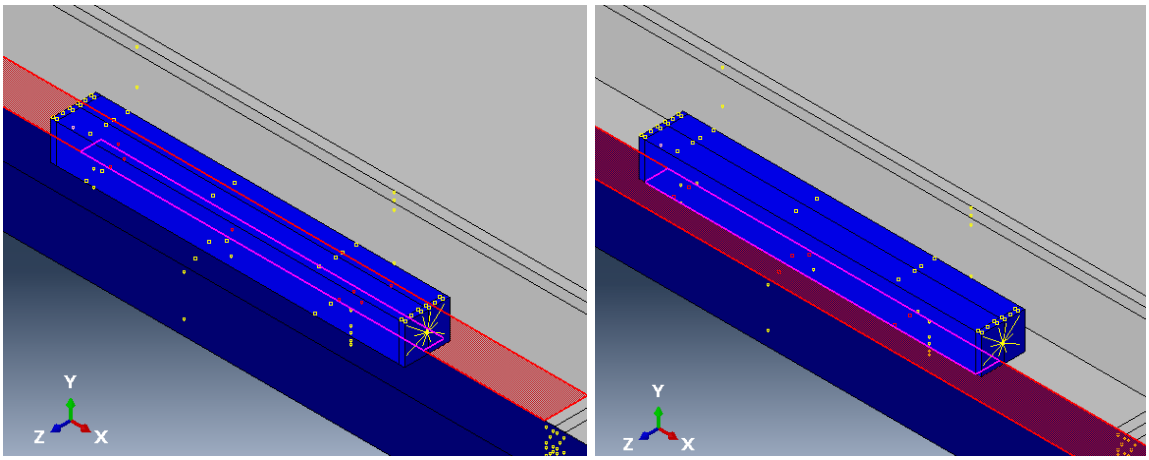

a) Example of setting/side block-to-aluminum mullion lip tie constraints in the CW model #5

b) Example of setting/side block-to thermal gasket interaction contact pair in the CW model #5

Figure 5-14: Illustrations of modeling tie constraints and interaction contact pairs for the setting/side blocks in the CW models generated for the glass thickness increase parameter

It is important to note that even though all the glass panel thicknesses were increased, only one element through the thickness was generated. Also, the glass-to-frame general contact interactions were not changed. This meant only the glass-to-frame contact interactions were modeled when the back half of the glass came into contact with the mullion lip during the in-plane simulation. However, no glass-to-rubber contact interaction was modeled between the thermal gaskets and the glass side. This meant no stress distribution was modeled and analyzed once the clearance between the glass and the thermal gasket was closed. This is because it was assumed that the primary contribution to the CW's lateral resistance during glass-to-frame contact stages was mainly between the mullion lip and the glass contacts.

5.3.2.3.Description of CW Models #8 - #11 for Change in Glass-to-Frame Clearances

Both decreases and increases to the glass-to-frame clearances were made to CW models #8 - #11. To achieve the glass-to-frame clearances listed in Table 5-2, the glass panel dimensions in the baseline CW model were changed to obtain the new clearances on all four sides of each panel. The glass panels would still follow the same meshing procedure implemented in the baseline CW model to get a refined mesh along the perimeter of the glass (at a 50mm offset), and a coarser mesh near the center glass regions. This was done so that no matter the glass size/position, the glass cracking stress would still be determined at the same corner element locations identified in Chapter 4 for consistency.

Additionally, the heights of the setting/side blocks for each CW model were appropriately decreased or increased to establish these different glass-to-frame clearances in Table 5-2. Because of the glass dimension increases/decreases for each model, the setting blocks were relocated so they always would rest at the quarter points at the base of the newly dimensioned glass panel. The meshing, kinematic coupling constraints, and interactions/constraints implemented in the baseline CW model for these blocks were otherwise kept the same as in Chapter 4.

For the CW models that had decreased glass-to-frame clearances, the glass panels would extend past the width of the fixed glazing gaskets as shown in Figure 5-15. However, for the models which increased the glass-to-frame clearances (by decreasing the glass panel dimensions), the widths of the fixed glazing gaskets were decreased as well so that no gasket overhangs were present along the glass edges as shown in Figure 5-15. While this was done to represent a configuration which could have been designed by an engineer, the

width of the gaskets could have been kept unchanged. This would represent the case where in construction the glass manufactured was smaller than required which is another case of an increased glass-to-frame clearance configuration not looked at in this study.

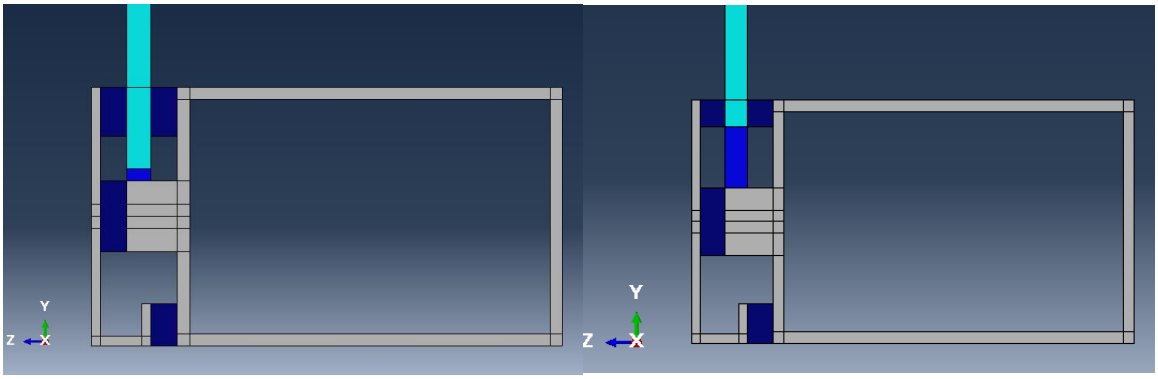

a) Example of CW cross section profile view with a decreased glass-to-frame clearance configuration in the CW model #8

b) Example of CW cross section profile view with an increased glass-to-frame clearance configuration in the CW model #10

Figure 5-15: Illustrations of the CW cross section profile views with different glass-to-frame clearance configurations in the CW models

While the widths of the fixed glazing gaskets for CW models #10-#11 were decreased, the number of elements through the thicknesses (in both orthogonal directions) of the gasket cross sections were still kept to two, as shown in Figure 5-16. This was to ensure that enough elements were generated to capture bending, even if the width of the fixed glazing gaskets were decreased.

The last change made to the models with the increased glass-to-frame clearance configurations (CW models #10-#11) was to adjust the lengths of the vertical fixed glazing gaskets. These lengths were decreased to make sure they were aligned with the height of the glass dimensions that were decreased as shown in Figure 5-16. This was done to follow

the same approach used in the single CW unit modeled in Chapter 4. This length modification was not implemented in CW models #8-#9 since it would not make sense to extend the vertical fixed glazing gasket past the horizontal fixed glazing gaskets to align with the increased height of the glass panels.

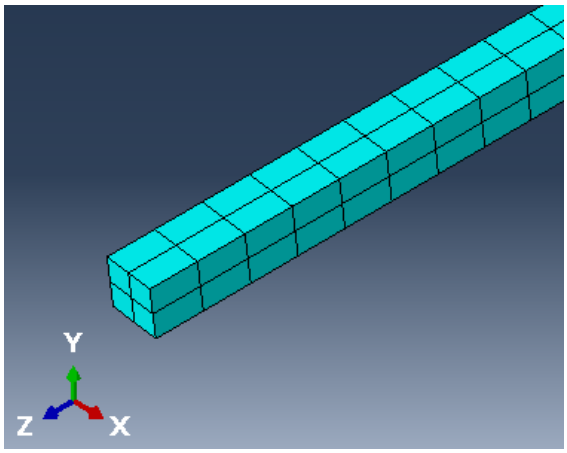

a) Example of the mesh for fixed glazing gaskets for the increased glass-to-frame clearance configuration in the CW model #10

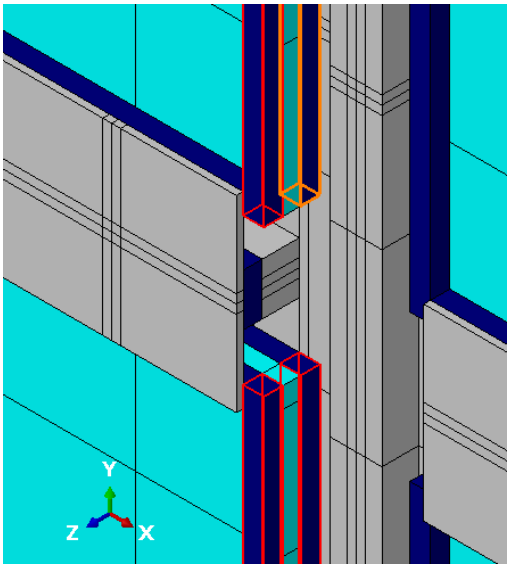

b) Example of the adjusted length of vertical fixed glazing gaskets for the increased glass-to-frame clearance configuration in the CW model #10

Figure 5-16: Illustrations of additional modifications required for the increased glass-to-frame clearance configurations in CW models #10-#11

5.4. Curtain Wall Simulation Observations and Related Damage States

In the literature review, several in-plane and out-of-plane damage states (DS) were observed to occur during experimental racking displacement tests and uniform pressure tests, respectively. A summary of these reviewed structural DS and their descriptions due to these test protocols is shown in Table 5-4 and Table 5-5. Based primarily on the typical

glass CW serviceability limit states shown in Table 5-4 and Table 5-5, several key structural damage states that the CW models were able to approximate in this analysis were then identified for this study. These identified structural DS included: 1) initial glass-to-frame contact (in-plane only); 2) initial glass cracking; 3) glass/frame breaches; 4) yielding of aluminum mullions; and 5) yielding of steel anchors.

Table 5-4: Summary of Experimental Seismic Related (In-Plane) Damage States Observed in the Literature Review

In-Plane Damage States (DS)	
DS Name	**DS Description**
Glass Cracking	**Serviceability limit state:** Thru-thickness cracking/crushing in the vision/non-vision areas
Glass Fallout	**Ultimate limit state:** Glass fragments >1 in^2 fallout
Gasket Degradation	**Serviceability limit state (Dry-glazed):** (1) gasket distortion (2) gasket pull-out (3) gasket push-in and (4) gasket shifting
Seal Degradation	**Serviceability limit state (Wet-glazed):** (1) sealant elongation/distortion (2) sealant tearing and (3) sealant cohesive/adhesive failures
Framing Damage	Transom-mullion connection (shear block attachment) damages; plastic deformations/gouging within glazing pocket (mullion lip); frame member twisting
Glass Pullout	Glass panel pops out of glazing pocket; can occur due to glass buckling or loss of clamping force along pressure plates
Frame Dislodging	Unitized CW panel units unhinge along the male/female framing joints

Table 5-5: Summary of Experimental Hurricane Related (Out-of-Plane) Damage States Observed in the Literature Review

Out-of-Plane Damage States (DS)	
DS Name	**DS Description**
Glass Cracking	Thru-thickness cracking/crushing of glass
Glass Fallout	Glass fragments falling out
Complete Glass Failure	Complete blow out (fracture) of glass
Gasket Degradation	(1) gasket distortion (2) gasket pull-out
Seal Degradation	(1) sealant elongation/distortion (2) sealant cohesive/adhesive failures
Frame/Anchor Damage	Complete failure of these components; primarily due to poor installation/inadequate design
Glass Pullout	Glass panel pops out of glazing pocket; can occur due to glass buckling or excessive glass deflection
Delamination of Laminate Glass	PVB interlayers tear; delamination of outer glass lites from the PVB interlayer

To properly determine the identified structural damage states for this study from the CW model simulations, in-plane and out-of-plane CW structural responses were analytically observed during post processing of the analysis results. Each of the identified analytical observations were then directly linked to the occurrence of the identified key structural damage states for the in-plane and out-of-plane simulations. These analytical observations to structural damage state relationship links are shown in Table 5-6 and Table 5-7 for each loading simulation. In the following sections, the analytical observations in both tables are described in more detail.

It is evident through the literature review that the occurrence of these structural damage states has a negative impact on the curtain wall system's performance during and/or after an actual seismic or hurricane event. The performance measures specifically looked at in this study were based on the CW system's moisture resistance, air infiltration (condensation) resistance, and thermal performance. These were all related to the primary

elements that a CW system must protect against from penetrating/affecting the interior of a structure. As such, the occurrence of different levels of water penetration, air infiltration and thermal losses were identified and labeled as different non-structural damage states herein as shown in Table 5-6 and Table 5-7. The different levels of these non-structural damage states were identified as either primary or secondary within each CW performance measure. Primary non-structural damage states are defined as the immediate damages that may occur during or immediately after the natural hazard event has occurred once the related structural damage state has occurred. The secondary non-structural damage states are defined as the damages that may occur should repairs not be made in time before the next natural hazard event occurs. These non-structural damage states are directly linked to different structural damages states also defined in Table 5-6 and Table 5-7. As such, the following sections overview how each of the structural observations were made during post-processing to identify when seismic-related or hurricane related structural damage states have occurred.

Table 5-6: Seismic-Related (In-Plane) Damage States Observed in CW Model

Curtain Wall Observation	Type of DS	DS #	Structural Damage States (S)	DS #	Water Damage States (W)	DS #	Air (Condensation) Damage States (A)	DS #	Thermal Damage States (T)
Observation #1	**Simultaneous (SM)**	**1**	Initial Glass-to-Frame Contact [Serviceability Limit]	-	N/A	-	N/A	-	N/A
Observation #2	**Simultaneous (SM)**	**2**	Initial Glass Cracking [Serviceability Limit]	**1**	Primary DS (Low): Minimal local water damages, if any; Possibly leads to corrosion of glass and/or interior insulations	-	N/A	-	N/A
Observation #3	**Simultaneous (SM)**	**3**	Glass/Framing Breach [Serviceability Limit]	**2**	Primary DS (Low): Minimal water damages due to the occurance of rain during the actual hazard event Secondary DS (High): If gap is not repaired by the next rain cycle, an increase in water damages is expected	**1**	Primary/Secondary DS (High): Immediate concern (due to climate dependency)	**1**	Primary/Secondary DS (High): Immediate concern (due to climate dependency)
Observation #4	**Simultaneous (SM)**	**4**	Yielding of Steel Anchors [Serviceability Limit]	-	N/A	-	N/A	-	N/A
Observation #5	**Simultaneous (SM)**	**5**	Yielding of Aluminum Mulllions [Serviceability Limit]	-	N/A	-	N/A	-	N/A

Note: Naming Convention for any of the non-structural damage states: Water Damage State -Simultaneous-Primary/Secondary-DS Number = **W-SM-P-DS1.**
Note: Naming Convention for any of the structural damage states: Structural Damage State-Simultaneous-DS Number = **S-SM-DS1**

Table 5-7: Hurricane-Related (Out-Of-Plane) Damage States Observed in CW Model

Curtain Wall Observation	Type of DS	DS #	Structural Damage States (S)	DS #	Water Damage States (W)	DS #	Air (Condensation) Damage States (A)	DS #	Thermal Damage States (T)
Observation #1	**Simultaneous (SM)**	**1**	Glass/Framing Breach [Serviceability Limit]	**1**	Primary DS (High): Immediate water damages/leaks due to immediate hazard event Secondary DS (Low): Assuming profile yielding and/or permanent damage has occured	**1**	Primary/Secondary DS (Low): Minimal at this stage	**1**	Primary/Secondary DS (Low): Energy loss is minimal at this stage for temporary (elastic) wind loading
Observation #2	**Simultaneous (SM)**	**2**	Initial Glass Cracking [Serviceability Limit]	**2**	Primary DS (Low): Minimal local water damages, if any; Possibly leads to corrosion of glass and/or interior insulations	**-**	N/A	**-**	N/A
Observation #3	**Simultaneous (SM)**	**3**	Yielding of Steel Anchors [Serviceability Limit]	**-**	N/A	**-**	N/A	**-**	N/A
Observation #4	**Simultaneous (SM)**	**4**	Yielding of Aluminum Mulllions [Serviceability Limit]	**-**	N/A	**-**	N/A	**-**	N/A

Note: Naming Convention for any of the non-structural damage states: Water Damage State -Simultaneous-Primary/Secondary-DS Number = **W-SM-P-DS1.**
Note: Naming Convention for any of the structural damage states: Structural Damage State-Simultaneous-DS Number = **S-SM-DS1**

5.4.1. Analytical Observations Identified for Seismic-Related Damage States in CW Models

This section will summarize the different structural observations identified after the in-plane simulations have been completed for each CW model. Due to time constraints only CW models #1-#10 were simulated and analyzed. These post-processing analytical observations subsequently helped establish when each seismic-related damage state, shown in Table 5-6, had occurred during the in-plane racking displacement simulation.

5.4.1.1.In-Plane Analytical Observation #1

This identified in-plane observation is described as the initial glass-to-frame contact. This is when a corner from any of the glass panels within the entire glass curtain wall model has made the first glass-to-frame contact. This can occur between either side of a glass corner and the mullion lip inside the glazing pocket as shown previously in Figure 4-37.

5.4.1.2.In-Plane Analytical Observation #2

This observation is related to the first indication of the initial glass cracking stress being reached by one of the glass panels within the CW section. For this glass cracking stress criteria to be met, the minimum principal stress of at least 28.8 MPa must be observed

at two element locations. The specified element locations are at opposing corners along a diagonal of the glass as shown previously in Figure 4-38, which were earlier identified as key points of stress measurements taken in the experimental tests. Within the model, the obtained minimum principal stresses were located at the middle integration point within the continuum shell element (SC8R) as shown in Figure 5-17.

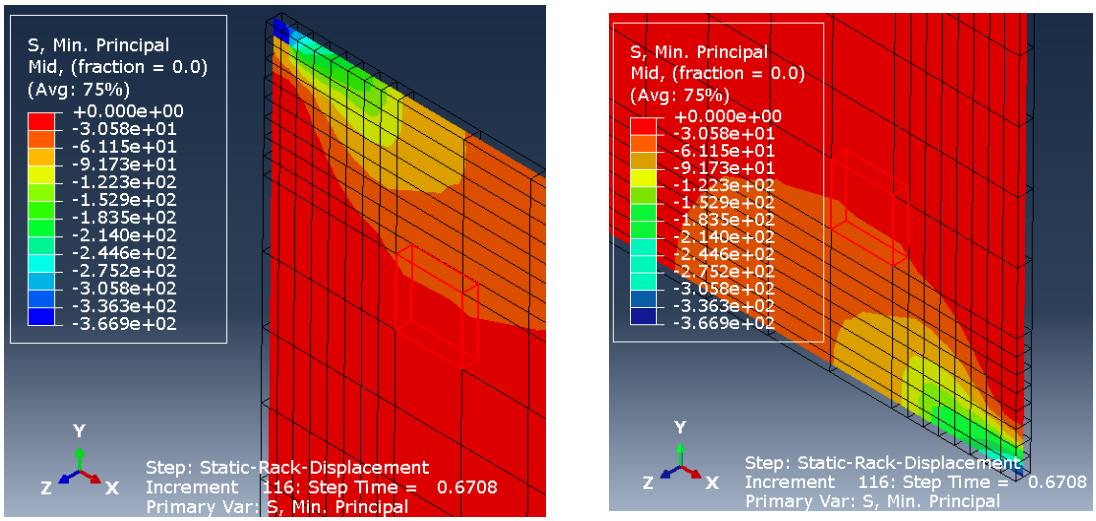

a) Example of element selected at top left corner for minimum principal stress output (at the middle integration point)

b) Example of element selected at bottom right corner for minimum principal stress output (at the middle integration point)

Figure 5-17: Illustrations of in-plane observation #2 glass cracking stress

5.4.1.3.In-Plane Analytical Observation #3

This is identified as the initial occurrence of an in-plane gap opening observed between any of the fixed glazing gaskets and glass panels present within the entire glass CW model. In order for this to be considered a full gap opening, the gap must be present through both exterior and interior fixed glazing gaskets and the glass panel as shown

previously in Figure 4-41. This gap will have occurred due to enough in-plane translations/rotations of the glass panel within the glazing pocket.

5.4.1.4.In-Plane Analytical Observation #4

The identified structural observation presented here is related to the first indication of yielding of the steel angles in the CW model. It was determined that this occurs once the average of the Von Mises stresses obtained along a column of elements (on the y-axis) of an angle leg, as shown in Figure 5-18, has reached greater than or equal to the nominal yield stress of A36 steel (σ_y=250 MPa). Since these angle legs were modeled with continuum shell (SC8R) elements, the Von Mises stresses obtained were at the exterior integration point location within the elements. These regions along the angles were observed to have the higher stress concentrations during in-plane loading of the CW model.

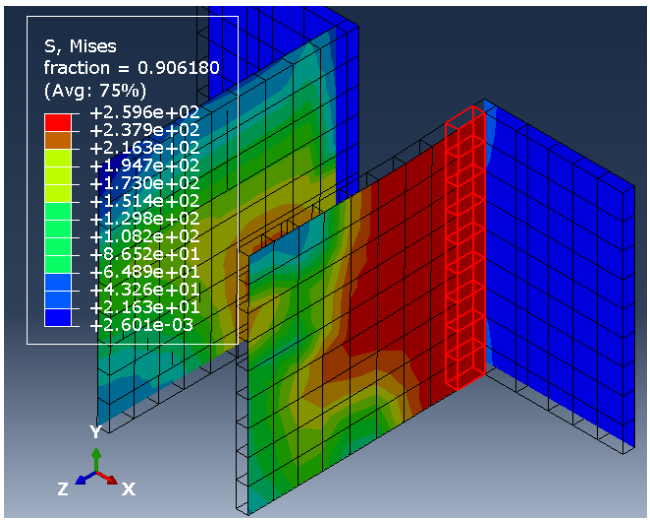

Figure 5-18: Example of in-plane observation #4 yielding of steel angles

5.4.1.5.In-Plane Analytical Observation #5

The identified structural observation presented here is related to the first indication of yielding of the aluminum mullions in the CW model. It was determined that this occurs once the average of the Von Mises stresses obtained along a row of elements (on the z-axis) of a mullion side wall, as shown in Figure 5-19, has reached greater than or equal to the nominal yield stress of aluminum 6063-T6 (σ_y=215 MPa). Since the thin side walls of the mullions were modeled with continuum shell (SC8R) elements, the Von Mises stresses obtained were at the exterior integration point location within the elements. These regions along the mullion side walls near the steel angles were observed to have the higher stress concentrations during in-plane loading of the CW model.

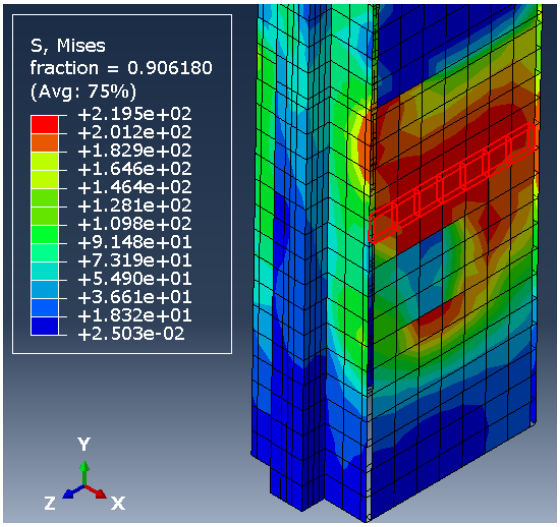

Figure 5-19: Example of in-plane observation #5 yielding of aluminum mullions

5.4.2. Analytical Observations Identified for Hurricane-Related Damage States in CW Models

This section will summarize the different analytical observations identified after the out-of-plane simulations have been completed for each CW model. The out-of-plane simulations were completed for all 11 CW model configurations (i.e. CW models #1- #11). These post-processing analytical observations subsequently helped establish when each hurricane-related damage state, shown in Table 5-7, had occurred during the out-of-plane uniform pressure simulation.

5.4.2.1.Out-of-Plane Analytical Observation #1

This out-of-plane observation is defined as the first indication of an out-of-plane gap opening present between the fixed glazing gaskets and the glass panels present within the entire glass CW model. Specifically, the gap must be present along the exterior surface of the glass panel and the entire surface height of the exterior fixed glazing gasket as shown in Figure 5-20. While gaps are present along all four sides of a glass panel throughout the pressure simulation, only the gap near the mid-span at the base of the glass panels were checked to simplify observations. Furthermore, to be considered a full gap opening the distance between the separated top edge of the fixed glazing gasket and the glass panel must be greater than or equal to 0.5mm. This is because gaps through the surface height of the fixed glazing gaskets were present even before the pressure was applied. These gaps then grow as the pressure loading is applied, more so on the top half of the exterior fixed glazing gasket. The distance is measured using one node on the glass surface and the nearest node on the fixed glazed gasket as shown in Figure 5-20. These gaps occur due to enough out-of-plane translations/rotations of the glass panel within the glazing pocket.

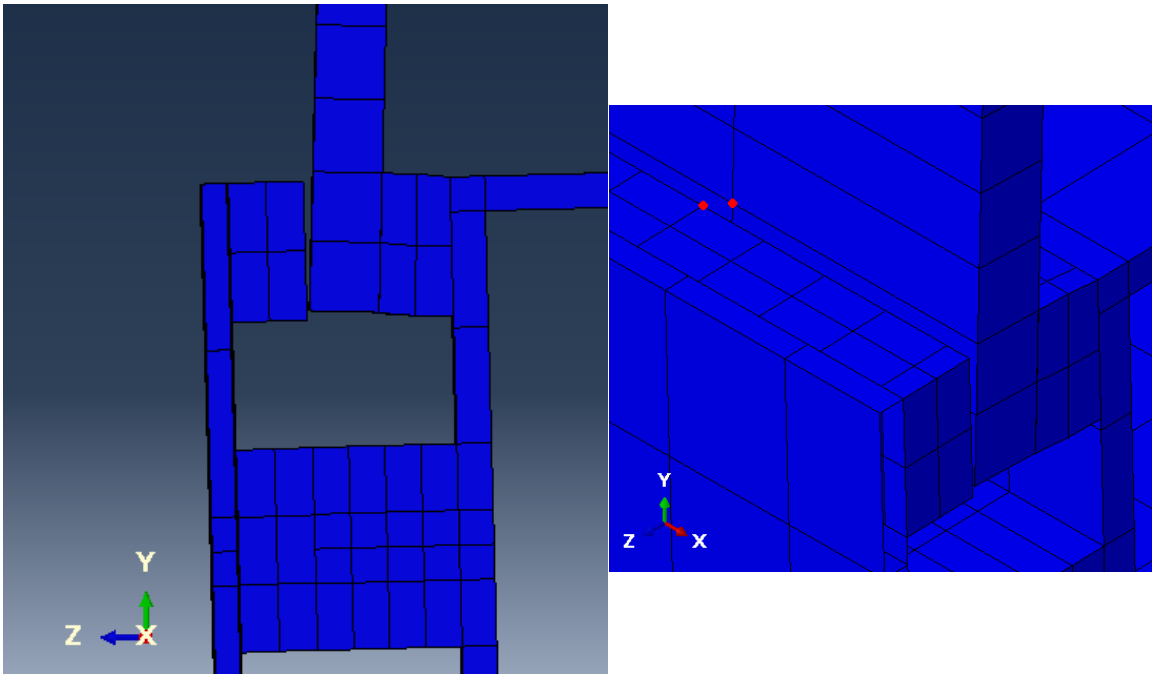

a) Example of gap between entire surface height of exterior fixed glazing gasket and the exterior surface of glass

b))Example of nodes selected in red to check distance between top edge of fixed glazing gasket and glass panel

Figure 5-20: Example of out-of-plane observation #1 gap opening

5.4.2.2.Out-of-Plane Analytical Observation #2

This identified out-of-plane observation was related to the first indication of the initial glass cracking stress being reached by one of the glass panels within the CW section. For this glass cracking stress criteria to be met, the minimum principal tensile stress of at least 28.8 MPa must be reached by any one of the four corners of a single glass panel. This slight difference in stress criteria, when compared to the in-plane criteria, was because the glass cracking origin was noted to occur primarily near the corners, edges or centers of the glass during experimental tests. It was determined through early runs that this cracking

stress would occur first near the panel corners at the middle section of the CW model. Therefore, it was necessary for this criteria to be met at only one of the corners using the same element location offsets from the corner as shown previously in Figure 4-38. Within the model, the obtained minimum principal tensile stresses were located at the interior integration point within the continuum shell (SC8R) element as shown in Figure 5-21.

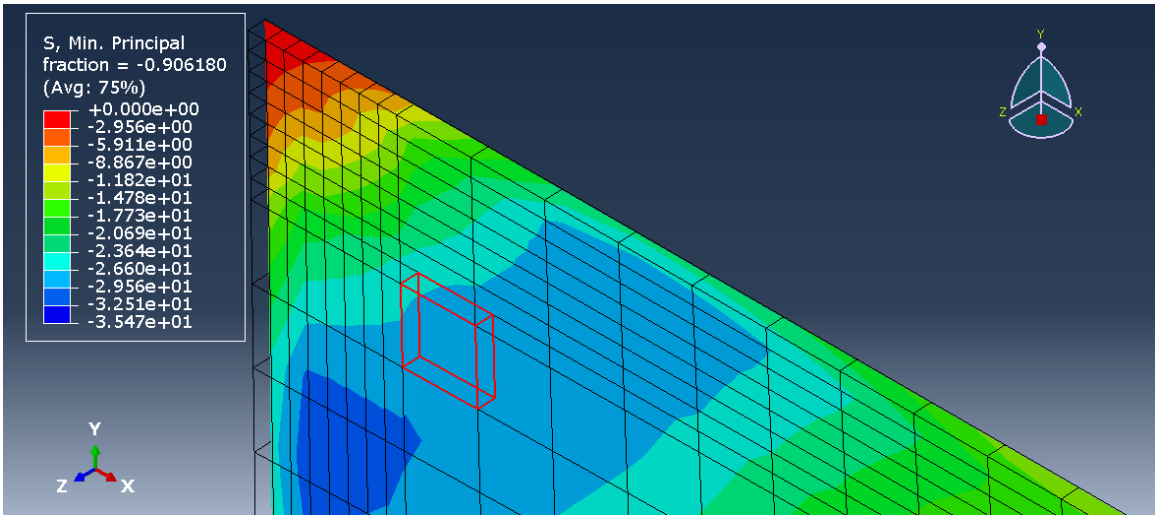

Figure 5-21: Example of minimum principal tensile stress being obtained for out-of-plane observation #2

5.4.2.3.Out-of-Plane Analytical Observation #3

This identified out-of-plane structural observation was related to the first indication of yielding of the steel angles in the CW model. It was determined that this occurs once the average of the Von Mises stresses obtained along a column of elements (on the y-axis) of an angle leg, as shown in Figure 5-22, has reached greater than or equal to 80% of the nominal yield stress of A36 steel (σ_y=250 MPa). This is due to the relative location of stress

concentrations and the possible plastic hinges near the corner regions as shown in Figure 5-22. Since these angles were modeled with continuum shell (SC8R) elements, the Von Mises stresses obtained were at the exterior integration point location within the elements.

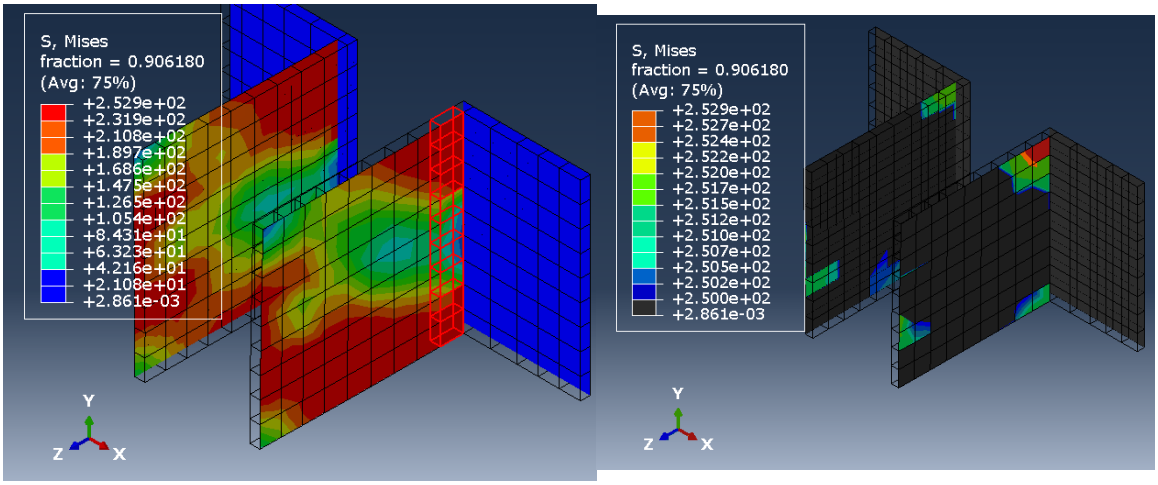

a) Example of column of elements selected for out-of-plane observation #3

b))Example of stress concentrations near the inner corner regions of the steel angles during out-of-plane observation #3

Figure 5-22: Example of out-of-plane observation #3

5.4.2.4.Out-of-Plane Analytical Observation #4

The identified structural observation presented here was related to the first indication of yielding of the aluminum mullions in the CW model. It was determined that this occurs once the average of the Von Mises stresses obtained has reached greater than or equal to the nominal yield stress of aluminum 6063-T6 (σ_y=215 MPa) along a section of elements (on the y-axis) on the backside of a mullion wall, as shown in Figure 5-23. The dimensions for this section of elements must have a length of at least 229 mm (the center to center screw spacing) and a width of 63.5 mm (mullion width). Since the side walls of

the mullions were modeled with continuum shell (SC8R) elements, the Von Mises stresses obtained were at both the interior and exterior integration point locations within the elements. This essentially describes yielding through the thickness of the mullion backside wall since only one element through the thickness was implemented in the meshing process.

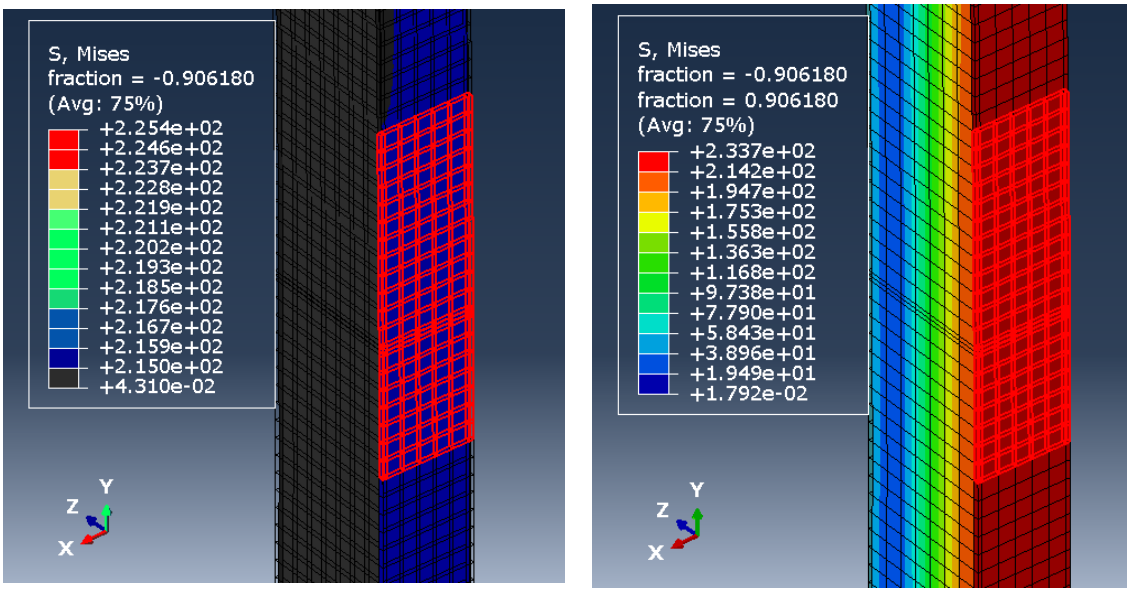

a) Selected section of elements once aluminum yielding is reached at the interior integration point (meaning through-thickness yielding) for the out-of-plane observation #4

b) Selected section of elements at the exterior integration point once the interior integration point has also reached yielding (meaning through-thickness yielding) for the out-of-plane observation #4

Figure 5-23: Example of out-of-plane observation #4 yielding of the mullion members

5.5. Results of the CW Model Simulations

Once all the analytical observations were made for the CW models subjected to both analysis simulations, recording of each engineering demand parameter (EDP) at

which a damage state has occurred at was recorded as shown in Table 5-8 and Table 5-9. As will be described more in detail in Chapter 6, the in-plane EDP was defined as the interstory drift ratio (IDR) and the out-of-plane EDP was defined as the out-of-plane deflection ratio (ODR). This section will go over the results of how the parameter changes affected the structural damage states for both simulations in each CW model, some of which are linked directly the non-structural damage states presented in Table 5-6 and Table 5-7.

5.5.1. In-Plane Structural Damage State Results

The IDRs corresponding to each of the in-plane damage states analyzed in all the CW models (with exception to CW model #11 as this was not simulated) are presented in Table 5-8. Overall, the order the in-plane damage states (DS) occurred in was: 1) DS1-initial glass-to-frame contact (at top left corner of center glass panel), 2) DS3-glass/frame breach (at bottom left corner of center glass panel), 3) DS2-initial glass cracking (at center glass panel), 4) DS4-yielding of steel anchors (one of the inner steel angles at the base), and 5) DS5-yielding of aluminum mullions (near the same region as the yielding of steel angle). In this study, the DS would be defined as simultaneous because the order of occurrence might be switched during simulations, depending on the different CW configurations. The initial glass-to-frame contact occurred before both the glass/frame breach DS and glass cracking DS which corresponds well with the validated single CW model. This is because enough glass translation/rotation within the glazing pocket must occur before DS2 and DS3 can occur. In the one story baseline CW model (CW model #1),

it was evident that the larger glass panels along the middle section experienced more damages as opposed to the side panels during the increasing applied lateral drift. This corresponds well with the observation in FEMA P-58 that larger glass panels are more susceptible to damage from movement. The maximum seismic IDR allowed in most buildings is 0.02. Therefore, only the initial glass-to-frame contact occurred at an IDR approximately 35% lower than the seismic IDR limit. Damage states such as initial glass cracking and aluminum mullion yielding occurred at an IDR approx. 19% and 30% higher than 0.02, respectively.

Table 5-8: Summary of In-Plane Damage States and Corresponding EDPs for CW Models #1-#10

Curtain Wall Model Number	**Structural DS1:** Initial Glass-to-Frame Contact			**Structural DS2:** Initial Glass Cracking **Water DS1:** Primary (Low)			**Structural DS3:** Glass/Frame Breach **Water DS2:** Primary (Low)/Secondary (High) **Air DS1:** Primary/Secondary (High) **Thermal DS1:** Primary/Secondary (High)			**Structural DS4:** Yielding of Steel Anchors			**Structural DS5:** Yielding of Aluminum Mullions		
	mm	in.	I.D.R	mm	in.	I.D.R	mm	in.	I.D.R	mm	in.	I.D.R	mm	in.	I.D.R
1-Baseline	60.1	2.36	0.0141	103	4.05	0.0241	92.0	3.62	0.0216	105	4.11	0.0245	116	4.56	0.0271
2	58.6	2.31	0.0137	102	4.01	0.0239	92.8	3.65	0.0218	103	4.07	0.0243	116	4.55	0.0271
3	60.1	2.36	0.0141	103	4.04	0.0241	92.0	3.62	0.0216	104	4.10	0.0244	116	4.58	0.0273
4	60.1	2.36	0.0141	>90.6	>3.57	>0.0212	>90.6	>3.57	>0.0212	>90.6	>3.57	>0.0212	>90.6	>3.57	>0.0212
5	61.6	2.42	0.0144	123	4.83	0.0288	93.6	3.68	0.0219	103	4.04	0.0241	116	4.57	0.0272
6	61.6	2.42	0.0144	>86.0	>3.39	>0.0202	>86.0	>3.39	>0.0202	>86.0	>3.39	>0.0202	>86.0	>3.39	>0.0202
7	63.1	2.48	0.0148	>125	>4.94	>0.0294	101	3.98	0.0237	103	4.04	0.0241	117	4.62	0.0275
8	19.0	0.75	0.0045	>33.0	>1.30	>0.00773	>33.0	>1.30	>0.00773	>33.0	>1.30	>0.00773	>33.0	>1.30	>0.00773
9	34.2	1.35	0.0080	64.6	2.54	0.0152	>69.6	>2.74	>0.0163	67.7	2.66	0.0159	>69.6	>2.74	>0.0163
10	85.9	3.38	0.0201	141	5.55	0.0330	40.3	1.59	0.0094	139	5.46	0.0325	149	5.85	0.0348

Note: "*>value*" = Drift/IDR inequality values are shown when the damage state (DS) was not reached by the end of the incompleted simulation. The values are the final drifts/IDRs at the end of the incompleted simulation which stopped before the total 152 mm displacement could be applied. It was assumed that if the CW model was able to complete the full displacement simulation, then the DS would most likely occur at a higher drift/IDR than the value presented in this table.

For the applied equivalent clamping load parameter change, a decrease in the equivalent clamping load (CW models #2) had a negative impact on the initial glass-to-frame contact (DS1), initial glass cracking (DS2) and yielding of the steel anchors (DS4) which all occurred at a lower IDR than the baseline CW model, down by 3% in the DS1. Only the glass/frame breach (DS3) had a better IDR capacity as it was increased by 1%. The main factor effecting DS1-DS2 was a decrease in the developed friction forces along the glass perimeters. This allowed for less lateral resistance during the initial drift stages which decreased the drift capacities as the glass was allowed to slip more easily within the glazing pocket. The exception was to the glass/frame breach DS as it actually benefited in having a lower clamping load.

With an increased clamping load (CW models #3-#4), a positive impact was analyzed only to the mullion yielding DS as it's IDR increased by 1%, and a negative impact only to the steel angle yielding DS with an IDR decreased by 1%. Therefore, the assumption that a higher clamping load would benefit the IDR capacity for the glass related DS (i.e. DS1-DS3) was not entirely proven yet since no change in the IDR capacity was analyzed when compared to the baseline CW. However, a conclusive statement could not be made as the CW model with the highest clamping load applied (CW model #4) did not finish the analysis before the other glass related damage states could occur. This was due to non-convergence being reached as a result of excessive deformations in the gaskets near the clamping loads.

For the glass thickness parameter change (CW models #5-#7), an increase in the glass thickness had a positive impact to the IDR capacity for all the damage states except

the steel angle yielding DS which had a 2% decrease in IDR capacity. The IDR capacities increased by up to 5% for initial glass-to-frame contact (DS1), up to 18% for initial glass cracking (DS2), up to 10% for glass/frame breach (DS3), and up to 1% for mullion yielding (DS5) compared to the baseline CW model. It is evident that as the glass panels increase, so do the IDR capacities for the glass-related DS as more drift had to be applied for the glass-to-frame contact to occur. It also took longer for the panels to rotate/translate in the glazing pocket before the CW breach could occur. Likewise, the thicker the glass panel became the lesser the stress developed near the corners, even if they were both in contact along the glass panel diagonal. This was evident as the glass cracking stress was not even obtained when the glass thickness was increased up to 25mm (1 in.). Therefore, it is assumed that thicker glass panels in this CW model help decrease the likelihood of glass cracking and glass/frame breach since they both occur past the seismic IDR limit of 0.02.

For the glass-to-frame clearance parameter changes, a decrease in clearance (CW models #8-#9) had negative impacts throughout the different damage states (DS1-DS5) analyzed. Unfortunately, even though DS1 was reached and glass-to-frame contacts were present on both diagonal corners for all three glass panels in the middle section of the CW, CW model #8 (3mm clearance) was not able to complete enough of the applied drift simulation due to excessive distortions in the gaskets causing non-convergence early on. However, CW model #9 (6mm clearance) completed more of the in-plane simulation which still gave a good understanding of the negatively effects smaller clearances have on the CW performance. Therefore, compared to the baseline CW model, the IDR capacity decreased by 104% for the glass-to-frame contact (DS1), by 46% for the glass cracking (DS2), and by 43% for the steel angle yielding (DS4). Nothing can be said of the mullion

yielding since neither of the models completed enough of the analysis by that drift. However, for the 6mm clearance configuration (CW model #9), enough of the simulation was analyzed to determine that the IDR capacity for the glass/frame breach DS was going to be reached after the steel angle yielding, unlike the baseline CW simulation with the 11mm clearance. This makes sense since to achieve smaller clearances, only the glass panel dimensions were increased which increased the glass bite (portion of glass hidden behind pressure plate). Since the glass bite is increased, more glass panel rotation/translation is required in order for this glass/frame breach to occur.

In the increased glass-to-frame clearance scenarios (only CW model #10 since #11 was not analyzed), the CW configurations behaved in the opposite manner of the decreased clearance configurations. Therefore, compared to the baseline CW model, the IDR capacities increased by 35% for the glass-to-frame contact (DS1), by 31% for the glass cracking (DS2), by 28% for the steel angle yielding (DS4) and by 25% for the mullion yielding (DS%). The IDR capacity decreased by 28% for the glass/frame breach (DS3) as this time the glass bite was decreased as the glass-to-frame clearances were increased. This made it easier for gaps to occur much earlier since little rotation/translations of the glass panel was needed, and DS3 occurred before DS4 again.

5.5.2. Out-of-Plane Structural Damage State Results

The ODRs corresponding to each of the out-of-plane damage states analyzed in all the CW models are presented in Table 5-9. Overall, the order the out-of-plane damage states (DS) occurred in was: 1) DS1-glass/frame breach (at the top middle glass panel base),

2) DS2-initial glass cracking (at the top corners of the top middle glass panel), 3) DS3-steel anchor (angle) yielding (at the two inner base steel angles), and 4) DS4-aluminum mullion yielding (at the mid-span of the two inner vertical mullions). It is evident that most of the damage states are reached primarily at the center section of the CW model during the applied out-of-plane pressure. Also, since the baseline CW model was symmetrical in boundary conditions and geometry dimensions, the max deflection would be analyzed at the center glass panel. This helps with comparing the deflection of the entire CW system to relevant deflection limits reviewed in the literature set by ASTM E1300 standard for glass panels.

Table 5-9: Summary of Out-of-Plane Damage States and Corresponding EDPs for CW Models #1-#11

Curtain Wall Model Number	**Structural DS1:** Glass/Frame Breach **Water DS1:** Primary (High)/Secondary (Low) **Air DS1:** Primary/Secondary (Low) **Thermal DS1:** Primary/Secondary (Low)					**Structural DS2:** Initial Glass Cracking **Water DS2:** Primary (Low)				**Structural DS3:** Yielding of Steel Anchors				**Structural DS4:** Yielding of Aluminum Mullions			
	Applied Pressure		Center Deflection Δ_c		O.D.R	Applied Pressure		Center Deflection Δ_c		O.D.R	Applied Pressure		Center Deflection Δ_c		O.D.R	Applied Pressure		Center Deflection Δ_c		O.D.R
	MPa	psf	mm	in.	$=\Delta_c/h_s$	MPa	psf	mm	in.	$=\Delta_c/h_s$	MPa	psf	mm	in.	$=\Delta_c/h_s$	MPa	psf	mm	in.	$=\Delta_c/h_s$
1-Baseline	0.00113	23.5	34.1	1.34	0.0208	0.00303	63.2	75.4	2.97	0.0461	0.00473	98.7	111	4.39	0.0681	0.00478	99.7	112	4.43	0.0687
2	0.00143	29.8	40.2	1.58	0.0246	0.00323	67.4	80.0	3.15	0.0489	0.00473	98.7	111	4.39	0.0681	0.00478	99.7	112	4.43	0.0687
3	0.000926	19.3	29.7	1.17	0.0181	0.00293	61.1	73.1	2.88	0.0447	0.00473	98.7	111	4.39	0.0681	0.00478	99.7	112	4.43	0.0687
4	0.000726	15.2	25.0	0.99	0.0153	0.00283	59.0	70.9	2.79	0.0433	0.00473	98.7	111	4.39	0.0681	0.00478	99.7	113	4.43	0.0688
5	0.00128	26.6	22.2	0.87	0.0136	a	a	a	a	a	0.00488	101.8	95.0	3.74	0.0581	a	a	a	a	a
6	0.00133	27.7	17.7	0.70	0.0108	a	a	a	a	a	a	a	a	a	a	a	a	a	a	a
7	0.00253	52.7	29.6	1.17	0.0181	a	a	a	a	a	a	a	a	a	a	a	a	a	a	a
8	0.00113	23.5	33.8	1.33	0.0205	0.00418	87.2	99.7	3.92	0.0603	0.00473	98.7	111	4.36	0.0670	0.00478	99.7	112	4.40	0.0677
9	0.00113	23.5	33.9	1.33	0.0206	0.00363	75.7	88.5	3.48	0.0537	0.00473	98.7	111	4.37	0.0674	0.00478	99.7	112	4.41	0.0681
10	0.00103	21.4	32.3	1.27	0.0199	0.00353	73.6	87.5	3.45	0.0538	0.00468	97.6	111	4.39	0.0685	0.00478	99.7	114	4.47	0.0698
11	0.000626	13.1	23.0	0.90	0.0142	a	a	a	a	a	0.00463	96.6	111	4.38	0.0687	0.00473	98.7	114	4.47	0.0700

Note: For the O.D.R, h_s is the height of the shortest side of the glass panel where the center deflection was observed. For example: h_s = 1,636.5mm for CW models #1-#7

Note: "a" = Damage state was not reached by end of the completed pressure simulation. This meant no pressure, center deflection and ODR results were recorded. It was assumed that the damage state would occur if a pressure >0.005MPa was applied to the CW model.

Following the ASTM E1300 procedures for calculating the deflection limit for 6mm (1/4 in.) thick glass panels with simply supported boundary conditions, the maximum deflection limit for the 1,636.5mm x 2398.5mm center panel was approx. at 23 mm. And since the ODR was the engineering demand parameter for the pressure simulations, the max ODR limit is 0.0141. Therefore, the baseline CW model (CW model #1) has damage states occurring at ODRs 38% larger than the ODR limit such as glass/frame breach (DS1) and even up to 132% larger than the ODR limit for yielding of steel angles and aluminum mullions DS (DS3-DS4).

For the applied equivalent clamping load parameter change, a decrease in the equivalent clamping load (CW model #2) had a positive impact on the ODR capacity for damage states of glass/frame breach (DS1) and initial glass cracking (DS2), up to a 17% increase in DS1 compared to the baseline CW. For an increased equivalent clamping load (CW models #3-#4), a negative impact on the ODR capacity for DS1-DS2 is analyzed up to a 31% and 6% decrease compared to the baseline CW ODR limit. In either clamping load scenario, the yielding damage states (DS3-DS4) had no change in ODR capacity. Particularly for DS2, these responses make sense since with an increased clamping load the glass edges restraints are increased which should limit the glass panel out-of-plane rotations/translations and deflections. This generates more stresses near the glass corners/edges during pressure application meaning glass cracking occurs sooner. However, what happens to the ODR capacity as the clamping load is increased does not make sense since it seems that DS1 occurs sooner as well, which should not be the case. Upon closer inspection, the reason for this is how the fixed glazing gaskets deform away from the glass

surfaces in between the center-to-center spaces of the applied clamping load, creating an initial small gap before any load is applied. Therefore, as the clamping load increased the already developed gap grew as well which led to an earlier occurrence of the glass/frame breach DS1. The behavior of the fixed glazing gaskets during clamping load application must be further studied in the future to get more accurate simulations.

For the glass thickness parameter change, both the ODR capacity and the applied pressure at each damage state had to be taken into account as the glass thickness increased. For instance, while the ODR capacity for the glass/frame breach DS decreased up to 14% (25mm thickness) when compared to the baseline CW model results, the applied pressure to reach this lower ODR capacity was much higher. This makes sense since after considering the thickness increase with the ASTM E1300 max deflection procedure, the ODR limit changed down to 0.0031. Additionally, while all the models in this group successfully completed the entire loading simulation, not enough pressure was applied for the DS2-DS4 to occur by the simulation end. As the thickness increased, the stresses generated along the glass panels decreased and this meant decreased out-of-plane deflections and no yielding of the anchors/mullions as well.

Finally, for the glass-to-frame clearance parameter change, as the clearance decreased (CW models #8-#9) a negative impact in the ODR capacity was initially observed for the damage states glass/frame breach (DS1) and yielding of the mullions/angles (DS3-DS4). Up to a 2% decrease in the ODR capacity was observed for each DS when compared to the baseline CW model. Only the initial glass cracking DS2 saw a positive impact as the ODR capacity increased by 27%. This makes sense for DS2 since the decreased clearance was achieved by increasing the glass dimensions. Therefore,

the glass bites were increased while the fixed glazing gaskets were left unchanged. It would affect the boundary conditions since the gaskets were now offset from the glass perimeters. This essentially benefited the CW system by increasing the out-of-plane deflection resistance of the glass panels. The increased height of the center glass panel was also taken into account as it decreased the ODR capacities as well. So although at first glance it seems the ODR capacity was negatively impacted compared to the baseline CW model, it in fact is performing as it should during out of plane loading with decreased clearances at higher applied loadings. This explains why the ODR capacities drop as well for DS1 and DS3-DS4, even though the deflection demand is the same as the baseline CW model.

For the increased glass-to-frame clearances (CW models #10-#11), different responses were analyzed as the clearances were obtained with a decreased glass bite (due to decreased glass dimensions), and decreased width of the fixed glazing gaskets. Therefore, this presented different boundary conditions as the clearances were decreased up to 19mm. While understanding that the ODR calculations accounted for changing glass heights and the applied pressure at which demand deflections were reached, the ODR capacities increased for DS2-DS4 when compared to the baseline CW. In the case of DS2 (glass cracking), the ODR capacity was increased by 15% (16mm clearance), and for the 19mm clearance the DS2 was not even reached by the end of the applied pressure simulations. For the glass/frame breach DS1 the ODR capacities were decreased. While a decreased in deflections is expected with smaller panels, the decreased width of the glazing gaskets allowed for more rotations at the glass perimeter which explained the ODR capacity decrease up to 39%. On the other hand, DS3-DS4 had increased ODR capacities, but the glass dimensions effected how the ODR is calculated even though these occurred

at relatively the same demand deflections as the baseline CW model. Based on the results, it can be assumed that glass-to-frame clearance changes do not affect the yielding of angles/mullions as much as it does for the glass/frame breach and initial glass cracking DS.

5.6. Summary

An FE model of the designed 14'x14' one-story CW section was generated to further support the validated 3D FE model, and to analyze the performance of a much larger multi-panel CW section during applied simulations. The larger CW model also included steel anchors to observe the effects of a less rigid CW framing system-to-structural system connection often not included in laboratory tests. Additional one-story CW models with different parametric configuration changes to the baseline CW model (i.e. equivalent clamping load, glass thickness, and glass-to-frame contact) were generated to analyze their effects on the CW performance.

Analytical observations of structural CW responses were identified and linked to different structural DS. For in-plane and out-of-plane simulations, these structural DS included: 1) initial glass-to-frame contact (only in-plane); 2) initial glass cracking; 3) glass/frame breach; 4) yielding of aluminum mullions; and 5) yielding of steel anchors. Non-structural DS were also identified and linked to the occurrence of some of the structural DS as they related to the CW's water, air (condensation) and thermal performance.

The observations and conclusions determined from the results after applying in- and out-of-plane loading simulations to different large one-story CW configurations include:

1. In-plane IDR capacities decreased for all DS with a decreased equivalent clamping load. Demonstrates that tightening the screws along pressure plates to at least the necessary torque was important for maintaining the CW's in-plane performance.
2. ODR capacities increased for all out-of-plane DS with a decreased equivalent clamping load. Opposite effect was observed for increasing the clamping load. Demonstrates that the screws should not be tightened along pressure plates past the necessary torque as it negatively affects CW's out-of-plane performance.
3. An increase to glass thickness improved the in-plane CW performance as the in-plane IDR capacities had increased for most DS. This is opposite of what is expected in the field with thicker, heavier glass panels as was concluded from surveys conducted in the FEMA P-58 Seismic Fragility Development study.
4. Increases to glass thickness affected the out-of-plane CW performance by decreasing the ODR capacities for the out-of-plane DS. However, the applied pressure must be analyzed in tandem with the ODR capacities to determine whether or not the CW performance improved.
5. A decrease to the glass-to-frame clearance decreased the CW performance as in-plane IDR capacities decreased for some DS. However, increasing the

clearance had the opposite effect to the in-plane performance. Since glass dimensions were increased to obtain smaller clearances, larger glass bite sizes can negatively affect the in-plane performance as the glass comes into contact sooner with the frame.

6. No definitive conclusions were made when the ODR capacities increased for some of the out-of-plane DS and decreased for others when either a decrease or increase to the glass-to-frame clearances was made. However, the applied pressure must be analyzed in tandem with the ODR capacities to determine whether or not the CW performance improved.
7. Modeling of the rubber components (i.e. material behavior and element meshing) should be improved to allow the analysis to complete further (i.e. before non-convergence occurs), and to better capture the bending and shear behaviors during the different applied loading simulations (i.e. drift, pressure and equivalent clamping load). This can also affect when certain damage states may occur.

Chapter 6

Development of Fragility Curves for Multi-Hazard PBE of Glass Curtain Walls

6.1. Introduction

The focus of this computational study was to support the development of seismic-related and hurricane-related fragility curves for glass curtain walls based on results obtained from running simulations on finite element models of glass CWs. Fragility curves allow engineers/researchers to estimate the probability of reaching a damage state (e.g. glass cracking, or glass fallout) given a specified magnitude of an engineering demand parameter (e.g. specified magnitude of interstory drift ratio or out-of-plane deflection ratio).

Based on the literature review, a framework for seismic fragility curve development based primarily on experimental CW tests has been established by FEMA/ATC. The test results are used to derive the required fragility parameters needed for fragility curve development. These parameters also account for uncertainty and dispersion within a set of tests. While this framework incorporates experimental tests to determine when different damage states occur, it allows for analytical methods to be used in lieu of these tests. However, there are no specific examples of analytical methods being employed to approximate CW damage states to be used specifically with this fragility framework. The framework also accounts for uncertainty and dispersion in the analytical results differently

when compared to the experimental related approaches. Comparisons between these two methods for obtaining the fragility parameters and how they affect the fragility curves have also not been fully considered. Furthermore, an equivalent framework has not been established for the development of hurricane-related fragility curves for CWs. However, for the purposes of this computational study, it was assumed that hurricane fragility curves could be similarly developed with the use of the seismic fragility procedures.

Therefore, this chapter presents the development of fragility curves derived from the analytical results obtained after in-plane and out-of-plane simulations were applied to the one story CW model described in Chapter 5. Before fragility curves were developed, a review of the FEMA P-58 seismic fragility development framework was necessary to understand the two derivation approaches utilized to derive the required fragility parameters (i.e. the actual demand data method and the derivation method).

The second stage was to implement the derivation method to obtain fragility curves for the in-plane and out-of-plane damage states analyzed for each of the different one-story CW model simulations. The seismic fragility curve for the initial glass cracking damage state from the FE model was then compared to the fragility developed for a single glass CW unit with similar glazing configurations in the FEMA P-58 document. This would check the adequacy of the analytical CW model in capturing the seismic drift capacity for the glass cracking damage state, and to show how analyzing a larger section of CW effects results when compared to a single CW unit.

Finally, a small dispersion study was implemented on fragility curves for one of the damage states analyzed in both the in-plane and out-of-plane simulations of the baseline CW study. This was done to help better understand the effects of accounting for different

values of dispersion in the analytical results as opposed to using the fixed value implemented in the literature for analytically derived fragility curves.

Overall, this chapter will show the effectiveness of using analytical FE models for approximating the damage states observed in glass CWs to derive fragility curves for multi-hazard performance based engineering.

6.2. Review of Established Seismic Fragility Curve Development Guidelines for Glass Curtain Wall Systems

With the combined effort of the Applied Technology Council (ATC) and the Federal Emergency Management Agency (FEMA), seismic fragility curve procedures based on experimental test results were developed in the FEMA P-58/BD-3.9.1 Background Document (Memari et al. 2011a). It was created to assist engineers in evaluating glass CWs using a performance based engineering design approach for building envelope performance assessment (Memari et al. 2011a). The generated database of fragility curves helped estimate the damages that a glass CW system could sustain during a seismic event in terms of a probability of failure for different types of CW components (Applied Technology Council (ATC) 2012; Memari et al. 2011a; O'Brien et al. 2012). Fragility curves are formally defined as a lognormal cumulative distribution function, shown in a symbolic-simplified manner in Equation 6-1, where $F_i(D)$ denotes the prediction of the probability of a CW damage state (i.e. glass cracking, glass fallout) occurring as a function of a given engineering demand parameter, D, (i.e. interstory drift ratio, displacement).

$$F_i(D) = \Phi\left(ln\frac{\frac{D}{\theta_i}}{\beta_i}\right) \quad (6\text{-}1)$$

In the right hand side of Equation 6-1, Φ denotes the standard normal (Gaussian) cumulative distribution function; θ_i and β_i represents the median value and logarithmic standard deviation (or dispersion) from a set of test results, respectively; and i denotes the specified damage state of interest (Applied Technology Council (ATC) 2012; Memari et al. 2011a; O'Brien et al. 2012).

A set of experimental racking tests must be completed to obtain drift values related the occurrence of damage states. In FEMA P-58, these were converted to an interstory drift ratio (IDR) which is the ratio between the drift and the height over which the drift occurred (i.e. center-to-center spacing of the horizontal transom members of the glass CWs). With these sets of IDR values, the fragility parameters θ (median) and β (dispersion) are derived to develop each damage state fragility curve. This dispersion β parameter represents the uncertainty in the actual value of the demand D value (i.e. the IDR) at which the damage state is likely to occur. ATC (2012) states that for cases in which a limited experimental database is completed, this dispersion parameter is determined using Equation 6-2. This equation accounts for the random variability in the experimental data, β_r; and the differences between the physical construction configurations and loading conditions expected on an actual building versus the existing conditions in the experimental test specimen, β_u. It is mentioned that the β_u term can also denote the uncertainty related to the ability to properly capture the variability of the CW specimens' behaviors based on the adequacy of an experimental database (Memari et al. 2011a).

$$\beta = \sqrt{{\beta_r}^2 + {\beta_u}^2} \quad (6\text{-}2)$$

Summarized within the FEMA P-58 Background Document (Memari et al. 2011a; O'Brien et al. 2012), the ATC-58 guidelines recommend different prescribed values and methods derived for determining the dispersion related fragility parameters in Equation 6-2. For instance, the default value for β_u is set to 0.25 if: 1) five or fewer specimens have been tested with the same loading protocol; 2) different configurations of the CW components installed on the building are possible, but experimental test specimens all had the same configuration; and 3) the CW systems on the actual building experience different loading conditions (i.e. in multiple directions) but the laboratory specimens were only tested in one direction. Otherwise, the value is set to 0.10.

Likewise, there are five derived methods which develop these fragility parameters, the median (θ) and the dispersion (β) values, which are based on the availability of experimental test data. The five methods included are: 1) Actual Demand Data—When the damage state D is observed in each tested CW specimen; 2) Bounding Demand Data—When the damage state D is only observed in some of the tested CW specimens and the expected maximum demand is known, even though it may not occur at the observed damage state D; 3) Capable Demand Data—When the damage state D is not observed by any of the CW test specimens, even though the expected maximum demand is known; 4) Derivation—When no experimental data is available, but the CW behavior is modeled and the demand at which the damage state D can occur is predicted analytically; 5) Expert Opinion—When the demand corresponding to the occurrence of the damage state D is estimated based solely on opinions of experts. Since this chapter implements both the

actual demand data method and the derivation method, both sets of equations required for the median and dispersion values are presented herein. The procedures to carry out all five fragility parameter derivation methods are detailed explicitly within the FEMA P-58-1 Seismic Performance Assessment of Buildings Methodology document (Applied Technology Council (ATC) 2012).

For the actual demand data method, the median and random dispersion values can be obtained using Equations 6-3 and 6-4. Where M is the total number of specimens tests and d_i is the demand in test "i" at which the damage state was first observed to occur (Applied Technology Council (ATC) 2012).

$$\theta = e^{\left(\frac{1}{M-1}\sum_{i=1}^{M}\ln d_i\right)} \tag{6-3}$$

$$\beta_r = \sqrt{\left[\frac{1}{M-1}\sum_{i=1}^{M}\left(\ln\left(\frac{d_i}{\theta}\right)\right)^2\right]^2} \tag{6-4}$$

With the derivation method, the median value can be obtained using Equation 6-5. Where Q is the capacity of the component in terms of d, the engineering demand parameter (Applied Technology Council (ATC) 2012). The logarithmic standard deviation is taken as $\beta = 0.4$ (Applied Technology Council (ATC) 2012).

$$\theta = 0.92Q \tag{6-5}$$

6.3. Development of Fragility Curves for CW Models

As shown in Table 5-8 and Table 5-9, engineering demand parameters (EDP) were identified from the in-plane and out-of-plane simulations, respectively, to describe the demand corresponding to the structural damage states.

For the in-plane simulations, the demand drift was converted into an interstory drift ratio (IDR) which is the ratio between the demand drift and the height of the entire one story glass CW model (i.e. 14ft = 4,266 mm). The entire height was implemented because the fragility curves describe the probability of failure for any one of the damage states occurring over the entire glass CW section, instead of just an individual glass CW unit as was done in the FEMA P-58 study. This is a more applicable approach for using fragility curves in PBE design since engineers/researchers should want to know how the entire CW system will perform during a seismic or hurricane event.

Similarly, for the out-of-plane simulations, the center deflection obtained from the center glass panel was converted to an out-of-plane deflection ratio (ODR). This ratio is between the maximum out-of-plane deflection (at the center glass panel) and the smaller side dimension of the glass panel (i.e. the height of the center glass panel). This non-dimensional EDP helped represent the out-of-plane curvature of the glass panel observed during increasing pressure. Similar to the in-plane fragility curves, while the out-of-plane EDP was analyzed at the center glass panel of the CW section, the demands corresponded to the occurrence of the damage states within the entire one-story CW model.

Using the EDP results, the derivation method was implemented to obtain the fragility parameters required for the in-plane and out-of-plane damage state fragility curves of each model simulation as shown in Table 6-1 and Table 6-2, respectively. The median θ was determined with Equation 6-5, and β was set to 0.4 in all cases.

Table 6-1: Summary of Calculated Fragility Parameters for In-Plane Damage States

Curtain Wall Model Numbering	**Structural DS1:** Initial Glass-to-Frame Contact		**Structural DS2:** Initial Glass Cracking **Water DS1:** Primary (Low)		**Structural DS3:** Glass/ Frame Breach **Water DS2:** Primary (Low)/Secondary (High) **Air DS1:** Primary/Secondary (High) **Thermal DS1:** Primary/Secondary (High)		**Structural DS4:** Yielding of Steel Anchors		**Structural DS5:** Yielding of Aluminum Mullions	
	θ	β	θ	β	θ	β	θ	β	θ	β
1	0.0130	0.4	0.0222	0.4	0.0198	0.4	0.0225	0.4	0.0250	0.4
2	0.0126	0.4	0.0220	0.4	0.0200	0.4	0.0223	0.4	0.0249	0.4
3	0.0130	0.4	0.0222	0.4	0.0198	0.4	0.0225	0.4	0.0251	0.4
4	0.0130	0.4	a	a	a	a	a	a	a	a
5	0.0133	0.4	0.0265	0.4	0.0202	0.4	0.0222	0.4	0.0250	0.4
6	0.0133	0.4	a	a	a	a	a	a	a	a
7	0.0136	0.4	a	a	0.0218	0.4	0.0222	0.4	0.0253	0.4
8	0.0041	0.4	a	a	a	a	a	a	a	a
9	0.0074	0.4	0.0139	0.4	a	a	0.0146	0.4	a	a
10	0.0185	0.4	0.0304	0.4	0.0087	0.4	0.0299	0.4	0.0320	0.4

Note: "a"= Fragility parameters were not calculated for the damage state if no specific IDR value was recorded. As explained in Table 5-8, this is due to the damage state not occuring before the final applied drift/IDR at the end of the incompleted displacement simulation.

Table 6-2: Summary of Calculated Fragility Parameters for Out-of-Plane Damage States

Curtain Wall Model Numbering	**Structural DS1:** Glass/Frame Breach **Water DS1:** Primary (High)/Secondary (Low) **Air DS1:** Primary/Secondary (Low) **Thermal DS1:** Primary/Secondary (Low)		**Structural DS2:** Initial Glass Cracking **Water DS2:** Primary (Low)		**Structural DS3:** Yielding of Steel Anchors		**Structural DS4:** Yielding of Aluminum Mullions	
	θ	β	θ	β	θ	β	θ	β
1	0.0191	0.4	0.0424	0.4	0.0626	0.4	0.0632	0.4
2	0.0226	0.4	0.0450	0.4	0.0626	0.4	0.0632	0.4
3	0.0167	0.4	0.0411	0.4	0.0626	0.4	0.0632	0.4
4	0.0141	0.4	0.0398	0.4	0.0627	0.4	0.0633	0.4
5	0.0125	0.4	a	a	0.0534	0.4	a	a
6	0.0100	0.4	a	a	a	a	a	a
7	0.0166	0.4	a	a	a	a	a	a
8	0.0188	0.4	0.0555	0.4	0.0617	0.4	0.0622	0.4
9	0.0189	0.4	0.0494	0.4	0.0620	0.4	0.0626	0.4
10	0.0183	0.4	0.0495	0.4	0.0630	0.4	0.0642	0.4
11	0.0130	0.4	a	a	0.0632	0.4	0.0644	0.4

Note: "a"= Fragility parameters were not calculated for the damage state if no specific ODR value was recorded. As explained in Table 5-9, this is due to the damage state not occuring by the end of the completed pressure simulation.

With the median and dispersion values as inputs, the LOGNORMDIST excel function was implemented to obtain the fragility curves as a lognormal cumulative distribution function. Only the in-plane and out-of-plane fragility curves for each of the analyzed damage states in the baseline CW model (CW model #1) were derived as shown in Figure 6-1 and Figure 6-2, respectively.

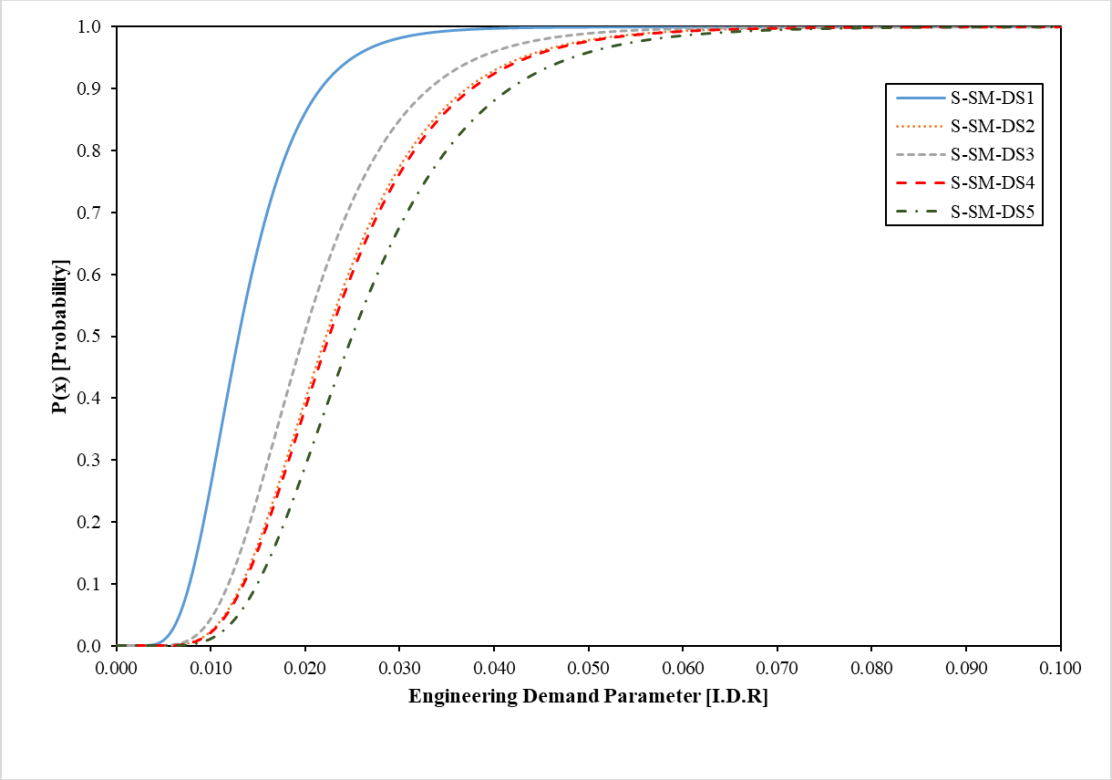

Figure 6-1: Generated fragility curves for the in-plane damage states of baseline CW model #1

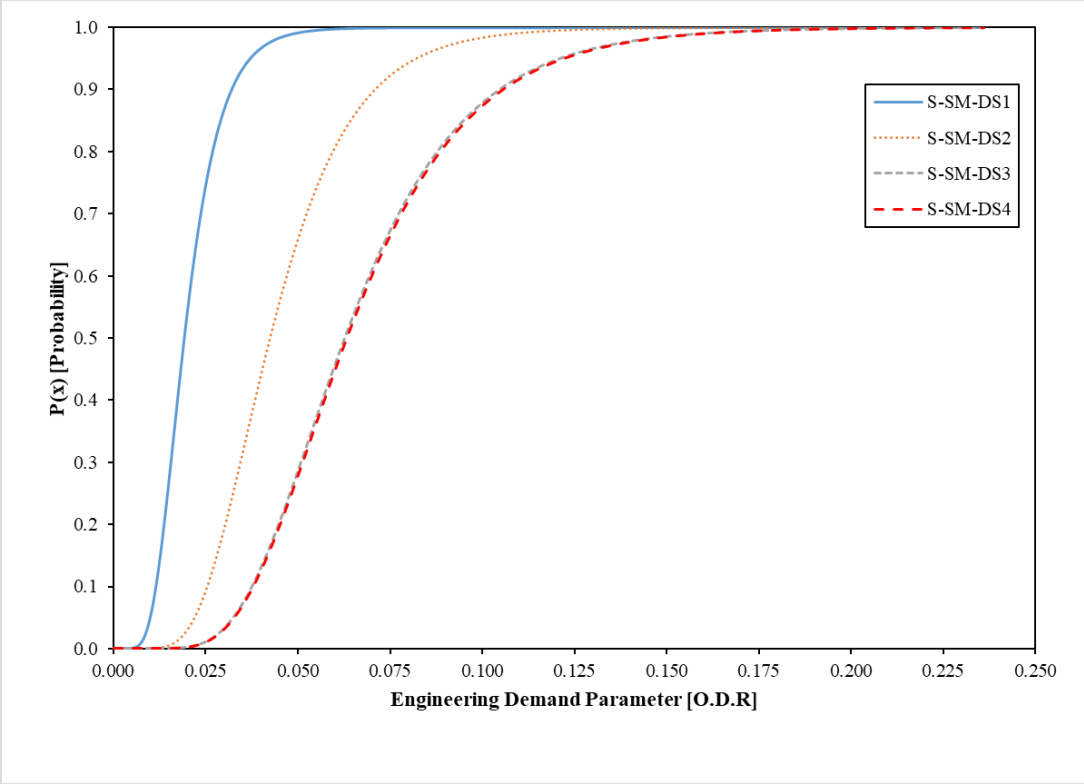

Figure 6-2: Generated fragility curves for the out-of-plane damage states of baseline CW model #1

Additional plots for the comparison of fragility curves is presented in Appendix B. These additional graphs show how one damage state is affected across the three sets of parameter changes involving equivalent clamping loads, glass thicknesses, and glass-to-frame clearances.

6.4. Comparison of Fragility Curves Developed for Multi-Panel CWs vs. Single-Panel CWs

In-plane and out-of-plane fragility curves in this study were generated using damage state results obtained from a one-story, multi-panel curtain wall section. However, the seismic fragility database generated for the FEMA P-58 study were obtained through

experimental testing of single panel curtain wall systems (Memari et al. 2011a). Comparisons between the seismic fragility curves were completed to check how analyzing a full scale, multi-panel CW section instead of a single panel CW section would affect the glass cracking damage states. Likewise, the effect of considering semi-rigid CW framing system-to-structural system connections was considered. In general, the fragility curves in the FEMA P-58 were obtained using tests that had rigid connections meaning more conservative fragility curves. However, connections in the field typically vary, meaning different connection flexibilities which could yield less than 100% drift transfer between the structure and the CW system.

Based on the limited database within the FEMA P-58 study, there was not an exact single panel CW configuration which tested with exact panel dimensions as compared to one of the glass panels included in the baseline CW model in this study. However, the FEMA P-58 document describes a method that engineers may use to develop modified fragility curves based on the original fragility curves generated within their study. Therefore, this was implemented to create a modified fragility curve for a single glass panel CW configuration similar to one of the 1,636.5 mm x 2,398.5 mm (5.37ft x 7.87ft) glass panels in the baseline CW model. Since the height to width aspect ratio (AR) of this modeled glass panel was about 0.68, the experimental configuration with the closest AR was chosen (FEMA P-58 configuration #15), which was a 4ft x 8ft (1,219.2mm x 2,438.4mm) glass panel (i.e. AR=0.5). Next, the modification factor, r, was determined to modify the original glass cracking damage state median IDR, θ, from the FEMA P-58 database. This r factor is the ratio of the experimental glass panel height to the analytical glass panel height. The product of the r modification factor (i.e. r=0.745) and the original

demand median (i.e. θ=0.0220) determined the modified demand median (θ_{new}=0.0164). With the modified demand median and the original glass cracking dispersion value (β=0.277), the modified glass cracking fragility for the 1,636.5 mm x 2,398.5 mm was generated. This modified single panel fragility was then compared to the glass cracking fragility generated from the multi-panel baseline CW results (CW #1) as shown in Figure 6-3 .

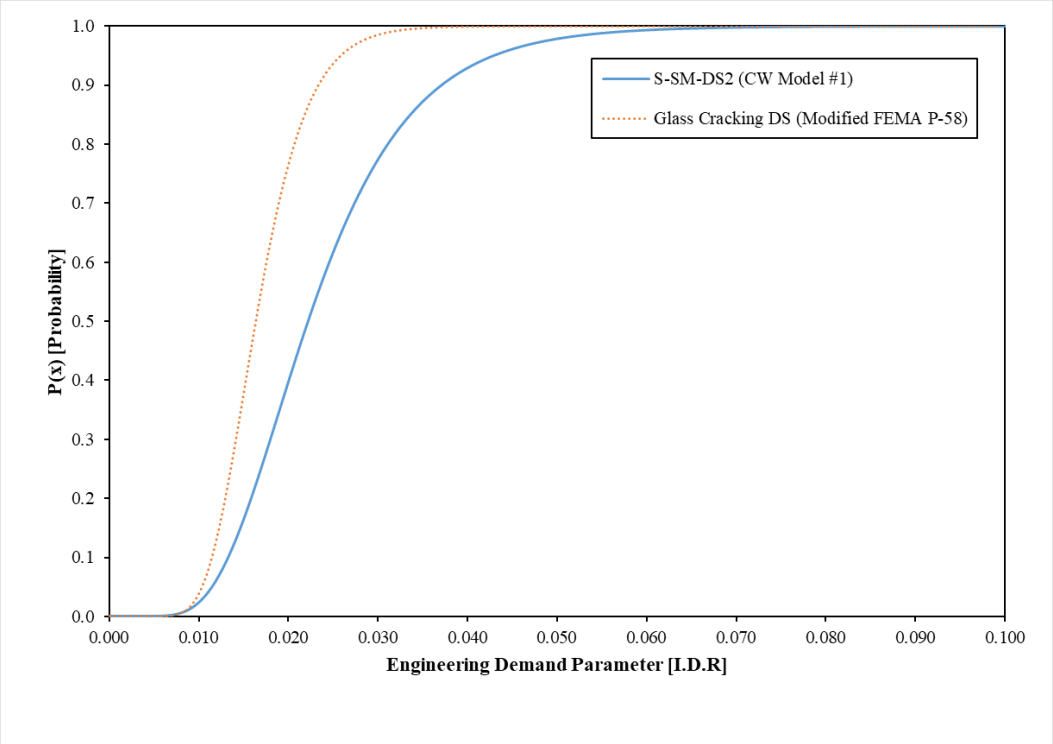

Figure 6-3: Comparison of the generated fragility curves for the glass cracking stress damage state between the multi-panel CW (CW#1) and modified single CW panel (FEMA P-58) configuration

As shown in Figure 6-3 and summarized in Table 6-3 at different levels of increasing probability of failure, the glass cracking damage state from the modeled multi-glass panel seemed to occur at a larger demand IDR when compared to the single CW unit.

This was likely evident due to the modeled multi-panel glass curtain wall having more flexible connections than the single CW unit may have had in the lab tests. Other contributing factors captured within the modeled multi-panel CW that may have effected this increase in IDR capacities include: the inclusion of different glass panel dimensions and aspect ratios; possible component interactions/responses that may increase/decrease likelihood of damages in different components (i.e. the occurrence of one damage state in one panel may negatively/positively affect the performance of another adjacent panel); and the continuity of the CW framing members across a larger span. Since the derivation method incorporated in the fragility parameters for this study included a small safety factor for the median IDR value (θ=0.92Q), this may have increased the conservativeness of the fragility curve generated here as well.

Based on these overall comparison results, deriving fragility curves that incorporate results from a multi-panel CW section seems to be a more applicable approach when implementing performance based engineering for CWs. If an engineer decides to use the fragility database from the FEMA P-58 study, they must take into consideration that a certain level of conservativeness is present when considering the performance results of just a single glass CW panel as opposed to a CW section with multiple panels.

Table 6-3: Summary of Demand IDR θ_{crack} Values from FEMA P-58 CW Configuration #15 and CW Model #1 Results at Different Probabilities

P(x)	CW#1 θ_{crack}	Modified θ_{crack}	% Difference
0.2 (20%)	0.0159	0.013	20.1
0.5 (50%)	0.0222	0.0164	30.1
0.8 (80%)	0.0311	0.0207	40.2

6.5. Effects of Generated Fragility Curves Accounting for Different Dispersions in Results

The effect of accounting for a different dispersion value for the analyzed results was studied to observe how the fragility curves for the in-plane and out-of-plane glass cracking damage state may be affected. This was looked into since the dispersion value was set to β=0.4 when using the derivation method defined by FEMA P-58-1 (Applied Technology Council (ATC) 2012). However, based on the experimental results in FEMA P-58 the actual demand data method was used to obtain the fragility parameters which included the dispersion value. For instance, the geometric mean of the dispersion value for the glass damage state was approximately 0.275 for a set of similar Kawneer 1600 CW systems subjected to seismic drift as shown in Table 6-4.

Table 6-4: Summary of β Values for Damage States of the Dry Glazed CW Systems Tested in FEMA P-58 Study

ID	Glass Cracking β	Glass Fallout β	Gasket Degradation β
1	0.262	0.315	
2	0.3	0.295	
3	0.298	0.29	
4	0.322	0.346	0.32
5	0.289	0.268	0.317
6	0.343	0.311	
10	0.252	0.251	
11	0.261	0.359	
12	0.252	0.262	
13	0.25	0.25	
14	0.262	0.25	
15	0.277	0.271	
24	0.286	0.284	
25	0.293	0.293	
26	0.25	0.25	
27	0.256	0.257	
28	0.261	0.28	
29	0.25	0.317	
30	0.297	0.296	
31	0.255	0.255	
Geom. Mean of β	0.275	0.285	0.319

A different dispersion value was obtained by using a subset of the CW model configurations. Five configurations were selected (CW models #1-#5) which represented different levels of CW installation quality that might be present when conducting experimental lab tests on one configuration. They also could represent different levels of adequacy of the analytical model generated for the baseline CW configuration. The IDR and ODR results from this data set recorded in Table 5-8 and Table 5-9, respectively, were used to develop the new fragility parameters based on the actual demand data method defined in FEMA P-58 and reviewed in this chapter. Because analytical results were used instead when using this method, it was deemed as a pseudo-actual demand data method for the derivation of the fragility parameters. This method included a different calculation for the new median value (from Equation 6-3). Also, the new dispersion value was determined with the analytical database (in lieu of an experimental database). Therefore, in this application the dispersion takes into account the random variability in the analytical data set, β_r (Equation 6-4); and the uncertainty related to the ability to properly capture the CW behaviors based on the adequacy of the analytical database, β_u=0.25 (since data set includes only 5 analytical tests). Each set of in-plane and out-of-plane fragility parameters determined with this actual demand data method is summarized in Table 6-5. The new in-plane and out-of-plane glass cracking damage state fragility curves were then generated as shown in Figure 6-4 and Figure 6-5, respectively.

Table 6-5: Summary of Generated In-Plane and Out-of-Plane Fragility Parameters Derived from Actual Demand Data Method

Structural DS2 (In-Plane): Initial Glass Cracking			
θ	**β_r**	**β_u**	**β**
0.0251	0.0779	0.250	0.262
Structural DS2 (Out-of-Plane): Initial Glass Cracking			
θ	**β_r**	**β_u**	**β**
0.0457	0.0446	0.250	0.254

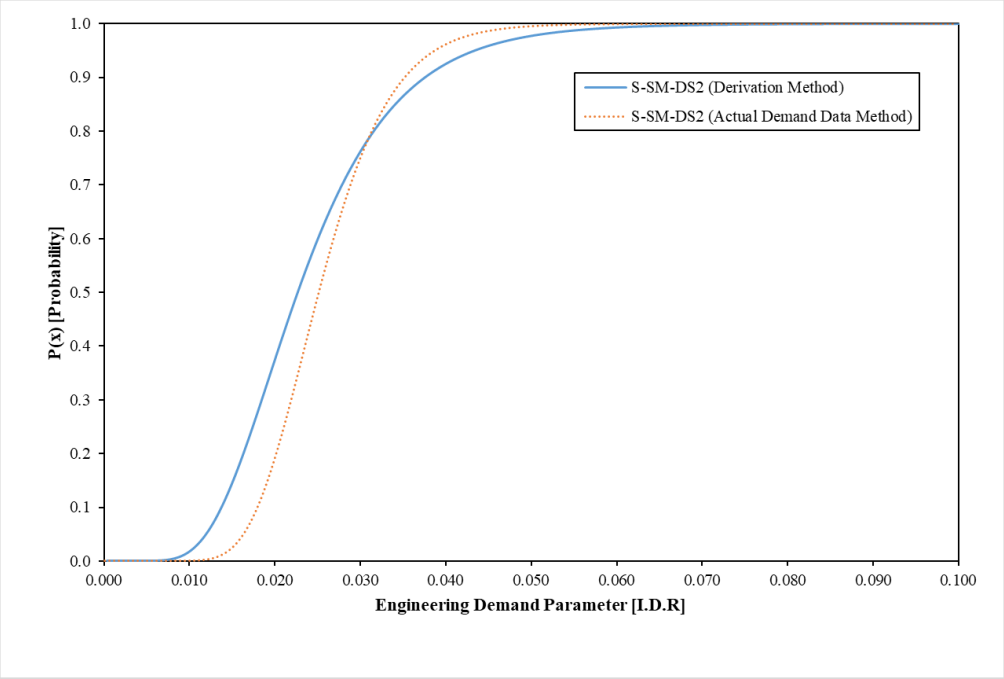

Figure 6-4: Comparison of generated fragility curves for the in-plane glass cracking DS from CW model #1 using derivation and actual demand data method

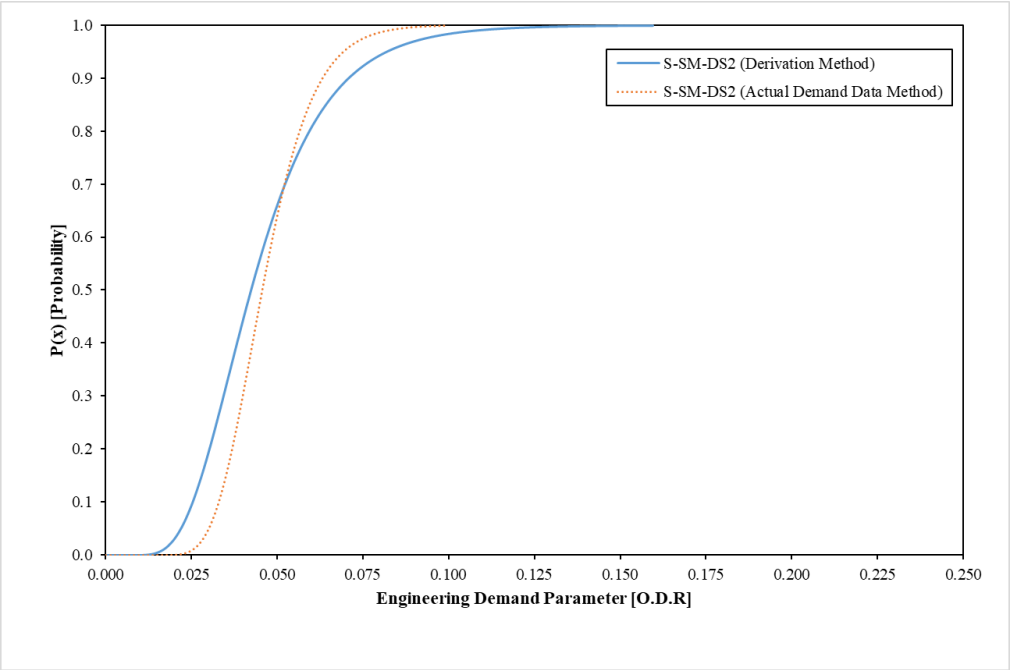

Figure 6-5: Comparison of generated fragility curves for the out-of-plane glass cracking DS from CW model #1 using derivation and actual demand data method

As observed in both plots, the fragility derived from the derivation method is more conservative up to approximately a probability of 80% in the in-plane case, and up to a probability of 70% in the out-of-plane case. After these aforementioned probability ranges, the fragility curves derived from the actual demand data method were more conservative. More comparisons between different levels of probabilities and their corresponding demand EDP values for each scenario were summarized in Table 6-6 and Table 6-7. These comparisons supported the need to consider different levels of dispersion from damage state demand results obtained from analytical CW models. This is because accounting for different levels of dispersion may affect how conservative the fragility curves may become.

These could affect how CWs are designed when implementing these analytically derived fragility curves for multi-hazard performance based engineering of glass curtain walls.

Table 6-6: Summary of Demand IDR θ_{crack} Values at Different Probabilities Using Actual Demand Data Method and Derivation Method

P(x)	θ_{crack} (Derivation)	θ_{crack} (Actual Demand Data)	% Difference
0.2 (20%)	0.0159	0.0202	23.8
0.5 (50%)	0.0222	0.0252	12.7
0.8 (80%)	0.0311	0.0314	1.0

Table 6-7: Summary of Demand ODR θ_{crack} Values at Different Probabilities Using Actual Demand Data Method and Derivation Method

P(x)	θ_{crack} (Derivation)	θ_{crack} (Actual Demand Data)	% Difference
0.2 (20%)	0.0303	0.0369	19.6
0.5 (50%)	0.0424	0.0457	7.5
0.8 (80%)	0.0594	0.0566	4.8

Finally, the development of a modified actual demand data method, which incorporates different levels of dispersions and uncertainty from analytical results, should be considered for the generation of fragility curves based on analytical models of glass curtain walls. It could incorporate the use of the actual demand data method for analytical data similar to what was implemented in this dispersion study. And it could be similarly based on how uncertainty is modeled for building structures being analyzed for seismic performance established in the FEMA P-58-1 document (Applied Technology Council (ATC) 2012). Where the dispersion accounted for the quality/confidence associated with building definitions and for the adequacy/completeness of the analytical model generated for the building for seismic response analysis.

6.6. Summary

Using results from Chapter 5, the derivation method implemented in the seismic fragility guidelines in FEMA P-58 was followed to calculate the fragility parameters (i.e. the median and dispersion) required to generate the in-plane and out-of-plane fragility curves for the simulated multi-panel CW. Multi-hazard fragility curves for the multi-panel CW system were generated and studied within this chapter.

Comparisons between the multi-panel CW fragility curves generated in this study and the single panel CW fragility curves created within the seismic fragility guidelines in FEMA P-58 were explored for the initial glass cracking damage state. This was done to check the applicability and performance effects of modeling with multi-panel CW instead of just a single CW panel. It was determined that the single panel CW fragility curves were conservative compared to the multi-panel CW fragility curves which had the glass cracking damage state occurring at smaller demand IDRs. Up to a 20% difference in the demand IDR capacity at a 20% probability of failure, and up to a 40% difference at the 80% probability of failure level. Even though the derivation method implemented for the analytically based fragility curves provided additional conservativeness, there were still other contributing factors that increased the demand IDR capacity in the multi-panel CW system that must be considered during performance based engineering of multi-panel CW sections. These include: the inclusion of different glass panel dimensions and aspect ratios within the CW section; the possible component interactions/responses that may decrease/increase likelihood of damages in different components (i.e. the occurrence of

one damage state in one panel may positively/negatively affect the performance of another adjacent panel); and the continuity of the CW framing members across a larger span.

While the dispersion value for the analytically derived fragility curves in this study was prescribed by the derivation method from FEMA P-58 (β=0.4), a different dispersion value was explored to observe the effects on the generated glass damage state fragility curves. Using the demand capacity results from a set of five CW model configurations analyzed in this study, the actual demand data method from the FEMA P-58 guidelines was implemented to develop different dispersion and median values. The fragility curves generated with the new dispersion values showed that after a certain level of probability is reached, the demand capacities from the fragility curves derived with the derivation method become less conservative than the fragility curves derived using the actual demand data method. For the in-plane glass cracking fragility, this switch in conservativeness occurred at a 80% probability of failure, while this changed at a 70% probability of failure for the out-of-plane fragility. Therefore, the applied alternative derivation method for modeling dispersion in the analytically based fragility curves was recommended to allow engineers to account for: the random dispersion in the analytical results, and the adequacy of the analytical model to capture the CW response behavior during simulations.

Chapter 7

Summary and Conclusions

7.1. Summary

This study completed computational research of glass curtain wall (CW) systems to support fragility curve development for multi-hazard performance-based engineering (PBE) design of CWs. A literature review was completed to primarily understand: identified earthquake- and hurricane-related damage states (DS) observed from tests and reconnaissance reports; previous FE modeling attempts of CWs; and experimental tests which could be used to validate the FE models generated in this study.

Based on the literature review, the Kawneer 1600 CW system was chosen as the basis for this computational study. A small scale experimental test series was completed to determine the equivalent clamping load at each screw location along the pressure plates as screws were tightened to a required torque. This load would then be applied in the FE model instead of modeling the screws/holes.

A 3D FE model of a single glass panel CW, based on the Kawneer 1600 CW system, was then generated in ABAQUS. The modeling approach incorporated explicit 3D FE modeling of the different CW components and component interactions. The specific interactions included: the aluminum-to-rubber component constraints; and the rubber component-to-glass and glass-to-frame component contact interactions. Additionally, semi-rigid transom-mullion framing connections were modeled and calibrated. The CW

model was then validated for in-plane and out-of-plane loading simulations by comparing the analytical results against experimental test results selected from the literature to simulate.

A one-story multi-panel CW section was then modeled to analyze the CW performance during applied loading simulations. This CW section included steel anchor connections modeled to observe the effects of a less rigid CW framing system-to-structural system connection, often not explored in laboratory tests. Additional CW models were then generated to include different parametric configuration changes (i.e. equivalent clamping loads, glass thicknesses, and glass-to-frame clearances) to analyze their effect on the overall CW performance. Analytical observations were identified and linked to different in- and out-of-plane structural DS. Non-structural DS were then identified as they related to the CW's moisture, air (condensation) and thermal performance.

The multi-panel CW models were then analyzed for identified engineering demand parameters (EDP) at which the structural DS had occurred. With these analytically derived EDP results, fragility curves were generated from calculated fragility parameter values (i.e. median and dispersion) using the Derivation method overviewed in the FEMA P-58 study. The generated seismic fragility curves based on the multi-panel CW models were then compared to the single panel CW fragility curves derived experimentally within the FEMA P-58 study. Finally, the effect of accounting for different dispersions and uncertainties in the generated fragility curves was studied.

7.2. Conclusions

From the small scale experimental testing of the Kawneer 1600 CW system, it is concluded that:

1. The total equivalent clamping load at each screw location due to an applied screw torque of 95 lb-in (11.3 N-m) was 1,800 N.
2. While a slightly uneven distribution was observed of the total equivalent clamping load to the gaskets in the glazing pocket cross-section (due to excessive deformations and non-linear behavior of the gaskets), it was assumed that the clamping load was evenly distributed in this study.

From the generated FE models of the single/multi-panel CW based on the Kawneer 1600 CW system, it is concluded that:

1. In addition to capturing similar CW damage states (i.e. glass cracking and glass-to-frame contact) approximated in the previous simplified FE modeling attempts, the generated 3D FE models could approximate additional key structural DS that represent actual breaches in the CW (i.e. glass/frame breach DS), which was not possible in the simplified FE models.
2. The ability to model and analyze different parametric CW configurations by incorporating different CW detailing and installation variations within the 3D FE model is more viable and practical when utilizing the 3D FE model. The previous simplified FE models could not easily replicate these since they did not explicitly model the components, which may lead to more calibrations being needed.

From the FE modeling of the one-story multi-panel CW section and the development of fragility curves, it is concluded that:

1. Key structural DS can be approximated when linked to analytical observations identified in the post-processing stage. These structural DS can also be linked to non-structural damage states (i.e. different levels of water penetration, air infiltration and thermal losses) since they can affect the CW's resistance to elemental impacts such as moisture, air, and heat.
2. When generating fragility curves, multi-panel CW sections should be analyzed instead of just single panel CWs. Not only is it more representative of field conditions, but there are also additional CW configuration factors that should be considered which could affect the overall multi-panel CW section's performance during either in-plane racking or out-of-plane pressure simulations, and subsequently the developed fragility curves.
3. The CW framing system-to-structural framing connections (with steel anchors) should be properly considered and modeled since these were analyzed to have provided more rotational flexibility to the connection fixities in the multi-panel CW section. Specifically, for the in-plane simulations, the modeled semi-rigid connections increased the demand interstory drift ratio capacities for the DS analyzed in the multi-panel CW model.
4. The fragility curves derived from the single panel CWs in the FEMA P-58 study were more conservative than those derived from the analyzed multi-panel CW section in this study. Factors that could explain this, which had not been previously considered or analyzed in past research, included: the effects of

multiple glass panel dimensions/aspect ratios; the possible component interactions/responses that may decrease/increase likelihood of damages in different components; and the continuity of the CW framing members across a larger span. More experimental testing of multi-panel CWs should be completed to further validate these conclusions.

5. The conservativeness of the analytically-derived fragility curves, can be affected when using dispersion values other than β=0.4 from the Derivation method implemented in FEMA P-58. Instead of using the default dispersion value, this study derived fragility parameters from the analytical results using a pseudo-Actual Demand Data method, similar to the Actual Demand Data method in FEMA P-58.

7.3. Limitations and Recommendations for Future Work

The limitations of the 3D finite element models generated for the single panel and multi-panel CW section in this study include:

1. Not being able to model other gasket degradation damage states (i.e. shifting, pullout, and push in) observed in experimental test studies, since the rubber gaskets were tie-constrained to the aluminum parts.
2. Not allowing the setting/side blocks the ability to slip/fallout of glazing pocket once enough glass panel rotation/translation had occurred.

3. Not capturing glass fracture/fallout since glass was modeled with a linear elastic material behavior. The glass model could be improved by using non-linear material behaviors which includes brittle cracking/fracture mode behaviors.
4. Not being able to complete the analysis as the fully applied drift (up to 152 mm or 6 in.) was never reached in the in-plane racking displacement simulations. This was due to excessive deformations of the rubber components which increased the difficulty of reaching convergence past a certain drift.
5. Being limited for now to only simulating static in-plane displacement and uniform pressure simulations with the CW models, as dynamic/cyclic simulations have not been validated yet. Contact interactions modeled for the CWs could be affected as a result of implementing a dynamic/cyclic analysis.

Recommendations for future work include:

1. Completing more component level testing of the different CW components/interactions to help model more accurately the material/component behaviors. This can improve the CW model's ability to approximate the actual CW's performance during loading simulations. Should primarily test on the different rubber components (i.e. gaskets and setting/side blocks) to improve and capture any excessive deformations during analysis.
2. Completing out-of-plane pressure tests for the modeled glass CW system (instead of just the glass panel) to further verify the out-of-plane validation process used in this study, and the ability to capture the out-of-plane CW behaviors with the 3D CW models.

3. Executing more experimental CW tests (on both single and multi-panel CWs) to further validate the use of the explicit 3D FE models generated to properly analyze actual CW response when different configurations are considered (i.e. panel sizes, steel anchor connections, different framing system extrusions, glass-to-frame clearances, etc.).
4. Considering implementing an alternative derivation method for modeling dispersion in the analytically-based fragility curves. This alternative derivation method could be similar to the approach followed in this study, or the approach established in FEMA P-58-1 for modeling uncertainty when analyzing seismic performance response of building structures (Applied Technology Council (ATC) 2012).

References

AAMA. (2009a). AAMA 501.4-09: Recommended Static Test Method for Evaluating Curtain Wall and Storefront Systems Subjected to Seismic and Wind Induced Interstory Drifts. AAMA.

AAMA. (2009b). AAMA 501.6-09: Recommended Dynamic Test Method For Determining The Seismic Drift Causing Glass Fallout From A Wall System. AAMA.

ABAQUS. (2017). "SIMULIA Online User Assistance." <http://docs.software.vt.edu:8080/abaqus/v2017/English/DSSIMULIA_Established.htm> (Nov. 29, 2018).

Abiassi, J. J. (1981). "The strength of weathered window glass using surface characteristics." PhD Thesis, Texas Tech University.

Aiello, C., Caterino, N., Maddaloni, G., Bonati, A., Franco, A., and Occhiuzzi, A. (2018). "Experimental and numerical investigation of cyclic response of a glass curtain wall for seismic performance assessment." Construction and Building Materials, 187, 596–609.

AISC. (2017). AISC Steel Construction Manual, 15th Edition.

American Architectural Manufacturers Association. (2015). AAMA TIR-A11-15: Maximum Allowable Deflection of Framing Systems for Building Cladding Components at Design Wind Loads. AAMA.

American Society of Civil Engineers. (2017). Minimum Design Loads and Associated Criteria for Buildings and Other Structures. American Society of Civil Engineers, Reston, VA.

Ander, G. D. (2016). "Windows and Glazing | WBDG Whole Building Design Guide." Whole Building Design Guide, <https://www.wbdg.org/resources/windows-and-glazing> (Jan. 22, 2018).

Applied Technology Council (ATC). (2012). "FEMA P-58-1 Seismic Performance Assessment of Buildings: Volume I-Methodology." 278.

Architectural Engineering Institute. (2013). Curtain Wall Systems: A Primer. ASCE manuals and reports on engineering practice, (A. M. Memari, ed.), American Society of Civil Engineers, Reston, Virginia.

Bailey, J. R., Minor, J. E., and Tock, R. W. (1990). "Response of structurally glazed insulating glass units to wind pressures." Journal of Wind Engineering and Industrial Aerodynamics, 36(Part 2), 1163–1171.

Barluenga, G., Ladipo, O., Reichard, G., and Leon, R. T. (2016). "CEMENT BASED FACADES FOR MID-RISE COMMERCIAL SUSTAINABLE AND RESILIENT BUILDINGS." 9.

Beason, W. L. (1980). "Failure Prediction Model for Window Glass. | National Technical Reports Library - NTIS."

<https://ntrl.ntis.gov/NTRL/dashboard/searchResults/titleDetail/PB81148421.xhtml> (Jan. 27, 2018).

Beason, W. L., Meyers, G. E., and James, R. W. (1984). "Hurricane related window glass damage in Houston." Journal of Structural Engineering, 110(12), 2843–2857.

Bedon, C., and Amadio, C. (2018). "Numerical assessment of vibration control systems for multi-hazard design and mitigation of glass curtain walls." Journal of Building Engineering, 15, 1–13.

Behr, R. A. (1998a). "Seismic Performance of Architectural Glass in Mid-Rise Curtain Wall." Journal of Architectural Engineering, 5(3), 105–106.

Behr, R. A. (1998b). "Seismic Performance of Architectural Glass in Mid-Rise Curtain Wall." Journal of Architectural Engineering, 4(3), 94–98.

Behr, R. A., and Belarbi, A. (1996). "Seismic Test Methods for Architectural Glazing Systems." Earthquake Spectra, 12(1).

Behr, R. A., Belarbi, A., and Brown, A. T. (1995a). "Seismic Performance of Architectural Glass in a Storefront Wall System." Earthquake Spectra, 11(3), 367–391.

Behr, R. A., Belarbi, A., and Culp, J. H. (1995b). "Dynamic racking tests of curtain wall glass elements with in-plane and out-of-plane motions." Earthquake engineering & structural dynamics, 24(1), 1–14.

Behr, R. A., and Minor, J. E. (1994). "A survey of glazing system behavior in multi-story buildings during hurricane andrew." The Structural Design of Tall and Special Buildings, 3(3), 143–161.

Behr, R. A., Minor, J. E., and Kremer, P. A. (1996). "Effects of accelerated weathering on architectural laminated glass in a windstorm environment." Science and Technology of Building Seals, Sealants, Glazing, and Waterproofing: Sixth Volume, ASTM International.

Behr, R. A., Minor, J. E., Linden, M. P., and Vallabhan, C. V. G. (1985). "Laminated glass units under uniform lateral pressure." Journal of structural Engineering, 111(5), 1037–1050.

Bouwkamp, J. G. (1961). "Behavior of window panels under in-plane forces." Bulletin of the Seismological Society of America, 51(1), 85–109.

Broker, K. A., Fisher, S., and Memari, A. M. (2012). "Seismic Racking Test Evaluation of Silicone Used in a Four-Sided Structural Sealant Glazed Curtain Wall System." Journal of ASTM International, 9(3), 104144.

Brueggeman, J. L., Behr, R. A., Wulfert, H., Memari, A. M., and Kremer, P. A. (2000). "Dynamic Racking Performance of an Earthquake Isolated Curtain Wall System.pdf." Earthquake Spectra, 16.

Caterino, N., Del Zoppo, M., Maddaloni, G., Bonati, A., Cavanna, G., and Occhiuzzi, A. (2017). Seismic assessment and finite element modelling of glazed curtain walls.

Cauffman, S. A. (2006). Performance of Physical Structures in Hurricane Katrina & Hurricane Rita: A Reconnaissance Report. DIANE Publishing.

Dean, S., Memari, A., Chen, X., Kremer, P., and Behr, R. (2006). "Seismic Performance of Two-Side Structural Silicone Glazing Systems." Journal of ASTM International, 3(10), 100407.

Deschenes, J. P., Behr, R. A., Pantelides, C. P., and Minor, J. E. (1991). "Dynamic Racking Performance of Curtain Wall Glass Elements. | National Technical Reports Library - NTIS." <https://ntrl.ntis.gov/NTRL/dashboard/searchResults/titleDetail/PB92140631.xhtml> (Jan. 23, 2018).

Duser, A. V., Anand, J., and Bennison, S. J. (1999). "Analysis of Glass/Polyvinyl Butyral Laminates Subjected to Uniform Pressure." Journal of Engineering Mechanics, 125(4), 435–442.

E06 Committee. (2004). ASTM E283-04 (Reapproved 2012): Test Method for Determining Rate of Air Leakage Through Exterior Windows, Curtain Walls, and Doors Under Specified Pressure Differences Across the Specimen. ASTM International.

E06 Committee. (2012). ASTM E998-12: Test Method for Structural Performance of Glass in Windows, Curtain Walls, and Doors Under the Influence of Uniform Static Loads by Nondestructive Method. ASTM International.

E06 Committee. (2013). ASTM E1886-13a: Test Method for Performance of Exterior Windows, Curtain Walls, Doors, and Impact Protective Systems Impacted by Missile(s) and Exposed to Cyclic Pressure Differentials. ASTM International.

E06 Committee. (2014a). ASTM E330/E330M-14: Test Method for Structural Performance of Exterior Windows, Doors, Skylights and Curtain Walls by Uniform Static Air Pressure Difference. ASTM International.

E06 Committee. (2014b). ASTM E1233/E1233M-14: Test Method for Structural Performance of Exterior Windows, Doors, Skylights, and Curtain Walls by Cyclic Air Pressure Differential. ASTM International.

E06 Committee. (2015). ASTM E997-15: Test Method for Evaluating Glass Breakage Probability Under the Influence of Uniform Static Loads by Proof Load Testing. ASTM E997, ASTM International.

E06 Committee. (2016a). ASTM E331-00 (Reapproved 2016): Test Method for Water Penetration of Exterior Windows, Skylights, Doors, and Curtain Walls by Uniform Static Air Pressure Difference. ASTM International.

E06 Committee. (2016b). Practice for Determining Load Resistance of Glass in Buildings. ASTM International.

E06 Committee. (2017). ASTM E1996-17: Specification for Performance of Exterior Windows, Curtain Walls, Doors, and Impact Protective Systems Impacted by Windborne Debris in Hurricanes. ASTM International.

FEMA 488. (2005). "Hurricane Charley in Florida: Observations, Recommendations, and Technical Guidance. Mitigation Assessment Team Report. | National Technical Reports Library - NTIS." <https://ntrl.ntis.gov/NTRL/dashboard/searchResults/titleDetail/PB2008108231.xhtml> (Dec. 22, 2017).

FEMA 489. (2005). "Hurricane Ivan in Alabama and Florida: Observations, Recommendations, and Technical Guidance. Mitigation Assessment Team Report. | National Technical Reports Library - NTIS." <https://ntrl.ntis.gov/NTRL/dashboard/searchResults/titleDetail/PB2008108266.xhtml> (Dec. 22, 2017).

FEMA 548. (2006). “Summary Report on Building Performance. Hurricane Katrina 2005. | National Technical Reports Library - NTIS.” <https://ntrl.ntis.gov/NTRL/dashboard/searchResults/titleDetail/PB2008107010.xhtml> (Dec. 22, 2017).

Galli, U. (2012). “Seismic behaviour of curtain wall facades: a comparison between experimental mock up test and finite element method analysis.”

Gavanski, E. (2010). “Behaviour of glass plates under wind loads.” Ph.D., The University of Western Ontario (Canada), Canada.

Gent, A. N. (1958). “On the Relation between Indentation Hardness and Young’s Modulus.” Rubber Chemistry and Technology, 31(4), 896–906.

Haldimann, M. (2006). “Fracture Strength of Structural Glass Elements - Analytical and Numerical Modelling, Testing and Design.” 222.

Horst, A. D. (1991). “Behaviour of Heat Strengthened Laminated Glass in Severe Windstorm Environments.” M.S. Thesis, University of Missouri-Rolla.

Huang, B., Chen, S., Lu, W., and Mosalam, K. M. (2017). “Seismic demand and experimental evaluation of the nonstructural building curtain wall: A review.” Soil Dynamics and Earthquake Engineering, 100, 16–33.

International Code Council, Inc. (2015). 2015 International Building Code.

Johar, S. (1981). “Dynamic Fatigue of Flat Glass, Phase II: Final Report.” Ontario Research Foundation.

Kanabolo, D. C., and Norville, S. H. (1985). “The Strength of New Window Glass Plates Using Surface Characteristics.” 124.

Kawneer. (2019a). “Kawneer North America | Aluminum Curtain Walls, Storefront Framing.” Kawneer.com, <https://www.kawneer.com/kawneer/north_america/en/info_page/home.asp> (Jul. 9, 2019).

Kawneer. (2019b). “Kawneer 1600 Wall System TM 1 Curtain Wall - Architectural Detail Manual.” <https://www.kawneer.com/kawneer/north_america/catalog/97911/ADMD010EN.pdf> (Feb. 15, 2019).

Lim, K. Y. S., and King, A. B. (1991). The Behaviour of External Glazing Systems Under Seismic In-Plane Racking.

Linden, M. P., Minor, J. E., Behr, R., and Vallabhan, C. V. G. (1983). “Evaluation of Laterally Loaded Laminated Glass Units By Theory and Experiment. | National Technical Reports Library - NTIS.” <https://ntrl.ntis.gov/NTRL/dashboard/searchResults/titleDetail/PB84216423.xhtml> (Dec. 22, 2017).

Linden, M. P., Minor, J. E., and Vallabhan, C. V. G. (1984). “Evaluation of Laterally Loaded Laminated Glass Units by Theory and Experiment. Supplemental Report No. 1. | National Technical Reports Library - NTIS.” <https://ntrl.ntis.gov/NTRL/dashboard/searchResults/titleDetail/PB85111532.xhtml> (Feb. 1, 2018).

Memari, A. M., Behr, R. A., and Kremer, P. A. (2003). “Seismic behavior of curtain walls containing insulating glass units.” Journal of architectural engineering, 9(2), 70–85.

Memari, A. M., Behr, R. A., and Kremer, P. A. (2004). “Dynamic Racking Crescendo Tests on Architectural Glass Fitted with Anchored Pet Film.” Journal of Architectural Engineering, 10(1), 5–14.

Memari, A. M., Fisher, S., Krumenacker, C., Broker, K. A., and Modrich, R.-U. (2012). “Evaluation of the Structural Sealant for Use in a Four-Sided Structural Sealant Glazing Curtain-Wall System for a Hospital Building.” Journal of ASTM International, 9(4), 104143.

Memari, A. M., Kremer, P. A., and Behr, R. A. (2006). “Architectural Glass Panels with Rounded Corners to Mitigate Earthquake Damage.” Earthquake Spectra, 22(1), 129–150.

Memari, A. M., O’Brien, W. C., Kremer, P. A., and Behr, R. A. (2011a). “Architectural Glass Seismic Behavior Fragility Curve Development.” FEMA.

Memari, Ali. M., Shirazi, A., Kremer, P. A., and Behr, R. A. (2011b). “Development of Finite-Element Modeling Approach for Lateral Load Analysis of Dry-Glazed Curtain Walls.” Journal of Architectural Engineering, 17(1), 24–33.

Nagalla, S. R., Vallabhan, C. V. G., Minor, J. E., and Norville, H. S. (1985). “Stresses in Layered Glass Units and Monolithic Glass Plates. | National Technical Reports Library - NTIS.” <https://ntrl.ntis.gov/NTRL/dashboard/searchResults/titleDetail/PB86142015.xhtml> (Dec. 22, 2017).

NIST. (2006). “Performance of Physical Structures in Hurricane Katrina and Hurricane Rita: A Reconnaissance Report. | National Technical Reports Library - NTIS.” <https://ntrl.ntis.gov/NTRL/dashboard/searchResults/titleDetail/PB2006112362.xhtml> (Dec. 22, 2017).

O’Brien, W. C., Memari, A. M., Kremer, P. A., and Behr, R. A. (2012). “Fragility Curves for Architectural Glass in Stick-Built Glazing Systems.” Earthquake Spectra, 28(2), 639–665.

Overend, M., and Zammit, K. (2012). “A computer algorithm for determining the tensile strength of float glass.” Engineering Structures, 45, 68–77.

Pantelides, C. P., and Behr, R. A. (1994). “Dynamic in-plane racking tests of curtain wall glass elements.” Earthquake Engineering & Structural Dynamics, 23(2), 211–228.

Pantelides, C. P., Horst, A. D., Shankland, R. B., and Minor, J. E. (1991). “Behavior of Laminated and Filmed Glass in Severe Windstorm Environments. | National Technical Reports Library - NTIS.” <https://ntrl.ntis.gov/NTRL/dashboard/searchResults/titleDetail/PB93167666.xhtml> (Dec. 22, 2017).

Puga, H., Olmos, B., Olmos, L., Jara, J. M., and Jara, M. (2015). “Damage Assessment of Curtain Wall Glass.” Journal of Physics: Conference Series, 628, 012052.

Reznik, P. L. (1986). “Failure strengths of laminated glass units.” PhD Thesis, Texas Tech University.

SEAOC. (2013). 2012 IBC: SEAOC Structural/Seismic Design Manual, Volume 1:Code Application Examples. SEAOC.

Shanmugam, V. (1993). “Dynamic Testing of Curtain Wall Glass Components with In-Plane and Out-of-Plane Motions.pdf.” M.S. Thesis, University of Missouri-Rolla.

Shelby, J. E. (2007). “Compositions and Properties of Commercial Glasses.” Introduction to Glass Science and Technology, Royal Society of Chemistry, Cambridge, 262–274.

Shirazi, A. (2005). “Development of a Seismic Vulnerability Evaluation Procedure for Architectural Glass Curtain Walls.” Pennsylvania State University.

Svensson, D. (2015). “Computational Method for Bulging in Insulating Glass Units.” Lund University, Sweden.

Tahir, H. (2016). “Development of Fragility Curve Database for Multi-Hazard Performance Based Design.” 148.

Thurston, S. J., and King, A. B. (1992). Two-Directional Cyclic Racking of Corner Curtain Wall Glazing.

Vallabhan, C. V. G., Aşik, M. Z., and Kandil, K. (1997). “Analysis of structural glazing systems.” Computers & Structures, 65(2), 231–239.

Vega, R. E., and Konz, R. C. (2010). “Cladding Performance of High-Rise Buildings in the Houston CBD during Hurricane Ike.” Forensic Engineering 2009: Pathology of the Built Environment, 739–748.

Venkata, V. K. (2004). “Development and testing of hurricane resistant laminated glass fiber reinforced composite window panels.” M.S., University of Missouri - Columbia, United States -- Missouri.

Vigener, N., and Brown, M. A. (2016a). “Curtain Walls | WBDG Whole Building Design Guide.” Whole Building Design Guide, <https://www.wbdg.org/guides-specifications/building-envelope-design-guide/fenestration-systems/curtain-walls> (Sep. 9, 2018).

Vigener, N., and Brown, M. A. (2016b). “Fenestration Systems | WBDG - Whole Building Design Guide.” Whole Building Design Guide, <https://www.wbdg.org/guides-specifications/building-envelope-design-guide/fenestration-systems> (May 26, 2019).

Appendix A

Commentary for Chapter 4: Finite Element Modeling

A.1. Overview of C3D8R Elements, SC8R Elements, and C3D8 Elements in ABAQUS

In ABAQUS, he C3D8R elements are described as a first-order (linear), reduced-integration with hourglass control, 8-node "brick" elements which only have 3 translational degrees-of-freedom per node. The reduced-integration means there is only one Gaussian integration point used within the element in ABAQUS. This was sometimes used in lieu of the full-integration because the increase to 8 Gauss points in the fully integrated C3D8 brick element would have increased the computational time. However, to avoid the hourglass mode which is more likely to occur with reduced integration, the local mesh seeds along the thickness of a part is usually set to make sure at least 4 elements through the thickness are generated during automated meshing.

The SC8R elements are described by ABAQUS as a first-order (linear), reduced integration with hourglass control, quadrilateral in-plane general-purpose continuum shell element. In contrast to conventional shell elements, the continuum shell element can be used to discretize a solid 3D part and use solid's nodal geometry to define its own thickness (ABAQUS 2017). Therefore, while modeled as a solid element in appearance, the SC8R element still uses the same kinematic and constitutive behavior as a conventional shell element in its underlying element formulation (ABAQUS 2017). A simple way to envision this is with a continuum shell element, the user is generating a shell element from a solid

body rather than generating a solid body from a shell element, as is the case for conventional shell used in thin wall structural bodies. However, the SC8R element only has 3 translational degrees-of-freedom since it is based on a solid continuum.

The SC8R element is also capable of accounting for finite membrane strains, large rotations, and changes in thickness which make it advantageous during a geometric non-linear analysis. For the section integration, five Gauss points through the thickness were decided as sufficient enough for capturing the sectional behaviors of the thin mullion walls and the glass panels in this study. Additionally, these continuum shell elements can be used to model contact problems which is needed for the mullion and glass components in this FE modeling scheme. The SC8R continuum shell element is allowed to be directly connected to first-order solid "brick" elements without the need for kinematic transitions (i.e. a shell-to-solid coupling constraint) because if combined, the continuum shell element and continuum element would have shared nodes essentially. This is exploited for the mullion parts when modeling the mullion lip region. This is because the mullion lip, which is modeled as a solid element, sits directly on top of the thin mullion wall, which is modeled as a continuum shell as shown in Figure 4-5.

The C3D8 solid "brick" elements use a full-integration formulation to solve for the sectional behaviors with 8 Gauss points, unlike the reduced-integrations C3D8R elements which uses only 1 Gauss point for the element stiffness integration. Caution was used when using these full integration elements since using these may cause shear locking issues. Shear locking can occur in these full-integration elements during bending because due to their numerical formulation, shear strains that do not exist may generate and cause the shear stiffness in the element to activate, which causes overstiff behavior when trying to model

flexural behavior. While the recommended number of elements used through the thickness is at least four when trying to minimize these shear locking effects, only two elements through the thickness of the mesh were used in some instances in the FE model such as the gasket parts. This is because the mesh did not show any issues with shear locking through different model runs. Furthermore, the computational time was an another reason for choosing only two full-integration elements through the thickness with larger in-plane mesh size, rather than having to use at least four reduced-integration elements through the thickness with smaller in-plane mesh size in order for elements to have acceptable dimension aspect ratios.

A.2. Overview of Modeling with Kinematic Coupling Constraints in ABAQUS

This kinematic coupling constraint in ABAQUS essentially constrains the motion of all the nodes on a selected surface to the rigid body motion of the reference point. This reference point becomes a new node with six degrees of freedom (3 translational/3 rotational) in the global coordinate system during analysis. With the kinematic coupling option, the degrees of freedom (DOF) on the selected surface nodes are eliminated as they become constrained to the selected degrees of freedom on the reference node, which for the framing model would only include the translational DOF because the continuum shell elements meshed to the mullion walls have only 3 translational DOF's. For the case of the setting blocks, these also only have 3 translational DOF's so the reference node would only constrain these three. The reference point can be generated either to lie directly on a surface or offset from the surface specified.

A.3. Overview of ABAQUS Contact Interactions and Constraints Methods

This section highlights how each of the three used interactions and constraint methods were employed within ABAQUS in the curtain wall system FE models generated in this study. These are tie constraints, contact pairs, and general contacts (ABAQUS 2017).

A.3.1. Tie Constraints

These tie constraints constrain the translational degrees of freedom to have the same displacements on both surfaces in the aluminum-to-gasket contact pair. This works even if the mesh on either surface is not identical. A master and slave surface must be defined between the contact pair surfaces selected. Both the master and slave surfaces are element-based which allow ABAQUS/Standard and ABAQUS/Explicit to use the surface-to-surface formulation to enforce these tie constraints. Additionally, ABAQUS uses a position tolerance criterion which ensures that only the slave and master nodes which are close to each other (within the position tolerance distance) are actually tied together. This is useful in cases where the slave surface is smaller than the master surface and there is no need for additional partitioning to make the surfaces exact. Example being the fixed glazing gaskets surfaces in contact with either the mullion or pressure plates. Furthermore, when using the surface-based constraint, tie coefficients are generated to interpolate quantities between the master nodes to a slave node. With the surface-to-surface formulation, which is useful for mismatched meshes, ABAQUS determines these tie coefficients using an average based the a number of master nodes in a finite region per slave node (ABAQUS 2017).

A.3.2. Contact Pairs

For the normal behavior contact property modeled throughout the FE model, the "Hard" contact pressure-overclosure relationship was primarily chosen for this mechanical behavior. This default relationship allows for any possible pressure to generate and transmit between the surfaces once contact has occurred. It also allows for surface separation after contact, so when the surfaces have separated no pressure can be generated. A constraint enforcement method must also be chosen to determine how this Hard contact relationship will be enforced numerically to help with convergence. Therefore, the penalty method was chosen, specifically the linear behavior choice, which essentially implements a stiff approximation of the hard contact relationship and allows for pressure to generate proportionally to the amount of penetration allowed to occur between the two surfaces.

For the tangential behavior, sliding friction between the gasket-to-glass surfaces can be defined within the contact properties with a Coulomb friction model within ABAQUS. Under the default "Penalty" friction formulation in this frictional model, it relates allowable shear stress to the contact pressures developed along two contact surfaces. Likewise, the coefficient of friction (isotropic friction) input is incorporated in calculations to determine when points along the surfaces begin to slip/stick relative to one another once critical shear stresses have developed (ABAQUS 2017).

With the normal and tangential contact properties previously established, ABAQUS implements these throughout the analysis using contact formulations which involve a contact discretization, tracking approach and the master-slave role assignments. For this interaction, the contact pair algorithm was chosen such that these inclusions within

the contact formulation could be manually chosen. Within the contact pair, the surface-to-surface discretization was selected for the application of conditional constraints along the contact surfaces which generates contact constraints based on average regions surrounding multiple slave nodes. This contact discretization provides better stress and pressure results than the node-to-surface formulation. The finite-sliding tracking approach was implemented, in tandem with the ABAQUS' path-based tracking algorithm, to allow for arbitrary relative separation, sliding and rotation between any point on both contact surfaces at every increment throughout the analysis run (ABAQUS 2017). This works best when geometric non-linearity occurs in the analysis which in this computational study is necessary due to large displacements occurring in both in-plane and out-of-plane directions between the contact surfaces. In addition, appropriate selection of the master and slave surface roles, which are based on guidelines established in the ABAQUS documentation, were required when using the contact pair algorithm to allow the formulation to perform accurately. For example, in the rubber gasket-to-glass interaction, the glass panel surfaces (on both face sides) were selected as the master surfaces due to having a stiffer body and coarser mesh relative to the selected slave surface which was the fixed glazing gasket surfaces in contact with the glass panel faces. Similar master-slave surface roles were also applied to the setting/side block surfaces in contact with the glass edge surfaces (i.e. master=glass; slave=rubber blocks). Therefore, this shows how the contact pair interaction, with the finite-sliding, surface-to-surface formulations, is used to capture the changing contact conditions relating to the normal and tangential contact behaviors which will be calibrated in the following sections.

A.3.3. General Contact

This general contact algorithm was chosen because it implemented the same underlying formulations used in the contact pair algorithm discussed above for defining a contact discretization, tracking approach and the master-slave role assignments. The only difference that constituted the use of the general contact algorithm were the additional contact discretization methods offered in addition to the surface-to-surface contact, which included the edge-to-surface, edge-to-edge, and vertex-to-surface contact. While the surface-to-surface discretization is still the primary contact formulation, the other supplementary formulations come into effect once necessary feature angle criteria are met during contact. This was useful because while glass-to-frame contact could occur in the glass corner regions, there was a possibility that there would not only be just a simple surface-to-surface contact occurring, but rather an edge-to-surface contact or both occurring in sequential analysis increments. In which case the edge of the glass corners could touch that flat surface of the mullion glazing lip and then further glass rotation/translation would lead to a full on surface-to-surface contact. As for the tracking approach, the default for general contact is the finite-sliding tracking approach which is the same as what was implemented for the contact pair algorithm in previous section.

Additionally, manual selection of the master-slave role assignments was completed to define the surface pairs that were known to get into contact. For this case, the master surfaces are the mullion lip surfaces just opposite of the glass edge surfaces, and the slave surfaces are the glass edge surfaces as shown in Figure 4-21.

A.4. Overview of Non-Linear FE Analysis using ABAQUS/Standard

This section will overview some key information regarding the non-linear analysis methods implemented to run the in-plane and out-of-plane simulations on the single CW system model in Chapter 4.

A.4.1. Newton Raphson Numerical Analysis

ABAQUS/Standard implements the Newton-Raphson numerical analysis method which seeks to establish equilibrium for every increment of an applied displacement (or load) by calculating the response at an increment of time within an analysis step (ABAQUS 2017). During the first iteration within a given time step increment, a calculated residual force (and subsequently a residual moment) is checked for equilibrium, which is the difference between the applied force and an initial "guess" of the restoring force in the structural system. If this magnitude of the residual force (moment) is within acceptable tolerance criteria, then the system is deemed to have converged and in approximate equilibrium before proceeding to the next time step increment. However, if convergence is not met then another iteration is performed by calculating a new trial displacement based on an updated displacement correction (and rotation correction), which incorporates the previous iteration's non-convergent residual force (moment) and tangent stiffness. This updated trial displacement (rotation) is then used to obtain a new tangent stiffness and consequently calculate the new residual force in the non-linear system. This iterative Newton-Raphson process is repeated until the residuals at every time step increment have converged within the acceptable tolerance criteria set for the force and moment residuals

to obtain the non-linear solution. The primary default convergence residual tolerance criterion for ABAQUS is set at 0.5% (0.005) for both the non-linear residual force and residual moment checks. Subsequently, the default displacement (rotation) correction tolerance was set to 1% (0.01) of the total incremental displacement (rotation) of a given time step increment. These convergence tolerances were deemed appropriate for allowing an acceptable level of engineering error during the non-linear analysis.

Appendix B

Generated Fragility Curves for CW Model

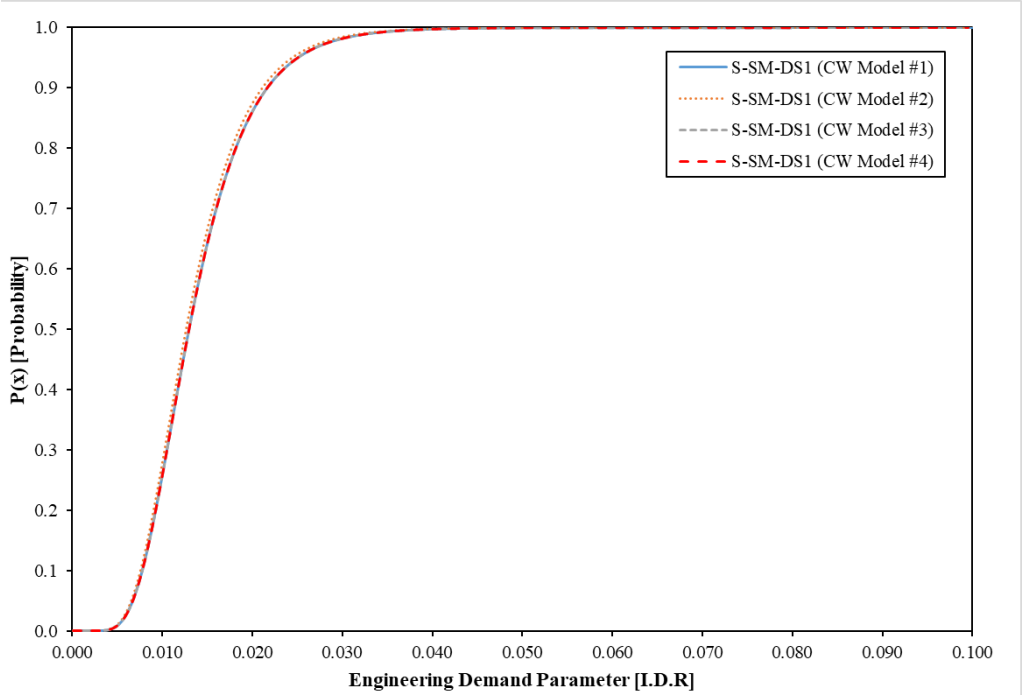

Appendix Figure B-1: Generated fragility curves for initial glass-to-frame contact damage state affected by equivalent clamping load (CW models #1, #2-#4)

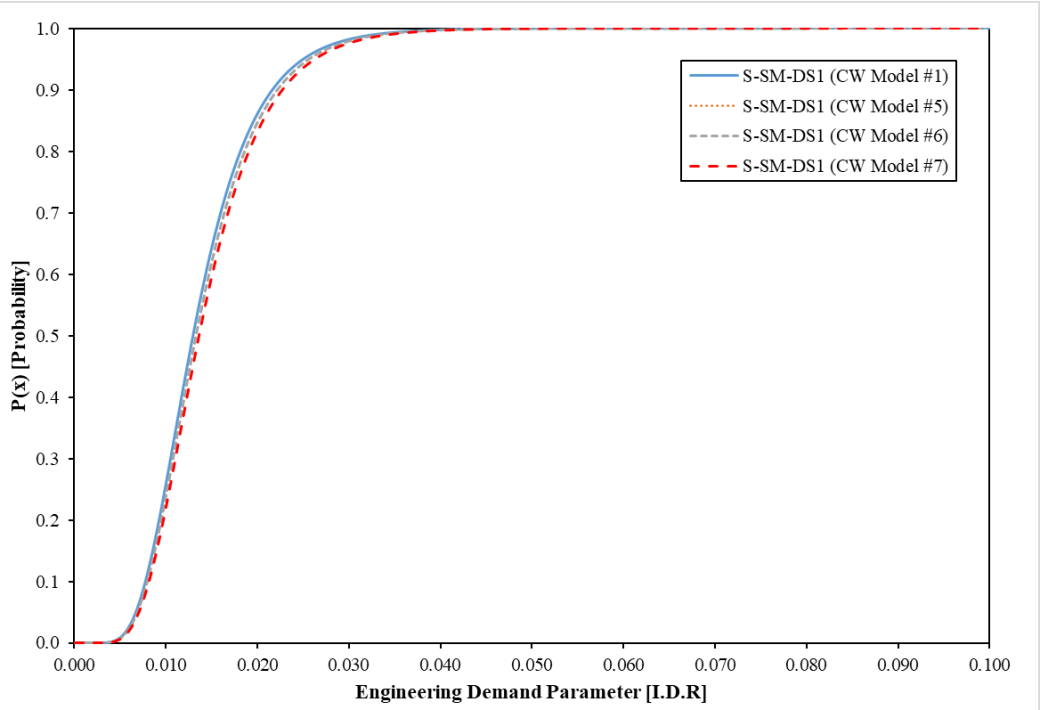

Appendix Figure B-2: Generated fragility curves for initial glass-to-frame contact damage state affected by glass thickness (CW models #1, #5-#7)

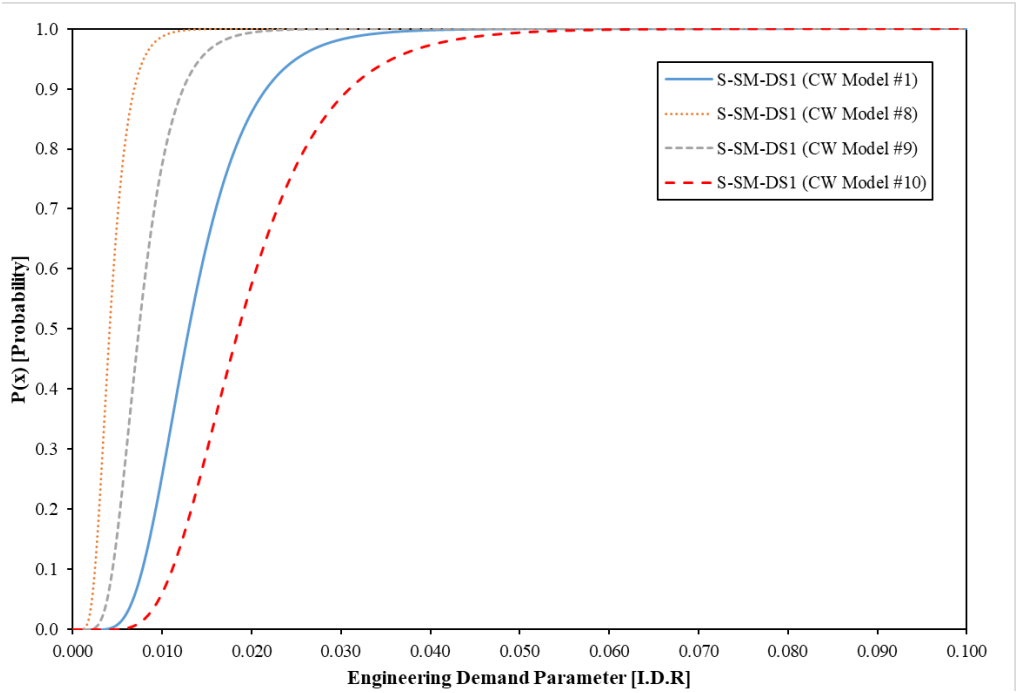

Appendix Figure B-3: Generated fragility curves for initial glass-to-frame contact damage state affected by glass-to-frame clearance (CW models #1, #8-#10)

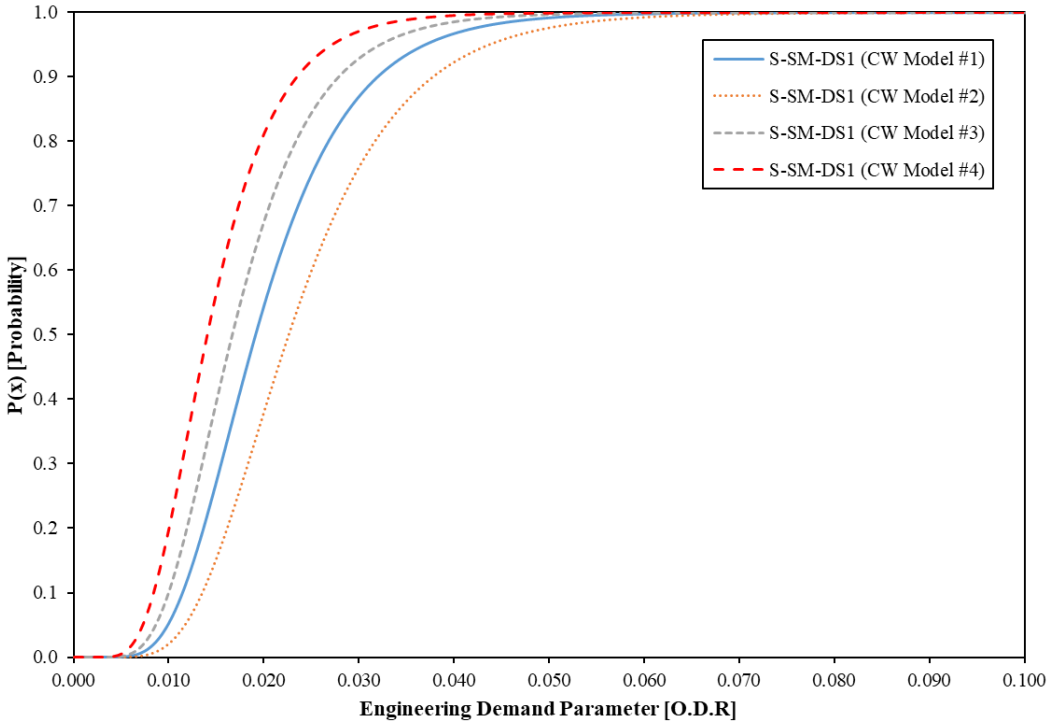

Appendix Figure B-4: Generated fragility curves for glass/frame breach damage state contact damage state affected by equivalent clamping load (CW models #1, #2-#4)

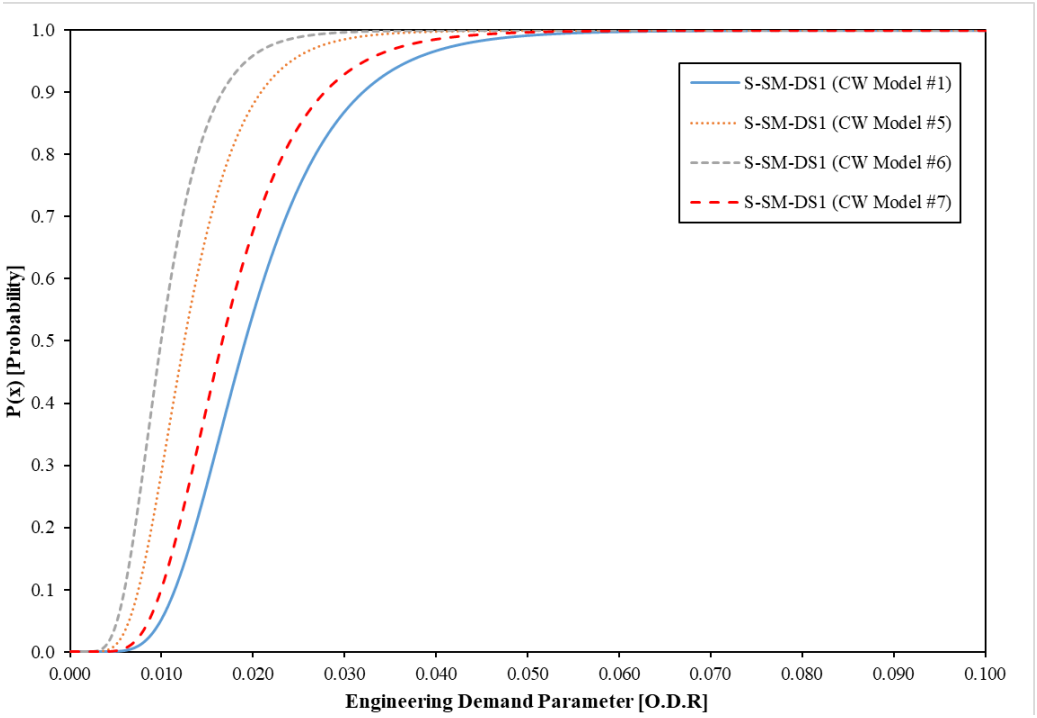

Appendix Figure B-5: Generated fragility curves for glass/frame breach damage state contact damage state affected by glass thickness (CW models #1, #5-#7)

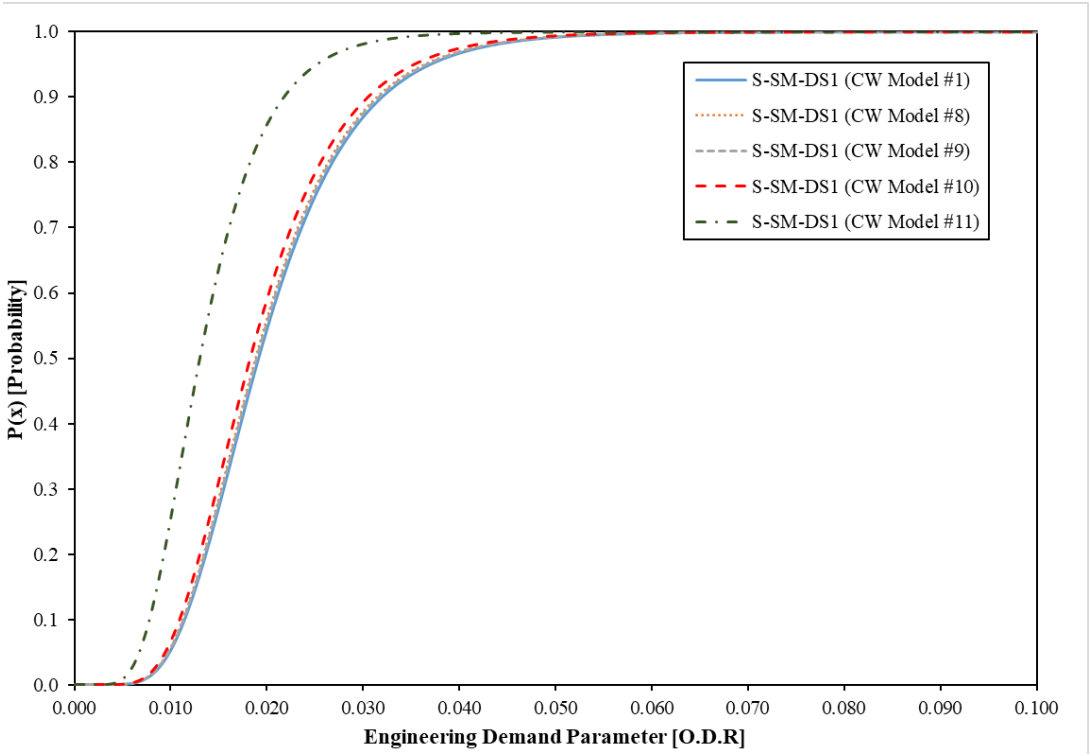

Appendix Figure B-6: Generated fragility curves for glass/frame breach damage state contact damage state affected by glass-to-frame clearance (CW models #1, #8-#11)